Université de Strasbourg

École et observatoire des sciences de la Terre
Université de Strasbourg

UNIVERSITÉ DE STRASBOURG

ÉCOLE DOCTORALE SCIENCES DE LA TERRE ET DE L'ENVIRONNEMENT
Institute Terre et Environnement de Strasbourg

THÈSE

Présentée par :

Lucas MEDEIROS BOFILL

Soutenance prévu le :
19 Septembre 2024

Pour obtenir le grade de :

Docteur de l'Université de Strasbourg

Discipline : Sciences de la Terre et de l'Environnement
Spécialité : Sédimentologie et écoulement de fluide

From Outcrop to Fluid-Flow: Sedimentary Architecture, Permeability Heterogeneity, and Effect of Sedimentary Facies in Fluid-Flow Modelling: A Case Study of the Middle Buntsandstein Continental Sandstones (Lower Triassic, Eastern France)

Thèse dirigée par :
M. SCHÄFER Gerhard Professeur, Université de Strasbourg

Rapporteurs :
M. HINDERER Matthias Professeur, Technische Universität Darmstadt
M. GOLFIER Fabrice Professeur, Université de Lorraine

Autres membres du jury :
M. BOZETTI Guilherme Maître de conférences, Université de Strasbourg
Mme. BOURQUIN Sylvie Directrice de recherche CNRS, Université de Rennes 1

Président du jury :
M. SCHUSTER Mathieu Directeur de recherche CNRS, Université de Strasbourg

“*Fate shuffles the cards, and we play*” – Arthur Schopenhauer

ACKNOWLEDGEMENTS

It has been a long journey. Moving abroad to pursue a PhD is an amazing life opportunity, but it certainly comes with its costs. Living in a different culture, weather, and language, staying away from your loved ones, watching them getting older, and eventually losing people you love without the chance to say goodbye were the biggest challenges of this period. These were even more difficult than the actual work on the PhD, which was a great joy to undertake. I honour my dear Dona Nica, whom I considered a grandmother, and who passed away in May 2023.

Even though pursuing a PhD is often a lonely commitment, it would not have been possible without a solid foundation, which I would like to acknowledge.

Gui Bozetti, who believed in my potential and advocated for my selection since my first interview, provided all the support and freedom I needed to conduct this research. His passion as a sedimentologist, rigour as a paper reviewer, and constant striving for excellence have greatly enhanced the quality of this work. I certainly consider him a supervisor, even though it was not officially possible. Moreover, he became a friend, and it was a pleasure to get to know him and his family.

Gerhard Schäfer, who luckily for me, accepted to be my supervisor in an ongoing PhD project. His extensive knowledge, combined with a positive support and dedication to his PhD and master's students, always available for long discussions, were essential for the results obtained in this work.

To Laura, my wife, the greatest gift geology has given me and my foundation here in France. We have been on this journey together for almost eleven years. I want to thank her not only for being an amazing life partner, but also for assisting me in my work. Her insightful thinking during our talks enhanced the quality of this thesis.

Jean-François Ghienne and Mathieu Schuster, two reference sedimentologists, partners in field work and sedimentological discussions, whose sharp insights elevated the outcomes of our papers to another level. It was a pleasure to work with them.

Philippe Ackerer, for his scientific and personal support throughout the entire PhD process. His willingness to help Laura and me since our arrival demonstrated his quality as a human being, which had a great impact in our lives.

Claiton Scherer and Ezequiel de Souza, who I had the pleasure of hosting as visiting researchers in Strasbourg to assist in field work and discussions. Working with them since 2015 provided me the foundational skills to conduct this PhD. They are not only professional colleagues, but also friends from whom I am always learning.

I also acknowledge Garibaldi Armelenti for his robust knowledge in petrography, essential for our second paper (Chapter 3); the team from ES-Gèothermie, Albert Genter, Carole Glaas, and Eleonore Dalmais, for providing access and facilities to describe the core samples; Mike Heap for collaborating with petrophysical measurements; Felipe Guadagnin for sharing his knowledge about digital outcrop models; Gabriela Knobelock for her assistance in my last days of fieldwork and in our second paper; Philippe Duringer for indicating some of the key outcrops of the Buntsandstein sandstones; and Renato Paes de Almeida for sharing his knowledge in our insightful discussion about fluvial deposits.

I acknowledge the Interdisciplinary Thematic Institutes (ITI) for funding fieldwork, equipment, and conferences, which were fundamental for the development of my research and professional growth. To all the staff at Unistra, from the administrative team to those responsible for keeping our office clean, I thank them for their helpfulness and patience over these three years. I also extend my gratitude to all my PhD colleagues, researchers, professors at Unistra, and the friends I met during this period in Strasbourg.

To my parents, Gustavo and Maria Bernadette, for their unconditional love, wisdom, and dedication in providing the best education. They are responsible for everything. I will never forget the day we celebrated together my acceptance to the doctoral school. I also thank my siblings, Diego, Maria, and Carlos, who inspire me both personally and professionally, along with Sheena and Barbara, who I am lucky to have as sisters-in-law; and my dear nephews and nieces, Juju, Chico, Eloisa, Conrado, Camila, and Felipe. I would like to particularly express my gratitude to my sister, Maria, who, during this period, impeccably took care of all our parents' needs while being a dedicated high-performance mother, lawyer, and athlete (triathlete!).

To those that came all the way from Brazil to visit us: my lovely in-laws Julio, Joycela, and Luísa; and my dear friends Eduardo, João Rubens, Gabi, Ana Rita, and Max. And to the ones who could not come but gave support from a distance, my aunts

Tereca, Fátima, and Bety, and cousins (too many to list here) for their supportive messages, and in memory of my aunt Clara and uncles Pillo and Eduardo, I miss you all very much; my borrowed family Adair and Luciana for calling me and connecting me with my roots in Farol de Santa Marta; Andrea for her true love and commitment with my parents; and Vinicius and Marjorie, for their family friendship. And to all my long-term friends, whom I am lucky to have, for our constant exchange of messages and calls. All these people (and some I might have forgotten) helped to fuel my energy to stay strong during these three years of PhD. I also thank Anne for agreeing to be my guarantor for my apartment rental in Strasbourg.

I would finally like to thank the jury members, Mathias Hinderer, Sylvie Bourquin, and Fabrice Golfier, for making themselves available for reading, evaluating, and correcting my manuscript, and for their willingness to personally attend the defence in Strasbourg, demonstrating their commitment and support. I will extend this acknowledgement to the reviewers of our papers, Nigel Mountney, Oliver Wakefield, and the anonymous reviewers, for their comments that significantly enhanced the quality of our research.

Merci à tous.

Table of Contents

TABLE OF CONTENTS ..... **IV**

LIST OF FIGURES ..... **VI**

LIST OF TABLES ..... **XI**

RÉSUMÉ ÉTENDU EN FRANÇAIS **1**

1. CHAPTER 1: GENERAL INTRODUCTION **9**

1.1. RATIONALE 9
1.2. BACKGROUND AND CONTEXT 10
1.2.1. Sedimentary facies analysis *10*
1.2.1.1. Sedimentary processes and products 13
1.2.2. Braided fluvial systems *20*
1.2.3. Aeolian systems *21*
1.2.4. Triassic Reservoirs in Europe *22*
1.2.5. The Lower Triassic deposits in eastern France *22*
1.2.5.1. Geothermal and lithium exploration in the Lower Triassic deep reservoir 25
1.2.5.2. The Lower Triassic shallow aquifer 26
1.2.6. Permeability heterogeneity in fluvio-aeolian systems *27*
1.2.7. Permeability data in the Buntsandstein Group (Gr.) *28*
1.2.8. Groundwater flow and solute-transport modelling *29*
1.2.9. The use of sedimentary facies analysis in groundwater fluid-flow model *31*
1.3. SUPPLEMENTARY EXTERNAL ANALYSIS 32

2. CHAPTER 2: QUANTITATIVE FACIES ANALYSIS OF A FLUVIO-AEOLIAN SYSTEM: LOWER TRIASSIC BUNTSANDSTEIN GROUP, EASTERN FRANCE **33**

ABSTRACT 33
2.1. INTRODUCTION 34
2.2. STUDY AREA AND GEOLOGICAL SETTING 36
2.3. METHODS AND MATERIALS 37
2.4. RESULTS 40
2.4.1. Sedimentary facies and their associations *40*
2.4.1.1. Fluvial channel facies association (FC) 43
2.4.1.2. Wind- and water-laid facies association (WWL) 59
2.4.1.3. Lateral and vertical interactions between facies associations 66
2.5. DISCUSSION 68
2.5.1. Fluvial channel facies association (FC) depositional controlling factors *68*
2.5.2. Wind- and water-laid facies association depositional controlling factors *69*
2.5.3. Large-scale depositional system *71*
2.6. CONCLUSIONS 75

3. CHAPTER 3: SEDIMENTARY FACIES CONTROL ON PERMEABILITY HETEROGENEITIES: THE MIDDLE BUNTSANDSTEIN CONTINENTAL SANDSTONES (LOWER TRIASSIC, EASTERN FRANCE) **77**

ABSTRACT 77
3.1. INTRODUCTION 78
3.2. STUDY AREA AND GEOLOGICAL SETTINGS 81
3.2.1. Sedimentological background of the Lower Grès Vosgien Formation *82*
3.3. MATERIALS AND METHODS 85
3.4. RESULTS 88
3.4.1. Permeability at a facies association scale *89*
3.4.2. Permeability at a facies scale *89*

3.4.2.1. Fluvial channel facies association 90
3.4.2.2. Wind- and water-laid facies association 91
3.4.3. Outcrop scale vertical trends 93
3.4.4. Measurements of permeability in the laboratory 96
3.4.5. Petrographic characteristics 96
3.5. DISCUSSION 103
3.5.1. Fluvial flow-regime and permeability results 104
3.5.2. Sedimentology, architecture, and permeability of the wind- and water-laid facies association 105
3.5.3. Utility of outcrop data for subsurface predictions 105
3.6. CONCLUSIONS 111

4. CHAPTER 4: THE SIGNIFICANCE OF SEDIMENTARY FACIES HETEROGENEITY IN SOLUTE TRANSPORT MODELS: CASE STUDY USING AN OUTCROP OF THE LOWER TRIASSIC SANDSTONES AQUIFER, EASTERN FRANCE 113

ABSTRACT 113
4.1. INTRODUCTION 114
4.2. METHODS 117
4.2.1. From outcrop to discretised conceptual model 117
4.2.2. Stochastic distribution of K 121
4.2.3. Deterministic distribution of K 122
4.2.4. Fluid-flow and particle tracking modelling 122
4.2.5. Quantification of upscaled anisotropy 124
4.2.6. Quantification of macrodispersivity using time moments analysis 125
4.3. RESULTS 126
4.3.1. Scenarios of hydraulic conductivity (K) distribution 126
4.3.2. Particle tracking - Horizontal flow 132
4.3.2.1. Description 132
4.3.2.2. Interpretation 135
4.3.2.3. Comparison between scenarios 136
4.3.2.4. Macrodispersivity 137
4.3.3. Particle tracking - Vertical flow 139
4.3.3.1. Description 140
4.3.3.2. Interpretation 142
4.3.3.3. Comparison between scenarios 142
4.3.3. Upscaled anisotropy 145
4.4. DISCUSSIONS 145
4.4.3. Effects of different scales of heterogeneity 146
4.4.2. Macrodispersivity 147
4.5. CONCLUSIONS 148

5. CHAPTER 5: SUMMARY AND GENERAL CONCLUSIONS 151

5.1. FUTURE RESEARCH MAY FOCUS ON: 155

REFERENCES 157

ANNEX 190

LIST OF FIGURES

Figure 1-1: Facies analysis workflow (adapted from Dalrymple, 2010). 12

Figure 1-2: Bedforms stability fields relative to grain size and flow velocity (Southard and Boguchwal, 1990)..... 14

Figure 1-3: Bedforms developed by distinct flow regimes, in response to different flow velocities in a fixed flow depth and grain sizes of sands (adapted from Simons et al. (1965) (chez Miall, 2010). It also presented the facies observed in the Lower Grès Vosgien Formation (LGV), corresponding to their respective bedforms. Sr = ripple mark sandstone; St = trough cross-bedded sandstone; Ss = sigmoidal cross-bedded sandstone; Sl = low-angle cross-bedded sandstone; Sad = antidune sandstone. 14

Figure 1-4: Sedimentation units representing humpback bars, with overpassing gravel. (A) Characteristics of the unit. (B) Overpassing process responsible for generating (A) (Allen, 1983b). 16

Figure 1-5: Simple profile presenting the main processes of transport and deposition of aeolian deposits (Caputo, 2023). 18

Figure 1-6: Types of ripple stratification according to the climbing-angle settings (subcritical, critical, and supercritical) (Hunter, 1977b). 19

Figure 1-7: Processes of formation and examples of products, in rock record and in modern examples, of deflation lag surfaces. (A) Gilf Kebir, Libyan Desert, Egypt (Brookfield and Silvestro, 2010); (B) Namibia (Bristow and Mountney, 2013). (A) and (B) in a plan view. The rock record photo was taken by the current author, at the Ramstein Castle Ruin, in the Vosges du Nord region, eastern France. 20

Figure 1-8: Location of the study area, and geological settings. Adapted from Bouly and Demassieux (1996), Guillocheau et al. (2000), Herivaux and Marechal (2019) and Duringer et al. (2019). 24

Figure 2-1: (A) Study area location; (B) regional stratigraphy, adapted from Bouly and Demassieux (1996), Guillocheau et al. (2000), Herivaux and Marechal (2019) and Duringer et al. (2019). 37

Figure 2-2: Facies associations, their thickness proportion measured for the Lower Grès Vosgien Formation, their respective facies and facies proportions, and a schematic log showing the architectural elements. See further details on architectural elements in Sections 2.4.1.1 and 2.4.1.2. 41

Figure 2-3: Facies of the fluvial channel facies association: (A) trough cross-bedded sandstone, St. Red arrow: cross-set of gravelly sandstone. Green arrow: cross-set of slightly gravelly sandstone. Outcrop: LGV7; (B) sigmoidal cross-bedded sandstone, Ss. Gravel content is absent in the topset and concentrated in higher angle foresets. Outcrop: LGV7; (C) laminated mudstone,Fl, between foresets of facies St. Outcrop: LGV1; (D) breccia of angular mud clasts; (E) low-angle cross-bedded sandstone, Sl. Outcrop: LGV5; (F) planar view of parting lineation in facies Sl.Outcrop: LGV7; (G) convex-up top, with internal low-angle truncated cross-bedded sandstone, Sad, interpreted as antidune. Red arrows indicate planes where palaeocurrents, of opposite directions, were measured. Outcrop: LGV9; (H) Facies St, Ss and Sl recognised in core samples. Core EPS1, diameter: 8 cm. 45

Figure 2-4: Downstream transition between LS and TSE, within the same bed, separated by reactivation surfaces. Outcrop: LGV7. 46

Figure 2-5: Fluvial channel facies association (FC) quantitative data. GS = gravelly sandstone; SG = slightly gravelly sandstone; AWG = sandstone apparently without gravel; WG = sandstone without gravel. 47

Figure 2-6 : Aggradational element. (A) Outcrop LGV7; (B) outcrop LGV10. 52

Figure 2-7: (A) Downstream accretion element (DA). Outcrop: LGV8. (B) Trough simple element (TSE) and aggradational element (AE). Outcrop: LGV4. 53

Figure 2-8: (A) Sigmoidal simple element (SSE), and laminated sand sheet (LS). Outcrop: LGV12. (B) SSE, with the absence of gravel in the topset, concentrated in the foresets. Result of the overpassing process (Allen, 1983b). Outcrop: LGV8. 56

Figure 2-9: Fluvial architectural elements, their respective quantitative data, and illustration. 57

Figure 2-10: Wind- and water-laid facies association (WWL). (A) Translatent wind ripples, Sla. Outcrop: LGV5; (B) (C) centimetre-scale upward transition between facies Sla, Sa (and/or Mb) and Sw, indicating gradual outpace of water-table rise against sediment supply. Outcrop: LGV8 and LGV6, respectively; (D) largest aeolian dune described in the Lower Grès Vosgien Formation, delimited by the dashed yellow line. Outcrop: LGV6; (E) aeolian dune (AD) between hybrid sand sheet (HSS), overlying a blowout hollow surface. Outcrop LGV2; (F) WWL in outcrop (LGV5) and in the EPS1 core samples. 61

Figure 2-11: Wind- and water-laid facies association (WWL) quantitative data. 64

Figure 2-12: (A) Processes involved in generating the wind- and water-laid facies association (WWL); (B) different vertical architectures of the WWL, and their respective proportions of occurrences, recorded in the Lower Grès Vosgien Formation; (C) e.g. Architecture 1. Outcrop: LGV7; (D) e.g. Architecture 3. Outcrop: LGV1; (E) e.g. Architecture 4. Outcrop: LGV5; (F) e.g. Architectures 4 and 5. Outcrop: LGV10; (G) e.g. Architecture 1. Outcrop: LGV5; (H) e.g. Architecture 2. Outcrop: LGV7; (I) distribution of thickness of each architecture presented in (B). 65

Figure 2-13: Vertical and lateral architecture distribution of the Lower Grès Vosgien Formation, in an outcrop scale. Outcrop: LGV7. 67

Figure 2-14: Block diagram of wind- and water-laid facies association (WWL), representing two distinct temporal moments. (A) Formation of hybrid sand sheet architectural element, influenced by water-table level close to the depositional surface, and by ephemeral floods; (B) WWL during low water-table level. Sand deflation by winnowing, leaving behind deflation lag and blowout hollows, followed by accumulation and migration of aeolian dunes. 71

Figure 2-15: (A) Log from the core EPS1 exhibiting the intercalations between fluvial channel facies association (FC), and wind- and water-laid facies association (WWL) recorded within the upper 100 m of the Lower Grès Vosgien Formation (LGV); (B) fluvial cross-set thickness occurrences along 100 m of the EPS1 core, which represents the top of the LGV (Aichholzer, 2019). Rs and p-value in blue, all cross-sets (red and blue dots) are analysed. In red, only cross-sets thicker than 50 cm are analysed. Thinning-upward trends are observed, however, a strong correlation between cross-set thickness and depth is only observed for the larger (>50 cm) cross-sets; (C) strong correlation between FC thickness and depth; (D) weak negative correlation between WWL thickness and depth. However, the high p-value indicates that the dataset used for this analysis is not enough. 72

Figure 3-1: (A) Study area located in eastern France. (B) Schematic representation of the Buntsandstein Gr. geological settings, showing geographic proximity from outcrops (red dot in the Vosges mountains) to the shallow aquifer (west of the Vosges) and to the lithium-rich geothermal reservoir (east of the Vosges, in the Upper Rhine Graben – URG axis) (adapted from Bouly and Demassieux, 1996, Guillocheau et al., 2000, Herivaux and Marechal, 2019, and Duringer et al., 2019). (C) Outcrop locations in the Vosges mountains, and well EPS1 in the URG axis. 82

Figure 3-2: Main sedimentary facies in the Lower Grès Vosgien Formation, in outcrops and core. Facies code in white square and black letters belong to the fluvial channel facies association; facies code in black square and white letters belong to the wind- and water-laid facies association. Red solid lines represent the boundary between two facies associations, and the yellow dashed lines indicate limits between individual facies within the same facies association. 85

Figure 3-3: Distribution of outcrop permeability data based on facies association (f.a.) and facies scale. (A) The highest permeability values are related to the fluvial channel f.a. The wind- and water-laid

f.a. present a bimodal distribution of permeability. (B) In facies scale, the highest permeability values of the fluvial channel f.a. are related to the facies St, followed by facies Ss. Facies Sl consistently presented the lowest permeability values in the fluvial channel f.a. (C) In the wind- and water-laid f.a. the highest permeability values are related to aeolian dunes, and the hybrid sand sheets recorded the lowest values. The hybrid sand sheets show more than one mode of values, indicating permeability heterogeneity in a smaller scale influencing permeability values distribution. 92

Figure 3-4: (A) Permeability responses based on the different classes of gravel content in the fluvial channel f.a. The highest permeability values were measured in gravelly sandstones (GS) and slightly gravelly sandstones (SG), and the lowest permeability values measured in sandstones without gravel (WG), and sandstones apparently without gravel (AWG); (B) Permeability responses in bleached sand bodies. Bleached sandstones recorded the lowest permeability values. 93

Figure 3-5: Permeability logs tied with sedimentary logs from different outcrops (locations shown in Fig. 3-1), showing permeability responses to facies and facies associations variations. St = facies trough cross-bedded sandstone; Ss = facies sigmoidal cross-bedded sandstone; Sl = facies low-angle cross-bedded sandstone; HSS = hybrid sand sheet; AD = aeolian dune. 94

Figure 3-6: Outcrop scale of lateral facies and facies association distribution, combined with permeability logs. (A) Architectural analysis of the outcrop Out-5. (B) Facies association analysis showing consistent lower permeability, up to 4 orders of magnitude, in the WWL f.a. (C) Permeability contrasts following variation of facies within de fluvial channel f.a. (D) Layer of hybrid sand sheet generating a permeability contrast 3 orders of magnitude smaller compared to facies below and above. 95

Figure 3-7: Original (red symbols) and present (blue symbols) composition of the Lower Grès Vosgien Formation sandstones samples plotted on Folk (1968) diagram, showing that not significant composition changes happened during diagenesis. The original primary composition was weakly modified by the transformation of lithoclasts to lithic pseudomatrix. 97

Figure 3-8: Schematic diagenetic sequence for the analysed sandstones from the Lower Grès Vosgien Formation. Thick bars represent intense processes, thin and dashed lines progressively less prominent processes. The figure highlight eodiagenetic compaction as the main diagenetic process, followed by clay infiltration and formation of lithic pseudomatrix, both during eodiagenesis. 98

Figure 3-9: (A) Facies Sl with ductile lithoclasts of low-grade metamorphic rocks (red arrow); and lithic pseudomatrix (green arrows). (B) Compacted hybrid sand sheet, with abundant infiltrated clay (red arrow). (C) Pre-compaction quartz overgrowth (red arrows) stabilising the framework in facies St. (D) Syn-compaction quartz overgrowth (red arrows) filling intergranular porosity in facies St. (E) Intergranular porosity (light blue zones marked with IP) in aeolian dune. (F) Highly compacted fabric in hybrid sand sheet. 101

Figure 3-10: Mean values of petrographic characteristics observed per facies. From the left to the right, in the x-axis, the mean and median permeability values of each facies decrease (AD >Ss>Sl>HSS). (A) Variations of grain sizes among facies; (B) sorting degree based on graphic standard deviation (Folk, 1980); (C) percentage of ductile grains, mainly represented by low-grade metamorphic rocks, (E) lithic pseudomatrix formed by the squeeze of lithoclasts during compaction; (D) packing degree. (F) clay content, mainly represented by infiltrated clay; and (G) quartz overgrowth. All these characteristics contribute to compaction, which is the main diagenetic process affecting permeability and (H) porosity. St = facies trough cross-bedded sandstone; Sl = facies low-angle cross-bedded sandstone; AD = aeolian dune; HSS = hybrid sand sheet. 102

Figure 3-11: Log domain distribution of core permeability data: (A) facies association (f.a.) scale; (B) facies scale within the fluvial channel (FC) f.a.; (C) facies scale within the wind- and water-laid (WWL) f.a. Similar patterns of relative permeability between facies and facies association as observed in outcrops (Fig. 3-3). Rectangles represent values between the 1st and 3rd quartile

(Q1 and Q2), and dots represents individual samples which permeability value lies above 1.5 times the difference between Q1 and Q3 [1.5x(Q3-Q1)]..... 106

Figure 3-12: Permeability logs tied with sedimentary log from core samples. Similar trends as those observed in outcrop data of permeability response when transecting the distinct facies and facies associations (f.a.) (see Fig. 3-5)..... 107

Figure 3-13: Permeability and connected porosity measured from plug samples from outcrops (data from this study; orange and dark grey symbols) and from core samples of the well EPS1 (data from Goupil et al., 2022; blue symbols). Also included are laboratory data for other sandstones from the Buntsandstein from EPS1 (data from Griffiths et al., 2016; Heap et al., 2017; Kushnir et al., 2018, 2023; light grey symbols). All data are gas permeability measurements collected under a confining pressure of 1 MPa. LGV = Lower Grès Vosgien Formation; St = facies trough cross-bedded sandstone; Ss = facies sigmoidal cross-bedded sandstone; Sl = facies low-angle cross-bedded sandstone; AD = aeolian dune; HSS = hybrid sand sheet..... 109

Figure 3-14: (A) Geological conceptual model of facies distribution in the upper part of the Lower Grès Vosgien Formation (LGV), based on the well EPS1, and outcrop data from Bofill et al. (2024); (B) compilation of the two facies association in the LGV, their controlling factors of facies deposition, and permeability distribution per facies; (C) relationship between the permeability responses and the main petrographic characteristics..... 110

Figure 4-1: (A) Location of the outcrop (LGV7) used for this study; (B) Outcrop (Falkenstein Castle ruin – LGV7) used to realistically represent a 2D vertical section of an aquifer..... 118

Figure 4-2: Interpretation of outcrop LGV7, showing zones of dominance of specific sedimentary facies, in their respective facies association. FC = Fluvial channel facies association; WWL = wind- and water-laid facies association; St = trough cross-bedded sandstone facies; Ss = sigmoidal cross-bedded sandstone facies; Sl = low-angle cross-bedded sandstone facies; HSS = hybrid sand sheet facies; AD = aeolian dune facies. 118

Figure 4-3: Polygons generated in FEFLOW 8.0.® 119

Figure 4-4: Mesh of the numerical flow model, refined at the zones of specific facies polygon edges. 119

Figure 4-5: Mesh optimised using a built-in tool from FEFLOW, that improves the mesh quality by smoothing the distribution of internal angles of the mesh elements. (A) Before mesh smoothing; (B) after mesh smoothing. 120

Figure 4-6: Boundary conditions for horizontal flow (left) and vertical flow (right), to run the particle tracking across the model domain..... 123

Figure 4-7: Cumulative mean stabilisation behaviour of particles' residence time. 124

Figure 4-8: Scenario I used as a reference conceptual model, since incorporates the highest complexity. Discretised by facies, with hydraulic conductivity (K) distributed stochastically. Facies codes: St = trough cross-bedded sandstone; Ss = sigmoidal cross-bedded sandstone; Sl = low-angle cross-bedded sandstone; HSS = hybrid sand sheet sandstone. Remark: the dark lines shown in the overview correspond to very fine discretised grid with a high number of triangular cells..... 127

Figure 4-9: Scenario II, discretised by facies, with deterministic hydraulic conductivity (K) based on the median K measured for each facies..... 128

Figure 4-10: Scenario III is discretised by facies associations, with hydraulic conductivity (K) distributed stochastically, based on the weighted K values of the facies comprising each facies association..... 129

Figure 4-11: Scenario IV is discretised by facies association with deterministic hydraulic conductivity (K) based on the weighted median K values of the facies comprising each facies association. 130

Figure 4-12: Scenario V, weighted hydraulic conductivity (K) distributed stochastically not constrained by sedimentary features geometries, such as facies or facies associations..... 131

Figure 4-13: Histograms of the horizontal flow particles residence time at the difference scenarios. 132

Figure 4-14: Cumulative curves of horizontal flow particles' residence time across the distinct scenarios. 138

Figure 4-15: Comparison of particle tracking and macrodispersivity results, for the horizontal flow in the different scenarios. 139

Figure 4-16: Histograms of the vertical flow particles residence time at the difference scenarios. 140

Figure 4-17: Cumulative curves of vertical flow particles' residence time across the distinct scenarios. 144

Figure 4-18: Comparison of particle tracking and macrodispersivity results with the reference model (scenario I), for the vertical. 145

LIST OF TABLES

Table 2-1: Classes of gravel content in sandstone, and field criteria for their definition. 40

Table 2-2: Sedimentary facies observed in the Lower Grès Vosgien Formation. 41

Table 2-3: Fluvial channel facies association (FC) dataset concerning architectural element proportions; mean set thickness of sets below 78 cm, within the aggradational element (AE) (M.S.T. < 78 cm); coefficient of variance of cross-set thickness in the AE (CV) (calculated where data of minimum 30 sets were available); mean original dune height (Hm) (Eq. (1)); and mean flow depth (d) (Eq. (2)). The dataset is presented by individual FC, bounded by WWL deposits. The term “complete FC unit” refers to FC deposits where upper and lower boundaries are recognised. Where more than one FC unit is identified in the same outcrop, the point (outcrop code) is followed by a sequence number (e.g., LGV2-2). “Incomplete” refers to outcrops where lower or upper FC boundaries were not exposed. DA = downstream accretion element; TSE = trough simple element; SSE = sigmoidal simple element; LS = laminated sand sheet. Grey areas refer to no data available. 48

Table 3-1: Classes defined for gravel content in sand bodies of the Lower Grès Vosgien Formation, based on field criteria (Bofill et al., 2024). 83

Table 3-2: Descriptive statistics of permeability results in a facies association scale. LGV = Lower Grès Vosgien Formation. 89

Table 3-3: Descriptive statistics of permeability results, in a facies scale, of the fluvial channel facies association. LGV = Lower Grès Vosgien Formation; St = facies trough cross-bedded sandstone; Ss = facies sigmoidal cross-bedded sandstone; Sl = facies low-angle cross-bedded sandstone. 90

Table 3-4: Descriptive statistics of permeability results within the wind- and water-laid facies association. LGV = Lower Grès Vosgien Formation. 91

Table 3-5: Mean permeability and connected porosity per facies, measured in the laboratory. St = facies trough cross-bedded sandstone; Ss = facies sigmoidal cross-bedded sandstone; Sl = facies low-angle cross-bedded sandstone; AD = aeolian dune; HSS = hybrid sand sheet. 96

Table 3-6: Diagenetic constituents and their respective percentages. 100

Table 4-1: Permeability data used in Scenario I. Original median hydraulic conductivity (Ko) measured in the field, and median hydraulic conductivity of the stochastically generated data by Monte Carlo sampling (Kmc). σ2(o) is the variance of the original dataset in the log domain; σ2(mc) is the variance of the stochastically generated data, in the log domain. Kmc/Ko indicates how much the simulated data approximates the real data. 127

Table 4-2: Hydraulic conductivity (K) is based on the weighted median K of the facies association.. 129

Table 4-3: Original weighted median hydraulic conductivity (Ko) measured in the field, and median hydraulic conductivity of the stochastically generated data by Monte Carlo sampling (Kmc), by facies association. Kmc/Ko indicates how much the simulated data approximates the real data. 129

Table 4-4 Hydraulic conductivity (K) is based on the weighted median K of the Lower Grès Vosgien Formation using the proportion of each facies within the Lower Grès Vosgien Formation (Bofill et al., 2024). Ko = original K from field measurements. 131

Table 4-5: Percentage of particles from Scenario I that arrived before the first particles of the other scenarios; after the last particles of the other scenarios; and the overlap of particles that arrived in the same range of residence time observed in Scenario I 137

Table 4-6: Results obtained from the horizontal flow. 138

Table 4-7: Results obtained from the vertical flow. 144

Table 4-8: Upscaled anisotropy calculated for each scenario of heterogeneity representation 145

RÉSUMÉ ÉTENDU EN FRANÇAIS

CONTEXTE DE L'ÉTUDE

Le rôle important des systèmes sédimentaires continentaux en tant que réservoirs de géo-ressources, et l'importance des hétérogénéités à l'échelle des faciès dans le comportement de l'écoulement des fluides (Høimyr et al., 1992), justifient la longue histoire des études sur les facteurs qui contrôlent le dépôt dans les environnements continentaux (Miall, 1977; Røe, 1987; Kocurek, 1988; Langford, 1989; Havholm et Kocurek, 1994; Hjellbakk, 1997; Mountney et al., 1999; Scherer et Lavina, 2005; Fielding, 2006; Weissmann et al., 2010; Wang et Plink-Björklund, 2019; Ventra et Moscariello, 2023). L'application de l'analyse sédimentaire quantitative permet d'affiner les modèles d'évolution des paysages et d'améliorer les prédictions relatives aux réservoirs souterrains (Colombera et al., 2013). Le Groupe Buntsandstein inférieur dans l'est de la France sert de réservoir pour la saumure géothermique concentrée en lithium (Aquilina et al., 1997; Kölbel et al., 2020; Fries et al., 2022), étant identifié comme abritant les réserves de lithium les plus prometteuses d'Europe (Sanjuan et al., 2022). Ainsi, la compréhension des facteurs qui contrôlent l'évolution temporelle et spatiale de ces dépôts est important non seulement pour la reconstruction paléoenvironnementale, mais aussi pour la meilleure gestion de ses géoressources. Dans cette étude l'intérêt principal porte sur la formation du Grès Vosgien Inférieur, qui est la formation la plus épaisse du Groupe Buntsandstein. Elle est composée d'une épaisseur d'environ 200 m de dépôts clastiques d'origine mixte fluviale et éolienne (Bourquin et al., 2009).

Les hétérogénéités de perméabilité dans les grès se développent à différentes étapes de leur formation, des processus sédimentaires primaires qui déterminent la taille et la distribution des grains de sédiments, la composition et la structure, jusqu'aux étapes diagénétiques ultérieures, qui peuvent modifier de manière significative leurs caractéristiques d'origine (Bjørlykke, 2014). La compréhension de ces processus et l'évaluation de leurs influences respectives sur les architectures des géoréservoirs sont essentielles pour améliorer la prédiction des hétérogénéités de perméabilité (Davis et al., 1993). L'intervalle d'intérêt de cette étude est composée de dépôts fluvio-éoliens considérés comme des zones préférentielles pour la migration des fluides au sein du Groupe Buntsandstein (Haffen et al., 2013).

Le jeu de données pour la caractérisation des aquifères et des réservoirs repose principalement sur des forages. Cependant, à mesure que la distance par rapport au point d'observation augmente, les incertitudes concernant la continuité latérale de ces informations augmentent également (Lowden, 1993). Les méthodes géophysiques peuvent aider à résoudre ces incertitudes ; bien qu'elles présentent des limitations, notamment en ce qui concerne les caractéristiques situées entre les surfaces de délimitation identifiées dans les résultats géophysiques (Weissmann et al., 2015). L'utilisation des affleurements comme analogues de réservoirs est une méthode largement utilisée pour atténuer ces incertitudes (par exemple, Alexander, 1993 ; Aigner et al., 1996 ; Rogiers et al., 2013 ; Howell et al., 2014 ; Weissmann et al., 2015 ; Thompson et al., 2019). Elle permet l'observation directe des géométries des faciès sédimentaires et des transitions latérales, optimisant les estimations de volume, la compréhension de la connectivité des réservoirs, et l'identification des contrôles faciès et diagénétiques sur la distribution de la porosité et de la perméabilité (Alexander, 1993). Des différences systématiques dans les paramètres pétrophysiques, comme la perméabilité, sont courantes entre les valeurs des données d'affleurement et de forage (par exemple, Rogiers et al., 2013; Hossain et al., 2024). Cependant, des tendances similaires et des distributions de valeurs relatives des paramètres peuvent être attendues (Goggin et al., 1992 ; Rogiers et al., 2013).

Le contexte géologique du fossé rhénan, une vallée de rift de 350 kilomètres de long qui chevauche la frontière entre la France et l'Allemagne, offre un scénario idéal pour utiliser les affleurements comme analogues de réservoirs, car les roches qui affleurent dans les blocs soulevés du fossé appartiennent aux mêmes formations qui contiennent de l'eau géothermique riche en lithium (Sanjuan et al., 2022) dans l'axe du graben. De plus, à l'ouest des montagnes des Vosges (France), les mêmes formations existent à faible profondeur, hébergeant des eaux souterraines utilisées pour l'approvisionnement public en eau (Vaute et al., 2007; 2013). Cette proximité géographique entre le réservoir et ses affleurements analogues réduit les variations latérales qui peuvent se produire dans un environnement de dépôt spécifique, augmentant ainsi la probabilité de rencontrer des architectures de roches similaires dans les deux cas. Dans cette étude, les hétérogénéités présentes au sein des dépôts fluviatiles en tresses, au sein des dépôts éoliens et entre ces deux systèmes de dépôt sont analysées.

Les dépôts fluviaux en tresses présentent des variations significatives dans les géométries des corps sableux, les structures internes et les textures (Miall, 1988 ; Høimyr et al., 1993). La quantification de ces caractéristiques est difficile en raison de leur occurrence typique en dessous de la résolution des cellules de modélisation des réservoirs (dizaines à centaines de mètres) (Puig et al., 2019). Les nombreux processus érosifs et déposants associés à ces systèmes dépendent de variables spatiales et temporelles et sont difficiles à prédire. Ces caractéristiques limitent l'applicabilité de l'analyse statistique spatiale pour la caractérisation des réservoirs (Castle et al., 2004) et soulignent l'importance d'employer une description quantitative des faciès pour des prédictions plus réalistes du comportement de l'écoulement (Alexander, 1993).

Les dépôts éoliens sont généralement caractérisés comme étant plus perméables et plus poreux que les dépôts fluviaux (par exemple, Cowan, 1993 ; Fischer et al., 2007 ; Bjørlykke, 2014 ; Quandt et al., 2022). Cependant, des différences significatives de perméabilité peuvent être observées au sein des systèmes éoliens (par exemple, Chandler et al., 1989 ; Fischer et al., 2007 ; Newell et al., 2019 ; Thompson et al., 2019), soulignant la nécessité d'étudier les facteurs qui contrôlent ces variations.

La représentation précise des géométries des faciès sédimentaires de subsurface dans les modèles d'écoulement des fluides est une tâche critique mais difficile en hydrogéologie. Les incertitudes inhérentes proviennent de la variabilité spatiale et de l'hétérogénéité des dépôts sédimentaires (Miall, 1988 ; Høimyr et al., 1993), qui influencent considérablement le mouvement des fluides et le transport des particules dans les systèmes aquifères (Davis et al., 1993 ; Koltermann & Gorelick, 1996 ; Dai et al., 2004 ; Possemiers et al., 2012 ; Thompson et al., 2019 ; Ren et al., 2022 ; Yin et al., 2023). La compréhension des caractéristiques sédimentaires à l'échelle du décimètre au mètre sur un site particulier est essentiel pour caractériser la dispersivité des particules et, par conséquent, leur mouvement et leur propagation en subsurface à cet endroit (Gelhar et al., 1992 ; Zheng & Gorelick, 2005 ; Ramanathan et al., 2010 ; Ren et al., 2022).

L'analyse des faciès sédimentaires a été largement utilisée pour augmenter l'efficacité de l'exploration des hydrocarbures (Walker et James, 1992 ; Høimyr et al., 1993), cependant, elle reste en retard dans les études sur les eaux souterraines

(Crooijmans et al., 2016 ; Aberg et al., 2021). Étant donné que le principal indicateur utilisé pour reconnaître des faciès sédimentaires distincts en tant qu'unités hydrostratigraphiques distinctes est la différence de tailles de grains (Koltermann & Gorelick, 1996), l'hétérogénéité de la perméabilité entre les grès de tailles de grains similaires peut être considérée comme des «incertitudes inconnues » (sensu Hunt & Welter, 2010) dans les modèles conceptuels hydrogéologiques. L'intégration de l'analyse quantitative des faciès avec des mesures de conductivité aérolique sur le terrain à partir d'affleurements améliore le réalisme des modèles hydrogéologiques et notre compréhension des dynamiques d'écoulement en subsurface (Alexander, 1993). Cette approche est particulièrement bénéfique pour les régions dominées par des faciès gréseux déposés dans des systèmes fluviaux en tresses et éoliens, où des variations significatives de perméabilité existent malgré l'absence de couches de mudstone (par exemple, Chandler et al., 1989 ; Fischer et al., 2007 ; Newell et al., 2019 ; Thompson et al., 2019), comme dans la Formation du Grès Vosgien Inférieur.

OBJECTIFS

Les objectifs principaux de la thèse de doctorat sont au nombre de deux : il s'agit (i) de présenter et analyser finement l'influence des processus sédimentaires primaires sur la distribution de l'hétérogénéité de perméabilité dans les dépôts fluviaux et éoliens tressés, et (ii) d'étudier les effets de ces hétérogénéités sur l'écoulement des fluides au sein d'un aquifère rocheux, en utilisant la Formation du Grès Vosgien Inférieur comme exemple. La thèse comporte trois chapitres principaux.

Dans le Chapitre 2, l'objectif est d'utiliser la caractérisation qualitative et quantitative des faciès et de l'architecture, à différentes échelles, pour répondre aux questions suivantes : i) Quelles sont les proportions des différents éléments qui composent la Formation du Grès Vosgien Inferieur ? ii) Quelles sont les preuves des variations spatiales et temporelles des conditions d'écoulement dans les rivières arides? iii) Comment les fluctuations de la nappe phréatique et les crues éphémères contrôlent-elles l'architecture des dépôts éoliens ? iv) Comment les différentes associations de faciès évoluent-elles spatialement et temporellement, et que révèlent-elles sur le système de dépôt à grande échelle ?

Dans le Chapitre 3, l'objectif est de définir les contrôles sédimentaires sur l'hétérogénéité de perméabilité au sein de la Formation du Grès Vosgien Inferieur et

d'identifier la distribution de cette hétérogénéité à l'échelle des faciès (Dalrymple, 2010) et des associations de faciès (Collinson, 1969). Par conséquent, les questions de recherche suivantes sont abordées : i) les différents faciès sédimentaires au sein du groupe gréseux présentent-ils systématiquement des réponses de perméabilité distinctes ? ii) Quels sont les facteurs contribuant à l'hétérogénéité de perméabilité dans les systèmes fluviaux tressés et éoliens ? iii) Les processus sédimentaires primaires ou les stades diagénétiques ultérieurs gouvernent-ils la variabilité actuelle de la perméabilité dans les affleurements de la Formation du Grès Vosgien Inferieur ? iv) Dans quelle mesure la compréhension de la distribution de la perméabilité au sein des faciès et des associations de faciès dans les affleurements de la Formation du Grès Vosgien Inferieur améliore-t-elle notre compréhension des modèles d'hétérogénéité en subsurface ?

Enfin, le Chapitre 4 a pour objectif de présenter les effets de l'hétérogénéité observée sur les résultats de modélisation des écoulements horizontaux et verticaux de fluides, tels que la courbe de percée du temps de résidence des particules dans le domaine du modèle, la macro-dispersivité longitudinale et l'anisotropie mise à l'échelle. Ensuite, quantifier les modifications dans ces résultats de modèles conduit à des modèles conceptuels hydrostratigraphiques plus simplifiés.

RÉSUMÉ DU CHAPITRE 2 : ANALYSE QUANTITATIVE DES FACIES D'UN SYSTÈME FLUVIO-EOLIEN : GROUPE DU BUNTSANDSTEIN DU TRIAS INFÉRIEUR, EST DE LA FRANCE

Dans le Chapitre 2, une analyse des faciès à haute résolution a été appliquée à treize affleurements et à échantillons de carottes d'un puits géothermique pour quantifier les architectures de dépôt fluvial et éolien, et comprendre les conditions paléoenvironnementales lors de leur dépôt. Deux associations de faciès ont été identifiées. L'association de faciès de chenaux fluviaux (Fluvial channel facies association – FC), principalement composée de grès déposés dans des chenaux mal confinés et parfois éphémères, correspond à 93 % de l'épaisseur totale. L'analyse de plus de 800 ensembles de strates caractérisés par des structures sédimentaires de régime d'écoulement inférieur, de transition et supérieur, répartis dans différents éléments architecturaux, a permis de distinguer les variabilités temporelles et spatiales, ainsi qu'une estimation des caractéristiques paléohydrauliques fluviales. L'association de faciès déposés par le vent et l'eau (Wind- and water-laid facies

association – WWL), qui représente 7 % de l'épaisseur totale, témoigne d'une architecture contrôlée par un niveau fluctuant de la nappe phréatique et des crues éphémères. Les résultats ont révélé que les dunes éoliennes et les nappes de sable se sont accumulées à des moments temporels distincts. Les tendances verticales enregistrées dans le puits géothermique indiquent une augmentation ascendante de la fréquence des intercalations entre les deux associations de faciès, et une diminution des occurrences d'ensembles de grès à stratification croisée plus épais d'origine fluviale, ce qui, associé au modèle global d'empilement rétrogradant de la Formation du Grès Vosgien Inferieur (Bourquint et al., 2009), peut être interprété comme l'enregistrement préservé d'un grand système fluvial distributif. La présence de dépôts éoliens latéralement étendus, surmontant les dépôts fluviaux, est souvent associée par les auteurs à des périodes de conditions relativement plus arides à l'échelle régionale. Cependant, des preuves indiquent que l'avulsion des chenaux pourrait être une interprétation alternative pour l'établissement des deux associations de faciès. Ces découvertes améliorent notre compréhension des facteurs de contrôle du dépôt dans les systèmes fluviaux tressés et éoliens, et contribuent à l'amélioration des modèles prédictifs prenant en compte l'hétérogénéité des réservoirs dans les successions accumulées de ce type.

RÉSUMÉ DU CHAPITRE 3 : CONTRÔLE DES FACIÈS SÉDIMENTAIRES CLASTIQUES SUR LES HÉTÉROGÉNÉITÉS DE PERMÉABILITÉ : LES GRÈS CONTINENTAUX DU BUNTSANDSTEIN MOYEN (TRIAS INFÉRIEUR, FRANCE ORIENTALE)

Dans ce Chapitre, les principaux facteurs contrôlant la distribution de l'hétérogénéité de perméabilité des dépôts fluvio-éoliens de la Formation du Grès Vosgien Inférieur sont présentés à différentes échelles, en combinant les caractéristiques de perméabilité et pétrographiques avec la caractérisation sédimentologique quantitative du Chapitre 2. Les données de perméabilité ont été collectées à partir de sept affleurements différents situés dans les Vosges, ainsi que de carottes de forage du puits géothermique EPS1 à Soultz-sous-Forêts, en utilisant le perméamètre à air portatif non destructif TinyPerm 3 (fabriqué par New England Research). De plus, treize échantillons provenant de quatre affleurements ont été prélevés dans différents faciès, dans le but de mesurer la perméabilité et la porosité connectée dans un laboratoire pétrophysique contrôlé. Dans l'association de faciès de chenaux fluviaux (Fluvial channel facies association – FC), une relation inverse

entre les conditions de régime d'écoulement fluvial et la perméabilité de ses faciès est observée. Dans l'association de faciès déposés par le vent et l'eau (wind- and water-laid facies association - WWL), la distribution de la perméabilité est directement influencée par les conditions climatiques, où des nappes de sable hybrides à faible perméabilité ont été déposées dans des conditions plus humides, et des dunes éoliennes (aeolian dunes – AD) à haute perméabilité dans des conditions plus arides. Cependant, malgré la perméabilité élevée de l'AD, l'architecture du WWL implique un faible potentiel de connectivité. La compaction est le principal processus influençant la perméabilité et la porosité de la Formation du Grès Vosgien Inférieur, étant directement liée à la proportion de lithoclastes, d'argile infiltrée, de pseudomatrices lithiques et de surcroissance de quartz enregistrée pour chaque faciès. Malgré la surimpression diagénétique, les processus sédimentaires primaires et l'architecture gouvernent la distribution de l'hétérogénéité de perméabilité dans la Formation du Grès Vosgien Inférieur. Les données de perméabilité des affleurements ont montré des valeurs absolues plus élevées par rapport aux données en subsurface. Cependant, les mêmes faciès, et des tendances similaires de réponses de porosité-perméabilité relatives aux différents faciès, sont observées entre les affleurements et les échantillons de forage, mettant en évidence la sédimentologie comme un proxy indispensable pour les études d'hétérogénéité des réservoirs.

RÉSUMÉ DU CHAPITRE 4 : L'IMPORTANCE DE L'HÉTÉROGÉNÉITÉ SÉDIMENTAIRE DANS LES MODÈLES DE TRANSPORT DE SOLUTES : ETUDE DE CAS UTILISANT UN AFFLEUREMENT DE L'AQUIFERE DES GRES DU TRIAS INFERIEUR, EST DE LA FRANCE

Ce Chapitre vise à quantifier l'effet des caractéristiques sédimentaires à l'échelle du décimètre au mètre dans les résultats des modèles d'écoulement de fluides, tels que le temps de résidence des particules et la macro-dispersivité. Un modèle numérique d'affleurement, combiné à une caractérisation sédimentaire quantitative et à une distribution de perméabilité, est utilisé pour développer un modèle conceptuel hydrogéologique vertical réaliste en 2D en utilisant le logiciel FEFLOW 8.0. Ce modèle discrétise les faciès sédimentaires avec leurs caractéristiques de conductivité hydraulique associées, en se basant sur les données des Chapitres 2 et 3. Ensuite, cinq scénarios avec des modèles conceptuels hydrogéologiques de plus en plus simplifiés ont été générés pour quantifier les effets de cette simplification sur les résultats de la modélisation de l'écoulement. La simplification consistait à représenter

différentes échelles de discrétisation des hétérogénéités, allant d'une caractérisation détaillée des faciès individuels à un modèle conceptuel homogène. Elle consistait également en la manière de distribuer la conductivité hydraulique dans les éléments du maillage, entre une distribution stochastique (plus réaliste) et une distribution déterministe (K médian). Les conditions aux limites à charge constante ont été attribuées pour simuler l'écoulement horizontal et vertical en écoulement stationnaire. En utilisant l'outil de suivi des particules, le comportement du temps de résidence des particules à travers le domaine du modèle a été analysé. Les résultats indiquent que la discrétisation entre l'association de faciès de chenaux fluviaux (FC) et l'association de faciès déposés par le vent et l'eau (WWL) a un impact significatif sur les écoulements horizontal et vertical en ce qui concerne le temps de résidence des particules. Les résultats de la macro-dispersivité sont principalement affectés lorsque les données de perméabilité ne sont pas contraintes par la géométrie des caractéristiques sédimentaires. Pour l'écoulement horizontal, ne pas discrétiser les faciès sédimentaires individuels entraîne une sous-estimation des zones d'écoulement préférentiel, ce qui impacte la prédiction des premières arrivées de particules et met en évidence des inefficiences potentielles dans les plans de remédiation des contaminants des eaux souterraines. La queue longue observée dans la distribution du temps de résidence des particules suggère que la macro-dispersion ne peut pas être décrite par les concepts fickiens pour le domaine du modèle. De plus, la discrétisation entre les associations de faciès distincts – FC et WWL – génère une anisotropie mise à l'échelle (Kv/Kh) de 0,3, démontrant le rôle significatif de l'hétérogénéité sédimentaire dans la modélisation hydrogéologique.

1. CHAPTER 1: General Introduction

1.1. RATIONALE

The application of high-resolution sedimentary facies analysis to characterise heterogeneities in fluid-flow simulations is an established method in the petroleum industry, however still not widely used in groundwater studies (Crooijmans et al., 2016; Aberg et al., 2021), despite the strong influence that centimetre- to metre-scale sedimentary heterogeneity has on solute dispersion in groundwater (Zheng & Gorelick, 2005; Ramanathan et al., 2010; Ren et al., 2022). Inherent uncertainty exists when conceptualising the spatial distribution of sedimentary heterogeneity in the subsurface (Miall, 1988; Høimyr et al., 1993). Therefore, a model representing subsurface features is a simplified version of reality (Wang and Anderson, 1995). The reduction of such uncertainty is critical in predicting the behaviour of the fluid-flow pathways (Gelhar et al., 1992; Zheng & Gorelick, 2005; Ramanathan et al., 2010; Ren et al., 2022), which can be achieved by analysing outcrops as reservoir analogues. Outcrops are widely used to access the geometry, lateral transitions, proportions, and connectivity of sedimentary features (e.g. Alexander, 1993; Aigner et al., 1996; Rogiers et al., 2013; Howell et al., 2014; Weissmann et al., 2015; Thompson et al., 2019). However, regarding deep reservoirs, using outcrops as subsurface analogues presents its limitations (Alexander, 1993; Howell et al., 2014; Busch et al., 2022). These limitations are mainly related to the distinct diagenetic stages experienced by both (outcrop and deep reservoirs), which may imprint different characteristics such as permeability and porosity distribution between them (e.g. Rogiers et al., 2013; Hossain et al., 2024). That is why it should be taken into consideration the extent to which outcrops are good analogues for a specific reservoir.

The Lower Triassic deposits in eastern France, named the Buntsandstein Group (Gr.), represent an important aquifer for drinking and industrial water in shallow depths (Bouly and Demassieux, 1996), and for lithium-rich geothermal fluids when placed in higher depths in the Upper Rhine Graben (Sanjuan et al., 2022). The Buntsandstein Gr. crops out at the Upper Rhine Graben's shoulders, at the Vosges and Black Forest hills, in France and Germany respectively. This geological unit is composed dominantly of sandstones deposited in continental settings, mostly related to braided fluvial and aeolian systems (Bourquin et al., 2009).

The Lower Grès Vosgien Formation (LGV) is the thickest formation within the Buntsandstein Gr.; however, it is poorly understood its internal architecture of sedimentary facies, how these facies translate into permeability heterogeneity, and how such heterogeneities may influence the fluid-flow behaviour. Thus, the aim of this PhD thesis is (i) to enhance the comprehension of the temporal and spatial depositional controlling factors of the LGV, and its main architectures; (ii) to assess the extent to which its sedimentary facies and facies associations influence the permeability heterogeneity distribution; and (iii) to present the effects of discretising different scales of heterogeneity in fluid-flow modelling results related to solute transport in groundwater systems.

These aims are addressed in three chapters (Chapters 2, 3, and 4). Chapter 2 presents a quantitative analysis of the fluvial-aeolian deposits, by analysing their sedimentary facies, facies associations and architectural elements, and the temporal and spatial depositional controlling factors of these sedimentary features in the LGV; Chapter 3 unveils how permeability heterogeneity responds to the sedimentary features in different scales, and the usefulness of outcrop data as reservoir analogue for the LGV; and Chapter 4 shows the significance of the observed sedimentary heterogeneity, and the effects of heterogeneity simplification, into solute transport modelling of groundwater systems.

1.2. BACKGROUND AND CONTEXT

Given the transdisciplinary subjects approached in this thesis, the aim of this section is to provide a concise context and background, offering the basic information necessary for readers from the different domains to follow the subsequent chapters. Therefore, this section is not intended to be a literature review of the topics presented.

1.2.1. Sedimentary facies analysis

Facies analysis is an approach to interpreting sedimentary rocks based on the attributes of facies, facies associations, and facies successions (Walker and James, 1992; James and Dalrymple, 2010). It aims to assess the processes responsible for their formation and to interpret the depositional environment in which these processes occurred (James and Dalrymple, 2010). Finally, it allows for the assessment of the temporal and spatial controls on the distribution of sedimentary features, comprising

heterogeneities from a centimetre to hundreds of kilometres scale (e.g., variations in grain sizes between distinct laminae in a single sedimentary bed, and the juxtaposition of distinct depositional systems, respectively).

The elementary building block for conducting facies analysis is the facies (Teichert, 1958). A facies is a body of rock that is different from the surrounding bodies, characterised by a combination of lithology, sedimentary structures, and biological structures that are detectable in the field (De Raaf et al., 1965; Walker and James, 1992). These characteristics are used to interpret the processes related to the facies genesis (Teichert, 1958; Miall, 1977). Thus, weathering and diagenetic characteristics, such as colour, hardness, and types of cement, have limited value for facies interpretation (Dalrymple, 2010).

Depending on the objective, facies can be defined at scales ranging from individual beds to lithostratigraphic units such as geological formations (Dalrymple, 2010). In the present study, facies are defined at the scale of individual beds, as the objective is to analyse in high resolution the processes and environmental parameters associated with the genesis of the sedimentary succession of the LGV.

Individual facies can give ambiguous environmental interpretations since they represent only sedimentary processes (Walker, 1992). Therefore, the next step of facies analysis is to group facies into facies associations (Collinson, 1969). A facies association is a group of facies genetically related to each other that presents some environmental significance (Collinson, 1969). The genetically related characteristics and environmental significance are attributed to Walther's Law, which states that superimposed facies can primarily be observed beside each other in modern sedimentary systems (Middleton, 1973). Following the concept of Walther's Law, after defining facies associations, the next stage of the facies analysis is to deduce the depositional environment in which the facies associations were formed (Walker, 1992). This is achieved by comparing the genetically related processes (facies and facies associations) with modern examples of depositional environments, to identify, on a larger scale, a geographic and/or geomorphic area that presents an assemblage of the observed depositional processes and facies associations (Walker and James, 1992; Dalrymple, 2010).

Another subdivision used is architectural elements (Miall, 1985), which consist of a morphological subdivision of a specific depositional environment, composed of a particular geometry and assemblage of facies (Walker and James, 1992). The concept of architectural elements can overlap with facies associations. However, the present study uses architectural elements as an intermediary hierarchy between facies and facies associations, represented by specific geometries of facies assemblages (Miall, 1985) within the facies associations. Thus, the scales of observation presented in this study are, from the smallest to the largest: facies, architectural elements, facies associations, and depositional environments. The workflow associated with facies analysis is presented in Figure 1-1.

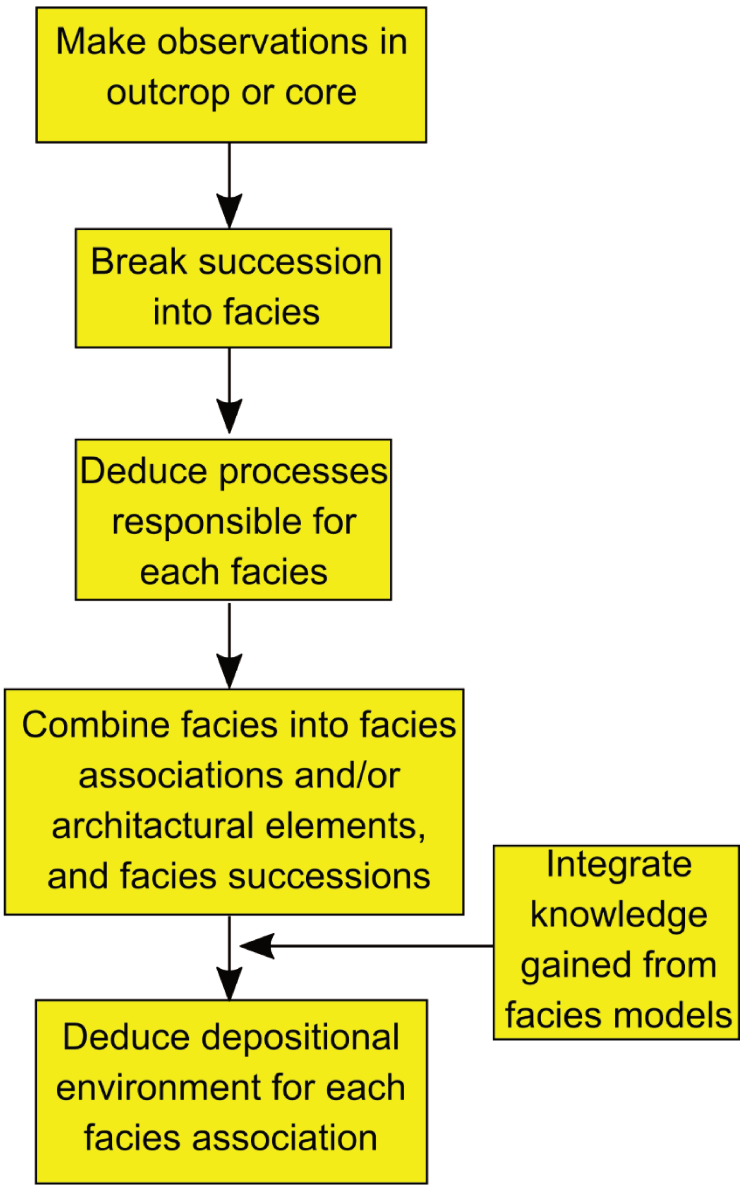


Figure 1-1: Facies analysis workflow (adapted from Dalrymple, 2010).

1.2.1.1. Sedimentary processes and products

As presented in the previous section, sedimentary facies can be interpreted as the product of specific sedimentary and biological processes. This section will discuss some of the processes responsible for forming the main sedimentary facies observed in the LGV.

- FLUVIAL PROCESSES

Given that most of the sedimentary succession in the LGV was deposited in fluvial channels, with a consequent virtual absence of mudstones (0.1% of the total thickness), the sedimentary processes and products presented here are related to those that occur within channels.

Most sediments inside fluvial channels are transported as bedload and in suspension (Allen, 1982; Collinson et al., 2006). Bedload transport involves the movement of grains in continuous or intermittent contact with the riverbed (Allen, 1982), primarily represented by traction transport process (Allen, 1982; Miall, 2010). In traction transport, loose sediments are transported individually by sliding and rolling, saltation, or intermittent suspension over varying distances (Miall, 2010). These are essential processes responsible for generating bedforms with specific internal stratification, which are now recognised in ancient deposits (Allen, 1982). Clay and silt fractions remain in suspension, moving at roughly the same rate as the fluid (Collinson et al., 2006), until the flow stops completely, allowing the grains to settle out. In fluvial systems, this typically occurs in abandoned channels or floodplain ponds (Bridge, 2003).

Sedimentary bedforms tend to be in equilibrium, or nearly in equilibrium, with the flow (Fielding et al., 2018). Their formation results from the combination of grain sizes and flow-regime conditions (Southard and Boguchwal, 1990) (Fig. 1-2), and their sizes related to flow depths (Leclair and Bridge, 2001). Simons et al. (1965) (*chez* Miall, 2010) experimentally described bedforms of medium-grained sands developed in different conditions of flow velocity, at a fixed flow depth, (Fig. 1-3). All bedforms – translated into facies – shown in Figure 1-3 are observed in the fluvial deposits of the LGV.

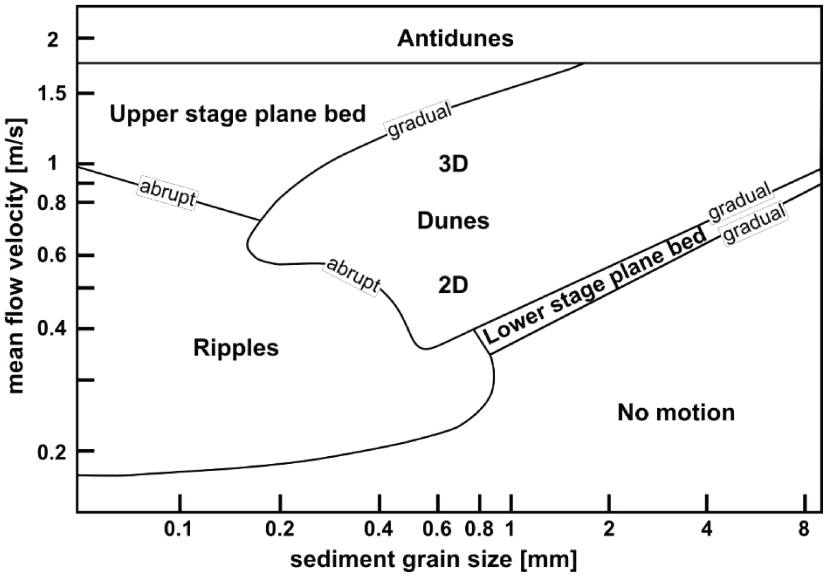


Figure 1-2: Bedforms stability fields relative to grain size and flow velocity (Southard and Boguchwal, 1990).

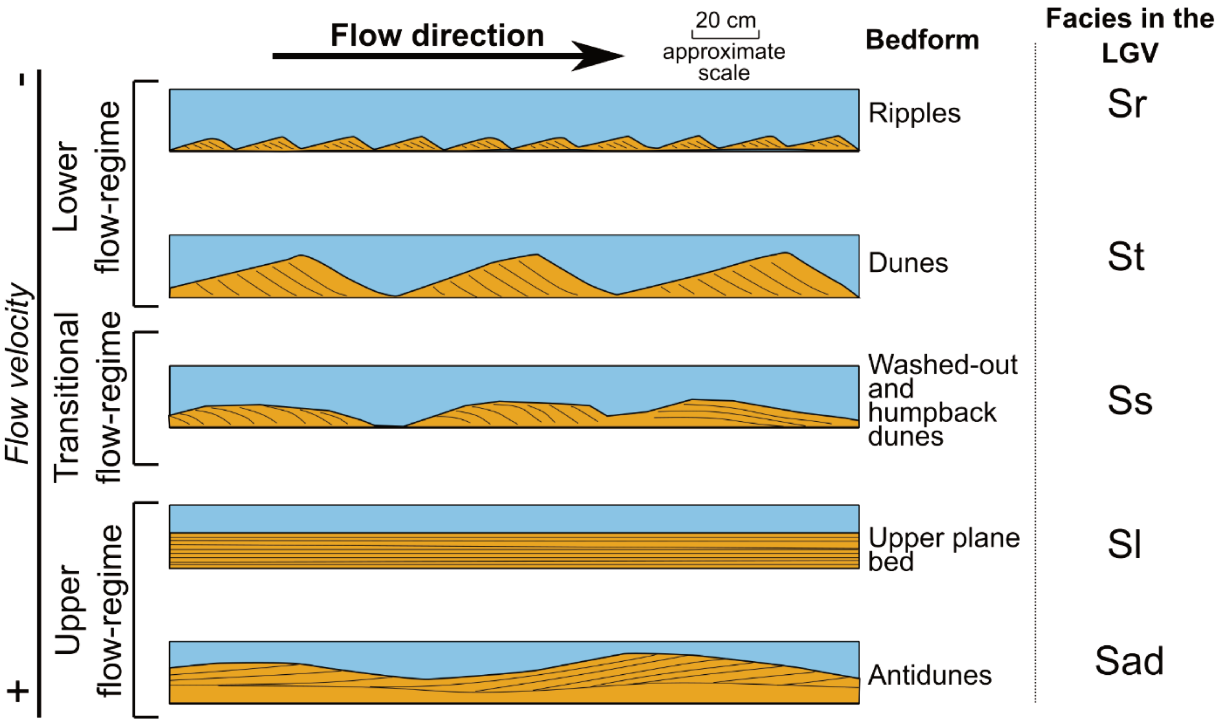


Figure 1-3: Bedforms developed by distinct flow regimes, in response to different flow velocities in a fixed flow depth and grain sizes of sands (adapted from Simons et al. (1965) (chez Miall, 2010). It also presented the facies observed in the Lower Grès Vosgien Formation (LGV), corresponding to their respective bedforms. Sr = ripple mark sandstone; St = trough cross-bedded sandstone; Ss = sigmoidal cross-bedded sandstone; Sl = low-angle cross-bedded sandstone; Sad = antidune sandstone.

Flow-regime conditions depend on the combination of flow velocity and water depth, which can be described by the Froude number (Fr), generally expressed as:

$$Fr = \frac{v}{\sqrt{(gd)}}$$

where, d is the flow depth, g is the gravitational acceleration, and v the average flow velocity.

Given the inverse relationship between flow-regime conditions and flow depth, local changes in the riverbed topography cause spatial variations in flow-regime conditions within the channels. Røe (1987) observed horizontally stratified sandstones (Fig. 1-3) in the topset of sigmoidal cross-bedded sandstones (Fig. 1-3), with evidence of upper flow-regime conditions, such as parting lineation (Crowell, 1955). However, downstream in the same sigmoidal facies, higher angle stratification records evidence of lower flow-regime conditions, such as current ripples (Fig. 1-3). This indicates that the same bedform was simultaneously affected by different flow-regime conditions. Allen (1983b) described sigmoidal cross-bedded sandstones with horizontally stratified topsets that were absent of gravel clasts. Although, within the same bedform, the downstream higher angle foresets were rich in gravel (Fig. 1-4). The author attributed these differences in gravel content to the overpassing process. This process occurs at the top of humpback bars composed of a bimodal grain-size distribution of sediment load (gravel and sand). Under upper-flow regime and high shear-stress conditions at the top of the bars, the large sub- to well-rounded gravel rolls over a firm bed of close-packed sand grains (Allen1983b; Carling, 1990) (Fig. 1-4B), depositing downstream where flow conditions change. The structures observed and interpreted by Allen (1983b) (Fig. 1-4) were recognised in the LGV (Figs. 2-3B and 2-8B).

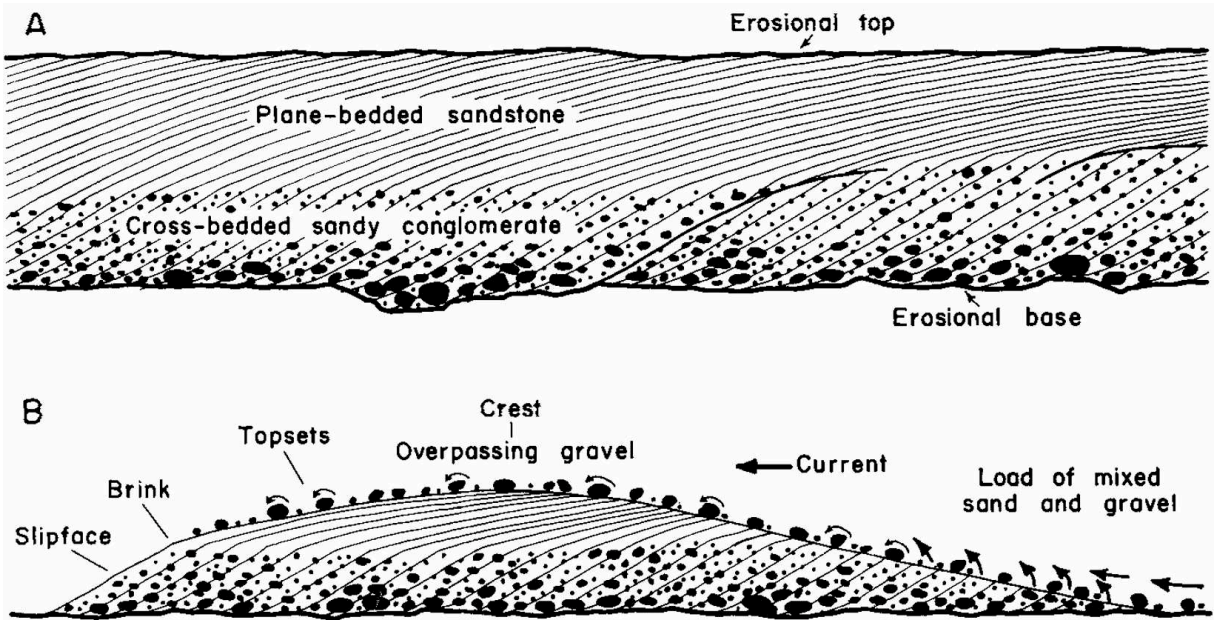


Figure 1-4: Sedimentation units representing humpback bars, with overpassing gravel. (A) Characteristics of the unit. (B) Overpassing process responsible for generating (A) (Allen, 1983b).

The processes previously discussed record the spatial distribution of flow-regime within the channel, based on changes in flow-depth. However, the flow-regime can also be affected by temporal variations in flow velocity due to fluvial discharge variabilities (Fielding, 2006; Fielding et al., 2018). Distinguishing between temporal and spatial factors that controlled the deposition in ancient systems is not simple when relying solely on the types of sedimentary facies preserved (Colombera et al., 2024). Given that in slow-changing discharges bedforms tend to be in equilibrium with the flow, whereas, in discharges associated with flashy hydrographs this equilibrium may never be reached (Fielding et al., 2018), different depositional architectures are formed depending on the “flashiness” of discharge variabilities (Fielding, 2006; Fielding et al., 2018). Thus, authors have proposed methods to evaluate the hydrograph behaviour of ancient fluvial systems, such as the use of the coefficient of variance (CV) of preserved cross-bedding set thickness, where CV lower than 0.88 would indicate bedform-flow disequilibrium (flashy hydrograph) (Paola and Borgman, 1991; Leary and Ganti, 2019; Lyster et al., 2022). Colombera et al. (2024) have shown that this relationship is not straightforward, and should not be overinterpreted based on this exact number. Therefore, to define if the system was subjected to discharge variabilities with high peaks and fast falling limbs, the CV should be associated with other field evidences, such as those presented in Section 2.5.1 (Chapter 2), for the fluvial deposits of the LGV.

Similar bedforms are found in ancient and modern examples of the same type of depositional environment. Miall (1977) observed this for braided rivers; after reviewing more than sixty papers on modern and ancient examples, the author identified up to three gravel facies, five sand facies, and two fine-grained facies. This indicates that, regardless of age and geographical location, a specific range of bedforms – translated into facies – are found in those systems. However, this does not mean that these facies are restricted to braided-fluvial systems, as similar processes in terms of sediments and flow conditions can be found in other depositional environments (Miall, 1977), as discussed in Section 1.2.1.

Given the limited types of facies observed, Miall (1977) proposed a method of facies classification using a code composed of two letters: the first letter, capitalised, indicates the predominant grain size (e.g. G for gravel, S for sand, and F for fine sediments such as silt and clay). The second letter, in lowercase, indicates the associated sedimentary structure (e.g. “t” for trough cross-bedding, “s” for sigmoidal cross-bedding). This logic has become a standard field method of facies classification (Miall, 2010), and it is also applied in this study.

- AEOLIAN PROCESSES

Aeolian strata differ from those formed subaqueously because of the distinct characteristics of the transport fluid (Brookfield and Silvestro, 2010). Both generate similar structures, and the main differences are observed in the laminae scale (Rubin and Hunter, 1982). The three main bedforms produced by aeolian processes are ripples, dunes, and draa (Brookfield, 1992). Their formation depends on wind saturation, deposition rate, wind velocity, and wind duration (Fryberger and Schenk, 1981), and requires obstacles or topographic lows to accumulate (Brookfield and Silvestro, 2010).

The main processes of aeolian transport are saltation, rolling, and sliding, and the main deposition processes are grainfall, grainflow (avalanche), and climbing ripples (Fryberger and Schenk, 1981) (Fig. 1-5). Grainfall deposition refers to grains settling out (Hunter, 1977), commonly occurring on zones of flow separation such as the lee side of a dune (Fig. 1-5) (Hunter, 1977a; Fryberger and Schenk, 1981). Grainflow deposition occurs when the slipface of a dune reaches a critical angle (between 32° and 34°), resulting in re-sedimentation as an avalanche (Fig. 1-5) (Hunter, 1977a;

Fryberger and Schenk, 1981; Bristow and Mountney, 2013). Climbing ripples, also termed translatent strata (Hunter, 1977b; Fryberger and Schenk, 1981), refer to the migration and deposition of superimposed wind ripples that climb over each other (Hunter, 1977b). The structures preserved depend on the angle of ripple climbing, defined as the angle between the vector of ripple climb and the generalised depositional surface (Hunter, 1977b) (Fig. 1-6). Wind ripples are flatter (higher length/hight ratio) than those formed by water, and commonly have more regular crest lines (Sharp, 1963). Their migration occurs mainly in interdune flats (or sand sheets), on the stoss side of dunes, and on the gently steep lee side of dunes (Hunter, 1977a; Bristow and Mountney, 2013). The strata produced by the migration of wind ripples are generally composed of thin (1-10 mm) parallel laminae marked by slight variations in grain size (Bristow and Mountney, 2013).

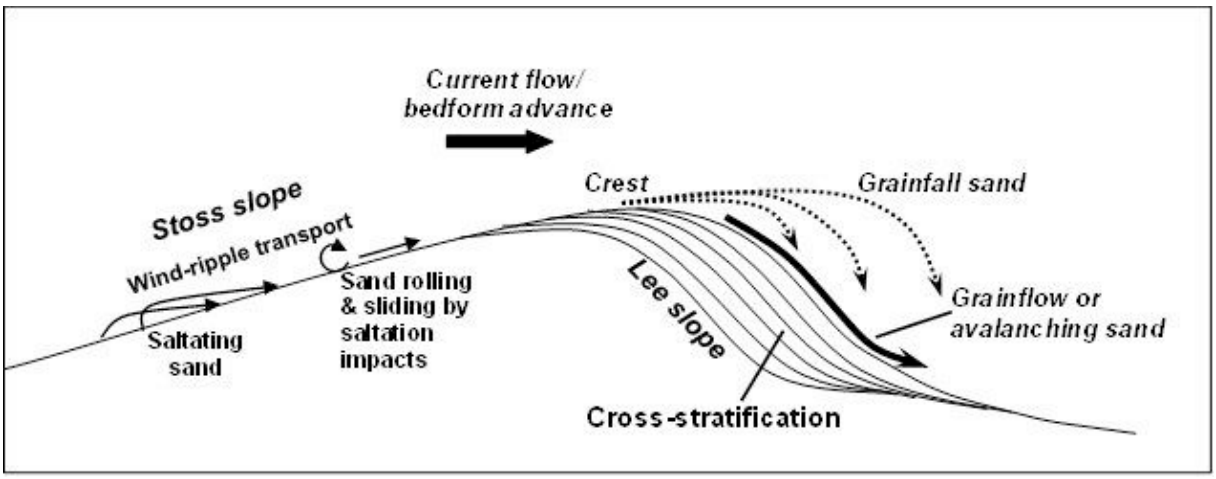


Figure 1-5: Simple profile presenting the main processes of transport and deposition of aeolian deposits (Caputo, 2023).

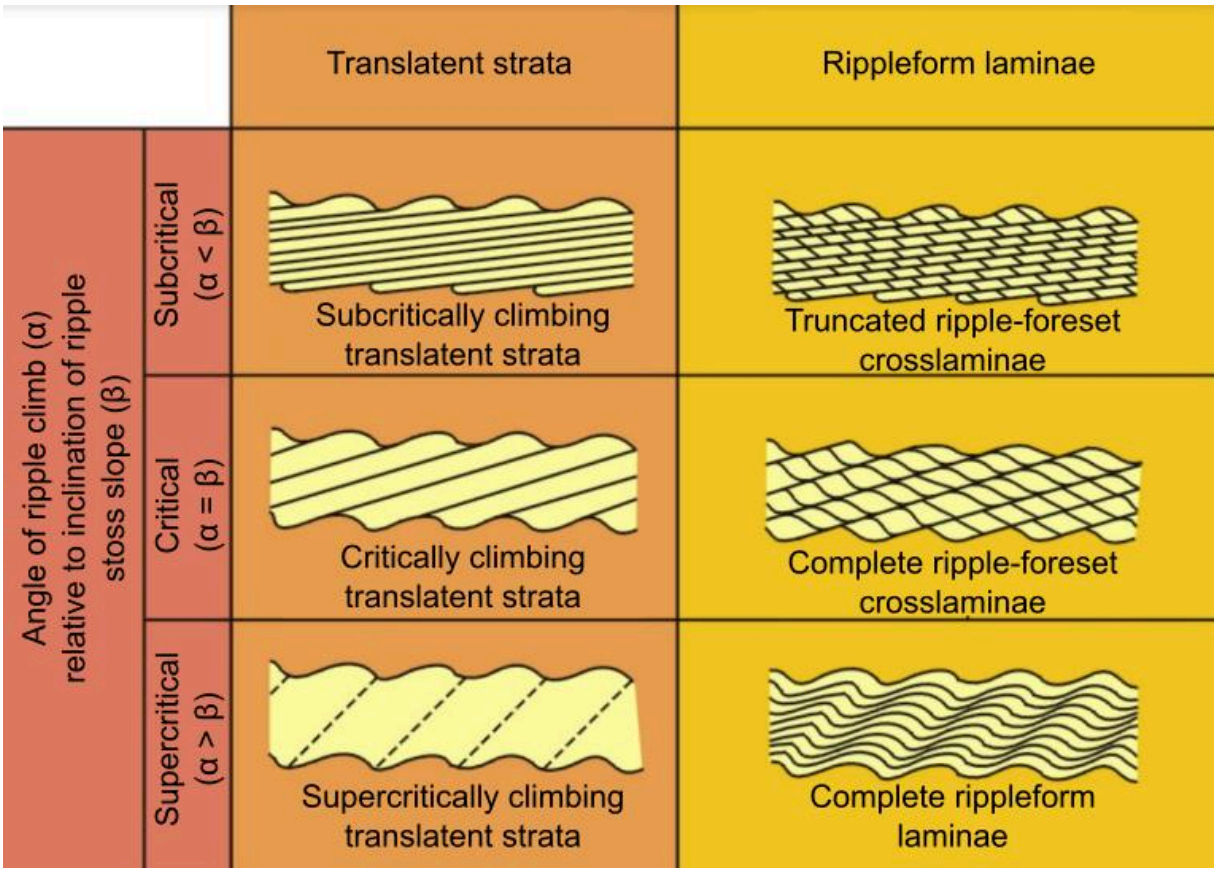


Figure 1-6: Types of ripple stratification according to the climbing-angle settings (subcritical, critical, and supercritical) (Hunter, 1977b).

The aeolian dunes are larger bedforms than ripples, varying from 10 cm to 100 m in height (Brookfield, 1992), and depending on wind regime characteristics they present different morphologies (e.g. barchan, transverse, linear, and star) (Brookfield, 1992). A draa is characterised by large sand bedforms, 20 to 450 m high, composed of superimposed dunes (Brookfield, 1992).

All aeolian processes tend to produce inversely graded grain segregation (Fryberger and Schenk, 1981), characterised by coarsening upward trends within laminae (Bristow and Mountney, 2013). The degree of sediment sorting may depend on the depositional environment, where well- to very well-sorted, fine sands, are expected in coastal dunes; moderately to well-sorted, fine- to medium-grained sands, in inland dunes; and poorly sorted sands in regions of interdunes or sand sheets (Brookfield, 1992). In interdune and sand sheet deposits the sand grains tend to present a bimodal size distribution (Brookfield, 1992). However, in interdunes and sand sheets that are affected by shallow water-table, these aeolian sedimentary processes may interact with moist depositional surfaces, changing the dynamics and textures

produced (Mountney and Thompson, 2002). For instance, the dry sediments get adhered to them, forming the sedimentary structure named adhesion structure (Kocurek and Fielder, 1982). Additionally, the wet substratum creates conditions to the growth of microbial mats, which form rapidly during periods of non-deposition, resulting in microbially induced sedimentary structures (Noffke et al., 1996; Gerdes, 2007).

The aforementioned processes involve the deposition and accumulation of wind-transported sands. However, the sand being deposited in one place has first been removed from somewhere upwind, eroding subaerially exposed sediments, and generating a surface known as a sand-drift or deflation lag surface (Clemmensen and Tirsgaard, 1990). Sand-drift (or deflation lag) surfaces typically form when strong, under-saturated winds remove loose sediments from the substrate, leaving behind a lag of coarser-grained sands or gravel (Clemmensen and Tirsgaard, 1990) (Fig. 1-7).

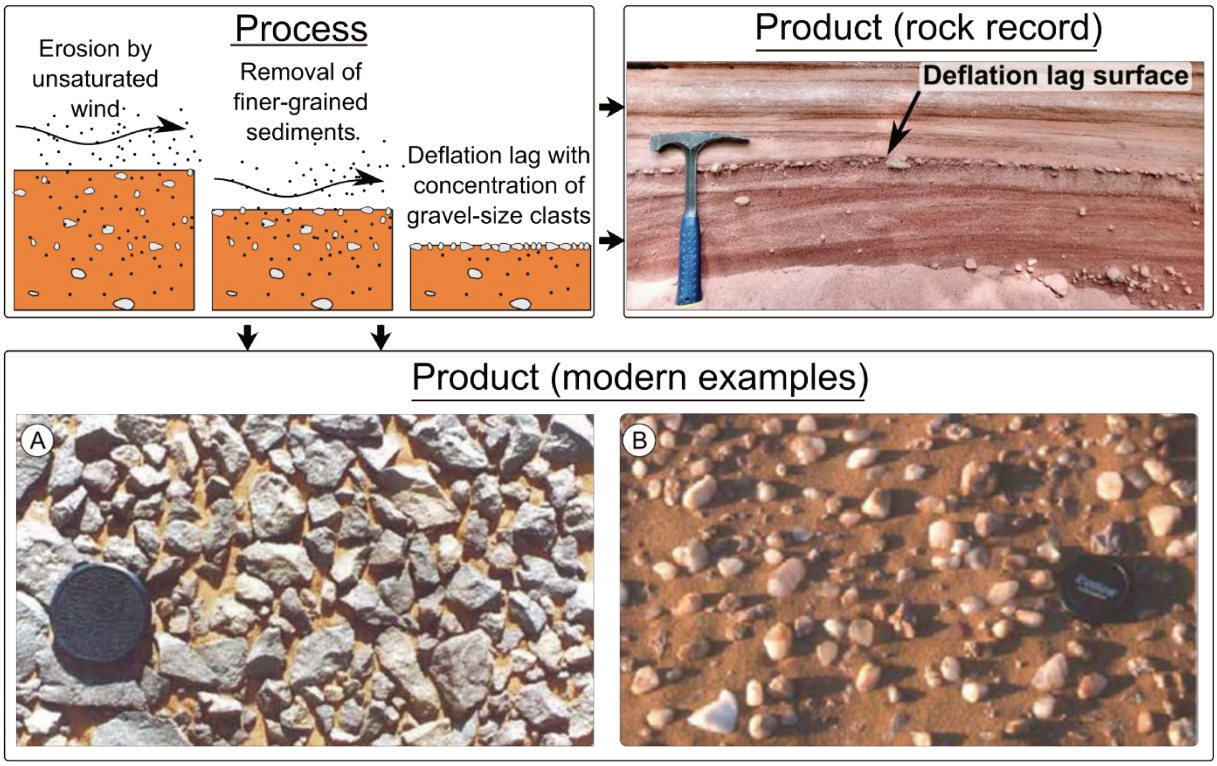


Figure 1-7: Processes of formation and examples of products, in rock record and in modern examples, of deflation lag surfaces. (A) Gilf Kebir, Libyan Desert, Egypt (Brookfield and Silvestro, 2010); (B) Namibia (Bristow and Mountney, 2013). (A) and (B) in a plan view. The rock record photo was taken by the current author, at the Ramstein Castle Ruin, in the Vosges du Nord region, eastern France.

1.2.2. Braided fluvial systems

The concept of braided fluvial systems is based on a morphological and process-response classification (Miall, 2006). These systems are recognised as those

comprising several low-sinuosity channels with bars and small islands in between (Miall, 1977), associated with high regional slopes, variable discharges, and abundant bedload sediment supply (Smith, 1970). Braided fluvial systems can be found in diverse settings of climate and relief with the necessary high bedload and discharge fluctuations necessary to generate them (Miall, 1977). One aspect observed in the LGV that contributes to the formation of a braided system is the lack of vegetation traces. The lack of vegetation in a drainage basin indicates a deficit of water and sediment storage capacity, which results in sediment-laden flash floods as an immediate response to high precipitation rates (Miall, 1977). The lack of vegetation also contributes to highly erodible channel banks, which gives rise to high width/depth ratios, and lateral movement of the channels and their associated bars (Collinson, 1996).

Evidence of discharge variability is also present in the study area, which is discussed in detail in Chapter 2. Discharge variability can be estimated from the rock record based on the type of sedimentary facies along with the architectural elements preserved, and the relationship between them. These aspects have been widely discussed in the literature (e.g. Miall, 1988; DeLuca and Eriksson, 1989; Bhattacharyya and Morad, 1993; Fielding, 2006; Miall, 2006; Fielding et al., 2009; Plink-Björklund, 2015; Fielding et al, 2018; Alexander et al., 2020; Arévalo, et al., 2022). The elements that evidence discharge variability, associated with a quantitative analysis of cross-bedding thickness preservation, may also indicate the characteristics of the hydrograph falling limb after a discharge peak (e.g. Røe, 1987; Fielding, 2006; Miall, 2006; Plink-Björklund, 2015; Fielding et al., 2018; Myrow et al., 2018; Leary and Ganti, 2019).

Braided fluvial systems are rarely associated with thick accumulations of overbank muddy sediments (Miall, 1985), reflecting the relatively high proportion of sandy channel deposits and a scarcity of floodplain fines on the rock record (Miall, 2006).

1.2.3. Aeolian systems

Aeolian systems are composed mainly of two elements: sand dunes and sand sheets (Bristow and Mountney, 2013), which may coexist in the same depositional environment, presenting different proportions between them. Dunes form if there is

enough sand, space, and time for their continuous growth and migration (Clemmensen and Abrahemsen, 1983). The processes responsible for their migration and deposition are grainflow and grainfall on their lee side (Hunter, 1977).

Sand sheets are areas of aeolian deposits where aeolian dunes are absent (Kocurek and Nielson, 1986). They are commonly associated with the margins of sand seas (Bristow and Mountney, 2013) in zones of transporting and bypassing (Brookfield and Silvestro, 2010). The development of these areas is often related to high water-table levels, periodic flooding, cementation of the depositional surface, vegetation, and coarse-grained sand populations (Kocurec and Nielson, 1986). In the LGV, high water-table levels and periodic flooding are the main aspects for the development of the sand sheets. The detailed characterisation of the processes involved, and the context for the accumulation of aeolian dunes and sand sheets in the LGV are presented in Chapter 2.

1.2.4. Triassic Reservoirs in Europe

The Triassic period is marked by the early stages of the breakup of the supercontinent Pangea, resulting in the formation of approximately 70 rift basins across Europe (McCann et al., 2006). Continental sedimentation predominantly composed of braided rivers and aeolian deposits is recorded in France, Switzerland, Luxembourg, Belgium, the Netherlands, Germany, Poland, the United Kingdom, and Denmark (Gall, 1977; Hounslow and Ruffell, 2006). Currently, these sedimentary deposits are important reservoirs for resources such as freshwater (Vaute et al., 2013; Coyler et al., 2021), geothermal fluids (Vernoux et al., 1995), lithium-rich brines (Sanjuan et al., 2022), and hydrocarbons (Lervik et al., 1989). They can also serve as carbon-sequestration reservoirs (Hossain et al., 2024), highlighting the necessity of detailed comprehension of their internal structures not only for the efficient management of georesources, but also for achieving the goal of making Europe the first climate-neutral continent by 2050 (Fetting, 2020).

1.2.5. The Lower Triassic deposits in eastern France

In eastern France, the Triassic deposits are present in the intracratonic Paris Basin, which became an independent basin only during the Carnian (Upper Triassic) (Goggin et al., 1997). Before the Carnian the Paris Basin was an embayment of the

Germanic Basin and maintained a close relationship with the south domains of the Germanic basin (Goggin et al., 1997).

The Triassic of the Paris Basin records the lithological subdivisions reported by Alberti (1834): (1) Lower Triassic: Buntsandstein Gr., predominantly continental sedimentation; (2) Middle Triassic: Muschelkalk Gr., marine deposits, and (3) Upper Triassic: Keuper, mainly continental deposits. (Bourquin & Guillocheau, 1996) (Fig. 1-8).

The Buntsandstein Gr. in eastern France can reach up to 500 meters in thickness, divided into Lower, Middle, and Upper Buntsandstein (Menillet et al., 1989) (Fig. 1-8). This whole sequence is characterised by fluvial systems that evolve from a fluvial-aeolian to a fluvio-marine environment, finalising with the Muschelkalk marine transgression (Guillocheau et al., 2002; Bourquin et al., 2006). The present study is focused on the Middle Buntsandstein.

The Middle Buntsandstein represents the thickest preserved deposits of the Buntsandstein Gr. (Bouly & Demassieux, 1996) (Fig. 1-8). Consists of a fluvial system in desert-type settings (Dalchroth, 1985; Bourquin, 2006; Bourquin et al., 2009), composed essentially of braided fluvial sandstones, with rare and interspersed centimetre thick floodplain clay layers, and aeolian sandstones that become more representative towards the top (Bourquin et al., 2006; Bourquin et al., 2009).

In France, the Middle Buntsandstein is divided into three main formations: Lower Grès Vosgien (LGV), Upper Grès Vosgien, and Conglomérat Principal (Duringer et al., 2019) (Fig. 1-8). The thickness of the Middle Buntsandstein increases towards Germany, resulting in subdivisions that are not identifiable in France (Perriaux, 1961; Menillet et al., 2015). For instance, the LGV corresponds to the Germanic nomenclature Trifels and Rehberg facies, and the Upper Grès Vosgien corresponds to the Karstal facies (Duringer, 2019).

The LGV is the thickest formation of the Buntsandstein Gr. reaching up to 200 metres in thickness (Gall, 1985; Aichholzer, 2019). It is dominated by medium- to coarse-grained arkosic sandstones, composed mainly of rounded quartz (85%) and feldspar (15%) (Perriaux, 1961; Menillet et al., 2015). In regions where the Lower Buntsandstein is present, the transition into the LGV is mainly marked by a sudden appearance of pebbles in a relatively large abundance. This forms an approximately

10-meter-thick level named Conglomérat Basal, with pebbles composed of quartzite, quartz, granite and gneiss (Perriaux,1961). This conglomerate records the first evidence of an arid climate that follows the whole unit deposition, as clasts are reworked and shaped by the wind (ventifacts) (Durand and Bourquin, 2013). However, the Conglomérat Basal is not present where the Middle Bunstsandstein overlies directly the bedrock (Perriaux,1961).

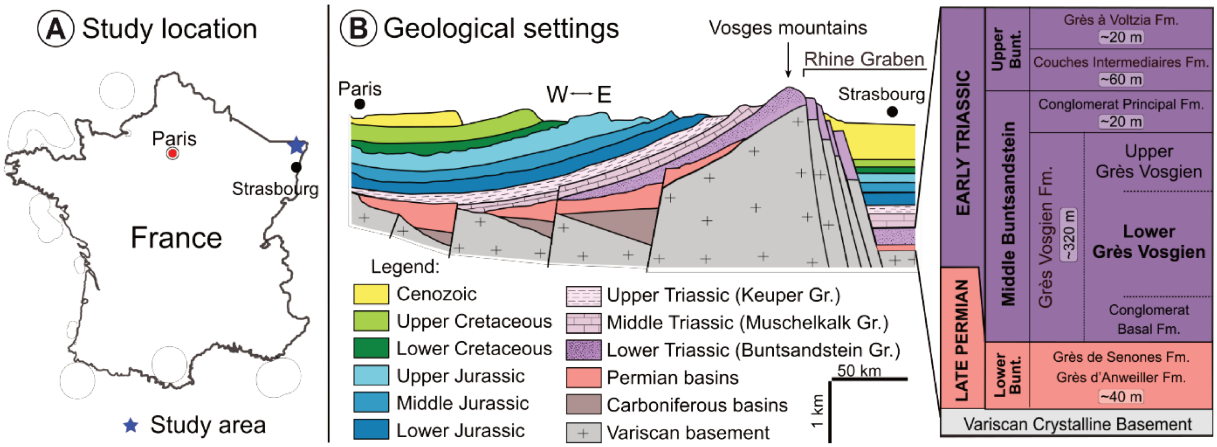


Figure 1-8: Location of the study area, and geological settings. Adapted from Bouly and Demassieux (1996), Guillocheau et al. (2000), Herivaux and Marechal (2019) and Duringer et al. (2019).

The LGV was deposited in a wide alluvial plain, devoid of vegetation, in which sedimentary dynamics were governed, mainly, by braided fluvial systems with an overall north-east flow direction, towards the centre of the Germanic Basin (Durand and Bourquin, 2013). This unit was built through vertical stacking of wide, shallow channels, interlayered with both reworked and in situ aeolian deposits, and presents a slight decrease of pebbles content towards the top as a result of the basin transgressive stage (Perriaux,1961; Bourquin et al., 2009). The channel's width often exceeds 100 m, presenting an erosive base frequently draped by gravel with a finning upward pattern of channel infill (Perriaux,1961; Gall, 1985; Bourquin et al., 2009; Durand and Bourquin, 2013). The aeolian deposits occurred between channels after events of river overflow followed by a level fall, during which the remaining subaerial deposits were then subjected to wind action causing a depletion of fine sediments by winnowing and, sometimes, the formation of wind dunes of variable sizes (Durand and Bourquin, 2013). In addition, another remarkable feature observed is deflation lags surfaces, which extend laterally for hundreds of metres, reflecting periods when the wind reworked fluvial deposits (Bourquin et al., 2009).

The LGV is composed mostly of lenticular bodies of cross-bedded medium- to coarse-grained fluvial sandstones with varied amounts of pebbles, rich in iron and manganese oxides at the base, and intercalated with some thin horizontally laminated sandstones, especially towards the top (Menillet et al., 2015; Duringer, 2019). Cementation by ferruginous coat and quartz overgrowth results in more resistant beds, and consequently, the LGV represents the main steep slopes in terms of geomorphology (Menillet et al., 2015), preserved mainly in the region of the Northern Vosges.

Despite the knowledge acquired in recent decades regarding the sedimentological characteristics of the LGV, there is still a lack of studies presenting a quantitative facies analysis of its deposits. This analysis is presented in Chapter 2 of this thesis.

1.2.5.1. Geothermal and lithium exploration in the Lower Triassic deep reservoir

The geothermal energy explored in Upper Rhine Graben relies mainly on fractured granites with high permeability (Vidal and Genter, 2018). These fractures also transect the overlying Triassic deposits, connecting the fluids from the granitic basement across the different lithologies of the Buntsandstein Gr. (Haffen et al., 2013). The highest permeabilities in the Triassic deposits are associated with fractured zones (Vidal and Genter, 2018). However, the permeabilities associated with these fractures are lower than those measured in the granitic basement (Vidal and Genter, 2018; Glaas et al., 2012), and varies depending on the sedimentary unit intersected by the fractures (Haffen et al., 2013).

In terms of flow-paths in the Triassic deposits, it is considered a composite network between the permeability of sedimentary deposits and the permeability of fractures (Haffen et al., 2013). Fractures control the vertical pathways that connect matrix-permeable stratigraphic levels, where horizontal flow takes place (Haffen et al., 2013). However, away from major fault zones, the Buntsandstein Gr. present low fracture density (Haffen et al., 2013). Thus, it is important to comprehend the sedimentary architecture and its respective permeability distribution when conceptualising the Triassic reservoir model.

The Buntsandstein Gr. in the axis of the Upper Rhine Graben has been identified as hosting the most promising zones for lithium exploration in Europe, due to the high concentration of lithium in geothermal brines (Dugamin et al., 2021; Sanjuan et al., 2022). The sources and the mechanisms of lithium enrichment are not completely understood (Dugamin et al., 2021). However, the main source in the Upper Rhine Graben is likely to be the alteration of the youngest unit of the Buntsadnstein Gr., the mica-rich Grès à Voltzia Formation (Fig. 2-1) (Sanjuan et al., 2022). Thus, the understanding of vertical and lateral solute transport through all formations of the Buntsandstein Gr. is essential for better prediction of zones hosting the higher concentrations.

The estimation of the lithium resource volume depends on the reservoir's porosity, storage coefficient, and recovery rates (Durgamin et al., 2021). These aspects are directly dependent on the geological characteristics (Flexer et al., 2018; Fries et al., 2022; Sanjuan et al., 2022). The exploration process includes the reinjection of the lithium-depleted water back into the reservoir, which may decrease the lithium concentration in the reservoir (Durgamin et al., 2021; Sanjuan et al., 2022). The rate of thermal and chemical breakthrough during reinjection depends on permeability and porosity distribution (O'Sullivan et al., 2023).

The complexity associated with lithium exploration makes it difficult to adapt a successful exploitation from one site to another (Flexter et al., 2018). Therefore, comprehending solute transport flow paths at a site scale, rather than just at a regional scale, is essential for an efficient exploration (Sanjuan et al., 2022). Considering that facies-scale heterogeneities strongly influence the recovery rates in oil fields (Høimyr et al., 1993), and the solute transport in groundwater (Zheng & Gorelick, 2005; Ramanathan et al., 2010; Ren et al., 2022), it is expected that this should also apply to lithium exploration.

1.2.5.2. The Lower Triassic shallow aquifer

In addition to the deep aquifer with high potential for exploration of lithium-rich geothermal brines, the Lower Triassic sandstones at shallow depths are also widely exploited for public water supply (drinking and industrial water) in five French departments: Bas-Rhin, Vosges, Moselle, Meurthe et Moselle, and Meuse, according to well data from the French Geological Survey (BRGM). The nomenclature used for

the Lower Triassic shallow aquifer is Grès du Trias Inférieur (GTI) (e.g. BRGM, 2002; 2023; Vaute et al., 2007; 2013).

In the unconfined zones of the GTI, the aquifer is considered highly vulnerable, and, locally, its groundwater shows degradation in chemical quality (BRGM, 2002). The area which the aquifer is unconfined is estimated to be 7423 km^2 (Vaute, 2007), extending over France, Germany, and Luxembourg, mostly in the western shoulder of the URG, considered the main recharge area for the GTI (Vaute et al., 2013). Towards the centre of the Paris Basin, to the west, the aquifer gradually gets deeper and confined by the Middle Triassic Muschelkalk Group (Vaute et al., 2007). Due to the shallower depths of exploration in the unconfined areas (2 m to 200 m), the groundwater has a low content of dissolved minerals (Vaute et al., 2007), making it ideal for human consumption. The groundwater mineralisation increases towards the west, in the confined sections (Vaute et al., 2007).

The fact that the most vulnerable zones have the best quality of drinking water highlights the importance of understanding aquifer heterogeneity, particularly for better predicting the transport of contaminants. Additionally, since these unconfined zones are close to the outcrops analysed in this study, it is more likely that similar heterogeneities observed in the outcrops occur within the aquifer.

1.2.6. Permeability heterogeneity in fluvio-aeolian systems

Fluvio-aeolian deposits represent an intersection of sedimentary processes, characterised by the interplay of fluvial (river and stream) and aeolian (wind) mechanisms. These deposits form in environments where water and wind collaborate to transport, deposit, and rework sediments. Typically found in arid and semi-arid regions, where intermittent water flow intersects with prevailing winds, fluvio-aeolian deposits can produce several distinct architectures depending on variations of spatial and temporal interactions between fluvial and aeolian mechanisms (e.g. Langford, 1989; Cowan, 1993; Trewin, 1993; Bongiolo and Scherer, 2010). Fluvial sediment supply, water table level, the degree of wind-sand-saturation, soil formation, and the presence of vegetation, are some of the factors influencing the construction of the fluvio-aeolian deposits architecture (Langford, 1989). The understanding of fluvio-aeolian deposits is crucial for interpreting past climatic conditions, sedimentary

environments, and reservoir heterogeneity associated with them (e.g. Langford, 1989; Cowan, 1993; Trewin, 1993; Bongiolo and Scherer, 2010).

Besides the focus of this study, the Buntsandstein sandstones, fluvio-aeolian succession are well-established reservoirs for geo-resources worldwide, such as the Sherwood and Bunter sandstones in the United Kingdom (Cowan, 1993; Alshakri, et al., 2023), the Rotliegend Group in the North Sea (Howell and Mountney, 1997), the Norphlet Sandstone in the Gulf of Mexico (Dixon et al., 1989) and the Guarani aquifer system in Brazil (Höyng et al., 2014).

When observed as a single geological unit, fluvio-aeolian deposits are considered to record good reservoir characteristics such as porosity and permeability (e.g. Haffen et al., 2013; Höyng et al., 2014). Increasing the scale of detail, aeolian deposits commonly record better reservoir characteristics than fluvial deposits (e.g. Cowan, 1993; Ellis, 1993; Fischer et al., 2007; Bongiolo and Scherer, 2010; Bjørlykke, 2014; Quandt et al., 2022 Alshakri, et al., 2023). Finally, when aeolian deposits are studied in detail, significant differences in permeability can be observed within these systems (e.g. Chandler et al., 1989; Fischer et al., 2007; Newell et al., 2019; Thompson et al., 2019), as is also presented in Chapter 3 of the present study. Therefore, the understanding of the fluvio-aeolian depositional controlling factors and their resulting architectures is essential for a better prediction of reservoir heterogeneity associated with this type of deposit.

1.2.7. Permeability data in the Buntsandstein Group (Gr.)

The permeability of the Buntsandstein Gr. in eastern France has been extensively measured and analysed. Haffen et al. (2013) presented permeability and porosity characteristics from core samples, associated with thermal gradient variation, to predict the main reservoir fluid-circulation zones; Heap et al. (2017) analysed, using core samples, the relationship between permeability and: microstructure; grain size and shape; pore size and throat size distribution; mineral content; porosity; P-wave velocity; and bedding orientation; Kushnir et al. (2018a) investigated the role of fractures on the permeability, also from core samples; Kushnir et al. (2018b) analysed porosity, permeability, thermal conductivity and P-wave velocity from outcrops located at the west of the Upper Rhine Graben; Goupil et al. (2022) investigated the permeability anisotropy of horizontally stratified sandstones from core samples; Busch

et al. (2022a) presented the relationship between petrographic characteristics and reservoir quality (permeability and porosity) from core samples; and Busch et al. (2022b) analysed permeability and porosity data from outcrops and core samples to evaluate the significance of outcrop data for reservoir quality assessment. However, despite the important contribution of these studies to a better comprehension of the petrophysical characteristics of the Buntsandstein Gr., no systematic facies controls of such data are presented. Therefore, the present study is the first to present the link between permeability data with the sedimentary facies, and their respective proportions and architecture, in high resolution, within the Buntsandstein Gr. in eastern France.

1.2.8. Groundwater flow and solute-transport modelling

A groundwater flow model is applied to determine the hydraulic heads and the flow velocity at any point within a model domain (Witherspoon and Neuman, 1972). The development of the model begins with generating the conceptual model. The conceptual model consists of the representation of features that govern the behaviour of the groundwater system (Istok, 1989), such as the hydrostratigraphic units and system boundary conditions (Witherspoon and Neuman, 1972; Anderson et al., 2015). The conceptual model and the modelling purpose guide the choice of the mathematical model and its associated code (Anderson et al., 2015).

The mathematical model to be used depends primarily on the flow problem category to be solved (Istok, 1989). In this study, a vertical, 2D, steady-state, with constant thickness, and saturated groundwater flow model is applied, using the partial differential equation:

$$\frac{\partial}{\partial x}\left(K_x \frac{\partial h}{\partial x}\right) + \frac{\partial}{\partial z}\left(K_z \frac{\partial h}{\partial z}\right) = 0$$

where h is the hydraulic head, K_x and K_z are the components of saturated hydraulic conductivity in the x and z coordinate directions.

The two main numerical methods used in groundwater studies are the finite difference method and the finite element method (Istok, 1989; Wang and Anderson, 1995). In this study, it is applied the finite element method because it better suits the objective of realistically representing irregular hydrostratigraphic complexities (Istok, 1989). The first step in using the finite element method is to discretise the aquifer

domain into a finite element mesh, which is an assembly of nodes and triangular elements that replace the hydrostratigraphic conceptual model (Istok, 1989). Although triangular mesh elements allow for a more precise representation of heterogeneity geometries, they typically require more computational effort when compared to the rectangular mesh elements used in finite difference methods (Istok, 1989). Therefore, a balance between the refinement of mesh elements and computational effort is necessary during the discretisation of aquifer heterogeneity. After generating the model mesh, the discretisation of the hydrostratigraphic model domain is completed by attributing the hydraulic properties (e.g. hydraulic conductivity, porosity, and anisotropy) to the mesh elements.

The final stage in completing the conceptual model is to incorporate the boundary conditions (Wang and Anderson, 1995). The boundary conditions used in this study are the specified head boundary conditions. The application of specified head boundary conditions involves fixing hydraulic head values at the nodes along the model boundaries; thus, the head values at these nodes do not change in response to hydrogeologic stresses (e.g. pumping, injection, recharge, and evapotranspiration) (Anderson et al., 2015). By applying the fixed head boundary conditions, the volumetric flow rate (Q [L3/T]) across the model domain is calculated using the general Darcy equation:

$$Q = \frac{KA\Delta h}{L}$$

where Δh is the hydraulic heads difference between inlet and outlet; L is the length of the considered domain; K is the hydraulic conductivity [L/T], and A is a representative area [L^2].

The solute-transport modelling applied in this study considers only advective transport. For this purpose, the post-processor particle tracking tool is applied to calculate the behaviour of flow paths and travel times across the model domain. The particle tracking tool uses outputs from groundwater flow results (heads and flow velocities distribution) and, combined with specified effective porosity values, calculates velocities at nodal points of the grid mesh, and finally the flow paths and their associated travel times (Anderson et al., 2015).

All these steps, from discretising the model domain into mesh elements to the particle tracking simulation, are applied using built-in tools within the software FEFLOW 8.0® (Diersch, 2014).

Groundwater modelling carries uncertainties related to the representation of groundwater processes (Anderson et al., 2015). These uncertainties can arise either from the specific code selected, which reduces all processes under consideration to those included in the code (Anderson et al., 2015), or from “Unknown unknowns”, which are aspects that influence the groundwater behaviour that “we don’t know we don’t know” (Hunt and Welter, 2010). The latter is particularly represented by unexpected heterogeneities in subsurface properties (Anderson et al., 2015).

The quality of a groundwater solute-transport model (particle tracking) relies directly on the quality of the groundwater flow model (Konikow, 2011). Solute transport in groundwater by advective and dispersive processes is affected by the velocity flow fields within the aquifer, which are linked to hydraulic heads and hydraulic conductivity (K) distribution (Konikow, 2011). Dispersion refers to mixing and spreading caused by both molecular diffusion and variations in flow velocity on a porous scale (Wang and Anderson, 1995). However, in a field-scale problem, such aspects may be negligible compared to dispersion caused by large-scale heterogeneities within the aquifer (Wang and Anderson, 1995). Therefore, the concept of macrodispersivity is applied to characterise dispersion caused by different flow velocities between these larger-scale heterogeneities (Dagan, 1990; Wang and Anderson, 1995). The method applied in this study, of realistically representing heterogeneities using outcrop data, and simulating the flow of particles through them, helps to calculate the macrodispersion associated to such heterogeneities more accurately.

1.2.9. The use of sedimentary facies analysis in groundwater fluid-flow model

Enhancing the complexity of hydrogeological conceptual models requires a greater number of hard datasets, more sophisticated numerical models for flow simulation, multidisciplinary professionals with higher expertise, and increased computational power. These factors increase costs and time-consuming processes. Thus, is necessary to evaluate the balance between modelling objectives and complexity. For instance, previous studies have shown that simplified conceptual

models can give as reasonable results as complex models to predict water balance and hydraulic heads, (Hudon-Gagnon et al., 2015; Åberg et al., 2021). If the objective is to characterise discharge and recharge patterns accurately, in settings of highly variable hydraulic conductivities between geologic units, it is worth understanding and discretising the complexity of such geological features (Åberg et al., 2021). Finally, if the objective of the numerical flow model is to predict solute transport, then a high-resolution (decimetre-scale) heterogeneity characterisation is important for an accurate prediction of the dispersion of groundwater contamination plume (Zheng & Gorelick, 2005; Ramanathan et al., 2010; Ren et al., 2022).

Therefore, this study investigates the effects of decimetre-scale heterogeneity on advective solute-transport model results. The heterogeneities under investigation were formed by distinct sedimentary processes. However, since they do not show significant differences in grain sizes (all sandstones), and given that the main proxy used to recognise heterogeneities is the differences in grain sizes (Koltermann & Gorelick, 1996), these heterogeneities are likely to be overlooked in conceptual models discretisation, possibly contributing to “unknown unknowns” (sensu Hunt and Welter, 2010) within numerical models.

1.3. SUPPLEMENTARY EXTERNAL ANALYSIS

Petrographic description, quantification, and the capture of photomicrography were conducted by Dr. Garibaldi Armelenti, from the Federal University of Rio Grande do Sul, Brazil. Petrophysical measurements (permeability and connected porosity) using laboratory equipment were conducted by Professor Mike Heap, from the University of Strasbourg.

2. Chapter 2: Quantitative facies analysis of a fluvio-aeolian system: Lower Triassic Buntsandstein Group, eastern France

Bofill, L.M., Bozetti, G., Schäfer, G., Ghienne, J.F., Schuster, M., Scherer, C., Souza, E., 2024. Quantitative facies analysis of a fluvio-aeolian system: Lower Triassic Buntsandstein Group, eastern France. Sedimentary Geology. 465, 106634. 22 p. https://doi.org/10.1016/j.sedgeo.2024.106634

ABSTRACT

Understanding the factors that control the temporal and spatial evolution of the Lower Triassic Buntsandstein Group, eastern France, is important not just for palaeoenvironmental reconstruction but also because it is an important reservoir for the lithium-rich geothermal brines in the Upper Rhine Graben region. The interval of interest in this study, the Lower Grès Vosgien Formation (LGV), is made up of c. 200 metres of clastic deposits of mixed fluvial and aeolian origin. Given the proximity between the outcrops and the areas of mineral and heat exploration, this region offers a unique opportunity for quantitative analysis and correlation between outcrops and reservoir. The LGV is the thickest Formation in the Buntsandstein Group. However, hitherto, no detailed architectural analysis has been published to reveal the controlling factors of its depositional elements. In this study, high-resolution facies analysis was applied to thirteen outcrops, and a core, to quantify fluvial and aeolian depositional architectures, and to comprehend palaeoenvironmental conditions during their deposition. Two facies associations were identified. The fluvial channel facies association, composed mainly of sandstones deposited in poorly confined, occasionally ephemeral channels, corresponds to 93% of the total thickness. The analysis of more than 800 sets of strata characterised by lower-, transitional-, and upper-flow regime sedimentary structures, distributed within different architectural elements, enabled the distinction of temporal and spatial variabilities, and an estimate of fluvial palaeohydraulic characteristics. The wind- and water-laid facies association, which accounts for 7% of the total thickness, records an architecture controlled by a fluctuating water-table level, and ephemeral floods. Results revealed that aeolian dunes and sand sheets accumulated in distinct temporal moments. The vertical trends, recorded in the core, indicate an upward increase in the frequency of intercalations between the two facies associations, and a decrease in the occurrences of thicker cross-bedded sandstone sets of fluvial origin, which, associated with the overall

retrogradational stacking pattern of the LGV, is interpreted as the preserved record of a large distributive fluvial system (DFS). The occurrence of laterally extensive aeolian deposits, overlying fluvial deposits, is often associated by authors with periods of relatively more arid conditions at a regional scale. However, evidence indicates channel belt avulsion as an alternative interpretation for the establishment of the two facies associations. The findings enhance the knowledge about the depositional controlling factors in braided fluvial and aeolian systems, and improves predictive models that account for reservoir heterogeneity in accumulated successions of this type.

2.1. INTRODUCTION

The major role of continental depositional systems as subsurface sedimentary reservoirs, which may act as hosts for georesources, and the significance of facies scale heterogeneities in fluid-flow behaviour (Høimyr et al., 1992), justify the prolonged history of studies on the factors that control deposition in continental environments (e.g. Miall, 1977; Røe, 1987; Kocurek, 1988; Langford, 1989; Havholm and Kocurek, 1994; Hjellbakk, 1997; Mountney et al., 1999; Scherer and Lavina, 2005; Fielding, 2006; Weissmann et al., 2010; Wang and Plink-Björklund, 2019; Ventra and Moscariello, 2023). The quantitative analysis of sedimentary deposits is crucial for understanding depositional processes and palaeoenvironmental conditions (e.g. Leclair and Bridge, 2001; Hansford and Plink-Björklund, 2020; Hartley and Owen, 2022; Reis et al., 2022; McLeod et al., 2023; Colombera et al., 2024). Likewise, quantitative sedimentary analysis aids in the refinement of landscape evolution models, and to improve predictions of subsurface reservoirs (Colombera et al., 2013).

Triassic continental deposits have long served as reservoirs for hydrocarbons and groundwater (e.g. Cowan, 1993; Liu et al., 1996; Rossi et al., 2002; Leleu et al., 2009; McKie, 2011; Medici et al., 2015). This is no different for the Lower Triassic Buntsandstein Group (Gr.) in eastern France (Fig. 2-1A), which serves as a potable groundwater aquifer (Vaute et al., 2007; 2013), and an established reservoir of lithium-concentrated geothermal brine (Aquilina et al., 1997; Kölbel et al., 2020; Fries et al., 2022; Sanjuan et al., 2022). This succession has also been identified as hosting the most promising lithium reserves in Europe (Sanjuan et al., 2022).

The Lower Grès Vosgien Formation (LGV), Middle Buntsandstein (Olenekian) (Fig. 2-1B), has been interpreted by Bourquin et al. (2009) to represent the preserved deposits of a braided fluvial system developed upon an arid alluvial plain, and fluvial-aeolian deposits of a marginal erg (aeolian dune field). The authors presented a robust dataset and interpretations of large-scale, vertical and lateral, distribution of the Middle Buntsandstein, undertaking analysis via application of sequence stratigraphic concepts to the continental succession. In this study, a detailed facies architecture characterisation is presented, focused on the LGV, in a scale not targeted by Bourquin et al. (2009).

Preserved intercalation between aeolian and fluvial deposits is often attributed to spatio-temporal alternations between dry and humid climatic phases, respectively (e.g. Clemmensen and Abrahamsen, 1983; Porter, 1987; Havholm and Kocurek, 1994; Jones and Blakey, 1997; Newell, 2001; Farraj and Harvey, 2004; Scherer and Lavina, 2005; Al-Masrahy and Mountney, 2015). The same has been interpreted by Bourquin et al., (2009) for the LGV. Alternatively, it may result from interactions between coexisting aeolian and fluvial processes that influence locally the dynamics of these systems (Jones and Blakey, 1997; Rittner et al., 2016).

Recent advances in interpreting fluvial discharge variability (Plink-Björklund, 2015; Fielding et al., 2018; Sharma et al., 2023; Walker and Holbrook, 2023), palaeohydraulics (Leary and Ganti, 2019; Alexander et al., 2020; Lyster et al., 2022; Ohata et al., 2022; Hartley and Owen, 2022; Colombera et al, 2023), and spatial versus temporal variations in fluvial (Colombera and Mountney, 2019; Herbert et al., 2019; Priddy and Clarke, 2021; Lyster et al., 2022; Walker and Holbrook, 2023), and aeolian (Cosgrove et al., 2021; Gross et al., 2022; Kifumbi et al., 2023) systems, emphasise the need to refine existing facies models of previously studied formations.

The aim of this study is to use qualitative and quantitative facies and architectural characterisation, at different scales, to understand the factors that controlled the depositional evolution of the Lower Grès Vosgien Formation. The following research questions are answered: i) What are the proportions of the different elements that compose the LGV? ii) What are the evidence of spatial vs. temporal flow conditions variations, in dryland rivers? iii) How do water-table level fluctuations, and ephemeral floods, control the architecture of aeolian deposits? iv) How do the different facies

associations evolve spatially and temporally, and what do they reveal about the large-scale depositional system?

2.2. STUDY AREA AND GEOLOGICAL SETTING

The study area is situated in eastern France, along the western shoulders of the Upper Rhine Graben (URG), where the Buntsandstein Group (Gr.) crops out at the Vosges mountains, and where the EPS1 well was drilled and cored, at Soultz-sous-Forêts (Fig. 2-1C) (e.g. Gérard et al., 2006; Kölbel and Genter, 2017). The Buntsandstein Gr. was deposited during the Lower Triassic along the western margin of the German Basin in a sedimentation area extending across eastern France, Switzerland, Luxemburg, Belgium, Netherlands, Germany, Poland and Denmark (Gall et al., 1977). The region experienced predominantly continental sedimentation attributed to braided-river deposition either on crystalline basement or on restricted Late Permian intracontinental basins (Dachroth, 1985; Deynoux et al., 1997; Bourquin et al., 2009). Different geological formations are recognised within the Buntsandstein Gr. depending on the lateral position in the basin (Mader, 1985).

This study targets the thickest unit of the Buntsandstein Gr. in eastern France, known as the Lower Grès Vosgien Formation (LGV) (Théobald et al., 1967) (Fig. 2-1B), which attains a maximum thickness of ~200 m in the region of Soultz-sous-Forêts (Aichholzer, 2019). The LGV is composed of braided fluvial and aeolian sandstones deposited under arid conditions (Dalchroth, 1985; Bourquin et al., 2006; Bourquin et al., 2009), interfingered with rare centimetre-thick claystone layers of floodplain origin (Ghienne et al., 1994; Bourquin et al., 2006; Bourquin et al., 2009).

During the Late Eocene, the URG was formed in front of the alpine compression, reactivating normal faulting structures from the Variscan orogeny (Grimmer et al., 2017) that resulted in burial of the Triassic Buntsandstein Gr. to depths of approximately 1000 m to 1400 m (Aichholzer, 2019). In contrast to the basin axis, the elevated portions of the URG expose the Buntsandstein Gr. deposits along the Vosges and Black Forest mountains. This geological setting offers an ideal opportunity to study these outcrops as analogues for reservoir characterisation, given the actual reservoir and its analogues belong to the same geological formation, and are situated geographically close to each other (Fig. 2-1).

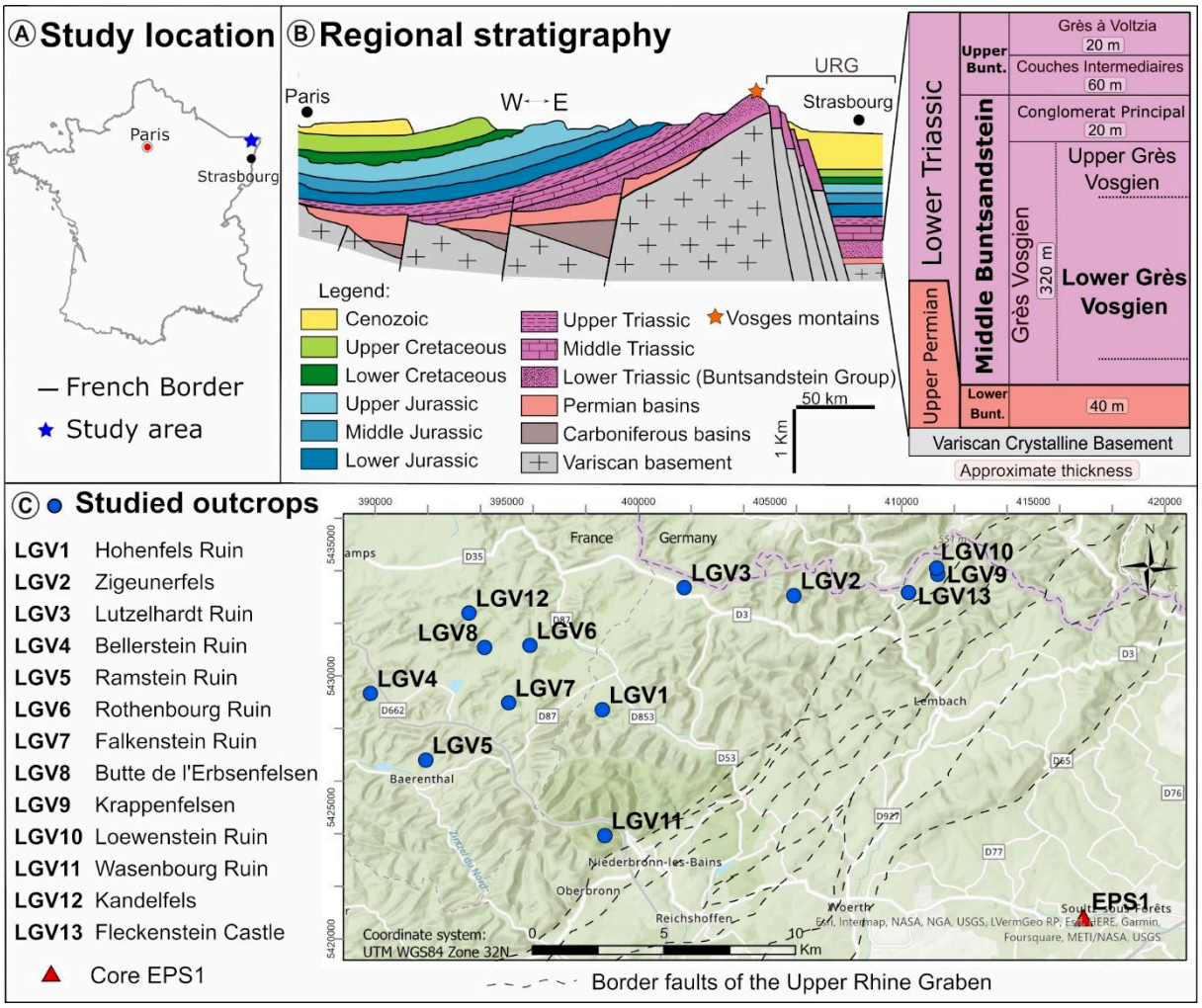


Figure 2-1: (A) Study area location; (B) regional stratigraphy, adapted from Bouly and Demassieux (1996), Guillocheau et al. (2000), Herivaux and Marechal (2019) and Duringer et al. (2019).

2.3. METHODS AND MATERIALS

Sedimentological data were collected through vertical profile descriptions at scale of 1:50 from thirteen outcrops (Fig. 2-1C), totalling 290 m of rock succession, and from the upper 100 m of the LGV of the well EPS1 (see sedimentary logs in the annex). The height of the outcrops varies from 7 m to 40 m. Facies were coded following the principles outlined by Miall (1977), and for facies analysis, the framework of Walker (1992) was adopted, grouping genetically related facies into facies associations. Within the facies associations, specific morphologies were defined as architectural elements (Allen, 1983a; Miall, 1985).

Considering that vertical profiles alone are insufficient for fluvial sedimentology analysis due to the numerous lateral facies changes (Miall, 1988), characterisation of fluvial architectural elements was conducted from seven out of the thirteen outcrops. In outcrop LGV7 (Fig. 2-1C), a Digital Outcrop Model was used, created with a DJI

Phantom 4 UAV drone, equipped with a built-in camera, and Global Navigation Satellite System. Photos of the outcrop face and top were manually captured with an overlap of approximately 70% between each photo. Subsequently, the photos were imported into the software Agisoft Metashape® to generate a dense point cloud, and then to create the final triangular mesh. Digital outcrop models facilitate measurements, understanding of lateral and vertical relationships of sedimentary structures, integration of field data, construction of geological models, and remote description of inaccessible outcrops.

The fluvial architectural analysis relies on 275 palaeocurrents measurements obtained from individual cross-bedding foresets, and 266 measurements of dip angle and dip direction of sets and cosets basal bounding surfaces. These measurements were added to the software Stereonet (Allmendinger et al., 2012; Cardozo and Allmendinger, 2013), which automatically calculates the mean vector and circular variance.

The estimation of the mean original fluvial dune height (h_m), from cross-set thickness, helps access information regarding local flow depth variations (Leclair and Bridge, 2001; Reesink et al., 2015; Leary and Ganti, 2019; Li et al, 2022). In this study, the approach defined by Leclair and Bridge (2001) (Equation 1) was used, which is still being applied in recent works (e.g. Hartley and Owen, 2022; McLeod et al, 2023):

$$h_m = 2.9 * (\pm 0.7) * (S_m) \quad (1)$$

where, S_m is the mean cross-set thickness. Before the application of Equation 1, a decompaction factor of 10% was applied to S_m (Hartley and Owen, 2022). This study is supported by 800 measurements of fluvial cross-set thickness. To calculate local flow depth (d), Leclair and Bridge (2001) defined:

$$6 < \frac{d}{h_m} < 10 \quad (2)$$

Despite being imprecise, it can complement flow depth estimative calculated from channel-bar thickness (Leclair and Bridge, 2001; Hartley and Owen, 2022). Hartley and Owen (2022) excluded from their analysis abnormally thick cross-sets to avoid overestimation of channel depth. However, since the authors did not mention the method used to define such thickness threshold, in this study was used the interquartile

range method (IQR), a widely used statistical method to estimate data outliers, to define the upper bound (UB):

$$UB = Q3 + 1.5(Q3 - Q1) \quad (3)$$

where, $Q3$ is the value below which 75% of the data falls, and $Q1$ is the value below which 25% of the data falls. Data points above the UB are considered outliers, which corresponded to 3.8% of the cross-sets.

The use of 1D data is unreliable for estimating channel-depth because of the absence of architectural elements control. Moreover, core data tends to yield smaller estimations of true set thickness (Colombera et al., 2024). Nevertheless, since this was the only way to access a continuous succession of cross-sets, on a larger scale (c. 100 m), it was tested whether the thickness of cross-sets exhibited any vertical trend. Then, to evaluate the strength of identified trends, Spearman's rank correlation coefficient (Rs) was used (Davis 2002), where Rs = (+ or -) 1 means perfect correlation, and Rs = 0 means no correlation. To analyse if eventual correlations occurred by chance, the p-value approach was adopted (Davis 2002). The significance level for the calculated p-values was set at the commonly used threshold of 5%. In cases where the obtained p-value exceeds this threshold, it indicates that the observed correlation obtained by Rs is not representative and, thus, should not be upscaled. Rs and p-value were calculated using Excel ® functions. Furthermore, to evaluate the correlation of facies with granulometry, gravel content, and set thickness, the rank correlation coefficient Kendall's Tau-c (τ) was employed. Kendall's Tau-c (τ) effectively handles tied values in rank datasets (Kendall, 1938; Akoglu, 2018), as often seen with categorical sedimentology data. The degree of correlation (τ) was assessed based on Botsch (2011), categorizing the relationship strength between two variables as very weak (0 to 0.1), weak (0.1 to 0.19), moderate (0.2 to 0.29), and strong (0.3 or above).

Additionally, the cross-set thickness coefficient of variance (CV) is calculated to investigate if the fluvial bedforms were preserved in steady-state or disequilibrium conditions (Paola and Borgman, 1991; Leary and Ganti, 2019). The CV is only calculated when more than 30 cross-sets samples (Belle and Martin, 1993) are preserved within a channel unit (Lyster et al., 2022).

A classification related to gravel content within individual sets based on field descriptions is presented in Table 2-1, aiming to quantify the variations of gravel content within the LGV.

Table 2-1: Classes of gravel content in sandstone, and field criteria for their definition.

Class	Code	Class criteria
Sandstone without gravel	WG	No gravel clasts present within the set
Sandstone apparently without gravel	AWG	Difficult to find gravel clasts. Sometimes, a single granule or pebble within the set (i.e., <<1%)
Slightly gravelly sandstone	SG	Easy to find granules and pebbles within the set (up to 5%, Folk et al., 1970)
Gravelly sandstone	GS	Rich in granules, pebbles, and occasionally cobbles. (5% - 30%, Folk et al., 1970)

2.4. RESULTS

2.4.1. Sedimentary facies and their associations

In the LGV, thirteen distinct facies were identified (Table 2-2). These facies are interpreted to have been accumulated in response to subaqueous or subaerial (wind-related) processes. They vary from fine- to very coarse-grained sandstones, well- to poorly-sorted, composed mainly of quartz, feldspar and lithoclasts, indicating subarkose to sublitharenite composition, with variable amounts of gravel (Table 2-1). These facies are arranged as the internal components of seven architectural elements developed within two distinct facies associations: fluvial channel facies association (FC) and wind- and water-laid facies association (WWL). The FC is the dominant association, representing 93% of the total thickness measured for the LGV, whereas the WWL accounts for 7% (Fig. 2-2). The following sections present the main characteristics of each facies association, and their interaction with one another. Description and interpretation for individual facies are provided in Table 2-2.

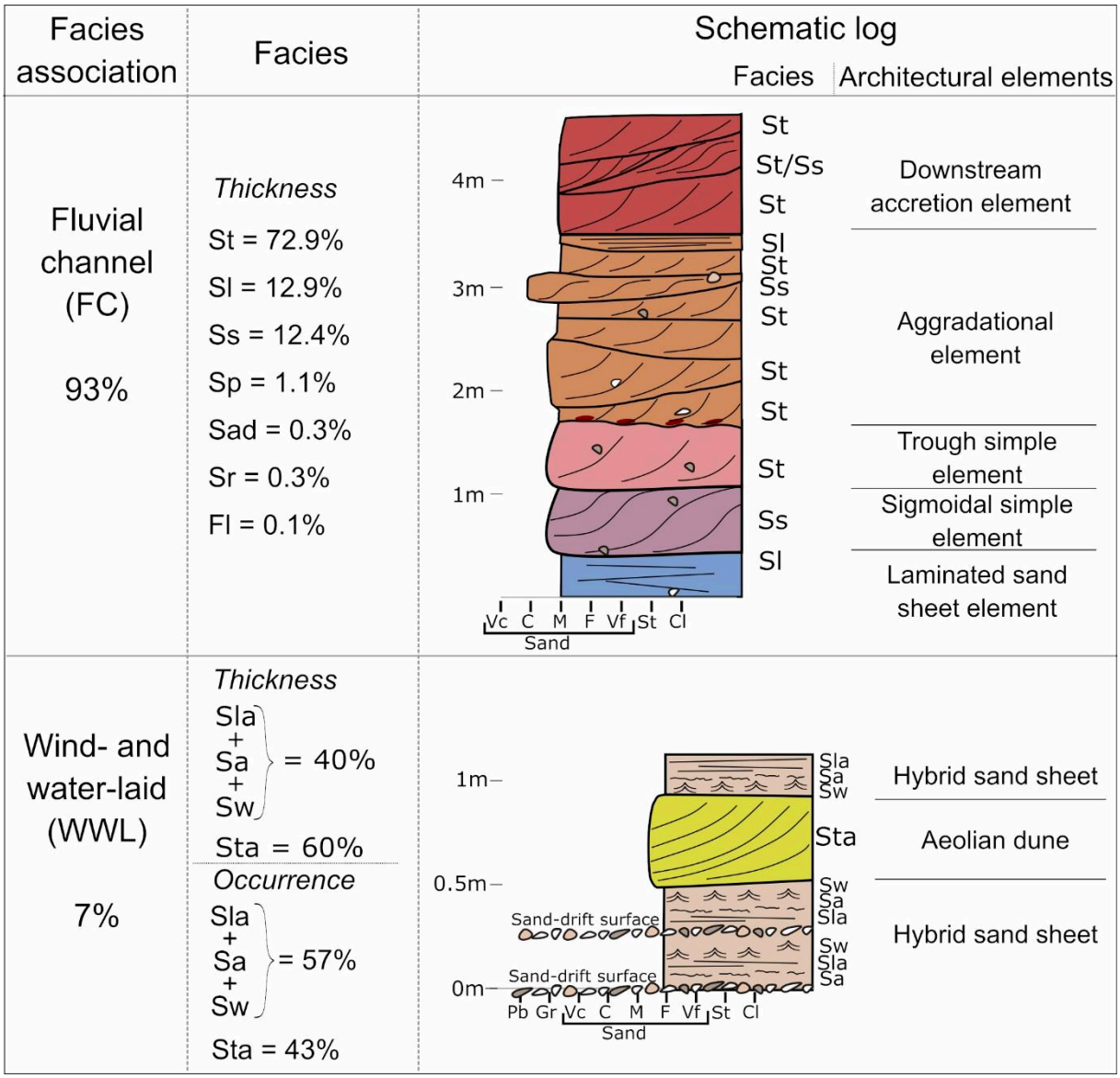


Figure 2-2: Facies associations, their thickness proportion measured for the Lower Grès Vosgien Formation, their respective facies and facies proportions, and a schematic log showing the architectural elements. See further details on architectural elements in Sections 2.4.1.1 and 2.4.1.2.

Table 2-2: Sedimentary facies observed in the Lower Grès Vosgien Formation.

Code	Facies description	Facies interpretation
St	Fine- to very coarse-grained sandstone, with trough cross-stratification; poorly- to well-sorted; it may have abundant quartz and quartzite clasts, occasionally up to cobble size, and 1 - 5 cm mud clasts, occasionally up to 35 cm; normal gradation in foreset laminae. Sets thickness varies from 10 cm up to 1.8 m. Presence of reactivation surfaces. Example: Fig. 2-3A.	Migration of subaqueous sinuous-crested and linguoid (3-D) dunes (Miall, 2006). Lower flow-regime (Zellman et al., 2020).

Code	Facies description	Facies interpretation
Sl	Fine- to very coarse-grained sandstone, with flat to low-angle cross-stratification (Fig. 2-3E), and, locally, convex-up laminations; poorly- to well-sorted; it may present abundant quartz and quartzite clasts up to pebble size; sub-angular to rounded grains. Parting lineation can be present when observed in planar view. Sets thickness varies from 10 cm up to 1.75 m. Example: Figs.2-3E, -3F and -3H.	Washed-out dunes (Miall,,1988; 2006), deposited in transitional flow-regime(Zellman et al., 2020); or deposition by breaking and upstream migrating antidunes, deposited under upper flow-regime (Fielding, 2006; Duller et al., 2008; Lang and Winsemann, 2013).
Ss	Medium- to very coarse-grained sandstone, with sigmoidal cross-stratification; poorly- to well-sorted; it may present abundant quartz and quartzite clasts up to pebble size; sub-angular to rounded grains. Sets thickness varies from 25 cm up to 1.4 m. Example: Figs. 2-3B, and -3H.	Humpback dunes (Saunderson and Lockett, 1981; Lang et al., 2021) formed at transitional flow-regime (Plink-Björklund, 2015), or by near-bed suspended sediment concentration (Bridge and Best, 1988). Bed features are formed by high-stage currents, transitioning from dune to plane bed (Røe, 1987). Different trajectories of the topset-foreset-transition point to different rates of deposition (Lang and Winsemann, 2013)
Sp	Medium- to coarse-grained sandstone, with planar cross-stratification; moderately- to well-sorted; it may present scattered granules and pebbles. Sets thickness varies from 45 cm up to 75 cm.	Migration of subaqueous straight-crested dunes, under lower flow-regime (Miall, 2006).
Sad	Medium-grained sandstone, with internal low-angle, truncated, cross-stratification, dipping in the opposite direction of the dominant cross-stratified sets above and below; records convex-up top; poorly- to well-sorted. Sets thickness varies from 7 cm up to 20 cm. Example: Fig. 2-3G.	Upstream migrating subaqueous antidunes under supercritical flow (Alexander et al., 2001; Fielding, 2006; Cartigny et al., 2014)
Sr	Fine- to medium-grained sandstone, with asymmetric ripple cross-lamination; moderately- to well-sorted; few centimetres sets thickness, forming up to 10 cm thick co-sets.	Migration of unidirectional subaqueous ripples. Lower flow-regime (Miall, 1977)
Sta	Fine- to medium-grained sandstone, with trough cross-stratification; moderately- to well-sorted; sub- to well-rounded grains; occasionally toesets consist of millimetrically spaced inversely-graded lamination, and pin-stripe lamination. Sets thickness varies from 10 cm up to 2.7 m. Occasionally records more than one set superimposed. Example: Figs. 2-10D and 2-10E.	Migration of crescentic aeolian dunes (Kocurek, 1991). Slip-face with intercalation of grain-fall and grain-flow (Kocurek, 1991). Occasionally forming draas (Kocurek, 1991).
Sla	Very fine- to medium-grained sandstone, showing grain size bimodality; flat to low-angle lamination; moderately- to well-sorted; sub- to well-rounded grains; pin-stripe laminations (Fryberger and Schenk, 1988), occasionally preserved inverse grading, and concentration of lenses up to 7 cm width, 5 mm thick, of coarse-grained sand; package thickness varies from 3 cm up to 40 cm. Example: Figs. 2-10A, -10B and -10C.	Translatent wind ripple climbing at sub-critical angles (Hunter, 1977; Cain and Mountney, 2009). Granule ripples (Fryberger et al., 1992).

Code	Facies description	Facies interpretation
Fl	Laminated mudstone, which might present bioturbation. Layer thickness varies from 1 mm to 15 cm. Often represented by levels with large mud cracks; laterally discontinuous due to erosion by succeeding flows. Example: Fig. 2-3D.	Deposition of suspended load by settling out in standing water (Miall, 2006)
Mb	Mudstone, with millimetric wrinkled lamination; laterally discontinuous; individual laminae thickness up to 1 mm; dominantly interfingered with facies Sla, occasionally at foreset base of facies Sta, sometimes with Sw; packages thickness where facies Mb is interfingered (Sla and Sw) varies from 5 cm up to 25 cm. Example: Fig. 2-10B.	Microbial mat formed rapidly between clastic depositional events, on wet substratum, resulting in microbially induced sedimentary structure (MISS) (Gerdes, 2007; Basilici et al., 2020)
Sw	Very fine- to medium-grained sandstone, with symmetric ripple-lamination; well-sorted; occasionally capped by mudstone laminae. Example: Fig. 2-10B and -10C	Sedimentation within oscillating ponds or shallow lakes, during windy periods (Ribes, 2015), followed by calm sedimentation (Miall, 2006)
Sa	Fine-grained sandstone, with wrinkled lamination; poorly- to well-sorted; individual laminae thickness up to 1 cm. Sets thickness up to 20 cm, interfingered with facies Sla and Slw. Example: Fig. 2-10C.	Adhesion of grains transported by the wind to a damp surface (Kocurek and Fielder, 1982).
Sm	Fine-grained sandstone, with no recognisable structures; well-sorted. Sets thickness varies from 5 cm up to 15 cm.	Rapid deposition of hyperconcentrated subaqueous gravity flow (Miall, 2006; Scherer et al., 2015), or appear massive due to diagenetic effects (Miall, 2006).

2.4.1.1. Fluvial channel facies association (FC)

The fluvial channel facies association (FC) comprises seven sedimentary facies (Fig. 2-2) arranged in amalgamated, lenticular and tabular sets, and distributed in five architectural elements. The architectural elements are quantitatively detailed in figure 2-9, identified by their geometry, facies, palaeocurrent, and bounding surfaces of sets and cosets.

2.4.1.1.1. Facies and general characteristics

Trough cross-bedded sandstone (St) (Figs. 2-3A, -3C, and -3H) is dominant (73%) (Fig. 2-2), followed by low-angle cross-bedded sandstone (Sl) (13%) (Figs. 2-3E, -3F, and -3H), and sigmoidal cross-bedded sandstone (Ss) (12%) (Figs. 2-3B, and -3H). Planar cross-bedded sandstone (Sp), upstream dipping, with convex-up lamination, cross-bedded sandstone (Sad) (Fig. 2-3G), ripples cross-laminated sandstone (Sr), and laminated mudstones (Fl) are rare (Fig. 2-2). Facies Fl are preserved as discontinuous millimetre- to centimetre-scale layers between sets, draping an erosional surface, and occasionally, between foresets (Fig. 2-3C).

However, mudstones are mainly preserved as mud clasts along cross-bedding foresets.

Facies Sl either form laterally extensive tabular deposits, or lenticular sandstone bodies with gentle concave-up basal surface. Convex-up lamination and parting lineation are associated. Typically, facies Sl transitions in a down-palaeocurrent direction to facies Ss through individual laminae traceable from the topset (horizontal/low-angle strata), to the toeset (concave-up strata) (Figs. 2-3B, and -8B). This horizontally to low-angle stratified topset may exhibit finer grain size, and less gravel content, than the down-palaeocurrent direction foresets. Facies Sl is included in facies Ss when this lateral relationship is evident. The transitions between facies Sl, Ss and St within the same bed also occur without the relationship mentioned above (Fig. 2-4). In such cases, they are defined as separated facies.

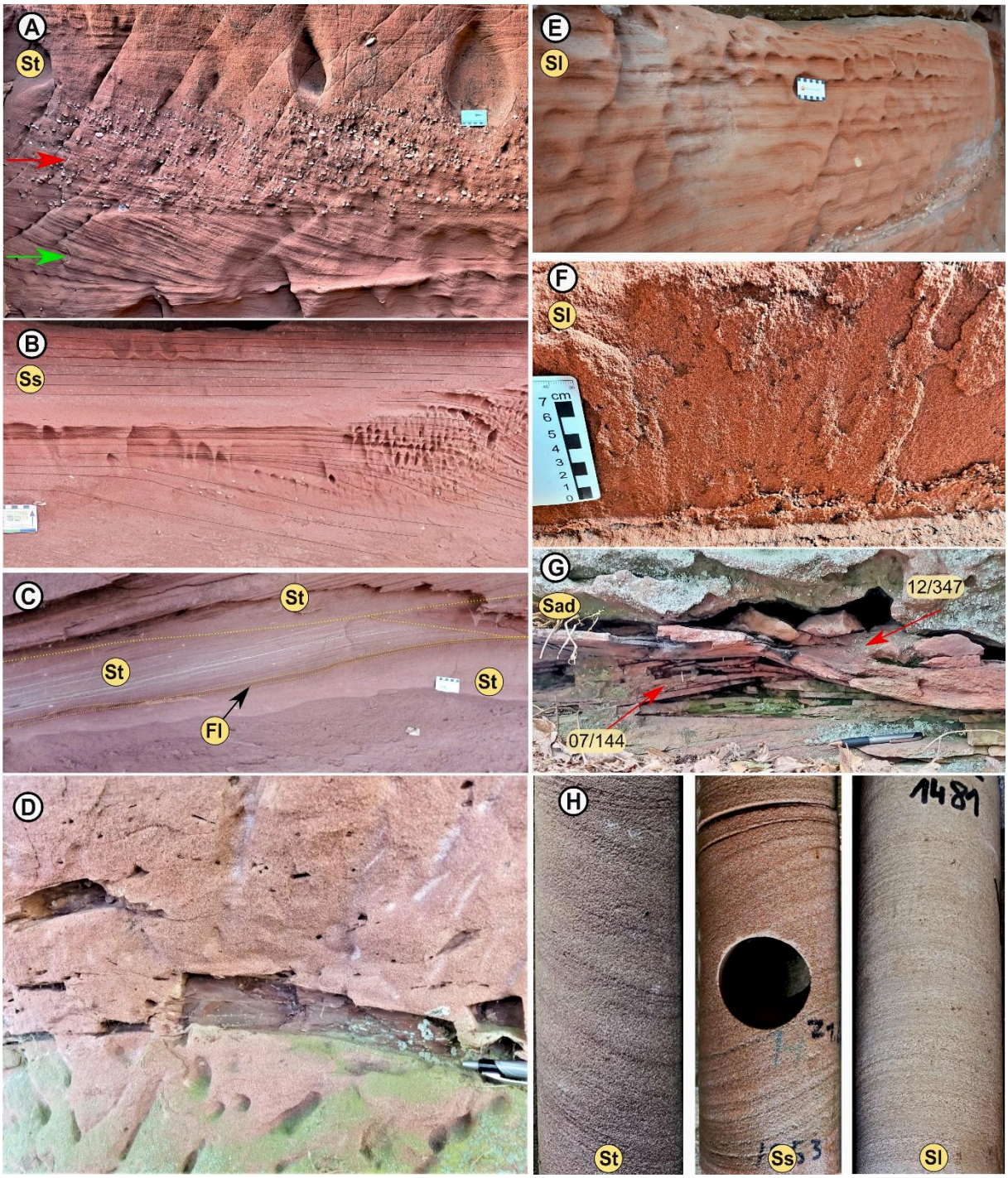


Figure 2-3: Facies of the fluvial channel facies association: (A) trough cross-bedded sandstone, St. Red arrow: cross-set of gravelly sandstone. Green arrow: cross-set of slightly gravelly sandstone. Outcrop: LGV7; (B) sigmoidal cross-bedded sandstone, Ss. Gravel content is absent in the topset and concentrated in higher angle foresets. Outcrop: LGV7; (C) laminated mudstone,Fl, between foresets of facies St. Outcrop: LGV1; (D) breccia of angular mud clasts; (E) low-angle cross-bedded sandstone, Sl. Outcrop: LGV5; (F) planar view of parting lineation in facies Sl.Outcrop: LGV7; (G) convex-up top, with internal low-angle truncated cross-bedded sandstone, Sad, interpreted as antidune. Red arrows indicate planes where palaeocurrents, of opposite directions, were measured. Outcrop: LGV9; (H) Facies St, Ss and Sl recognised in core samples. Core EPS1, diameter: 8 cm.

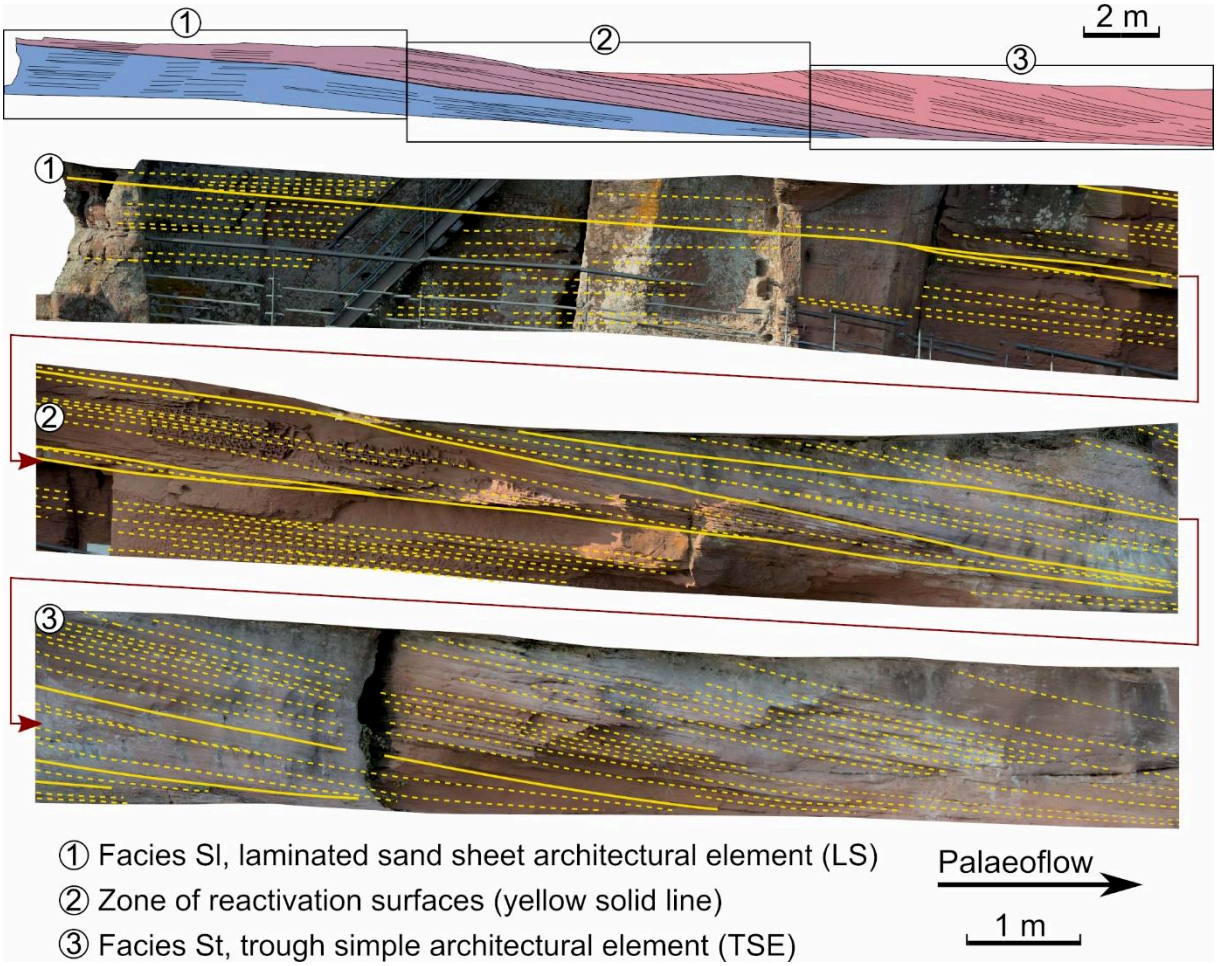


Figure 2-4: Downstream transition between LS and TSE, within the same bed, separated by reactivation surfaces. Outcrop: LGV7.

Most FC sandstone bodies record medium-grained sandstones (51%), followed by coarse-grained sandstones (36%), and a weak correlation between facies and granulometry is observed (Fig. 2-5A). It presents an overall bimodal character of sediment load, composed of gravel and sand. Bimodal is used in this case in a broad sense, when pebbles are in a sandy matrix without clasts of intermediate sizes (Steel and Thompson, 1983). Gravel clasts, mostly composed of milky quartz and quartzite, range from sub- to well-rounded, with low- to high-sphericity. Slightly gravelly sandstone (Table 2-1) dominates the gravel content classes (Fig. 2-5B). Granule to pebble clasts are concentrated along the foresets of facies St (Fig. 2-3A) and Ss (Figs. 2-3B, and -9B), occasionally at the set base. Similarly, rounded or angular mud clasts, up to 35 cm in diameter along their primary axis, may be concentrated as breccias directly above the bases of sets (Fig. 2-3D). Facies Sl exhibits the lower content of gravel, followed by facies Ss and facies St, respectively, which is confirmed by the strong correlation coefficient between facies and gravel content (Fig. 2-5B).

Cross-set thickness distribution throughout the entire FC deposits, has a median value of 30 cm (Fig. 2-5C). A weak correlation is observed between facies and cross-set thickness (Fig. 2-5C). Palaeocurrent data indicates a prevailing palaeocurrent to northeast, with varying circular variance depending on the architectural element (Fig. 2-9), as detailed in the following sections.

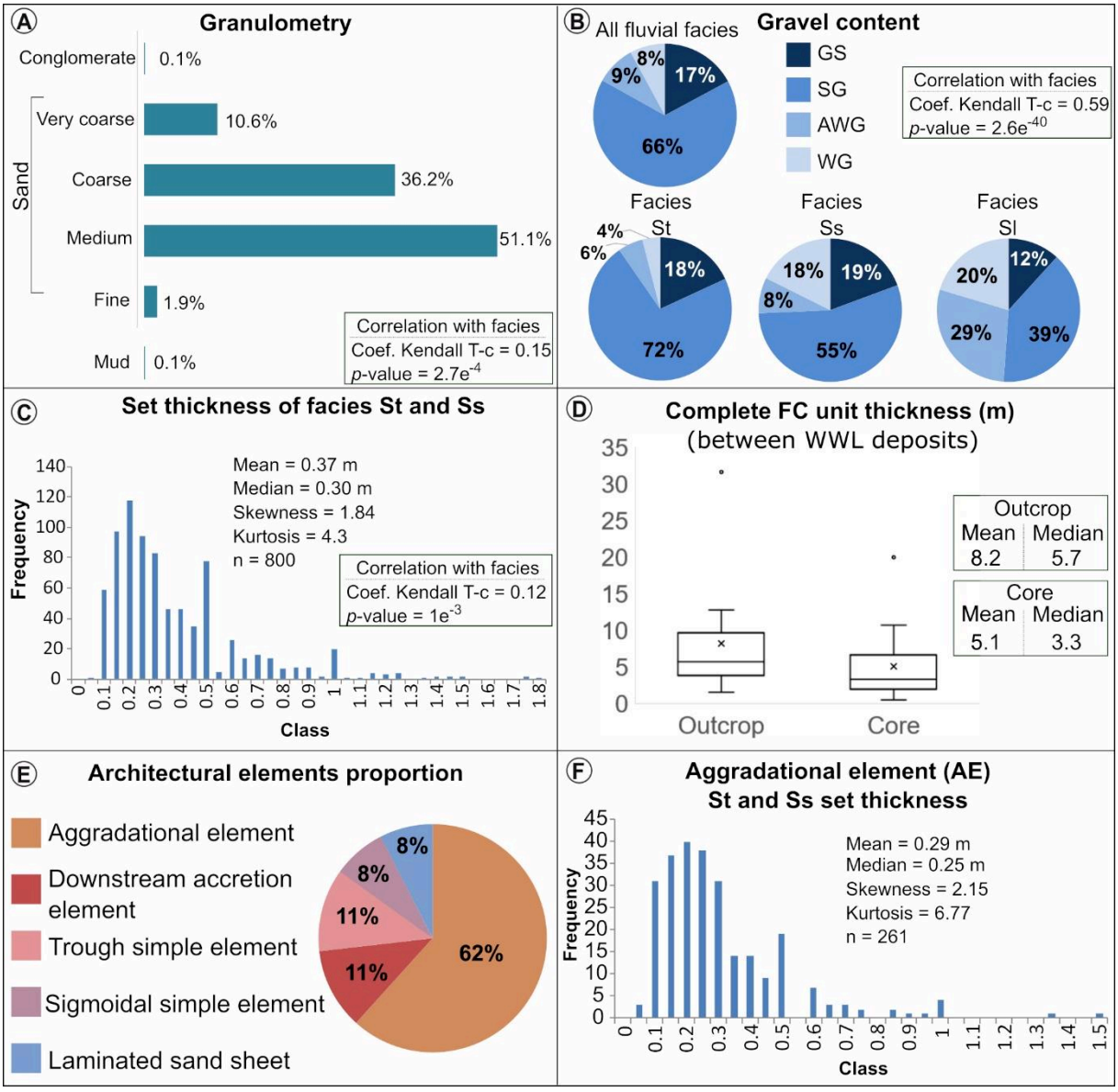


Figure 2-5: Fluvial channel facies association (FC) quantitative data. GS = gravelly sandstone; SG = slightly gravelly sandstone; AWG = sandstone apparently without gravel; WG = sandstone without gravel.

Core data revealed a thinning-upward trend of cross-set thickness (Fig. 2-15B) in the upper part of the LGV. When all cross-sets are considered, no correlation is observed between cross-set thickness and depth (Rs= 0.07; p-value = 0.06) (Fig. 2-15B). However, when the analysis is constrained to cross-sets thicker than 50 cm, a

strong correlation is observed (Rs = 0.61; p-value = 0.005) (Fig. 2-15B). Therefore, the occurrences of relatively larger cross-sets tend to decrease towards the top of the LGV.

The upper and lower boundaries of the FC are identified upon contact with the wind- and water-laid facies association (WWL). The basal contact is slightly erosive, truncating the WWL below at a low angle. The upper contact may be preserved as a flat, or an undulating surface, the genesis of which is further discussed in Section 2.4.1.2.1. Herein, the term “complete FC unit” is used descriptively, when both, lower and upper boundaries, are recognised. Table 2-3 presents quantitative data on architectural elements proportions of individual complete FC units. Figure 2-5D displays the overall thickness distribution of complete FC units, observed in outcrops and in the core.

Table 2-3: Fluvial channel facies association (FC) dataset concerning architectural element proportions; mean set thickness of sets below 78 cm, within the aggradational element (AE) (M.S.T. < 78 cm); coefficient of variance of cross-set thickness in the AE (CV) (calculated where data of minimum 30 sets were available); mean original dune height (Hm) (Eq. (1)); and mean flow depth (d) (Eq. (2)). The dataset is presented by individual FC, bounded by WWL deposits. The term “complete FC unit” refers to FC deposits where upper and lower boundaries are recognised. Where more than one FC unit is identified in the same outcrop, the point (outcrop code) is followed by a sequence number (e.g., LGV2-2). “Incomplete” refers to outcrops where lower or upper FC boundaries were not exposed. DA = downstream accretion element; TSE = trough simple element; SSE = sigmoidal simple element; LS = laminated sand sheet. Grey areas refer to no data available.

Point	Complete FC unit thickness (m)	Architectural elements proportion (%)					M.S.T. (cm) <78 cm	C.V. (AE)	*Hm* (m)		*d* (m)	
		AE	DA	TSE	SSE	LS			Min (x2.2)	Max (x3.6)	Min (x6)	Max (x10)
LGV1	4.0											
LGV2-1	5.4											
LGV2-2	3.7											
LGV3	31.5	68		14	18		29	0.51	0.70	1.15	4.2	11.5
LGV4-1	10.3	33	27	20		20	21	-	0.51	0.83	3.0	8.3
LGV4-2	5.7	46	40		14		29	-	0.70	1.15	4.2	11.5
LGV5-1	4.8											
LGV5-2	9.1											
LGV6	Incomplete	100					24	-	0.57	0.93	3.4	9.3
LGV7	12.8	53	12	9	8	18	24	0.48	0.58	0.95	3.5	9.5
LGV8-1	3.6	27			44	29	36	-	0.87	1.43	5.2	14.3
LGV8-2	6.1	100					21	-	0.51	0.83	3.0	8.3
LGV9	Incomplete	66	8	20		5	22	0.50	0.53	0.87	3.2	8.7
LGV10	1.5	100					18	-	0.44	0.71	2.6	7.1
LGV11	8.1											
LGV12	Incomplete	29		32	22	17	10	-	0.24	0.40	1.5	4.0

The occurrence of multistorey amalgamated and tabular sandstone bodies, bounded by erosive surfaces, and predominantly consisting of medium- to coarse-grained sandstones, well- to poorly-sorted, with mud clasts, gravel, and unidirectional cross-strata, indicates deposition in a fluvial channel (Collinson, 1996), with palaeocurrent to the north-east, in agreement with previous studies (Perriaux, 1961; Gall, 1972; Durand, 1978; Dachroth, 1985; Ghienne et al., 1994; Bourquin et al., 2009).

The dominance of facies St indicates that the FC records essentially the migration of 3D dunes (Miall, 2006) under lower-flow regime conditions (Zellman et al., 2021). However, one-quarter of the FC consists of facies Ss and Sl (Fig. 2-2), revealing significant occurrences of transitional (Røe, 1987; Wizevich, 1992; Fielding, 2006; Walker and Holbrook, 2023) to upper-plane beds (Hjellbakk, 1997; Fielding, 2006; Plink-Björklund, 2015). Facies Ss may represent the original bedform morphology (Røe, 1987; Fielding, 2006; Collinson et al., 2006), with the preserved convex-up shape at the crest, a consequence of rapid net vertical aggradation, preventing significant erosion due to high sediment load (Røe, 1987; Hjellbakk, 1997). Distinguishing sigmoidal stratification (facies Ss) in terms of Froude-number (Fr) flow conditions might be impossible, due to the wide range of circumstances in which facies Ss may occur (Ghienne et al., 2010; Plink-Björklund, 2015; Lang et al., 2021). Similar challenges apply to facies Sl (Yagishita et al., 2004; Ohata et al., 2022), whenever diagnostic features of Froude-supercritical flow, such as parting lineation and convex-up laminations, are not found. Thus, the classification based on the direct relationship between these sedimentary facies and Froude-number reaching supercritical conditions ($Fr > 1$) is avoided. Ss and Sl facies are interpreted based on Southard's (1991) diagram, as upper-plane beds for facies Sl, and transitional cross-bedding from 3D dune (St) to upper-plane bed for facies Ss.

The vertical and lateral intermixing of facies St, Ss, and Sl may be related to river discharge variability (DeLuca and Eriksson., 1989; Fielding, 2006; Miall, 2006; Plink-Björklund, 2015), changes in sediment supply, or spatial flow fluctuations (Røe, 1987; Hjellbakk, 1997; Zellman et al., 2021). Discharge variability is evidenced, for instance, by the presence of facies Fl between cross-bedded sandstone sets (Fig. 2-3C), and along foresets, which indicate ephemeral flows, subjected to rapid waning of floods (Miall, 2006; Plink-Björklund, 2015). Conversely, spatial flow fluctuation is observed in the downstream transition from low-angle topset to concave-up toeset of facies Ss, where the topset is affected by upper-flow regime, and the toeset by lower-flow regime (Hjellbakk, 1997). The concentration of coarser grains, and gravels, in the down-palaeocurrent direction foresets, compared to the topsets, indicates that coarser sediments rolled over the bedform to accumulate by settling and avalanching on the slipface (Sauderson and Lockett, 1983). Distinct evidence to support temporal or spatial flow variations is presented further.

The consistent occurrence of a smaller proportion of gravel content in facies Sl, followed by facies Ss and St (Fig. 2-5B) highlights an apparent inverse relationship between gravel content and flow regime, which is confirmed by the strong correlation coefficient between facies and gravel content (Fig. 2-5B). This is explained by the overpassing process (Allen, 1983b), which occurs in bimodal grain-size-distribution sediment load. At upper-flow regime and high shear-stress conditions, the large sub- to well-rounded gravel rolls over a firm bed of close-packed sand grains, (Allen1983b; Carling, 1990), depositing downstream where flow conditions change. In some cases, this process has been related to strong flashy floods events (Allen, 1983b).

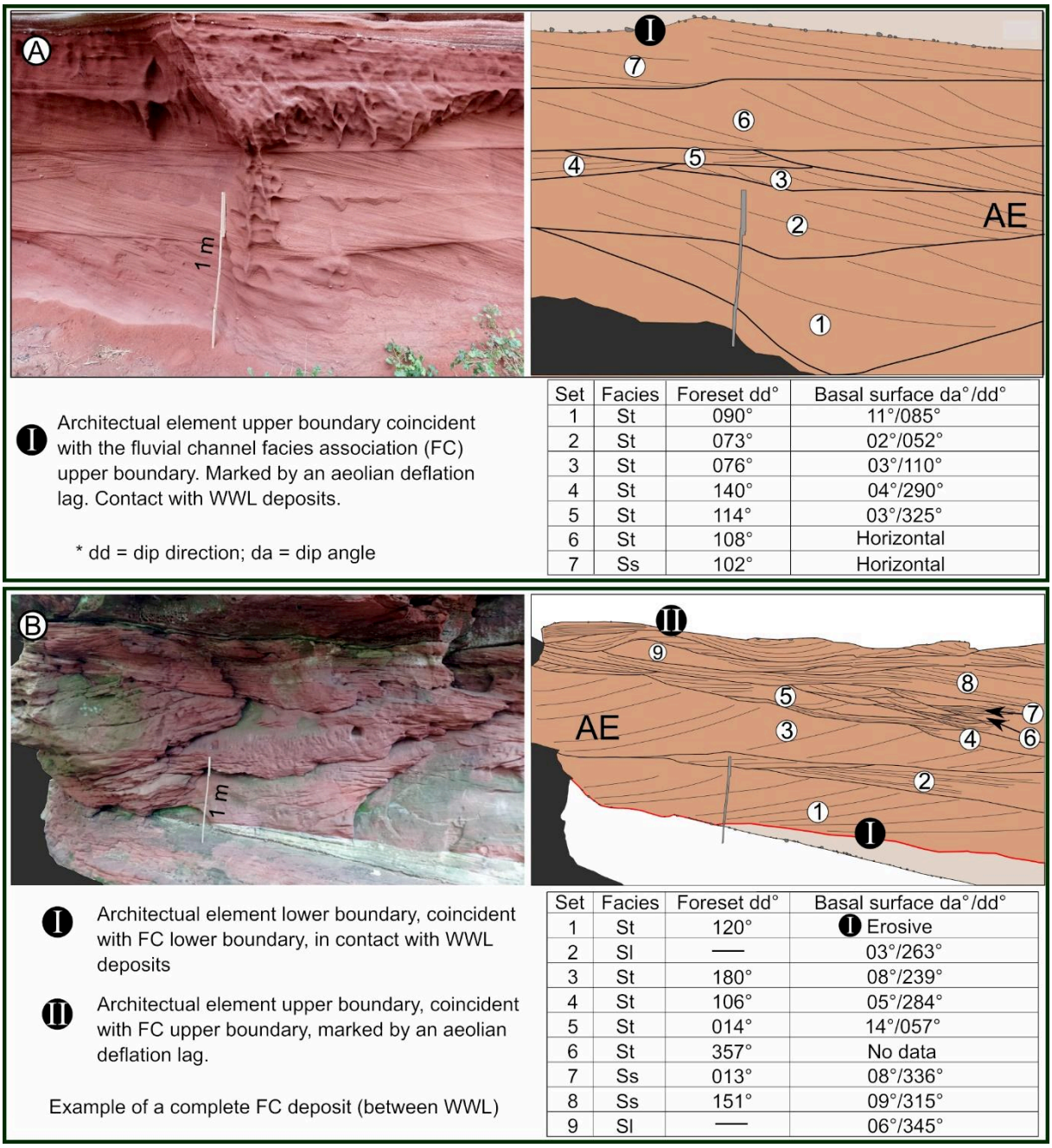
Rare occurrences of antidunes (Sad) indicate moments when channel flow reached supercritical conditions (Fielding, 2006). These facies can form and be preserved in shallow flows that rapidly reach Froude number equal to 1, or during extreme major flood events followed by rapid drop in water level (Fielding, 2006; Fielding et al., 2018). As these structures tend to be reworked during waning flow conditions (Miall, 2006; Myrow et al., 2018), preservation potential is low, making these deposits underestimated in the rock record.

2.4.1.1.2. Aggradational architectural element (AE)

The aggradational architectural element (AE) (Fig. 2-6) is the predominant architectural element within the FC (Fig. 2-5E). It has an erosional base, showing, in a dip-section, a downstream dip (<15°), where large (c. up to 35 cm) mud clasts are commonly concentrated. Gravelly sandstones (GS) lenses also often occur at the base of the elements. The AE comprises tabular (Fig. 2-6A) and amalgamated (Fig. 2-6B) sets of facies St, Ss and Sl (Fig. 2-6B), occasionally featuring discontinuous facies Sp, Sad, Sr, and Fl. The internal sets are bounded by horizontal to concave-up surfaces, sometimes erosional. Locally, it preserves thinning-upward trends, aligning with the observations of Ghienne (1994).

The coefficient of variance (CV) of cross-set thickness, calculated where more than 30 cross-set samples are preserved in the same architectural element, of a complete FC unit (LGV3, LGV7, and LGV9) (Table 2-3), presented a mean value of 0.5.

The AE is interpreted as the aggradation and coalescence of 3D (St), humpback, and washout dunes (Ss and Sl), within flat and wide channels, or atop large bars (Hjellbakk, 1997; Scherer et al., 2015). Thinning-upward sequences register the final stages of channel infills (Ghienne, 1994) or top of bars (Li et al., 2015). This architectural element corresponds to Hjellbakk's (1997) dune complexes (DC), or a combination of Miall's (1988) sandy bedforms (SB) and channel element (CH). Basal surfaces with angular mud clast breccia (Fig. 2-3G), suggest the erosion of semi-consolidated mud cracks, originating from sub-aerially exposed mud layers within ephemeral channels (Bridge, 2003; Bourquin et al., 2009), during flow stage fluctuations (Miall, 1988). It is not clear whether some channels experienced ephemeral flow while perennial channels were still active, or if the flow was intermittent in all channels. However, evidence of ephemeral flow is commonly recorded across the FC, leading to the possibility of an intermittent fluvial system.



Set	Facies	Foreset dd°	Basal surface da°/dd°
1	St	090°	11°/085°
2	St	073°	02°/052°
3	St	076°	03°/110°
4	St	140°	04°/290°
5	St	114°	03°/325°
6	St	108°	Horizontal
7	Ss	102°	Horizontal

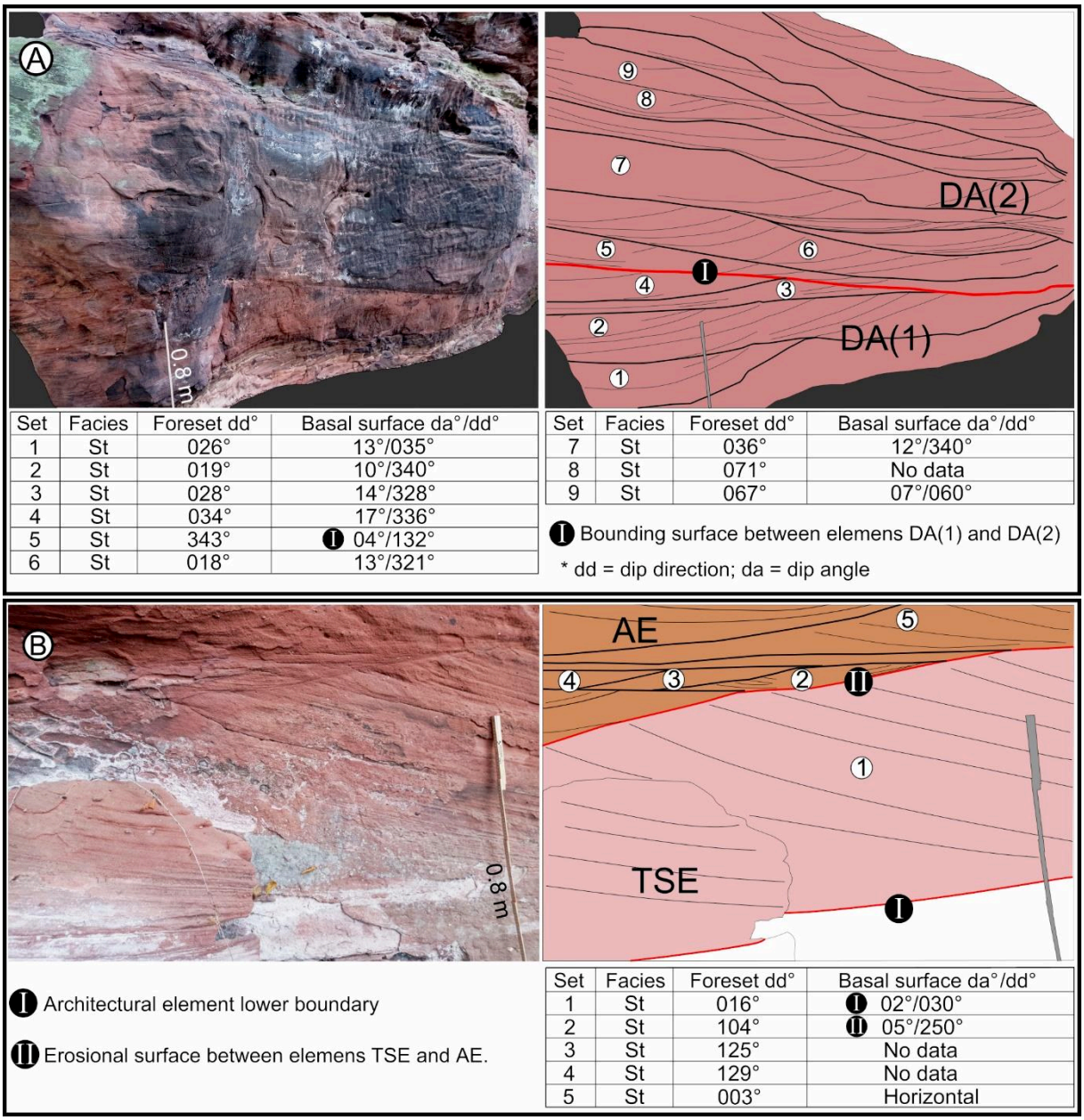
Set	Facies	Foreset dd°	Basal surface da°/dd°
1	St	120°	I Erosive
2	Sl	—	03°/263°
3	St	180°	08°/239°
4	St	106°	05°/284°
5	St	014°	14°/057°
6	St	357°	No data
7	Ss	013°	08°/336°
8	Ss	151°	09°/315°
9	Sl	—	06°/345°

Figure 2-6 : Aggradational element. (A) Outcrop LGV7; (B) outcrop LGV10.

The statistical distribution of set thickness in the AE element (Fig. 2-5F) indicates disequilibrium conditions induced by discharge variability (Myrow et al., 2018; Leary and Ganti, 2019; Colombera et al., 2024), and the CV may suggest abrupt waning-flow conditions associated with such variabilities (Myrow et al., 2018; Leary and Ganti, 2019).

2.4.1.1.3. *Downstream accretion architectural element (DA)*

The downstream accretion architectural element (DA) (Fig. 2-7A) is characterised by horizontal to undulating basal surfaces, composed of sets of facies St and Ss, bounded by surfaces dipping at angles ranging from 3° to 18° in the same direction, or obliquely (<60°), to the cross-bedding foresets direction (Fig. 2-9).



Set	Facies	Foreset dd°	Basal surface da°/dd°
1	St	026°	13°/035°
2	St	019°	10°/340°
3	St	028°	14°/328°
4	St	034°	17°/336°
5	St	343°	I 04°/132°
6	St	018°	13°/321°

Set	Facies	Foreset dd°	Basal surface da°/dd°
7	St	036°	12°/340°
8	St	071°	No data
9	St	067°	07°/060°

I Bounding surface between elemens DA(1) and DA(2)

* dd = dip direction; da = dip angle

I Architectural element lower boundary

II Erosional surface between elemens TSE and AE.

Set	Facies	Foreset dd°	Basal surface da°/dd°
1	St	016°	I 02°/030°
2	St	104°	II 05°/250°
3	St	125°	No data
4	St	129°	No data
5	St	003°	Horizontal

Figure 2-7: (A) Downstream accretion element (DA). Outcrop: LGV8. (B) Trough simple element (TSE) and aggradational element (AE). Outcrop: LGV4.

The DA is interpreted as middle-channel bars formed by superimposed dunes (Allen, 1983a; Miall, 1988; Scherer et al., 2015). The presence of facies Ss indicates

flows that locally, or temporally, reached the transition between dune and upper-plane bed stability field during the bar migration (Røe, 1987; Fielding, 2006).

2.4.1.1.4. Trough simple architectural element (TSE)

The trough simple architectural element (TSE) (Fig. 2-7B) is defined by horizontal to sub-horizontal basal surface. It consists of individual tabular sets of facies St, ranging between 45 cm to 1,8 m thick, with a lateral extension of tens of metres when viewed in a dip-section.

The TSE is interpreted as unit bars (Røe, 1987; Hjellbakk, 1997), deposited under steady-state flow conditions (Røe, 1987), with minor flow pulsations revealed by the reactivation surfaces (Røe, 1987). It may also represent large-scale 3D dunes (Miall, 2006). Distinguishing between unit bars and large dunes is challenging in channel-dominated deposits with undefined channel margins (Miall, 1988; Skelly et al., 2003), especially in the context of variable flow depths and discharge (Herbert et al., 2019).

2.4.1.1.5. Sigmoidal simple architectural element (SSE)

The sigmoidal simple architectural element (SSE) (Fig. 2-8) is defined by horizontal to sub-horizontal basal surface, composed of individual tabular sets of facies Ss, ranging between 45 cm to 1,8 m thick, with lateral extension of dozens of metres. It commonly presents aggradational foresets, and reactivation surfaces (Fig. 2-8B). When SSE is composed of gravelly sandstone (Table 2-1), gravel clasts are concentrated in the lee side, generally absent in the horizontal to low-angle stratified topset (Fig. 2-8B). Sometimes more than one SSE element may stack (Fig. 2-8A).

The SSE is interpreted as a humpback bar, product of single flood events of heavily suspension-laden currents in the transition from upper to lower-flow regime (Allen, 1983; Røe, 1987; Hjellbakk, 1997; Manna et al., 2021), within a shallow, high-energy channel (Hjellbakk, 1997). Occurrences of isolated SSE indicate abrupt temporal changes in flow conditions (Røe, 1987). The absence of gravel in the low-angle topsets, while they are abundant in coeval foresets, is addressed to gravel overpassing (Allen, 1983b), due to local upper-flow regime conditions at the top of humpback bars (Allen, 1983b; Carling, 1990), and concentrating in the lee side, which is affected by lower-flow regime conditions (Hjellbakk, 1997). When more than one set

of SSE is stacked, it suggests the increase of flow depth sufficiently deep to permit deposition as cosets (Røe, 1987; Carling, 1990).

2.4.1.1.6. Laminated sand sheet architectural element (LS)

The laminated sand sheet architectural element (LS) (Fig. 2-8A) is composed of laterally extensive, tabular sandstone packages, locally presenting pinch-out edges, ranging between 30 cm and 1.95 m thick, almost exclusively of facies Sl. Records rare facies Ss and St as isolated lenses, and facies Sm and Sr at the top. It is the architectural element with lower gravel content within the FC (Fig. 2-9), and rarely is formed by coarse-grained sandstone (Fig. 2-9).

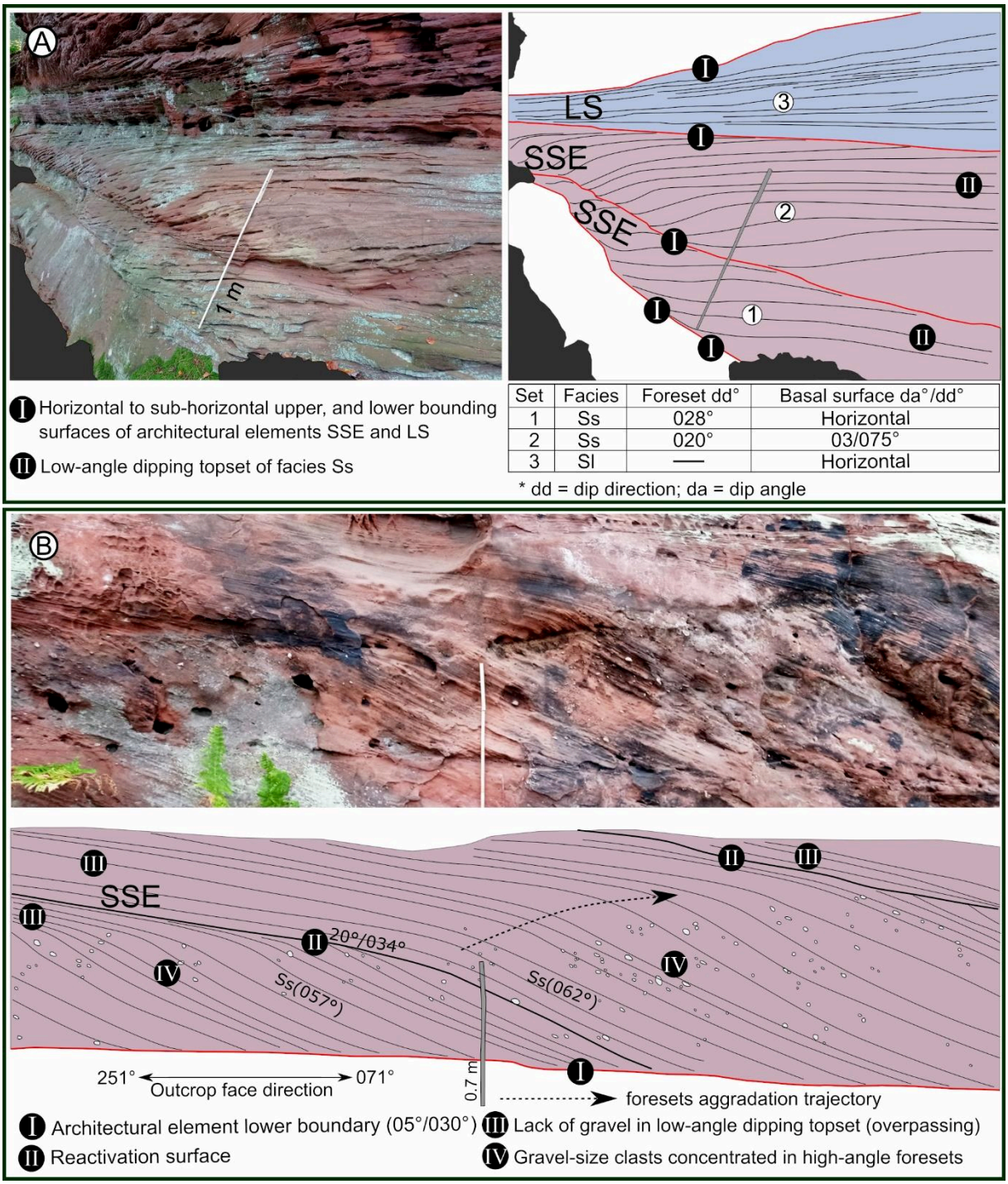


Figure 2-8: (A) Sigmoidal simple element (SSE), and laminated sand sheet (LS). Outcrop: LGV12. (B) SSE, with the absence of gravel in the topset, concentrated in the foresets. Result of the overpassing process (Allen, 1983b). Outcrop: LGV8.

The LS indicate shallow floods under upper-flow regime conditions (Fielding, 2006; Miall, 2006), filling in ephemeral channels (Miall, 2006). When pinch-out edges are present, they are interpreted as formed on the stoss-side of unit bars (Alexander et al., 2020). The local presence of facies Sm and Sr at the top represents fast waning flow and/or high sediment concentration in the final depositional stages (Allen and Leeder, 1980). The lower gravel content is attributed to the overpassing process (Allen,

1983b), and the lack of occurrences of coarse-grained upper-plane bed aligns with observations of Núñez-González and Martín-Vide (2010), which indicates that, in coarse grain sizes, the dune phase can be followed by antidunes, with no transitional plane bed stability.

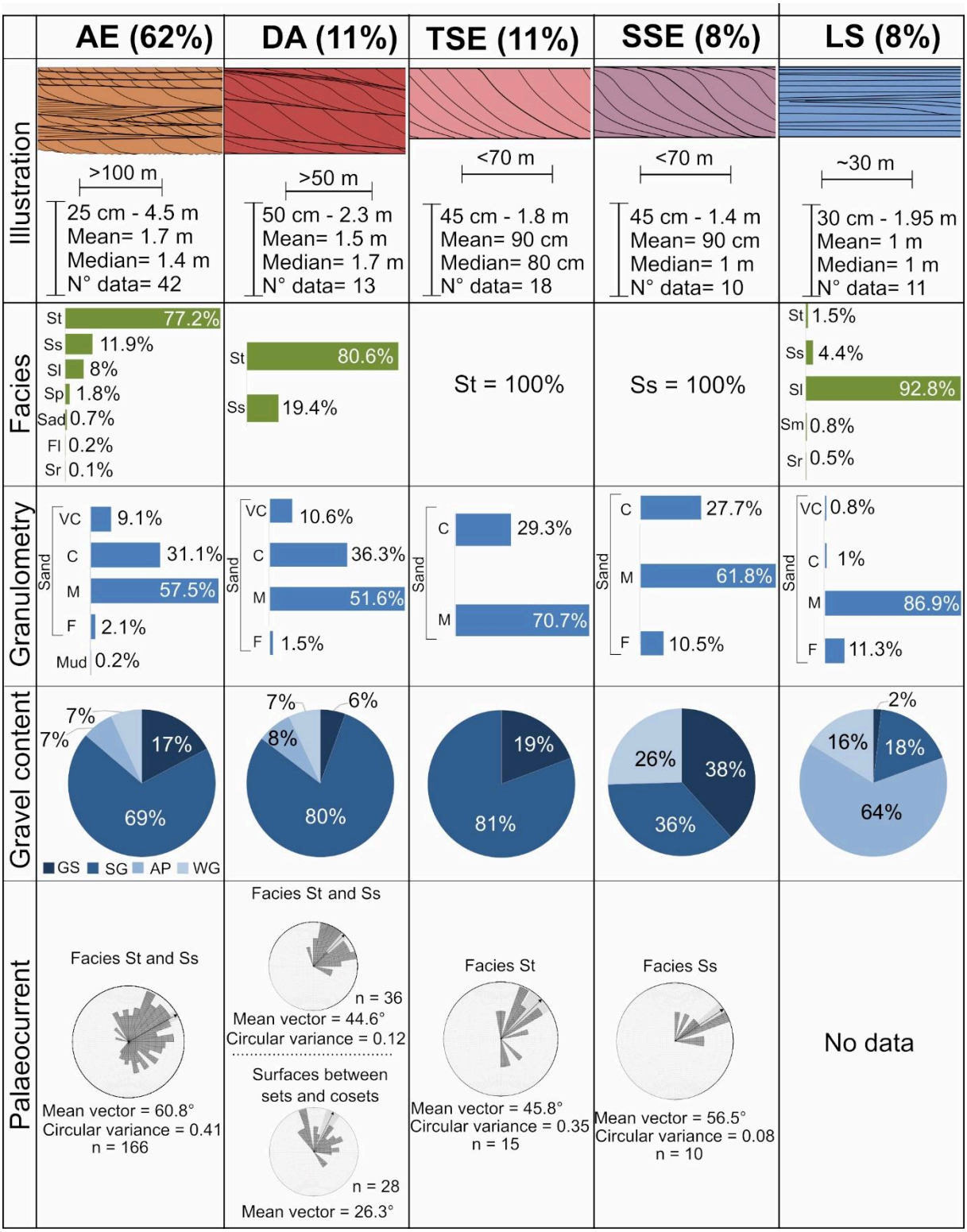


Figure 2-9: Fluvial architectural elements, their respective quantitative data, and illustration.

2.4.1.1.7. Interactions between FC architectural elements

These architectural elements can evolve down-dip. Figure 2-4 illustrates LS transitioning in a down-palaeocurrent direction to TSE. These transitions are commonly marked by reactivation surfaces zones between the elements (Fig. 2-4). Simple elements (TSE and SSE) can also evolve down-dip to DA (Fig. 2-13). The inverse transition is also observed, which is identified by other authors as a transitional element (Hjellbakk, 1997; Manna et al., 2021). Recognising all these transitions demands down-dip exposure and extensive outcrops. The downstream transition between LS and TSE, within the same bed (Fig. 2-4), suggests flow pulsations (Røe, 1987; Miall, 1988) and/or changes in channel cross-section geometry during bedform migration (Bridge, 2003). For instance, LS indicates lower confinement compared to TSE, or shallower conditions in the channel (Miall, 2006). The presence of reactivation surfaces between the elements suggests flow pulsations (Røe, 1987). The downstream transition from simple elements, TSE and SSE, to DA, indicates the coalescence of unit bars to form larger compound bars, a result of either increasing discharge, or a decrease in riverbed gradient (Li et al., 2022).

The top surface of TSE, when in contact with the AE, is often eroded, dipping upstream at a low angle (Fig. 2-7B). This is also observed in relatively larger, isolated, cross-sets within the AE, when underlying smaller cross-sets (Fig. 2-6B). Both cases are interpreted as the partial cannibalisation of large bedforms due to disequilibrium during a rapid decrease in flow (Myrow et al., 2018). These smaller sets could be considered low-discharge channels situated between mid-channel bars, while the isolated large sets within the AE, and the architectural elements TSE, SSE, and DA are indicative of high-discharge channels (Skelly et al., 2003). The higher palaeocurrent circular variance of cross-sets within the AE, compared to the other elements (Fig. 2-9), indicates increased sinuosity (Galeazzi et al., 2021) in the former, supporting the interpretation of cross-sets preferentially formed inside low-discharge channels, migrating between braided bars.

2.4.1.1.8. Channel depth estimation

To estimate the low-discharge channels' mean flow depth, only sets within AE elements were used. Sets thicker than 78 cm (3.8% of the dataset), were considered

outliers by the IQR method (Equation 3), and then excluded from the analysis to avoid overestimations (Hartley and Owen, 2022). A total of 251 sets remained.

Results revealed a range of mean original dune height (H_m) (Equation 1) varying from 64 cm to 1.05 m. Concerning low-discharge mean flow depth (d) (Equation 2; Leclair and Bridge, 2001), values range from 3.8 to 10.5 m. Such imprecision was anticipated (Leclair and Bridge, 2001; Reesink et al., 2015), and the lack of complete bar thickness recognition does not allow a finer calibration, as it would approximate the bank-full channel depth (Skelly et al., 2003; Bridge, 2003; Hartley and Owen, 2022).

To evaluate the potential impact of mixing different fluvial genetic units (Bourquin et al., 2006; 2009), individual d is also calculated by outcrop. In instances where a complete FC unit is exposed, the analysis is restricted to AE within its limits to constrain possible temporal variabilities of the system. Results (Table 2-3) showed a range of H_m from 24 cm to 1.43 m, and d from 1.5 m to 14.3 m. Nevertheless, most outcrops exhibited H_m and d within the values calculated using the entire AE dataset, suggesting no substantial changes, in terms of low-discharge flow depth, recorded across the studied outcrops of the LGV.

Although 1D data were not utilised to estimate channel depth, the observed reduction in the frequency of larger cross-sets (c. > 50 cm in thickness), towards the top of the LGV (Fig. 2-15B), is interpreted as the result of diminishing channel depths and/or a decline in the incidence of high discharge fluvial events.

2.4.1.2. Wind- and water-laid facies association (WWL)

This facies association comprises eight sedimentary facies, interdigitated laterally and vertically on a centimetre to decimetre scale. The facies are distributed in two architectural elements: the hybrid sand sheet (HSS) and aeolian dune (AD), which descriptions and interpretations are presented in Sections 2.4.1.2.2. and 2.4.1.2.3., respectively. The choice to combine aeolian dunes and sand-sheet deposits into the same facies association is made due to the limited prevalence of the WWL within the Lower Grès Vosgien Formation.

2.4.1.2.1. Facies and general characteristics

This facies association is composed mainly of fine- to medium-grained sandstone (Fig. 2-11B), well- to poorly-sorted. Granules and pebbles may be present mainly constrained to one surface as a lag deposit (Dixon, J.C., 2014). The WWL exhibits flat base deposits of greater extent that the maximum width of the individual outcrops in which they are observed (c. 100 m) (Fig. 2-13), occasionally being eroded out laterally by overlying FC (Fig. 2-13). Facies trough cross-bedded sandstone with grain-flow laminae (Sta) (Figs. 2-10D and, -10E), adhesion structures (Sa) (Fig. 2-10C), wave ripples (Sw) (Figs. 2-10B, and -10C), microbially induced sedimentary structures (Mb) (Fig. 2-10B), massive sandstone (Sm), and rare Fl, interdigitate laterally and vertically.

The lower boundary of the WWL is horizontal to sub-horizontal and abrupt, occasionally undulating, most frequently bounded by a lag deposit, with pebbles (Figs. 2-10D, -10E, and -10F), commonly faceted, displaying the same composition and sizes as those present within the FC. The gravel content can be arranged scattered in a single surface, or tightly packed and commonly embedded in a sandy matrix. Although most of these surfaces are overlain by facies composing the WWL, in some cases, overlying fluvial deposits present erosive contact with the WWL and are conformable with the lag surface. Thus, in these cases, the lag deposit bound two fluvial deposits (see Architecture 5 in Figs. 2-12B, and -12F). Figure 2-10B exhibits the overall thickness distribution of the WWL, observed in outcrops and core. Core data record thicker WWL towards the top of the LGV (Fig. 2-15D), in which a weak negative correlation is observed between WWL thickness and depth ($R_s = -0.36$). However, the p-value of 0.12, above the significance level of 0.05, indicates that in the dataset there is not enough evidence to correlate WWL thickness and depth.

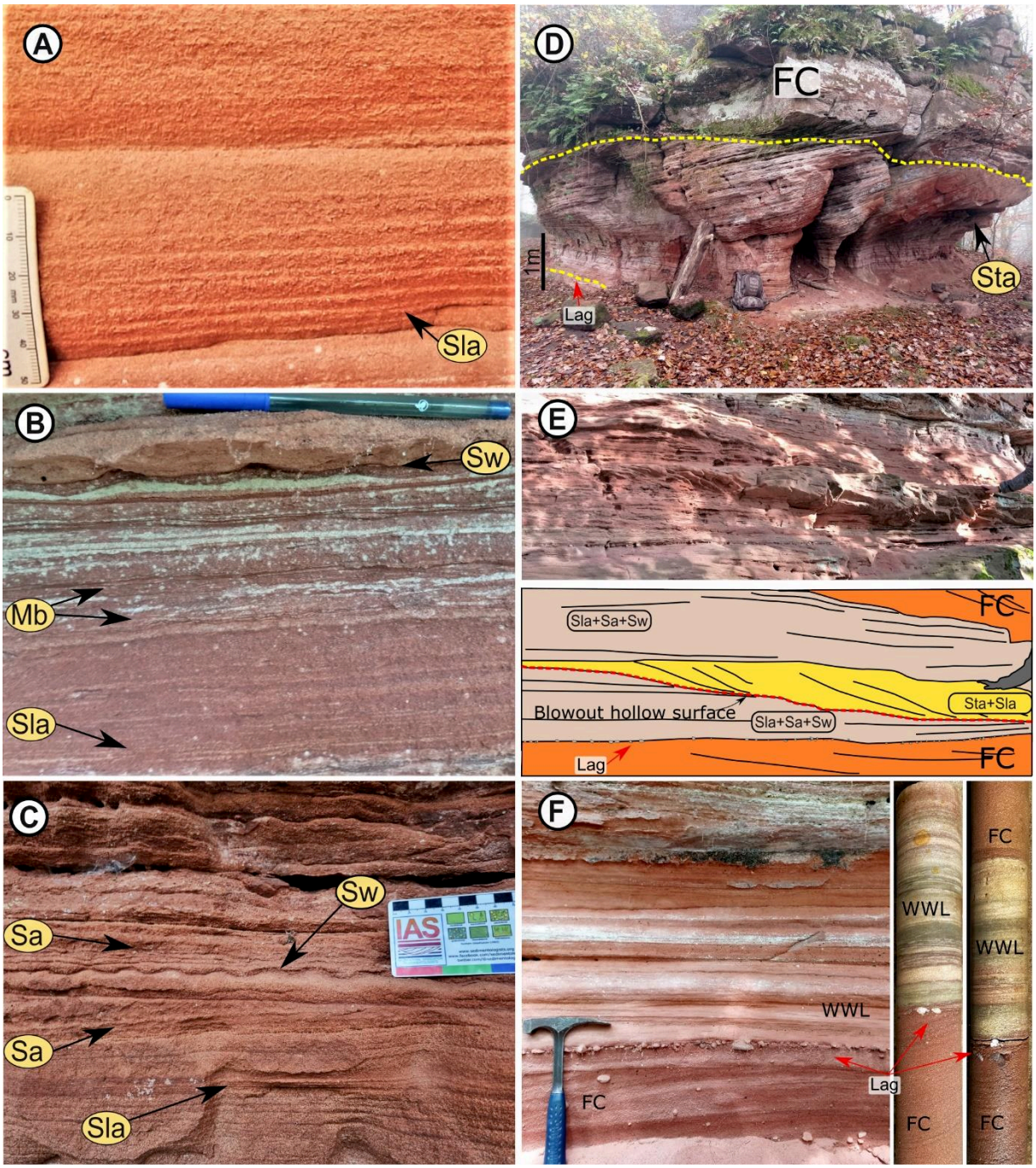


Figure 2-10: Wind- and water-laid facies association (WWL). (A) Translatent wind ripples, Sla. Outcrop: LGV5; (B) (C) centimetre-scale upward transition between facies Sla, Sa (and/or Mb) and Sw, indicating gradual outpace of water-table rise against sediment supply. Outcrop: LGV8 and LGV6, respectively; (D) largest aeolian dune described in the Lower Grès Vosgien Formation, delimited by the dashed yellow line. Outcrop: LGV6; (E) aeolian dune (AD) between hybrid sand sheet (HSS), overlying a blowout hollow surface. Outcrop LGV2; (F) WWL in outcrop (LGV5) and in the EPS1 core samples.

The first evidence of interruption of fluvial processes and establishment of WWL is the basal lag surfaces, interpreted as sand-drift surfaces formed when unsaturated winds eroded subaerially exposed fluvial deposits, leaving behind a deflation lag (Clemmensen and Tirsgaard, 1990) (Fig. 2-12A). Faceted pebbles are interpreted as ventifacts (Durand and Bourquin, 2013). Planar sand-drift surfaces indicate deflation

down to the water-table level (Havholm and Kocurek, 1994), and when undulating, it is interpreted as regions where deflation did not reach the water-table level (Gross, 2022). Where gravel clasts on sand-drift surfaces are tightly packed, and embedded in a sandy matrix, it suggests rework by ephemeral subaqueous flows (Fig. 2-12A) before the deposition of the overlying WWL. The resistance of sand-drift surfaces to erosion (Fig. 2-12F) may indicate early cementation, a common feature associated with sediments exposed to water-table level fluctuations (Fryberger et al., 1988; Fryberger, 1991).

Aeolian origin was attributed when at least two of the following criteria were observed: inverse graded lamination (Clemmensen and Abrahamsen, 1983), absence of gravel content, pin-stripe lamination (Fryberger and Schenk, 1988), granule ripples (Fryberger et al., 1992), and a laterally extensive deflation lag at the set base (Clemmensen and Tirsgaard, 1990).

2.4.1.2.2. Hybrid sand sheet architectural element (HSS)

The hybrid sand sheet architectural element (HSS) consists of tabular deposits with thickness varying from 7 cm to 1.85 m, with a median value of 35 cm (Fig. 2-11C), and a mean of 44 cm. It is composed of fine-grained sandstone, poorly- to well-sorted, with centimetre-scale interbedded facies Sla, Sa, Sw, Sm and Mb (Figs. 2-10B, and -10C). Bleaching is recurrently observed in HSS, both in outcrop and core (Figs. 2-10B, -10F, -12C, -12E, and -12F), sometimes making it difficult to distinguish facies. Occasionally, an upward trend of stacked facies Sla, Sa (and/or Mb), and Sw is recognised (Figs. 2-10B, and -10C). The contacts between facies are conformable. The HSS presents a sharp horizontal lower surface when overlying AD deposits.

The hybrid sand sheet architectural elements are composed of features that suggest the presence of water during their deposition (Fig. 2-14A), such as facies Sa (Kocurek and Fielder, 1982), Sw (Ribes, 2015), Mb (Gerdes, 2007; Basilici et al., 2021), and the occasional occurrence of Fl and gravel clasts (Miall, 2006). Additionally, facies Sla indicate occasions of dry sediments being deposited as translatent strata (Hunter, 1977; Cain and Mountney, 2009). The centimetre-scale intercalation of facies Sla, Sa, Sw, and Mb is interpreted to be mainly controlled by the balance between water-table level fluctuation and the rate of aeolian sediment supply (Clemmensen, 1991; Havholm and Kocurek, 1994; Carr-Crabaugh and Kocurek, 1998) (Fig. 2-12A).

These characteristics indicate deposition in the context of an aeolian sand-sheet (Clemmensen, 1991; Trewin, 1993; Basilici et al., 2021; Cosgrove et al., 2022; Gross et al., 2022). However, the term "hybrid" is used because of the dominance of water-related processes.

2.4.1.2.3. Aeolian dune architectural element (AD)

The aeolian dune architectural element (AD) consists of tabular to concave-up base deposits of facies Sta and Sla. Individual AD records thickness varying from 10 cm to 2.73 m, with a median value of 78 cm, and a mean of 84 cm (Fig. 2-11C). It can be preserved as a single set (Figs. 2-10D, -10E, -12C, -12G, and -12H), or with two sets (Fig. 2-12D). Foresets predominantly dip towards the north-northeast (Fig. 2-11E), with a maximum preserved dip angle of 20°, and transition downward to facies Sla (Figs. 2-12C, and -12D). Where they overlie HSS, the AD often lay above shallow erosional surface dipping in the same direction as the foresets of facies Sta (Figs. 2-10E, -12C, -12G, and -12H).

The AD represents 60% of the total WWL thickness. However, in terms of occurrences, it represents 43% (Fig. 2-11D).

The aeolian dune architectural element record sedimentation via the wind as migrating aeolian dunes (Hunter, 1977; Clemmensen and Abrahemsen, 1983; Kocurek, 1991; Scherer, 2000) (Fig. 2-14B). Accumulation of superimposed sets occurs via aeolian climbing dunes (Clemmensen and Abrahemsen, 1983; Kocurek, 1991). Considering the maximum dip angle measured from grain-flow strata of 20°, and the angle of repose of modern aeolian dunes, typically between 32° and 34° (Bristow and Mountney, 2013), it is interpreted that only the lowermost part of the dunes has been preserved. The shallow erosional surface at the base of the AD, in contact with HSS (Figs. 2-10E, -12C, -12G, and -12H), is interpreted as blowout hollows (Hesp and Walker, 2013) formed before the wind saturation with sand. This deflation process was followed by wind saturation, dune accumulation, and dune migration above these surfaces (Figs. 2-12A, and -14B).

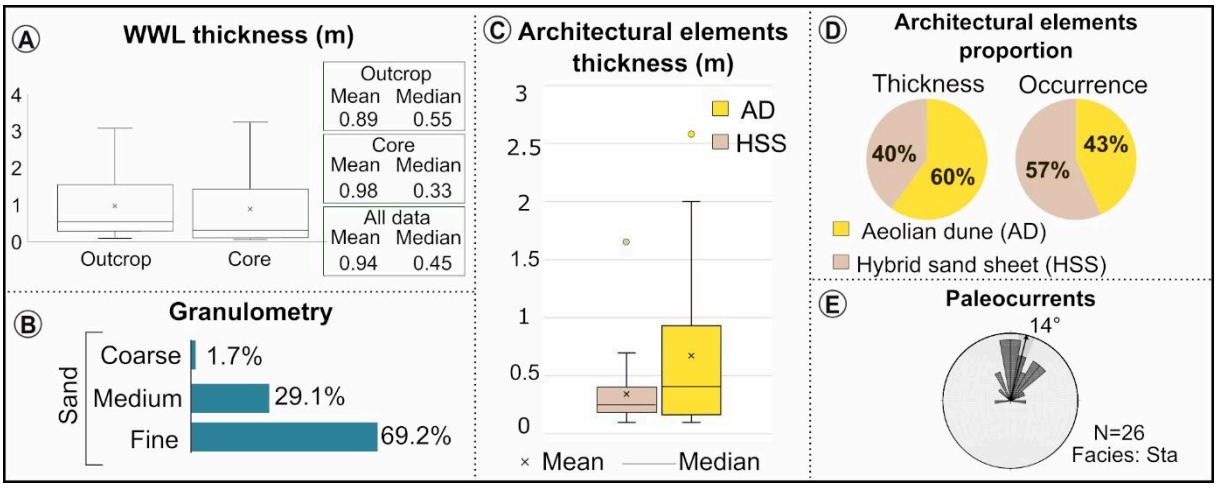


Figure 2-11: Wind- and water-laid facies association (WWL) quantitative data.

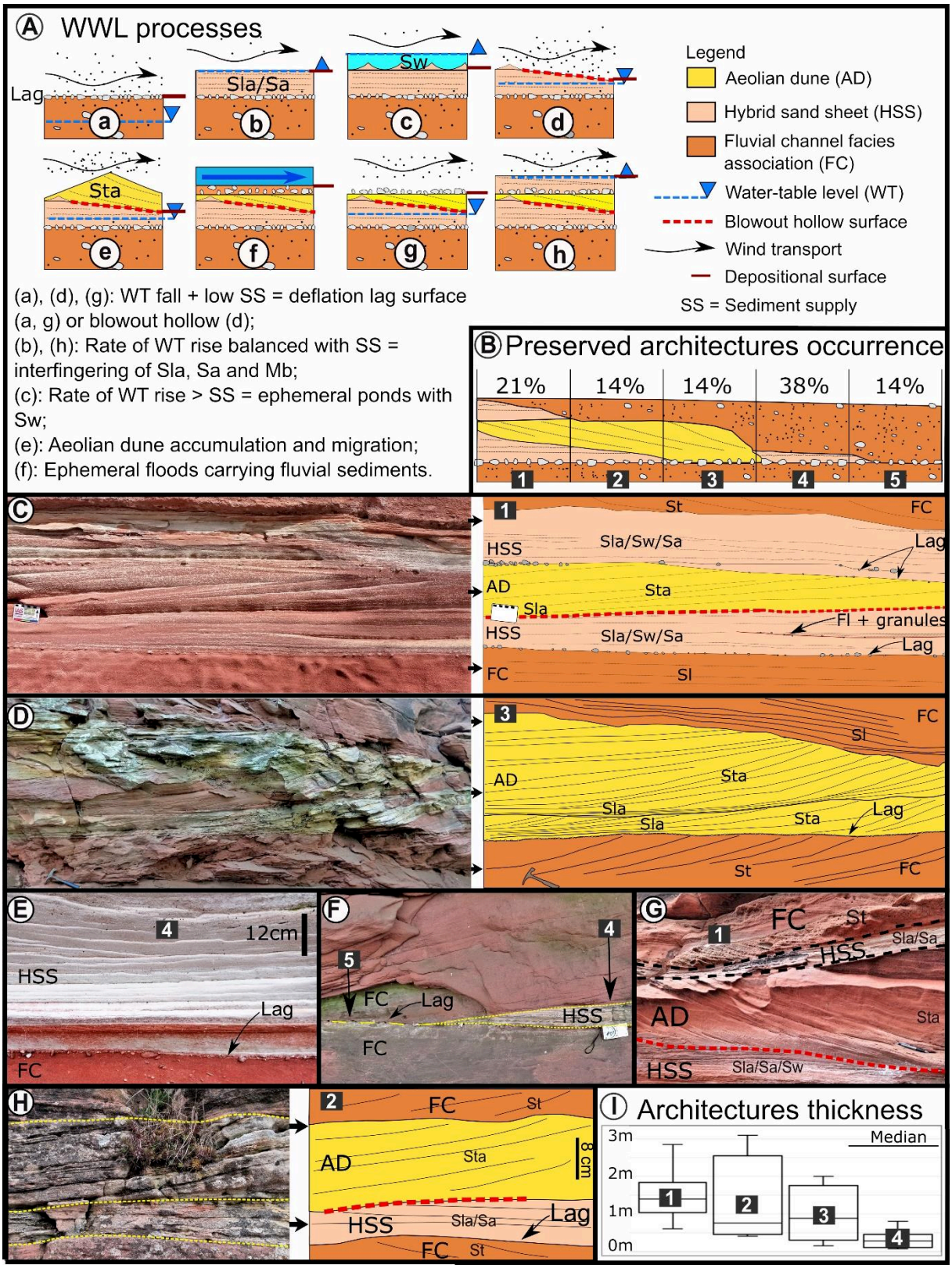


Figure 2-12: (A) Processes involved in generating the wind- and water-laid facies association (WWL); (B) different vertical architectures of the WWL, and their respective proportions of occurrences, recorded in the Lower Grès Vosgien Formation; (C) e.g. Architecture 1. Outcrop: LGV7; (D) e.g. Architecture 3. Outcrop: LGV1; (E) e.g. Architecture 4. Outcrop: LGV5; (F) e.g. Architectures 4 and 5. Outcrop: LGV10; (G) e.g. Architecture 1. Outcrop: LGV5; (H) e.g. Architecture 2. Outcrop: LGV7; (I) distribution of thickness of each architecture presented in (B).

2.4.1.2.4. Interactions between WWL architectural elements

Regarding the vertical arrangement of the architectural elements, the WWL records four main preserved architectures. The most frequently preserved architecture is composed solely of HSS (architecture 4 in Figs. 2-12B, -12E, and -12F), which also exhibits the thinnest preservation (Fig. 2-12I). The second most common architecture features HSS overlain by an AD, with a blowout hollow surface in between, followed by another HSS overlying the AD (Architecture 1 in Figs. 2-12B, -12C, and -12G). Occasionally, the upper HSS from this architecture is absent, possibly due to erosion from the subsequent fluvial process, which then records only a HSS overlaid by AD (Architecture 2 in Figs. 2-12B, and -12H). The fourth preserved architecture is characterised by the presence of only AD. Figure 2-12I illustrates that the thickest architectures are associated with AD, despite the prevalent occurrences of HSS (Figs 2-11D, and, -12B). These vertical architectures may evolve laterally between each other on an outcrop scale (Fig. 2-13).

2.4.1.3. Lateral and vertical interactions between facies associations

Figure 2-13 illustrates two levels of WWL displayed with a complete FC unit, of 12.8 m (Table 2-3), in between. The lower WWL level (number 3 in Fig. 2-13) present greater extent that the outcrop width, however, its thickness decreases laterally in a down-palaeocurrent direction of the overlying FC. The upper WWL level (number 4 in Fig. 2-13) also presents a thickness decrease following the palaeocurrent direction and; in this case, the entire WWL is laterally eroded by the overlying FC.

The outcrop LGV13 records the lower contact with Permian deposits (Bourquin et al, 2009). Thus, outcrops LGV13, LGV9, and LGV10 (see Fig. 2-1A for location), which are vertically stacked, represent the lower part of the LGV. Despite sections covered in between, combined they record 70 m of outcrop without WWL, indicating the absence, or relatively minor occurrences, of WWL in the lower part of the LGV. The core section described represents the upper 100 m of the LGV (Aichholzer, 2019). Core data record 13 occurrences of WWL, intercalated with FC, in the upper 76 m (Fig. 2-15). The frequency of intercalations increases upwards, while the FC thickness decreases. This is supported by the strong correlation between depth and FC thickness ($R_s = 0.71$; p-value = 0.049) (Fig. 2-15C).

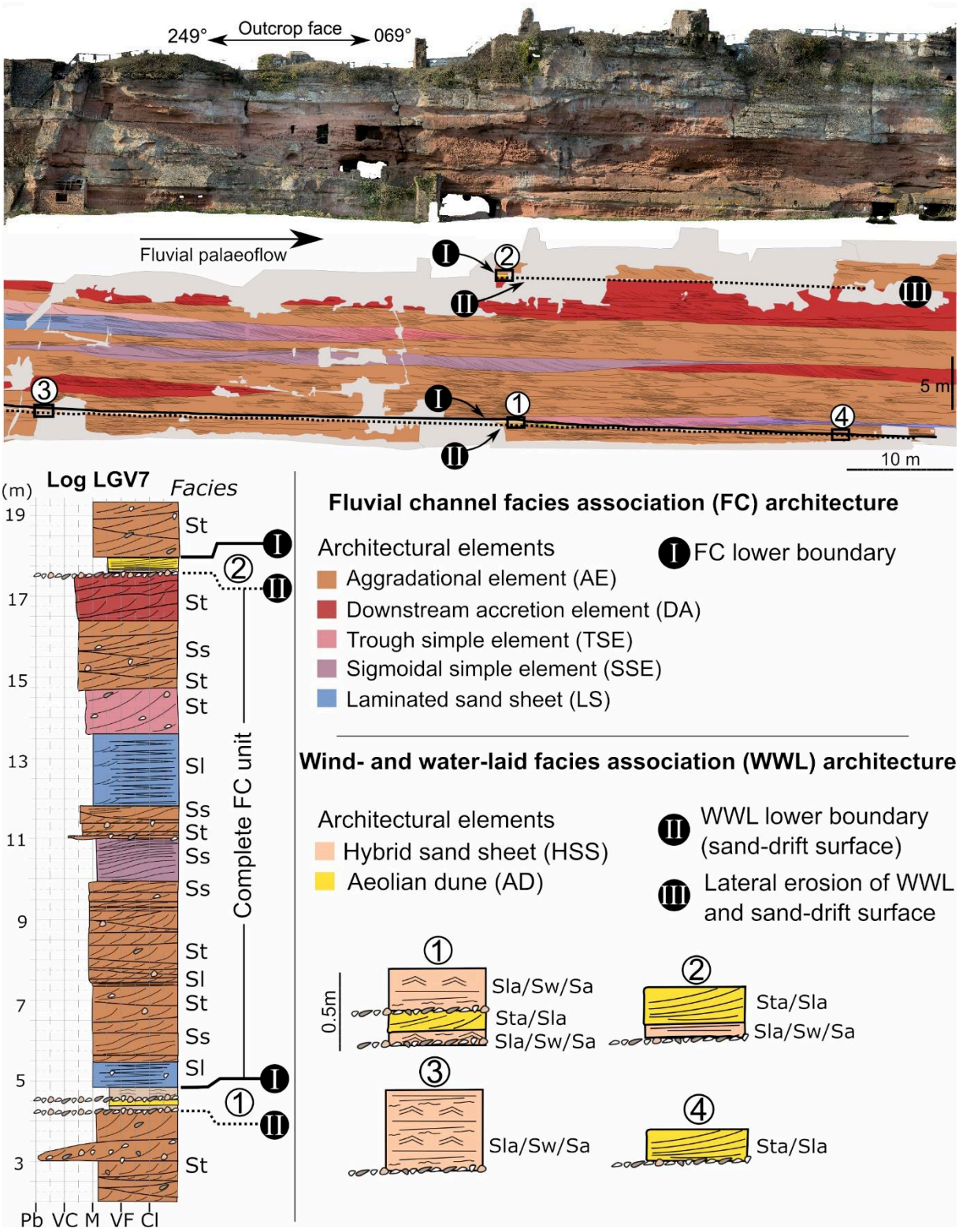


Figure 2-13: Vertical and lateral architecture distribution of the Lower Grès Vosgien Formation, in an outcrop scale. Outcrop: LGV7.

2.5. DISCUSSION

2.5.1. Fluvial channel facies association (FC) depositional controlling factors

The distribution of lower-, transitional-, and upper-flow regime sedimentary structures can be attributed to spatial effects, particularly highlighted by varying flow depths across humpback bars. The upper part of such bars, characterised by shallower water, records upper-flow regime conditions, whereas the lee-side, characterised by deeper flow depths, records lower-flow regime conditions. However, when these facies are associated with reactivation surfaces, gravelly sandstone lenses, mud clasts breccias, and evidence of ephemeral channels, such as mud draping sets and foresets, it indicates that discharge variability was also a controlling factor during the deposition of the FC (Miall, 1988; DeLuca and Eriksson, 1989; Bhattacharyya and Morad, 1993; Fielding, 2006; Miall, 2006; Fielding et al., 2009; Plink-Björklund, 2015; Fielding et al, 2018; Alexander et al., 2020; Arévalo, et al., 2022). The dominance of small dunes, and unit bars with signs of modification over time, indicates a system that was subjected to moderate discharge variability (Fielding et al., 2018). Rapid flow recession, associated to such discharge variabilities, is evidenced by (i) isolated SSE (Røe, 1987), (ii) Fl between cross-bedding sets and foresets (Miall, 2006; Plink-Björklund, 2015), (iii) antidunes (Fielding, 2006; Fielding et al., 2018), (iv) signs of cannibalisation of large bedforms (Myrow et al., 2018), and (v) the coefficient of variance (CV) of AE cross-set thickness (Table 2-3) (Leary and Ganti , 2019).

An equivalent to the FC can be made with observations by Skelly et al. (2003) in a modern aggrading braided river. The authors defined two main scales of channel elements, that alternate through time. Firstly, a channel complex active at low discharges, composed of small-scale dunes migrating between mid-channel bars. Secondly, a single channel active at high discharges, which contains not only large- and small-scale dunes, but also braided bars with height in the order of the bank-full channel depth. In the FC deposits of the LGV, the relatively low-discharge channel is represented by the sets within the AE deposits, and the high-discharge channel is represented by isolated larger sets within the AE and by the elements TSE, SSE and DA.

2.5.2. Wind- and water-laid facies association depositional controlling factors

When the rate of water-table rise was balanced with sediment supply, the conditions were favourable for depositing dry sediments in the form of facies Sla (Carr-Crabaugh and Kocurec, 1993; Scherer and Lavina, 2005). Alternatively, a damp surface could have been formed by the interception of the capillary fringe, then facies Sa (Kocurek and Fielder, 1982; Trewin, 1993; Mountney et al., 1999) and Mb (Fryberger et al., 1988; Gerdes, 2007; Rodríguez-López et al., 2014) were deposited (Figs. 2-12A, and -14A).

The presence of facies Sw suggest that the depositional surface was locally submerged, creating ephemeral ponds (Clemmensen, 1991; Carr-Crabaugh and Kocurec, 1993; Trewin, 1993; Basilici et al., 2021) (Fig. 2-14A). The absence of facies Fl, or any subaqueous transport structures associated with such ponds, implies that they were formed when the rate of water-table rise outpaced the sediment supply (Trewin, 1993; Basilici, et al., 2021) (Fig. 2-12A). Alternatively, another process responsible for generating such ephemeral ponds are sheet-flood events reaching the sand-sheet and related landforms (Clemmensen, 1991; Veiga et al., 2022; Ghinassi et al., 2004; Scherer and Lavina, 2005; Miall, 2006; Paim and Scherer, 2007; Bristow and Mountney, 2013; Al-Masrahy and Mountney, 2015) (Fig. 2-14A). In the latter, Sw is capped by a Fl laminae, indicating subsequent calm sedimentation (Miall, 2006). Ephemeral flood events are evidenced by gravel-size clasts, often aligned on a surface within the WWL, with no other subaqueous flow structures associated. This suggests wind winnowing processes that followed the ephemeral flood, leaving behind a deflation lag within the WWL facies (Figs. 2-12A, and -14B).

The lateral facies distribution within the hybrid sand sheet architectural element (HSS) was influenced by local topography, leading to distinct interactions between the water-table level and the depositional surface (Fig. 2-14A). The upward transition between facies Sla, Sa (and/or Mb) and Sw (Figs. 2-10B and, -10C), respectively, record the gradual outpace of water-table rise against sediment supply (Trewin, 1993; Basilici, et al., 2021).

The accumulation of aeolian dunes requires the availability of a substantial volume of sand for aeolian transport (Basilici et al, 2021) (Fig. 2-12A), and aeolian

dune preservation in otherwise fluvial dominated environments typically requires a continuous increase in the relative water-table level (Scherer and Lavina, 2005; Basilici et al, 2021). The growth of aeolian dunes is associated with events of water-table level fall, which generates the blowout hollows concomitant to the increase of dry sediments available for the wind to transport (Figs. 2-12A, and -14B). Thus, the AD and HSS deposits took place during distinct temporal moments (Fig. 2-14).

The common preservation of HSS, compared to AD (Fig. 2-11D), is associated with a system that experienced a persistent scarcity of fine-grained dry sand available (Trewin, 1993; Al-Masrahy and Mountney, 2013), combined with ephemeral floods able to remobilise them (Kocurek and Nielson, 1986; Langford, 1989; Clemmensen, 1991) (Fig. 2-12A). This scarcity can be attributed to (i) a sediment source area originating from inactive fluvial deposits, with a limited budget of available fine-grained sand (Fig. 2-5A) (Trewin, 1993; Mountney et al., 1999), (ii) constrained sediment transport distances due to active fluvial channels nearby (Trewin, 1993; Farraj and Harvey, 2004), and (iii) the repeated intersection of the water-table with the depositional surface, potentially inhibiting aeolian sediment transport (Langford, 1989; Carr-Crabaugh and Kocurek, 1993; Trewin, 1993; Scherer and Lavina, 2005).

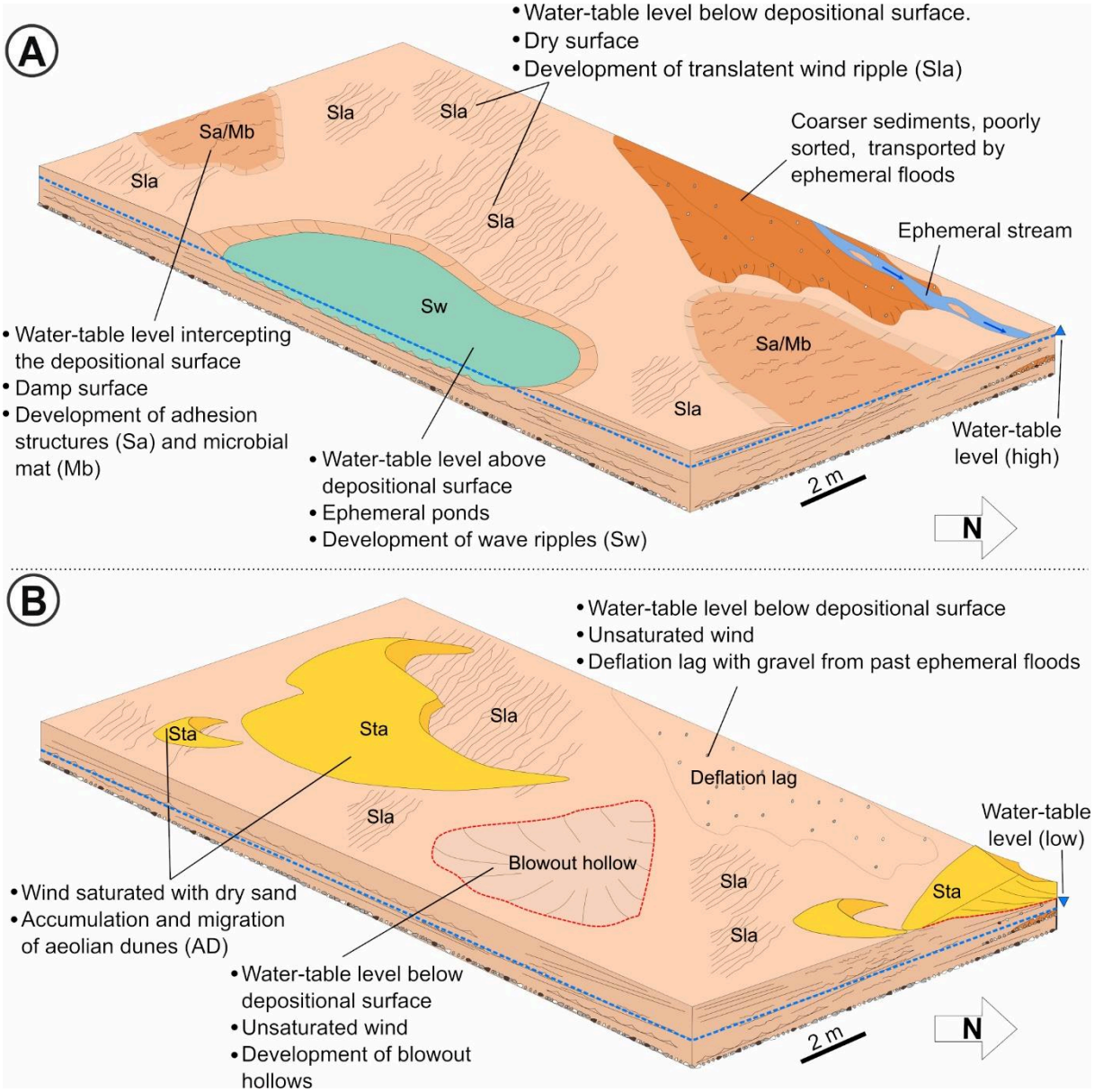


Figure 2-14: Block diagram of wind- and water-laid facies association (WWL), representing two distinct temporal moments. (A) Formation of hybrid sand sheet architectural element, influenced by water-table level close to the depositional surface, and by ephemeral floods; (B) WWL during low water-table level. Sand deflation by winnowing, leaving behind deflation lag and blowout hollows, followed by accumulation and migration of aeolian dunes.

2.5.3. Large-scale depositional system

Although this study mainly focuses on the fluvial and aeolian architecture, certain characteristics suggest the LGV as part of a fluvial fan system (distributive fluvial system – DFS/ megafan). The overall retrogradational context during the deposition of the Middle Buntsandstein (Bourquin et al., 2006; 2009), and the upward tendency for cross-set thickness decrease (Fig. 2-15B), may suggest shallower channels in the distal parts of the system. Despite the uncertainties of using 1D data to analyse cross-set thickness, this is a characteristic expected in DFS (Hartley et al., 2010; Weissmann

et al., 2015; Ventra and Moscariello, 2023). Also, the upward increase of interactions between FC and WWL might indicate an increase in avulsion frequency in more distal parts of the fluvial system, supporting the DFS hypothesis (Brookfield, 2008; Hartley et al., 2010; Weissmann et al., 2015; Reis et al., 2022).

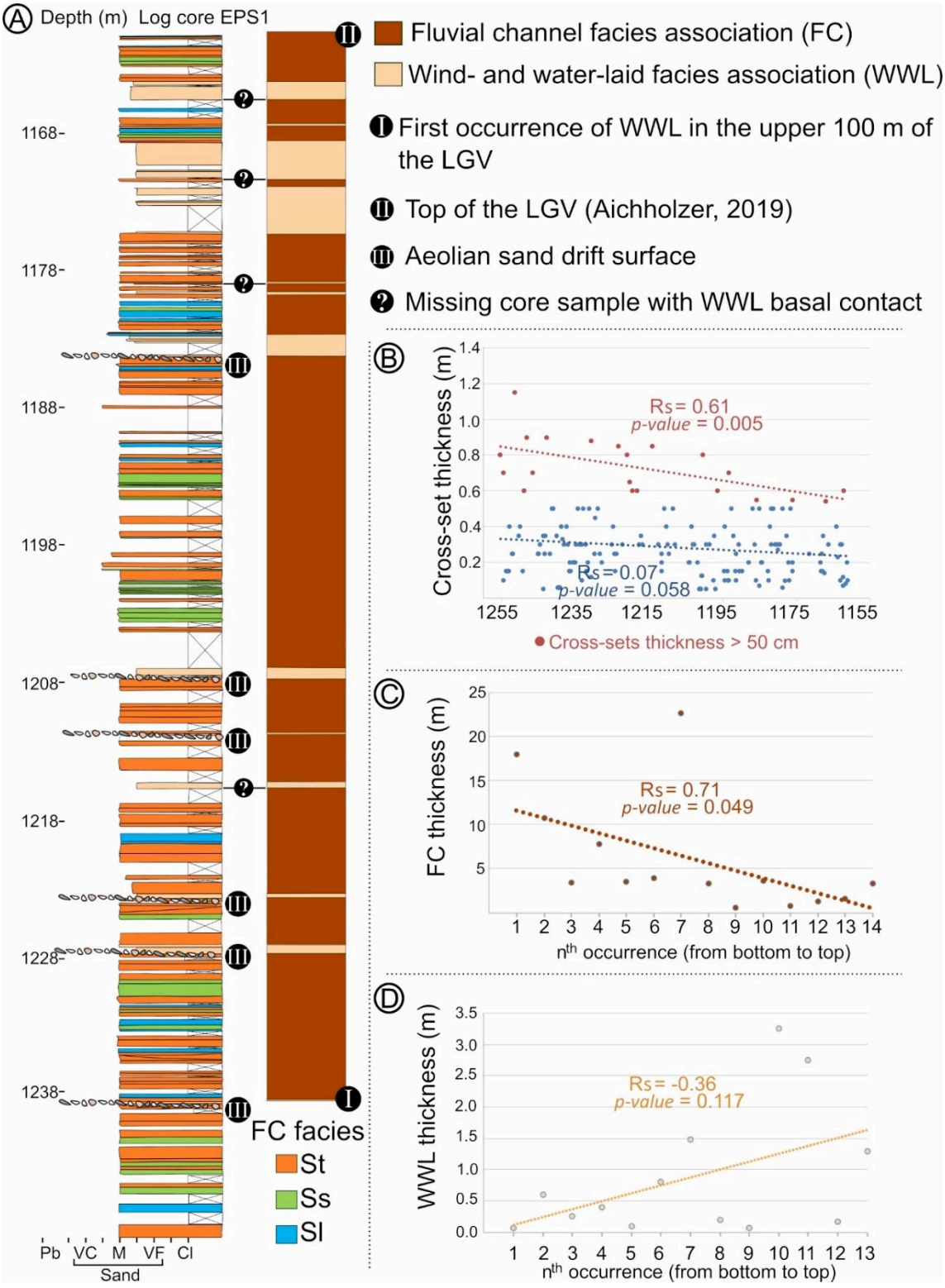


Figure 2-15: (A) Log from the core EPS1 exhibiting the intercalations between fluvial channel facies association (FC), and wind- and water-laid facies association (WWL) recorded within the upper 100 m of the Lower Grès

Vosgien Formation (LGV); (B) fluvial cross-set thickness occurrences along 100 m of the EPS1 core, which represents the top of the LGV (Aichholzer, 2019). Rs and p-value in blue, all cross-sets (red and blue dots) are analysed. In red, only cross-sets thicker than 50 cm are analysed. Thinning-upward trends are observed, however, a strong correlation between cross-set thickness and depth is only observed for the larger (>50 cm) cross-sets; (C) strong correlation between FC thickness and depth; (D) weak negative correlation between WWL thickness and depth. However, the high p-value indicates that the dataset used for this analysis is not enough.

Furthermore, other general aspects observed in the LGV also support the DFS interpretation. These include: (i) the correlation between fan formation and discharge variability (Leier et al., 2005; Hansford and Plink-Björklund, 2020; Ventra and Moscariello, 2023), where dynamic channel aggradation, and avulsion, result in a complex interfingering of channelised and sheet like deposits (Davidson et al., 2013), extending laterally for tens of kilometres (Miall, 2006), (ii) most of the modern DFS dissipate into aeolian systems (Hartley et al., 2010), forming aeolian sand-sheet deposits (Cain and Mountney, 2009), and interfingered sheet-floods with aeolian facies (Brookfield, 2008), and (iii) the hypothesis that DFS/megafans present the most efficient preservation potential among fluvial systems (Ventra and Moscariello, 2023), as the LGV records c. 200 m of fluvial-dominated sediments, deposited in about 1.8 m.y. (Bourquin et al., 2006; 2009).

Despite the common progradational trends (regressive context) observed in most fluvial fan systems (Weissmann et al., 2015; Wang and Plink-Björklund, 2019), examples of fluvial fans systems formed in a retrogradational context have also been documented (Cain and Mountney, 2009; Kukulski et al., 2013).

The coverage of the study area is restricted in terms of large DFS (megafans) scale. Thus, tendencies of lateral changes of channel dimensions, amalgamation, grain size, or floodplain preservation, often considered characteristics of DFS (Hartley et al., 2010; Weissmann et al., 2010; Hartley and Owen, 2022), were not observed. Moreover, the upward decrease in cross-set thickness presented in figure 2-15B, considered a characteristic of a retrogradational DFS, is based on 1D data, which carries uncertainties in correlating set thickness with dune size and, consequently, channel depths (Colombera et al., 2024). These aspects, associated with the possible overlap of characteristics between DFS with those of tributary fluvial systems (Sambrook Smith et al., 2010; Fielding et al., 2012), highlight that further studies covering the entire Buntsandstein Group, especially laterally extrapolating the study area, are necessary for a conclusive characterisation.

Bourquin et al. (2009) applied sequence stratigraphy concepts to the LGV, categorising the sand-drift surfaces as instances of base-level fall associated with climatic events, correlatable between outcrops regionally, and across the western part of the German Basin. However, in the context of the DFS hypothesis, major channel belt avulsions emerge as an alternative interpretation for the local absence of fluvial deposition, and, consequently, the development of these surfaces and the accumulation of WWL (Langford and Chan, 1989; Cowan, 1993).

The lack of evaporate deposits, the abundant water-related facies, and the already arid climate during the FC deposition (Peron et al., 2005), raise the question if the WWL, above the sand-drift surface, were deposited in different climatic conditions compared to the FC. Evidence indicates that the accumulation of WWL may have occurred concomitant with fluvial deposition. Given the close relationship between groundwater level, in braid plain, and river stages (Banks et al., 2022), the high-frequency intercalation of high and low water-table levels, observed within the HSS, could directly correspond to fluvial interannual high and low discharges, respectively. The ephemeral floods in HSS may be linked to crevasse-splay, a common feature in braided rivers preceding channel avulsion, during peak discharges (Ethridge et al., 1999). The limited availability of dry sand during HSS deposition aligns with the presence of relatively nearby active fluvial channels (Clemmensen, 1991; Trewin, 1993). Furthermore, the lowering of the water-table level, leading to the formation of blowout hollows and accumulation of aeolian dunes, indicates climatic (temporal) events at a lower frequency compared to those observed within the HSS. These events may be coeval with periods of ephemeral fluvial activity, as recorded by the laminated sand sheet elements, and by mud deposited between sets and foresets. The variable preservation thickness of WWL, ranging from a singular sand-drift surface to three metres, indicates the spatially distinct re-establishment of fluvial deposition. This, coupled with the slight erosional relationship between FC and the underlying WWL, also leads to channel avulsion interpretation (Hajek et al., 2010).

However, this alternative interpretation carries uncertainties, such as: (i) the lack of timescale control in the FC and WWL dynamics, to precisely evidence their contemporaneity, (ii) the unknown periodicity of avulsions in large DFS (megafans) (Wilkinson and Gunnell, 2023), and (iii) since avulsions (autogenic) may also be influenced by climatic (allogenic) events, differentiating them in the rock record

becomes challenging (Ventra and Clarke, 2018). Despite climatic or channel avulsion controlling the FC and WWL intercalation, complete WWL and sand-drift surfaces can be laterally eroded at the outcrop scale (Fig. 2-13). Thus, caution must be taken when extrapolating these surfaces beyond the scale of hundreds of metres, especially in the same direction of the fluvial palaeocurrents.

2.6. CONCLUSIONS

Two facies associations compose the Lower Grès Vosgien Formation (LGV): fluvial channel (FC) facies association, comprising 93% of the total thickness measured for the LGV, and wind- and water-laid facies association (WWL), which accounts for 7%. The FC records 75% of its thickness by lower-flow regime sedimentary structures, and 25% by transitional- and upper-flow regime sedimentary structures, deposited in shallow, sometimes ephemeral, and poorly confined, braided channels. The WWL records 60% of its thickness by aeolian dunes (AD), and 40% by hybrid sand sheets (HSS). However, in terms of occurrences, the HSS represents 57% of the WWL, while the AD, 43%, which indicates the persistent presence of water during the WWL deposition.

The distribution of lower-, transitional-, and upper-flow regime sedimentary structures, in the FC, provides evidence of temporal and spatial flow variabilities, sometimes making it challenging to distinguish between them. Spatial effects in flow variability are exemplified by the overpassing process that removes gravel from the top of humpback bars, affected upper-flow regime conditions, depositing at the lee-side of the bar influenced by lower-flow regime conditions. Temporal flow variabilities are mostly discernible through fluvial architectural analysis, by evidence of flow pulsations, and recognition of low- and high-discharge channels.

The WWL records persistent shallow water-table, and ephemeral sheet-floods, which reduced the availability of dry sands to be transported by the wind, inhibiting the accumulation of aeolian dunes, resulting in the dominance of hybrid sand sheets. Periods of water-table lowering, are first recorded by sand-drift surfaces and blowout hollows, followed by wind saturation with sand, and deposition of aeolian dunes. Thus, the hybrid sand sheets and the aeolian dunes took place in distinct temporal moments.

Distal parts of the LGV record an increase in the frequency of WWL occurrences, and a decrease in the number of larger fluvial cross-sets. These characteristics,

coupled with discharge variabilities, aggradation, and the extensive coverage of the Middle Buntsandstein fluvial deposits, support a hypothesis that the LGV was part of a large distributive fluvial system (fan/megafan). However, a larger-scale quantitative analysis is necessary for a conclusive characterisation.

Previous authors have interpreted the base of WWL, marked by sand-drift surfaces, as formed during climatic changes that can be correlated across the German Basin. However, ambiguity is highlighted, once evidence indicates that WWL and FC may be contemporaneous, and their establishment be associated with channel-belt avulsion events. Therefore, understanding the events responsible for the development of these surfaces is crucial before laterally extrapolating them for several kilometres, since in some cases, their lateral extension cannot be followed even at an outcrop scale (hundreds of metres).

3. Chapter 3: Sedimentary facies control on permeability heterogeneities: the Middle Buntsandstein continental sandstones (Lower Triassic, eastern France)

Bofill, L., Bozetti, G., Schäfer, G., Ghienne, J-F., Schuster, M., Heap, M., Knobelock, G., Scherer, C., Armelenti, G., Souza, E., 2024. Sedimentary facies control on permeability heterogeneities: the Middle Buntsandstein continental sandstones (Lower Triassic, eastern France). Marine and Petroleum Geology. Accepted.

ABSTRACT

Understanding the influence of sedimentary processes on reservoir architectures can be essential for improving the prediction of permeability heterogeneities. The Upper Rhine Graben offers an ideal geological context for using outcrops as reservoir analogues, as the rocks cropping out at the Graben's shoulders belong to the same formations that host lithium-rich geothermal brine in the Graben. The interval of interest in this study, the upper section of the Lower Grès Vosgien Formation (LGV), consists of fluvio-aeolian deposits considered preferential zones for fluid migration within the Buntsandstein Group. In this study, the main factors controlling permeability heterogeneity distribution of these fluvio-aeolian deposits are presented, in different scales, by combining permeability and petrographic characteristics with quantitative sedimentological characterisation of the LGV. The fluvial channel facies association (f.a.), predominantly composed of cross-bedded sandstones deposited in braided channels, exhibits higher permeability compared to the wind- and water-laid f.a., made up of sandstones deposited in a sand-sheet-dominated aeolian system. Vertical profiles reveal permeability contrasts of up to four orders of magnitude between these f.a. At the facies scale, the fluvial channel f.a. shows an inverse relationship between flow-regime conditions and permeability. Specifically, trough cross-bedded sandstones, formed under lower flow-regime conditions, exhibit higher permeability than low-angle cross-bedded sandstones, formed under upper flow-regime conditions. In the wind- and water-laid f.a. permeability distribution is directly influenced by paleoclimatic variations. Low-permeability hybrid sand sheets (HSS) were deposited under relatively humid conditions, while high-permeability aeolian dunes (AD) formed during more arid periods. Despite the high permeability of the AD, the architecture of the wind- and water-laid f.a. suggests that the AD have low connectivity potential. The lateral continuity of the wind- and water-laid f.a., extending over hundreds of metres, combined with the dominant occurrence of low-permeability HSS, indicates that this

facies association may act as flow baffles or barriers. Compaction is the main process influencing the permeability and porosity of the LGV. Samples with a higher proportion of lithoclasts and infiltrated clay recorded a more advanced degree of compaction. In contrast, samples with a higher percentage of quartz overgrowth were less compacted. The diagenetic overprint affected the distinct facies differently, indicating that primary sedimentary processes and architecture govern the distribution of permeability heterogeneity in the LGV. Permeability data from outcrops exhibited median values up to three orders of magnitude higher than those from subsurface data. However, the same facies, and similar trends of relative porosity-permeability responses to the distinct sedimentary features are observed between outcrops and borehole samples, highlighting sedimentology as an indispensable proxy for reservoir heterogeneity studies.

3.1. INTRODUCTION

Heterogeneities in sandstones develop at various stages of their formation, from primary sedimentary processes that determine sediment grain size and distribution, composition, and fabric; to later diagenetic stages, which can significantly alter its original characteristics (Bjørlykke, 2014). Understanding these processes and assessing their respective influences on reservoir architectures are essential in improving the prediction of permeability heterogeneities (Davis et al., 1993).

The study of facies-scale heterogeneities is a common practice in oil and gas production planning, and in the prediction of recovery efficiency (Høimyr et al., 1993). Yet, groundwater flow, transport, and heat-transfer modellers often overlook such heterogeneities (Crooijmans et al., 2016; Aberg et al., 2021), which may have profound implications, such as on the management of contaminated groundwater (Davis et al, 1993; Possemiers et al., 2012; Thompson et al., 2019), or on the performance of geothermal reservoirs (Bauer et al., 2019; Thompson et al., 2019).

The scale of observation is a paramount criterion when sampling and interpreting permeability data. Using a sampling interval, or grid, that does not account for the scales of heterogeneity patterns, may lead to misinterpretations such as that heterogeneous deposits are homogeneous (Chandler et al., 1989; Dreyer, 1993). The dataset for aquifer and reservoir characterisation primarily relies on boreholes. However, as the distance from the observation point increases, uncertainties regarding

the lateral continuity of this information also increase (Lowden, 1993). Geophysical methods can help address such uncertainties; although they come with limitations, particularly concerning features lying between bounding surfaces identified in geophysical results (Weissmann et al., 2015). The use of outcrops as reservoir analogues is a widely used method for mitigating these uncertainties (e.g. Alexander, 1993; Aigner et al., 1996; Rogiers et al., 2013; Howell et al., 2014; Weissmann et al., 2015; Thompson et al., 2019). It enables direct observation of sedimentary facies geometries and lateral transitions, optimising volume estimations, understanding reservoir connectivity, and identifying facies and diagenetic controls on porosity and permeability distribution (Alexander, 1993). Systematic differences in petrophysical data values, such as permeability, are common between outcrop and borehole samples due to their distinct burial and uplift paths (e.g. Rogiers et al., 2013; Busch et al., 2022; Hossain et al., 2024). However, similar trends and relative parameter value distributions can be expected (Goggin et al., 1992; Rogiers et al., 2013).

The geological context of the Upper Rhine Graben, a 350-kilometre-long rift valley that straddles the border between France and Germany, provides an ideal scenario for using outcrops as reservoir analogues (Bofill et al., 2024), given that the rocks cropping out at the shoulders of the graben belong to the same formations that host lithium-rich geothermal water (Sanjuan et al., 2022) in the axis of the graben. Moreover, to the west of the Vosges mountains (France), the same formations exist at shallow depths, hosting groundwater used for public water supply (Vaute et al., 2007; Vaute et al., 2013). This geographic proximity between the reservoir and its analogues reduces lateral variations that may occur within a specific depositional environment, thereby increasing the likelihood of encountering similar geobody architectures in both.

The focus of this study is the upper section of the Lower Grès Vosgien Formation (LGV) (Théobald et al., 1967), which has been characterised as preserving one of the most favourable zones for fluid migration in the Buntsandstein Group (Gr.) in the Upper Rhine Graben due to its relatively high porosity and permeability (Haffen et al., 2013). Previous authors have presented porosity and permeability characteristics of the Buntsandstein Gr. in the region (e.g. Ghienne et al., 1994; Haffen et al., 2013; Griffiths et al., 2016; Heap et al., 2017; Kushnir et al., 2018, 2023; Busch et al., 2022; Goupil et al., 2022; Quandt et al., 2022; Kontny et al., 2023). However, prior to the study by Bofill et al. (2024), there was an absence of a high-resolution quantitative facies

characterisation for the LGV, resulting in a lack of a systematic link between permeability and individual sedimentary facies.

The LGV is the thickest formation of the Buntsandstein Gr. (Fig. 3-1), composed of sandstones deposited by braided fluvial and aeolian systems (Dachroth, 1985; Bourquin et al., 2006; Bourquin et al., 2009; Bofill et al., 2024), with rarely preserved mudstone layers (Ghienne et al., 1994; Bourquin et al., 2006; Bofill et al., 2024).

Braided fluvial deposits exhibit significant variations in sand body geometries, internal structures, and textures (Miall, 1988; Høimyr et al., 1993). Quantifying these features is challenging due to their typical occurrence below the resolution of reservoir modelling cells (tens to hundreds of metres) (Puig et al., 2019). The numerous erosional and depositional processes associated with these systems depend on spatial and temporal variables that are difficult to predict. These characteristics limit the applicability of spatial statistical analysis for reservoir characterisation (Castle et al., 2004) and underscore the importance of employing quantitative facies description for more realistic predictions of flow behaviour (Alexander, 1993).

Aeolian deposits are generally characterised as being more permeable and porous than fluvial deposits (e.g. Cowan, 1993; Fischer et al., 2007; Bjørlykke, 2014; Quandt et al., 2022). However, within aeolian deposits, significant differences in permeability can be observed depending on their facies (e.g. Chandler et al., 1989; Fischer et al., 2007; Newell et al., 2019; Thompson et al., 2019), highlighting the necessity to study the controlling factors of such variations.

The objective of this study is to define the sedimentary controls on permeability heterogeneity within the LGV and to identify the distribution of such heterogeneity at both, facies (Dalrymple, 2010) and facies association (Collinson, 1969) scale. Therefore, the following research questions are addressed: i) do different sedimentary facies within the sandstone group consistently exhibit distinct permeability responses? ii) What are the factors contributing to permeability heterogeneity within braided-fluvial and aeolian systems? iii) Are primary sedimentary processes or later diagenetic stages that govern present-day permeability variability in outcrops of the LGV? iv) To which extent does understanding the distribution of permeability within facies and facies associations in outcrops of the LGV enhance our comprehension of subsurface heterogeneity patterns?

3.2. STUDY AREA AND GEOLOGICAL SETTINGS

The study area is situated in eastern France (Fig. 3-1A), within the Upper Rhine Graben (URG) region. The analyses involved outcrops along the western flank of the URG, in the Northern Vosges mountains (Fig. 3-1C), and core samples from a geothermal well located in the Graben's axis. During the Lower Triassic, continental sedimentation dominated in the western margin of the Germanic Basin, resulting in the deposition of the Buntsandstein Gr, which is predominantly attributed to braided rivers overlaying restricted Late Permian basins or crystalline basement (Dachroth, 1985; Deynoux et al., 1997; Bourquin et al., 2009). The Buntsandstein Gr. comprises different geological formations distributed spatially and temporally across the basin (Mader, 1985).

The URG formed during the Late Eocene (Grimmer et al., 2017) exposing the studied outcrops along the shoulders of the Graben at the Vosges, in France, and the Black Forest, in Germany. At the location of the geothermal well used in this study (Fig. 3-1C), the Buntsandstein Gr. is buried at depths of approximately 1000 m to 1400 m (Aichholzer, 2019).

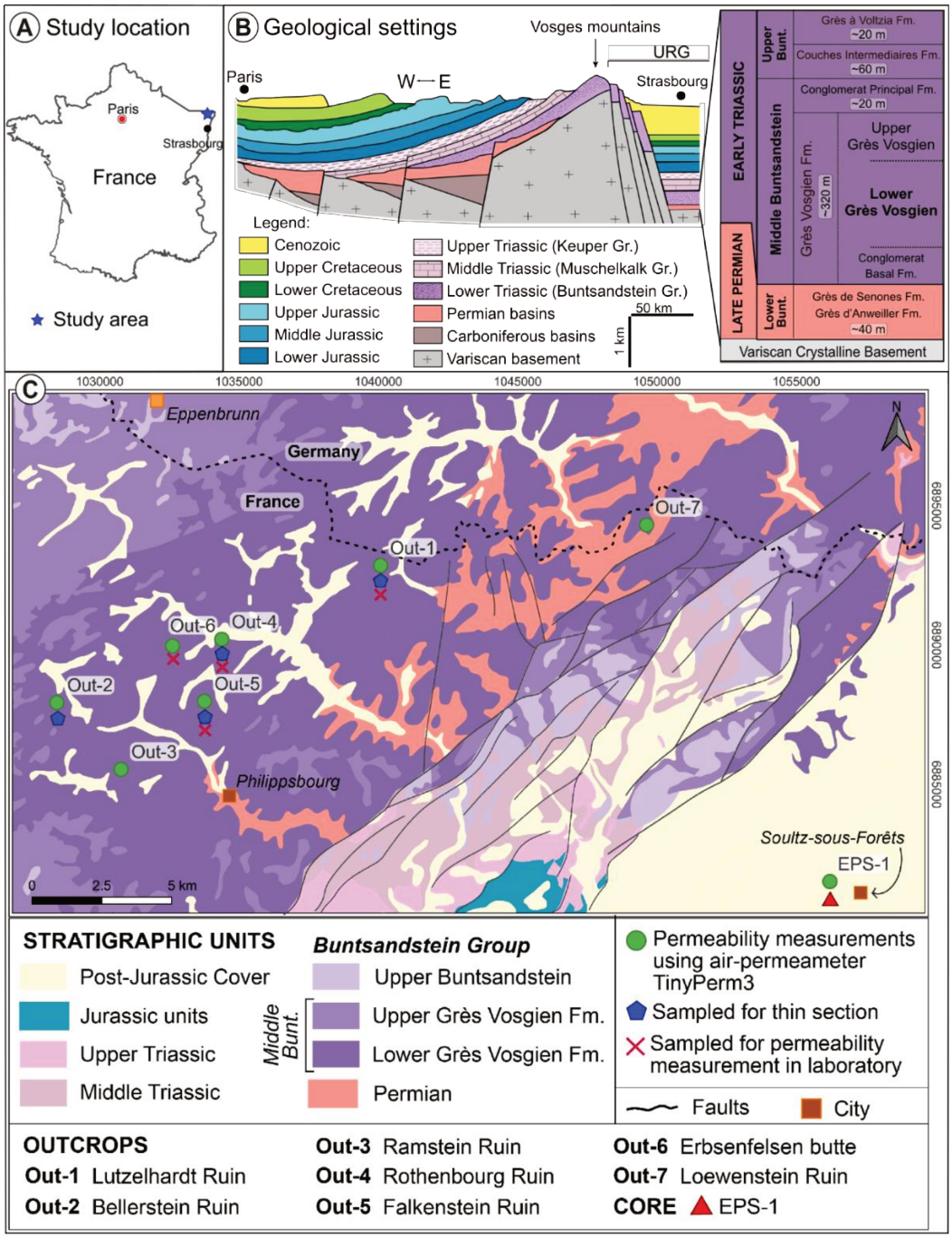


Figure 3-1: (A) Study area located in eastern France. (B) Schematic representation of the Buntsandstein Gr. geological settings, showing geographic proximity from outcrops (red dot in the Vosges mountains) to the shallow aquifer (west of the Vosges) and to the lithium-rich geothermal reservoir (east of the Vosges, in the Upper Rhine Graben – URG axis) (adapted from Bouly and Demassieux, 1996, Guillocheau et al., 2000, Herivaux and Marechal, 2019, and Duringer et al., 2019). (C) Outcrop locations in the Vosges mountains, and well EPS1 in the URG axis.

3.2.1. Sedimentological background of the Lower Grès Vosgien Formation

A precise quantification of facies is crucial for generating accurate predictions of reservoir performance (Alexander, 1993; Weissmann et al., 2015). This study uses the quantitative sedimentological characterisation of the Lower Grès Vosgien Formation

(LGV) presented by Bofill et al. (2024) as the reference; where authors quantified facies and facies association, and defined the processes that governed the deposition of the LGV at different scales. Two facies associations (f.a.) were identified: the fluvial channel and the wind- and water-laid f.a.

According to Bofill et al. (2024), the fluvial channel f.a. comprises 93% of the total thickness of the LGV, primarily consisting of medium-grained sandstones (51%), followed by coarse-grained sandstones (36%), and very coarse-grained sandstones (11%); and mudstones represent 0.1% of the total measured thickness (Bofill et al., 2024). Three sedimentary facies correspond to 98% of the total fluvial channel f.a. thickness: trough cross-bedded sandstone (St) (Fig. 3-2), accounting for 73%; sigmoidal cross-bedded sandstone (Ss) (Figs. 3-2B and -2F), accounting for 13%; and low-angle cross-bedded sandstones (Sl) (Figs. 3-2C and -2F), accounting for 12% of the total fluvial channel f.a. thickness. The distribution of these facies is directly related to flow-regime variations inside the fluvial channels (Røe, 1987; Miall, 1988; DeLuca and Eriksson, 1989; Fielding, 2006), either by temporal (e.g. climatic) or spatial (e.g. channel depth or width) variations (e.g. Røe, 1987; Bhattacharyya and Morad, 1993; Miall, 2006; Bofill et al., 2024). These facies are arranged in amalgamated, lenticular, and tabular sets, presenting set thicknesses ranging from 5 cm to 1.8 m, with a mean value of approximately 40 cm (Bofill et al., 2024).

Bofill et al. (2024) observed varying proportions of gravel-size clasts in deposits of the fluvial channel f.a. and defined four classes of gravel content per facies based on field criteria (Table 3-1). The authors identified a strong correlation between gravel content and facies, consistently finding facies Sl recording lower gravel content, followed by facies Ss and St, respectively, which suggest an inverse relationship between gravel content and fluvial flow stages.

Table 3-1: Classes defined for gravel content in sand bodies of the Lower Grès Vosgien Formation, based on field criteria (Bofill et al., 2024).

Class	Code	Class criteria
Sandstone without gravel	WG	No gravel clasts present within the set
Sandstone apparently without gravel	AWG	Difficult to find gravel clasts. Sometimes, a single granule or pebble within the set (i.e., <<1%)

Slightly gravelly sandstone	SG	Easy to find granules and pebbles within the set (up to 5%, Folk et al., 1970)
Gravelly sandstone	GS	Rich in granules, pebbles, and occasionally cobbles (5% - 30%, Folk et al., 1970)

The establishment of the wind- and water-laid f.a. marks periods of, at least locally, fluvial inactivity, during which deposition was controlled by changes in the balance between wind transport, fluctuations in the water-table level, and ephemeral floods (Bofill et al., 2024). The aeolian trough cross-bedded sandstone (Sta) facies correspond to aeolian dunes migrating (Kocurek, 1991) during periods of relatively low water-table level (Bofill et al., 2024). The facies Sta, hereafter referred to as aeolian dune (AD) (Fig. 3-2E), exhibits the highest thickness among the facies comprising the wind- and water-laid f.a. The AD consists of tabular, occasionally lenticular with concave-up base, beds with mean thickness of 84 cm, varying from 10 cm to 2.73 m. In terms of occurrence, the wind- and water-laid f.a. is dominated by hybrid sand sheet (HSS) deposits, which consist of millimetre- to centimetre-scale interdigitating facies of aeolian translatent-strata (Sla), adhesion structures (Sa), microbially induced sedimentary structure (Mb), and wave-ripple (Sw). These facies were deposited in a sand sheet, where a shallow and fluctuating water-table level influenced aeolian sediment transport and deposition (Bofill et al., 2024). Facies Sla indicates a dry depositional surface (Cain and Mountney, 2009); facies Sa and Mb indicate a damp depositional surface (Kocurek and Fielder, 1982; Basilici et al., 2021); and facies Sw indicates a wet depositional surface where ephemeral ponds were formed (Trewin, 1993). Additionally, the sand sheets were affected by ephemeral floods that deposited coarser and poorly-sorted sediments, which was an important process during their establishment (Kocurek and Nielson, 1986; Clemmensen, 1991; Bofill et al., 2024). Considering the millimetre- to few centimetre-scale thickness of the individual facies Sla, Sa, Mb, and Sw, along with scattered poorly-sorted sediments from the ephemeral floods, and aiming to maintain a similar scale of observation with the other facies presented (decimetre-scale), for the permeability analysis these facies are grouped as HSS (Figs. 3-2D, -2E, and -2F). The HSS records laterally extensive tabular beds, with a mean thickness of 44 cm, ranging from 7 cm to 1.85 m.

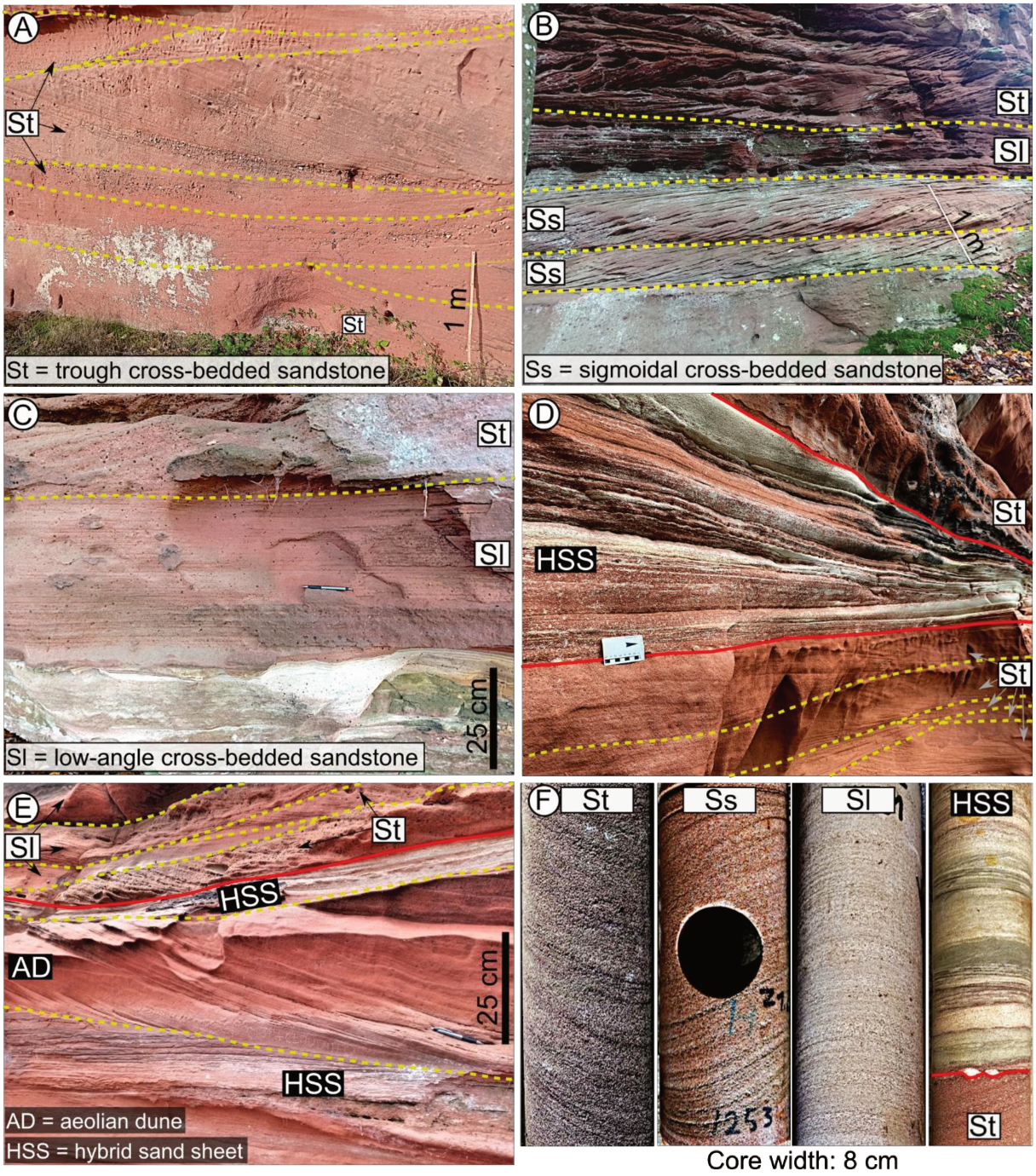


Figure 3-2: Main sedimentary facies in the Lower Grès Vosgien Formation, in outcrops and core. Facies code in white square and black letters belong to the fluvial channel facies association; facies code in black square and white letters belong to the wind- and water-laid facies association. Red solid lines represent the boundary between two facies associations, and the yellow dashed lines indicate limits between individual facies within the same facies association.

3.3. MATERIALS AND METHODS

Permeability data were collected from seven different outcrops along the Vosges mountains, and core samples from well EPS1 (e.g. Gérard et al., 2006; Kölbel and Genter, 2017) (Fig. 3-1C) in Soultz-sous-Forêts, using the non-destructive handheld air permeameter TinyPerm 3 (manufactured by New England Research), specified to

measurements between 1 mD and 10000 mD. To perform a measurement, a rubber nozzle is pressed against the rock and air is withdrawn from within the nozzle, creating a vacuum at the sample surface; permeability is then calculated using the decay of the vacuum within the nozzle. Measurements were taken in as a vertical profile to create temporal permeability logs. The spacing between measurements ranged from 5 cm to 25 cm, depending on specific outcrop characteristics and the features targeted for measurement. Data was preferentially acquired on fresh rock surfaces, avoiding moss and evident weathering that may generate non-realistic results. Before measurements, the surface was cleaned using a hard nylon brush followed by a soft toothbrush to remove fine superficial particles. Each permeability measurement was tied to categorical sedimentary characteristics such as facies, granulometry, and gravel content within the set. The permeability data was grouped according to facies associations, and data outliers were identified using the interquartile range (IQR) method and subsequently removed (e.g. Hosseini et al., 2019; Snowdon et al., 2021; Matinkia et al., 2023; Sheykhinasab et al., 2023), resulting in a dataset consisting of 1119 measurements.

To determine whether the permeability of two populations of datasets is statistically different, the permeability data was transformed into the log-normal domain, and a 95% confidence interval (C.I.) of the mean was calculated using built-in functions in Excel ®. The 95% C.I. represents the range above and below which the mean is expected to fall 95% of the time if the population is resampled. The absence of overlap between the mean +- 95% C.I. of the two populations suggests that they are statistically different; otherwise, any differences observed between mean values may be attributed to sampling size or distribution (e.g. Bulmer. 2024).

Moreover, 218 permeability measurements were taken from core samples from the well EPS1. Measurements were acquired in the core following the same method applied to outcrops, aiming to analyse if the results exhibit similar trends of association between sedimentary characteristics and permeability values observed in outcrops.

Additionally, thirteen plug samples from four outcrops (Fig. 3-1C) were acquired from different facies, aiming to confirm whether the permeability values obtained in the field were consistent with values obtained from controlled petrophysical laboratory measurements, or if they were only useful as relative values. The plug samples, 20 mm-diameter cylinders with a nominal length of 40 mm (i.e. within the guidelines

presented by Heap (2019) for porous sandstones), were prepared such that their bedding was parallel to the long axis of the plug (i.e. in the direction of fluid flow during the permeability measurement). The plugs were cored in this direction to match the measurements performed in the field. Once prepared, the samples were washed and then dried in a vacuum oven for 48 h at a temperature of 40 °C. Permeability was measured using a benchtop gas permeameter that uses nitrogen gas as the pore fluid (for schematics of the device, see Heap and Kennedy, 2016; Farquharson et al., 2016). Permeability was measured at ambient laboratory temperature using a confining pressure of 1 MPa (to ensure that the pore fluid passes through the sample). For each plug, volumetric flow rates, Q, were measured for six pore pressure differentials, ΔP. Permeability, k, was then calculated using Darcy's law:

$$k = \frac{Q}{P_m \Delta P} \frac{\mu L P_d}{A}, \quad (1)$$

where P_m and P_d are the mean pore fluid pressure and the downstream pressure, respectively, μ is the viscosity of the pore fluid, and L and A are the length and cross-sectional area of the plug, respectively. The data was used to check, and correct for, any fluid flow-related artefacts, namely the Forchheimer and Klinkenberg effects. The data were all corrected for the Forchheimer effect. Details of these corrections can be found in Heap et al. (2017). Additionally, connected porosity was calculated of each plug using their bulk sample volume, measured using digital callipers, and their skeletal volume, measured using a helium pycnometer (AccuPyc II, manufactured by Micromeritics).

An orthomosaic image was also generated from outcrop Out-5 (Fig. 3-1C), using a DJI Phantom 4 UAV drone equipped with a built-in camera. Photos were acquired with an overlap of approximately 70%, and then processed in Agisoft Metashape® software. The orthomosaic helps to comprehend lateral variations in facies and permeability responses. Most permeability data were acquired from outcrop Out-5, where 40 vertical transects were distributed across the outcrop, aiming to capture all accessible outcrop levels and facies variabilities.

Additionally, qualitative and quantitative descriptions were conducted on twelve thin-sections acquired from four different outcrops (Fig.3-1C), to complement the sedimentology and permeability data. Seven of them were sampled in the same sand

bodies, or as close as possible, as where plug samples were collected. Quantification of the primary composition, diagenetic constituents, and different types of porosity was conducted by counting 300 points perpendicular to sedimentary bedding, from each thin-section, on a moving stage within the software Petroledge® (De Ros et al., 2007). Modal grain sizes were determined by measuring c. 20 grains in each quadrant of the objective lens using the eyepiece reticle, then dividing the sum of the measurements by four. Sorting was defined using the visual comparators presented by Jerram (2001), which enables to estimate the graphic standard deviation (φ) classes defined by Folk and Ward (1957). Packing was calculated following Kahn (1956), by counting the percentage of grain-grain contacts that occur in a total of 100 grains limits, in a transect line perpendicular to the bedding. Photomicrography was captured using the Zeiss AXIO Lab A1 microscope. Thin-sections provide insights into the factors governing porosity distribution at a micro-scale, assisting in the permeability data analysis (e.g. Moraes and De Ros, 1990; Paxton et al., 2002; Morad et al., 2010; Busch et al., 2022).

This study follows the logic proposed by Chandler et al. (1989) regarding reservoir-heterogeneity hierarchies for aeolian systems, which is herein also applied to the fluvial deposits. The authors defined 1st order heterogeneity as the contact between aeolian and non-aeolian facies associations; 2nd order heterogeneity as the contact between aeolian dunes and aeolian sand sheet deposits, which herein is also applied to contacts between facies within the fluvial channel f.a.; 3rd order for heterogeneities related to internal arrangements within individual cross-sets; and 4th order heterogeneities related to pore-throat size and geometry. In this study, the analysis is mainly focused on the facies association scale (1st order), and the facies scale (2nd order).

Given the non-gaussian distribution of the permeability data, values are presented as the median for each sedimentary category, as the mean is more sensible to extreme values. However, mean values are also included in the tables.

3.4. RESULTS

The large range of values for each dataset population (Tables 3-2, -3, and -4) is interpreted as the consequence of higher order heterogeneities (3rd and 4th order) (sensu Chandler et al., 1989), related to local variations in grain size, sorting, cementation, and clay content, which may not be visually detectable in the field.

Additionally, different outcrops may experience distinct weathering effects that increase the variance of permeability values when data from all outcrops are grouped.

Ten measurements from outcrops recorded permeability values outside the range indicated by the manufacturer of the TinyPerm3, of which eight (0.7% of the total) were below 1 mD and two (0.2% of the total) were above 10000 mD. All measurements below the range were acquired in facies HSS, and the two above were acquired from facies AD and Ss.

3.4.1. Permeability at a facies association scale

A total of 972 permeability measurements were acquired for the fluvial channel f.a., recording a median value of 1292.7 mD (Table 3-2; Fig. 3-3A). The wind- and water-laid f.a. includes 147 measurements, exhibiting a median permeability of 176.4 mD (Table 3-2; Fig. 3-3A). The wind- and water-laid f.a. was slightly oversampled, as shown in Table 3-2, by comparing the proportion of each facies association thickness (Bofill et al., 2024) with the proportion of permeability measurements acquired in each facies association. This oversampling is due to the smaller spacing between each measurement (~ 5 cm), as a consequence of the limited thickness (decimetre scale) of these deposits. Additionally, most outliers removed from the analysis were measured in the fluvial channel f.a., contributing to the oversampling. The 95% confidence interval confirmed the fluvial channel f.a. and the wind- and water-laid f.a. as two statistically different populations of permeability. The overall permeability results at the facies association scale are presented in Table 3-2.

Table 3-2: Descriptive statistics of permeability results in a facies association scale. LGV = Lower Grès Vosgien Formation.

	Fluvial channel f.a.	Wind- and water-laid f.a.
Median (mD)	1292.7	176.4
Mean (mD)	2143.1	1133.4
Min (mD)	1.1	0.4
Max (mD)	10270.4	10405.4
Dataset (samples)	972	147
number/total dataset	87%	13%
% of the total LGV thickness (Bofill et al., 2024)	93%	7%

3.4.2. Permeability at a facies scale

Aiming to understand sedimentary processes that may control higher orders of heterogeneity (sensu Chandler et al., 1989) than those observed between facies

associations, the following sections present whether the main facies within each facies association exhibit distinct permeability distributions.

3.4.2.1. Fluvial channel facies association

In the fluvial channel facies association (f.a.), on the facies scale, facies St (Fig. 3-2) recorded a median permeability value of 2222.9 mD (Table 3-3; Fig. 3-3B), facies Ss (Figs. 3-2B and -2F) exhibited a median permeability of 1425.1 mD (Table 3-3; Fig. 3-3B), and facies Sl (Figs. 3-2C and -2F) showed a median permeability of 554.1 mD (Table 3-3; Fig. 3-3B). To analyse whether differences in permeability per facies are related to granulometric differences between them, only medium-grained sandstone facies are compared (Table 3-3). In this case, facies St recorded a median permeability value of 1693.4 mD, facies Ss exhibited a median permeability of 1917.8 mD, and facies Sl showed a median permeability of 455.8 mD. The results show that despite being in the same granulometric class range, facies Sl was characterised by a permeability more than three times lower than facies St and Ss. However, the permeability differences between facies St and Ss were lower, suggesting that granulometry controlled the permeability differences recorded between these two facies. In both scenarios of granulometry analysed, the 95% confidence interval indicates that the permeability of facies St and Ss facies are not statistically different. Conversely, the 95% confidence interval confirmed the permeability of facies Sl as statistically different from facies St and Ss.

Facies Sl has intentionally been oversampled, as evidenced by the high proportion of samples compared to its thickness proportion in the LGV (Table 3-3), to confirm whether the lower permeability values were consistent across different outcrops and levels within the vertical sections.

Table 3-3: Descriptive statistics of permeability results, in a facies scale, of the fluvial channel facies association. LGV = Lower Grès Vosgien Formation; St = facies trough cross-bedded sandstone; Ss = facies sigmoidal cross-bedded sandstone; Sl = facies low-angle cross-bedded sandstone.

	All dataset			Medium grained facies		
	St	Ss	Sl	St	Ss	Sl
Median (mD)	2222.9	1425.1	554.1	1693.4	1971.8	455.8
Mean (mD)	2859.3	2120.4	1241.6	2537.7	2427.5	1100.7
Min (mD)	1.1	22.1	3.1	1.3	22.1	3.1
Max (mD)	10270.4	8919	8864.7	8267.6	8751.6	8864.7
Dataset (samples)	445	178	349	224	119	277
number/total dataset	46%	18%	36%	36%	19%	45%
% of the total LGV thickness (Bofill et al., 2024)	74%	13%	13%			

Permeability data related to different classes of gravel content presented in Table 3-1 are also analysed (Fig. 3-4A). Sandstones without gravel (WG) recorded the lowest permeabilities, with a median value of 199.4 mD; followed by sandstones apparently without gravel (AWG), with a median value of 902.2 mD; and slightly gravelly sandstone (SG) with a median value of 1771.2 mD. Gravelly sandstones (GS) did not follow the same trend, recording lower permeability than SG, with a median value of 1076.9 mD. However, the GS has been under-sampled, as only 18 measurements (6% of the total), despite it representing 17% of the total thickness of fluvial channel f.a. (Bofill et al., 2024). The 95% confidence interval analysis indicates the classes WG, AWG, and SG, as statistically distinct in terms of permeability populations, and the GS as not statistically different from the WG and AWG, confirming the under-sampling of the class GS.

3.4.2.2. Wind- and water-laid facies association

Regarding the wind- and water-laid facies association (f.a.), 48 permeability measurements were performed in aeolian dunes (AD), with a median value of 2089.4 mD (Table 3-4; Fig. 3-3C), and 99 measurements were acquired in the hybrid sand sheet (HSS), recording a median permeability of 55.6 mD (Table 3-4; Fig. 3-3C). The permeability difference between AD and HSS is expressed by the bimodal distribution of the wind- and water-laid f.a. permeability data (Fig 3-3A). The confidence interval indicates that facies AD is not statistically different from the fluvial facies St and Ss.

The HSS has been oversampled as indicated by the high proportion of measurements compared to its thickness proportion (Table 3-4). This results from the smaller spacing between measurements (c. 5 cm) associated with its predominance in terms of occurrences (Bofill et al., 2024). The HSS showed a bimodal distribution of permeability (Fig 3-3C). This is interpreted as permeability differences between the millimetre- to centimetre-scale interdigitated facies that were grouped in the HSS, as indicated in Section 3.2.1., which facies deposited in dry conditions would record higher permeability than facies deposited in wet or damp depositional surfaces (e.g. Chandler et al., 1989).

Table 3-4: Descriptive statistics of permeability results within the wind- and water-laid facies association. LGV = Lower Grès Vosgien Formation.

	Aeolian dune (AD)	Hybrid sand sheet (HSS)
Median (mD)	2089.4	55.6

Mean (mD)	3120.9	169.7
Min (mD)	21.5	1.4
Max (mD)	10405.4	976.1
Dataset (samples)	48	147
number/total dataset	33%	67%
% of the total LGV thickness (Bofill et al., 2024)	60%	40%
% of the total LGV occurrences (Bofill et al., 2024)	43%	57%

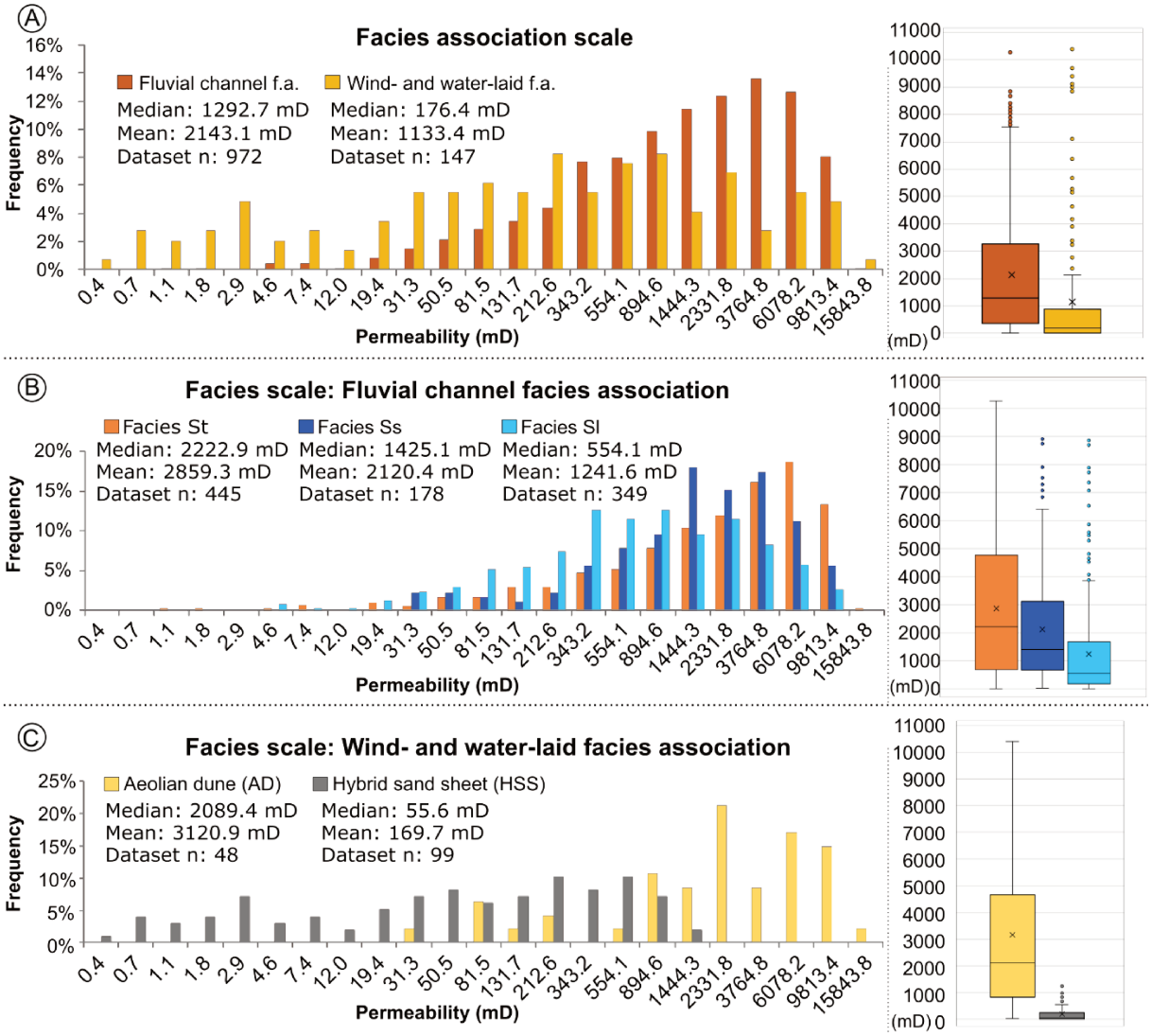


Figure 3-3: Distribution of outcrop permeability data based on facies association (f.a.) and facies scale. (A) The highest permeability values are related to the fluvial channel f.a. The wind- and water-laid f.a. present a bimodal distribution of permeability. (B) In facies scale, the highest permeability values of the fluvial channel f.a. are related to the facies St, followed by facies Ss. Facies Sl consistently presented the lowest permeability values in the fluvial channel f.a. (C) In the wind- and water-laid f.a. the highest permeability values are related to aeolian dunes, and the hybrid sand sheets recorded the lowest values. The hybrid sand sheets show more than one mode of values, indicating permeability heterogeneity in a smaller scale influencing permeability values distribution.

A common characteristic of the HSS, both in outcrops and in the core, is its bleached appearance (Figs. 3-2D, -2E, and -2F). Bleached zones, which lose the red-

bed appearance and become light-coloured, are predominantly associated with facies recording low permeabilities (Fig. 3-4B), despite often being attributed to zones with higher porosity and permeability (e.g. Newell et al., 2019; Schmidt, 2020; Busch et al., 2022).

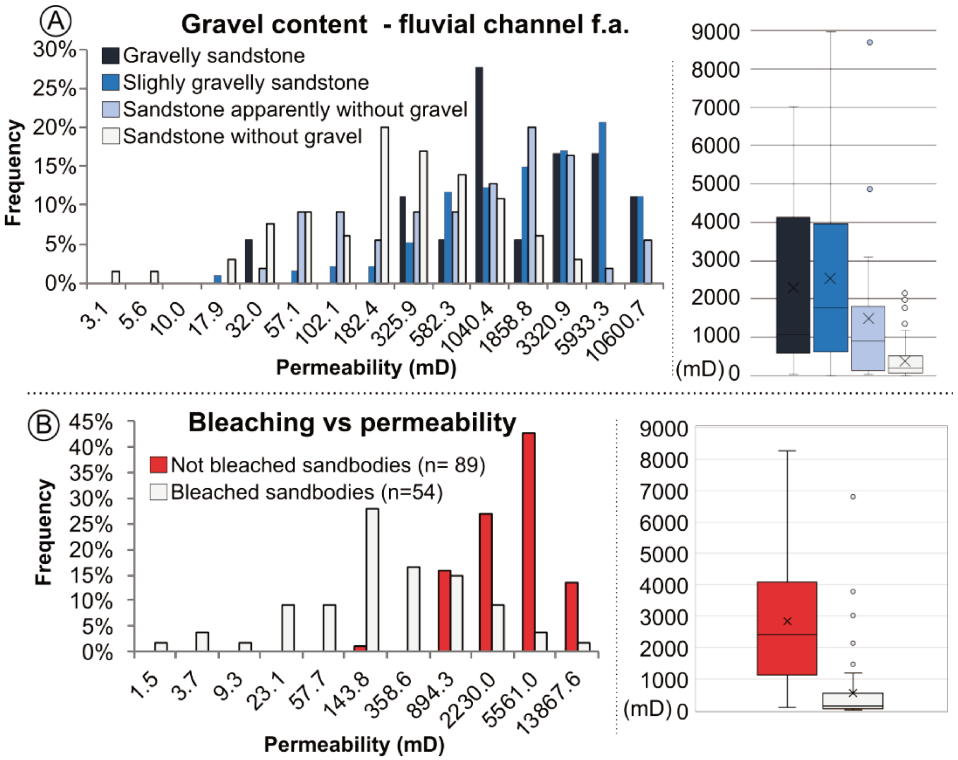


Figure 3-4: (A) Permeability responses based on the different classes of gravel content in the fluvial channel f.a. The highest permeability values were measured in gravelly sandstones (GS) and slightly gravelly sandstones (SG), and the lowest permeability values measured in sandstones without gravel (WG), and sandstones apparently without gravel (AWG); (B) Permeability responses in bleached sand bodies. Bleached sandstones recorded the lowest permeability values.

3.4.3. Outcrop scale vertical trends

The results presented above compile datasets from seven outcrops, indicating regional patterns that may incorporate local effects such as distinct weathering and diagenetic processes/stages. Thus, in this section, permeability is presented by individual outcrops as continuous vertical logs, tied with sedimentological logs, to visualise how permeability evolves with facies and facies association variations.

Vertical profiles highlight permeability contrasts reaching up to four orders of magnitude between the fluvial channel f.a. and the wind- and water-laid f.a. (Fig. 3-5). This is observed across outcrops that are up to 21 km apart from each other (Fig. 3-5). Such contrasts occur mainly due to the dominant occurrence of HSS at the base of

the wind- and water-laid f.a. (Figs. 3-5, -6B, -6D), as presented in Bofill et al. (2024). Moreover, within facies association, the vertical permeability profiles also respond to facies variability, with permeability contrasts reaching 2 orders of magnitude between facies (Fig. 3-5, -6C, and -6D).

Local contrasts of permeability that do not follow facies variations (e.g. Out-3 and Out-4 in Fig. 3-5) suggest heterogeneities that are not being captured by the scale applied in this study, such as variations in grain sizes across individual laminae (e.g. Hossain, et al., 2024) that could potentially result in changes in permeability by two orders of magnitude (Chandler et al., 1989).

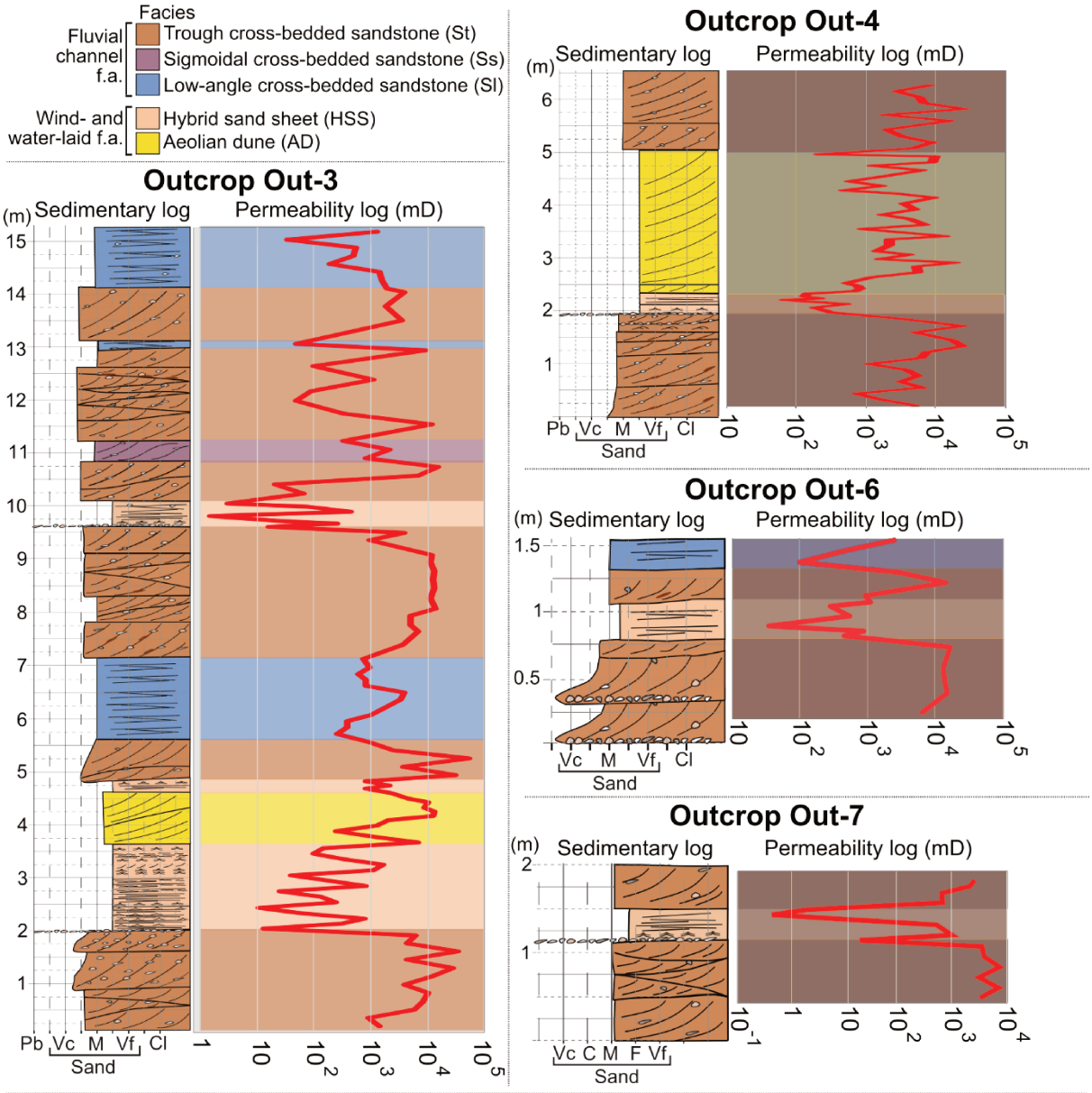


Figure 3-5: Permeability logs tied with sedimentary logs from different outcrops (locations shown in Fig. 3-1), showing permeability responses to facies and facies associations variations. St = facies trough cross-bedded

sandstone; Ss = facies sigmoidal cross-bedded sandstone; Sl = facies low-angle cross-bedded sandstone; HSS = hybrid sand sheet; AD = aeolian dune.

Vertical profiles alone are insufficient for heterogeneity analysis of fluvial deposits, given its inherent complex lateral facies variations (Miall, 1988). Thus, the use of orthomosaic images allows the comprehension of lateral facies and facies associations distribution (Fig. 3-6A), which confirms the lateral continuity of permeability responses associated with facies variations (Fig. 3-6B and -6C). The wind- and water-laid f.a. predominantly extends laterally beyond the outcrop width (hundreds-of-metre scale) (Bofill et al., 2024). Facies Ss and Sl mainly occur as isolated lenses with their main axis reaching tens-of-metre scale (Bofill et al., 2024); extending at times laterally beyond the outcrop width (Fig. 3-6A).

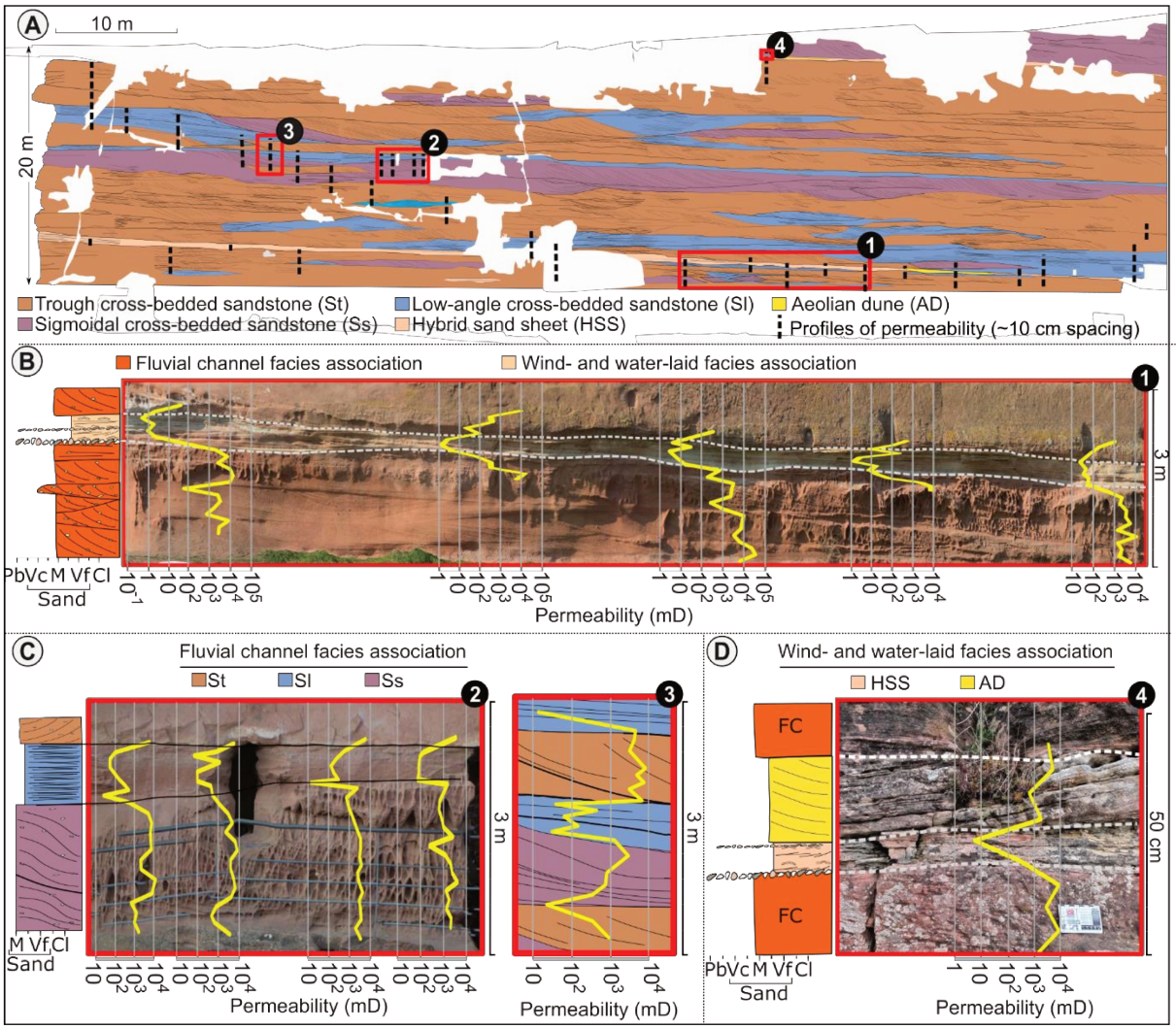


Figure 3-6: Outcrop scale of lateral facies and facies association distribution, combined with permeability logs. (A) Architectural analysis of the outcrop Out-5. (B) Facies association analysis showing consistent lower permeability, up to 4 orders of magnitude, in the WWL f.a. (C) Permeability contrasts following variation of facies within the

fluvial channel f.a. (D) Layer of hybrid sand sheet generating a permeability contrast 3 orders of magnitude smaller compared to facies below and above.

3.4.4. Measurements of permeability in the laboratory

Results from the thirteen plug samples show permeability values in the same range as field permeameter measurements, following the same trends observed in the field permeability data. A decrease in permeability values is observed from the AD, facies St, facies Ss, facies Sl, and HSS, respectively (Table 3-5). Additionally, the connected porosity of the same samples was measured, showing a direct relationship with permeability (Table 3-5), as expected for sandstones (e.g. Bourbie and Zinszner, 1985; Høimyr et al., 1993; Nelson, 1994; Aigner et al., 1996; Thompson et al., 2019; Quandt et al., 2022). The highest mean connected porosity is recorded in the AD, followed by facies St, Ss, Sl, and HSS (Table 3-5), respectively.

Table 3-5: Mean permeability and connected porosity per facies, measured in the laboratory. St = facies trough cross-bedded sandstone; Ss = facies sigmoidal cross-bedded sandstone; Sl = facies low-angle cross-bedded sandstone; AD = aeolian dune; HSS = hybrid sand sheet.

	AD	St	Ss	Sl	HSS
Average permeability (mD)	8060.4	4671.1	3195.1	1894.8	5.3
Average connected porosity (%)	32	28	26	25	12

3.4.5. Petrographic characteristics

Petrographic analysis was conducted on 12 thin-section samples to comprehend the main differences between the facies at the micro-scale. The dataset comprises seven samples of facies from the fluvial channel f.a. (five St, and two Sl), and five samples of the wind- and water-laid f.a. (three of the AD, and 2 of the HSS). It should be emphasized that this section focuses on evaluating the aspects controlling the different permeability responses, rather than presenting a detailed quantitative analysis of petrographic characteristics.

The original composition of the LGV sandstones did not record significant changes after diagenesis. Both their original and present compositions are characterised as feldspathic litharenite and sublitharenite (Fig. 3-7). Lithoclasts are predominantly represented by low-grade metamorphic rocks, followed by fragments of volcanic and sedimentary rocks.

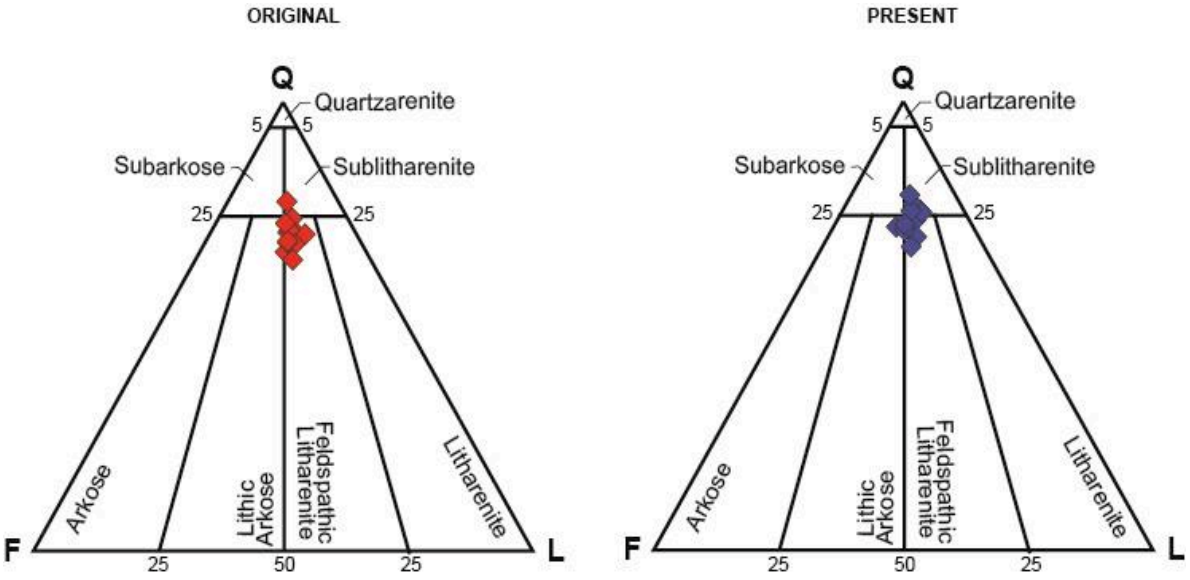


Figure 3-7: Original (red symbols) and present (blue symbols) composition of the Lower Grès Vosgien Formation sandstones samples plotted on Folk (1968) diagram, showing that not significant composition changes happened during diagenesis. The original primary composition was weakly modified by the transformation of lithoclasts to lithic pseudomatrix.

The main diagenetic process observed occurred during eodiagenesis, primarily represented by mechanical compaction, infiltration of clays, formation of lithic pseudomatrix, and quartz overgrowth, respectively (Fig. 3-8 and Fig. 3-9).

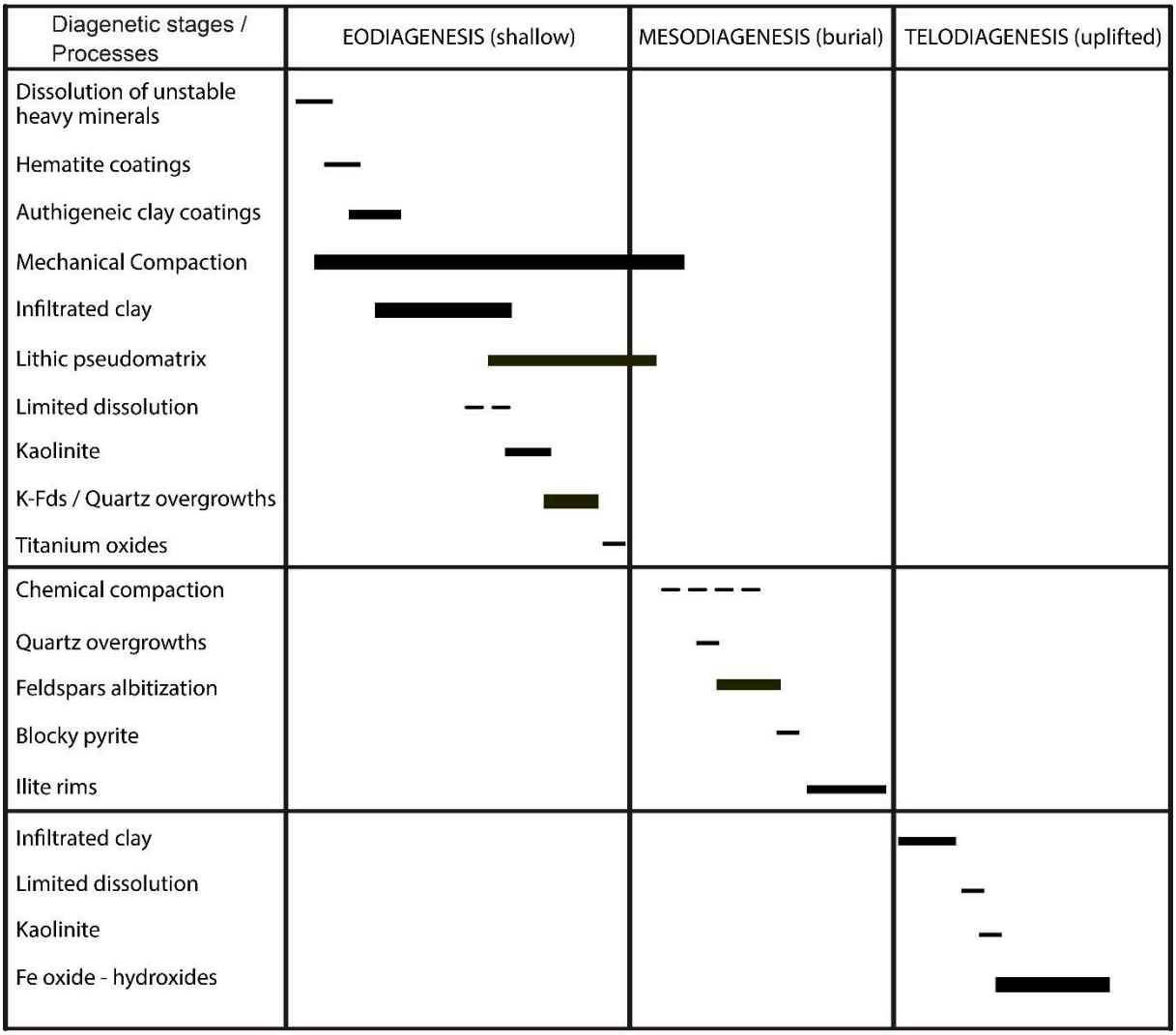


Figure 3-8: Schematic diagenetic sequence for the analysed sandstones from the Lower Grès Vosgien Formation. Thick bars represent intense processes, thin and dashed lines progressively less prominent processes. The figure highlight eodiagenetic compaction as the main diagenetic process, followed by clay infiltration and formation of lithic pseudomatrix, both during eodiagenesis.

The textural characteristics of the sandstones did not present significant variations between the samples. The modal grain size measured from facies St present an average value of 0.43 mm, while facies Sl has an average of 0.28 mm. The AD and the HSS samples recorded average modal grain sizes of 0.41 and 0.2 mm, respectively. Thus, only the HSS samples did not fall within the class of medium-grained sandstone (Fig. 3-10A), in agreement with the field descriptions. The graphic standard deviation (φ) (Folk, 1980) is used to classify sediment sorting. Facies St recorded a mean φ of 0.7 (moderately well sorted), and facies Sl a φ of 0.65 (moderately well sorted). Concerning the wind- and water-laid facies association, the

AD recorded a mean φ of 0.7 (moderately well sorted), while the HSS had a mean φ of 0.83 (moderately sorted) (Fig. 3-10B).

In terms of primary composition, grains that experienced ductile deformation, primarily represented by low-grade metamorphic rock lithoclasts (Fig. 3-9A), significantly influence permo-porosity variations. Herein, these grains are termed ductile grains. In the fluvial channel f.a., facies St recorded an average of 4% of ductile grains, and facies Sl recorded an average of 6.3% (Fig. 3-10C). In the wind- and water-laid f.a., the AD presented an average of 3.5% of ductile grains, while the HSS recorded 6.7% (Fig. 3-10C).

Given that ductile grains tend to be squeezed into pore-spaces during compaction (Fig. 3-9A), the percentage of ductile grains (Fig. 3-10C) are directly related to the packing degree (Fig. 3-10D) and with the percentage of lithic pseudomatrix (Fig. 3-10E). Samples of facies St recorded an average packing of 52% (Fig. 3-10D), while facies Sl had an average packing of 59% (Fig. 3-10D). The AD exhibited an average packing of 53%, while the HSS showed an average of 94% (Fig. 3-10D). Regarding lithic pseudomatrix (Fig. 3-10E), facies St recorded an average of 0.3%, facies Sl an average of 1.7%, the AD had 0% pseudomatrix, and the HSS had an average of 3.2% pseudomatrix.

Infiltrated clay constitutes the main diagenetic constituent (Table 3-6), often covering grains as discontinuous coating with irregular thickness, or as microcrystalline aggregates filling intergranular porosity (Fig. 3-9B). Mechanical clay infiltration, resulting from the seepage of muddy waters through coarser sediments (Moraes and De Ros, 1990), predominantly occurred during eodiagenesis, although less expressive telodiagenetic clays are also present (Fig. 3-8). The percentage of mechanically infiltrated clay did not exhibit significant differences among the fluvial facies, with facies St recording 6%, and facies Sl 5.2% (Fig. 3-10F). However, within the wind- and water-laid f.a., the AD recorded 3.2%, and the HSS recorded 16.5% (Fig. 3-10F). Minor occurrences of kaolinite, authigenic clay coatings, and illite also contribute to the total clay percentage (Table 3-6, Fig. 3-8, and -10F).

The overgrowth of quartz is the second most abundant diagenetic constituent (Table 3-6), which primarily occurred during eodiagenesis, as a syn-compaction constituent. Minor occurrences of pre-compaction quartz overgrowth are observed.

The syn-compaction quartz overgrowth reduces the volume and connectivity of the pores (Fig. 3-9D). Conversely, the pre-compaction quartz overgrowth protects intergranular porosity against compaction effects (Fig. 3-9C), as previously observed in the region (e.g. Busch et al., 2022; Quandt et al., 2022). Facies St recorded an average of 2.7% quartz overgrowth, while Facies Sl recorded an average of 1.7% (Fig. 3-10G). In the wind- and water-laid f.a., the AD recorded 2.6%, and the HSS 0.8% (Fig. 3-10G). The inverse relationship between the percentage of quartz overgrowth and clay content (Fig. 3-10F and -10G) is expected, given that the presence of clay coating inhibits the overgrowth of quartz (Moraes and De Ros, 1990).

Table 3-6: Diagenetic constituents and their respective percentages.

Digenetic constituents	**Average (%)**	**Maximum (%)**
Infiltrated clay	7.2	19.3
Quartz overgrowth	2.3	5
Microcrystalline albite	1.6	3.7
Kaolinite	1.3	3
Authigeneic clay coatings	1.1	3.7
Hematite coatings	1.1	2
Lithic pseudomatrix	1	3.3
Illite rims	<1	3
K-feldspars overgrowth	<1	1.7
Titanium oxide	<1	0.7
Blocky pyrite	<1	0.3
Microcrystalline jarosite	<1	0.3

The porosity is predominantly composed of intergranular pores (Fig. 3-9E). Compaction reduces the throats between the pores, affecting their connectivity. In the fluvial channel f.a., facies St recorded an average porosity of 16%, and facies Sl an average of 11% (Fig. 3-10H). In the wind- and water-laid f.a., the AD recorded an average porosity of 17%, and the HSS an average of 2% (Fig. 3-10H). The porosity values measured in thin-sections follow the same patterns as connected porosity measured in plug samples (Table 3-5). However, porosity measured in thin-sections systematically presented lower absolute values compared to porosity measured in the laboratory on the plugs. This can be explained by the presence of micropores that are difficult to identify under the petrographic microscope (Wu et al., 2018).

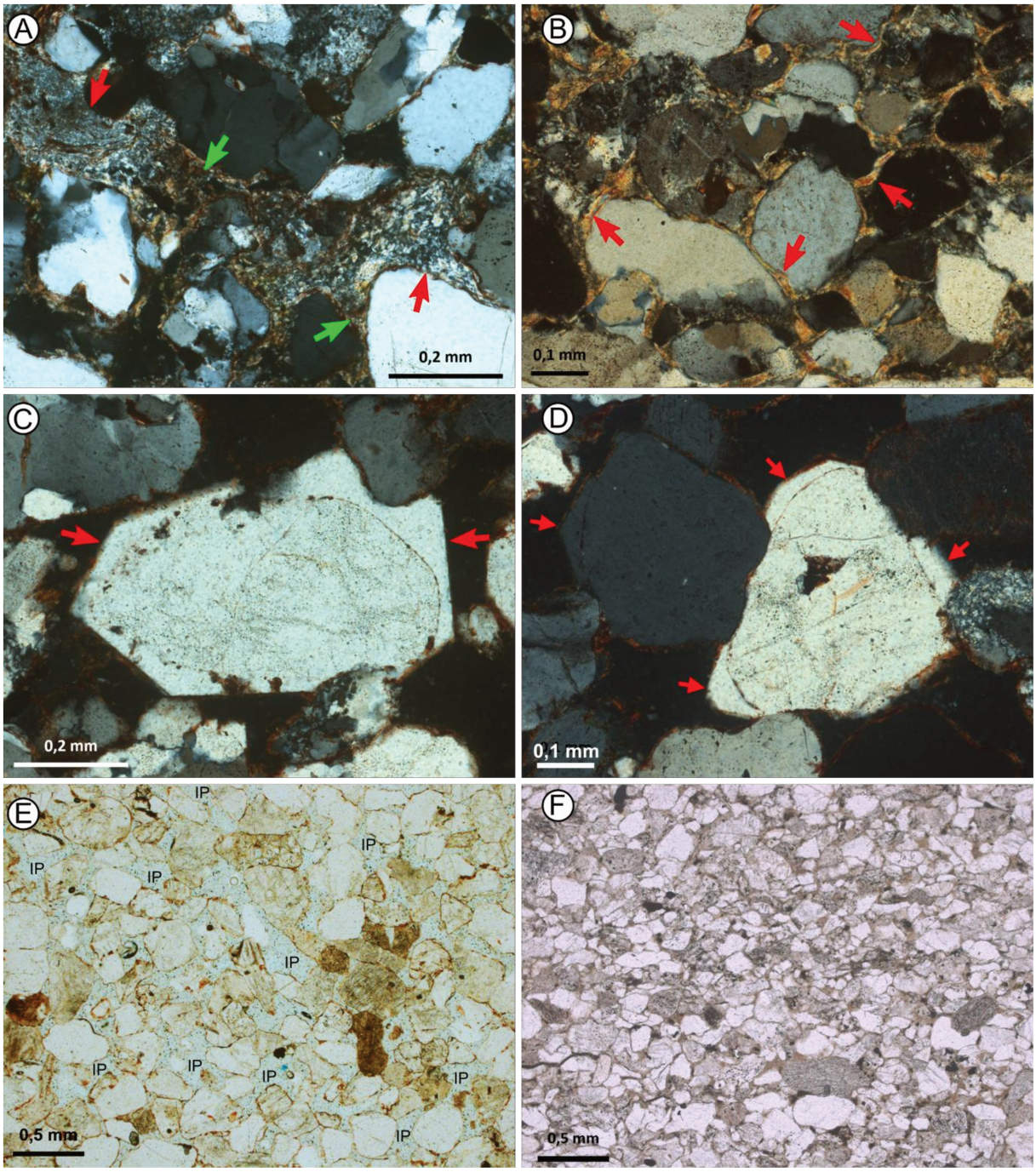


Figure 3-9: (A) Facies Sl with ductile lithoclasts of low-grade metamorphic rocks (red arrow); and lithic pseudomatrix (green arrows). (B) Compacted hybrid sand sheet, with abundant infiltrated clay (red arrow). (C) Pre-compaction quartz overgrowth (red arrows) stabilising the framework in facies St. (D) Syn-compaction quartz overgrowth (red arrows) filling intergranular porosity in facies St. (E) Intergranular porosity (light blue zones marked with IP) in aeolian dune. (F) Highly compacted fabric in hybrid sand sheet.

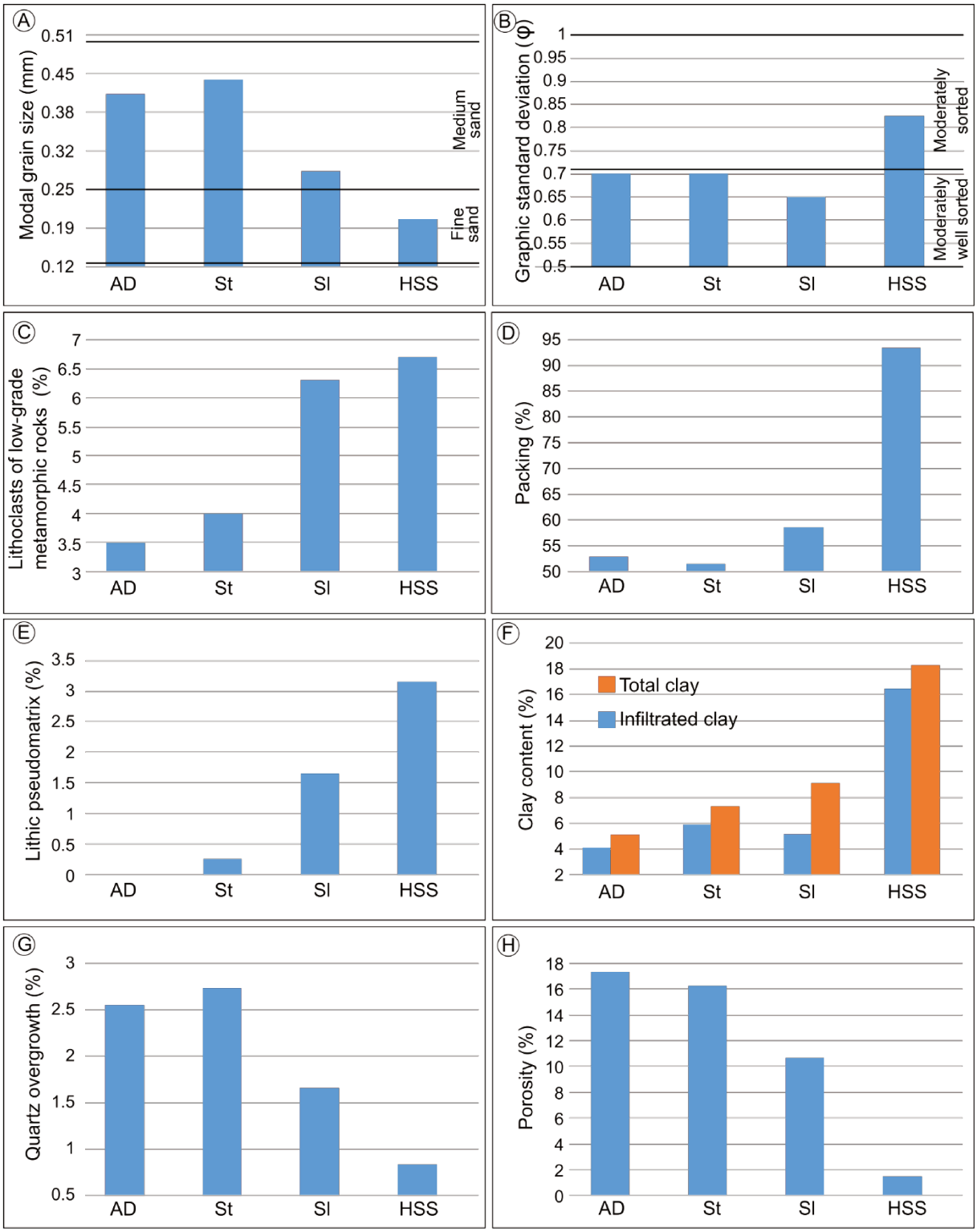


Figure 3-10: Mean values of petrographic characteristics observed per facies. From the left to the right, in the x-axis, the mean and median permeability values of each facies decrease (AD >Ss>Sl>HSS). (A) Variations of grain sizes among facies; (B) sorting degree based on graphic standard deviation (Folk, 1980); (C) percentage of ductile grains, mainly represented by low-grade metamorphic rocks, (E) lithic pseudomatrix formed by the squeeze of lithoclasts during compaction; (D) packing degree. (F) clay content, mainly represented by infiltrated clay; and (G) quartz overgrowth. All these characteristics contribute to compaction, which is the main diagenetic

process affecting permeability and (H) porosity. St = facies trough cross-bedded sandstone; Sl = facies low-angle cross-bedded sandstone; AD = aeolian dune; HSS = hybrid sand sheet.

3.5. DISCUSSION

The positive correlation between grain size and permeability is well documented (e.g. Chandler et al., 1987; Fisher et al., 1992; Høimir et al., 1993; Makeen et al., 2021; Scorgie et al., 2021; Quandt et al., 2022; Wadsworth et al., 2023), as is the influence of detrital composition on reservoir quality (e.g. Moraes and De Ros, 1990; Dutton et al., 2012; Bjørlykke, 2014; Makeen et al., 2021; Castro et al., 2023). Understanding primary sedimentary processes, sand body geometries, and architectures enhance the prediction of the distribution of such characteristics (e.g. Chandler et al., 1987; Alexander, 1993; Dreyer, 1993; Høimir et al., 1993; Rogiers et al., 2013; Weissmann et al., 2015; Thompson et al., 2019; Aberg et al., 2021). In the Lower Grès Vosgien Formation (LGV) different degrees of compaction were directly controlled by the percentage of lithoclasts and eodiagenetic mechanical clay infiltration, indicating that primary sedimentary processes governed the diagenesis.

Although the wind- and water-laid f.a. represents only 7% of the total thickness of the LGV, its lateral extent is generally greater than the maximum width of individual outcrops (hundreds of metres). This, coupled with the common contrast of up to four orders of magnitude between the fluvial channel f.a. and the wind- and water-laid f.a. (Figs. 3-5, -6B, -6D, and -11), highlights the need to distinguish between both facies associations in aquifer and reservoir conceptual models. Although it is common to observe aeolian deposits preserving higher porosity and permeability values than fluvial deposits (e.g. Cowan, 1993; Fischer et al., 2007; Bjørlykke, 2014; Heidsiek et al., 2020; Quandt et al., 2022), caution should be taken when exploring this concept to aeolian deposits influenced by water-related processes, as seen in the wind- and water-laid f.a. This facies association is potentially responsible for reservoir compartmentalisation in the LGV. The fluvial channel facies association (f.a.) represents flow zones, whereas the wind- and water-laid f.a. represent levels of flow baffles or barriers. The upward increase in the frequency of wind- and water-laid facies associations recorded in the core (Bofill et al., 2024), and the consequent decrease in the thickness of the fluvial channel facies association, indicate that the upper section of the LGV records an increase in the intercalation frequency between flow zones and baffle/barrier zones.

At a facies scale, the low-angle (<15°) to horizontally stratified sandstones, such as facies Sl and the HSS, exhibited lower permeability values compared to those with steeper cross-bedding (e.g. facies St, facies Ss, and AD). The results suggest a positive correlation between the angle of stratification and permeability in both facies associations. Similar patterns have been previously observed for fluvial (e.g. Fisher et al., 1992; Hornung and Aigner, 1999) and aeolian deposits (e.g. Chandler et al., 1989; Goggin et al., 1992; Fischer, 2007; Heidsiek, 2020). These aspects are discussed in the following sections for each facies association.

Individual facies exhibited a wide range of permeability values, attributed to higher-order heterogeneity (Chandler et al., 1989), such as granulometric variations between individual laminae (e.g. Hossain et al., 2024) or differences in permeability and porosity between the base and top of a cross-bedded sandstone (e.g. Ghienne et al., 1994).

3.5.1. Fluvial flow-regime and permeability results

In the fluvial channel f.a., an inverse relationship exists between the fluvial flow-regime and permeability. Facies St, deposited under lower flow-regime conditions (Miall, 2006), exhibit the highest median permeability values. Facies Ss, deposited in the transition between upper and lower flow-regime (Røe, 1987), show slightly lower median permeability than facies St. Meanwhile, facies Sl, deposited under upper flow-regime conditions (Lang and Winsemann, 2013) record the lowest median permeability in this facies association.

In the fluvial channel f.a., the gravel content also exhibits an inverse relationship with flow-regime conditions, recording a strong correlation between facies and gravel content (Bofill et al., 2024). Moreover, there is a direct relationship between gravel content and median permeability values, where sand bodies with the lowest gravel content recorded the lowest median permeability (Fig. 3-4A).

The lower gravel content preserved in upper flow-regime deposits is explained by Bofill et al. (2024) as a result of the overpassing process (Allen, 1983), wherein gravels roll over a firm bed of close-packed sand grains under high shear-stress conditions (Allen1983; Carling, 1990), which may be related to flashy flood events (Allen, 1983). These closely packed sand grains, associated with slightly lower modal grain size (Fig. 3-10A), a higher percentage of lithoclasts of low-grade metamorphic rocks (Fig. 3-

10C), and a lower percentage of quartz overgrowth (Fig. 3-10G), are interpreted to have contributed to greater compaction and lower permeability in facies SI.

The opposite relationship between granulometry and fluvial flow-regime conditions, and consequently permeability responses, has been described by Aigner et al., 1996. Therefore, the relationship between fluvial flow-regime and granulometry is not straightforward, and thus should be analysed by individual case.

3.5.2. Sedimentology, architecture, and permeability of the wind- and water-laid facies association

In the wind- and water-laid f.a., although AD exhibits the most favourable reservoir characteristics (i.e. high porosity and high permeability), the HSS displays the lowest permeabilities recorded in the LGV. Primary sedimentary processes directly influenced the poor reservoir characteristics of the HSS, such as water table fluctuations, which increase the amount of mechanically infiltrated clays (Moraes and De Ros, 1990), and ephemeral floods responsible for carrying relatively poorly sorted sediments into the grains fabric (Fig. 3-10B). The reason for the higher percentage of ductile lithoclasts of low-grade metamorphic in the HSS is unclear.

The understanding of sedimentary architecture is crucial for determining whether petrophysical measurements conducted in specific facies can be generalised to the entire facies association and/or formation (e.g. Chandler, 1989). For instance, the wind- and water-laid f.a. typically preserves a thickness of ~45 cm (Bofill et al., 2024), wherein both AD and HSS may coexist. This underscores the importance of clarity regarding which sedimentary feature permeability is being sampled. For example, only 14% of the wind- and water-laid f.a. described by Bofill et al. (2014) are composed solely of AD, and the majority presented HSS deposits associated with it, as exemplified in figures 3-5 and 3-6. Bofill et al. (2024) identified the prevailing architectural pattern of the wind- and water-laid f.a. as comprising AD with HSS deposits occurring both above and below. Thus, whereas AD preserves the highest porosity and permeability, they preserve low connectivity potential.

3.5.3. Utility of outcrop data for subsurface predictions

Permeability data acquired from outcrops may not match with subsurface data due to their distinct diagenetic stages (e.g. Goggin et al., 1992; Busch et al., 2022;

Hossain et al., 2024). Carbonate cement has been reported only in core samples of the Buntsandstein Gr. in the Upper Rhine Graben (Busch et al., 2022), which is associated with a more advanced degree of compaction, record lower permeability (generally by two orders of magnitude) and porosity in subsurface compared to outcrop samples (Busch et al., 2022).

However, in the LGV, despite the different absolute permeability values between outcrops and subsurface samples, similar relative permeability trends are observed, such as (i) significantly lower permeability of the wind- and water-laid f.a. in comparison to the fluvial channel f.a. (Fig. 3-11A); (ii) permeability trend increasing from facies Sl, Ss and St, respectively, in the fluvial channel f.a. (Fig. 3-11B); (iii) significantly lower permeability of the HSS among all facies (Fig. 3-11C). Note that only a few AD has been recognised in the core within the studied section, thus it is considered as an under-sampled facies. The sedimentary log of the EPS1 well, along with the permeability logs (Fig. 3-12), exhibits similar patterns of facies control on permeability heterogeneity to those observed in outcrops (Figs. 3-5 and -6).

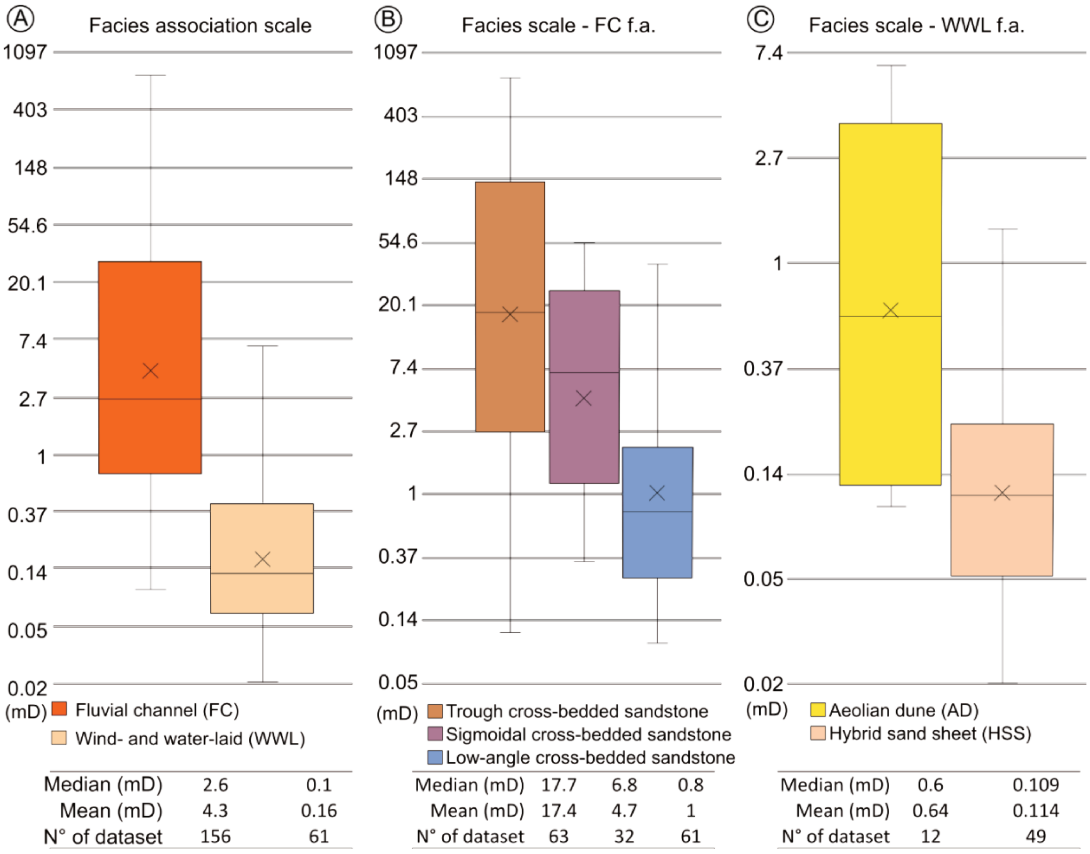


Figure 3-11: Log domain distribution of core permeability data: (A) facies association (f.a.) scale; (B) facies scale within the fluvial channel (FC) f.a.; (C) facies scale within the wind- and water-laid (WWL) f.a. Similar patterns of relative permeability between facies and facies association as observed in outcrops (Fig. 3-3). Rectangles

represent values between the 1st and 3rd quartile (Q1 and Q2), and dots represents individual samples which permeability value lies above 1.5 times the difference between Q1 and Q3 [1.5x(Q3-Q1)].

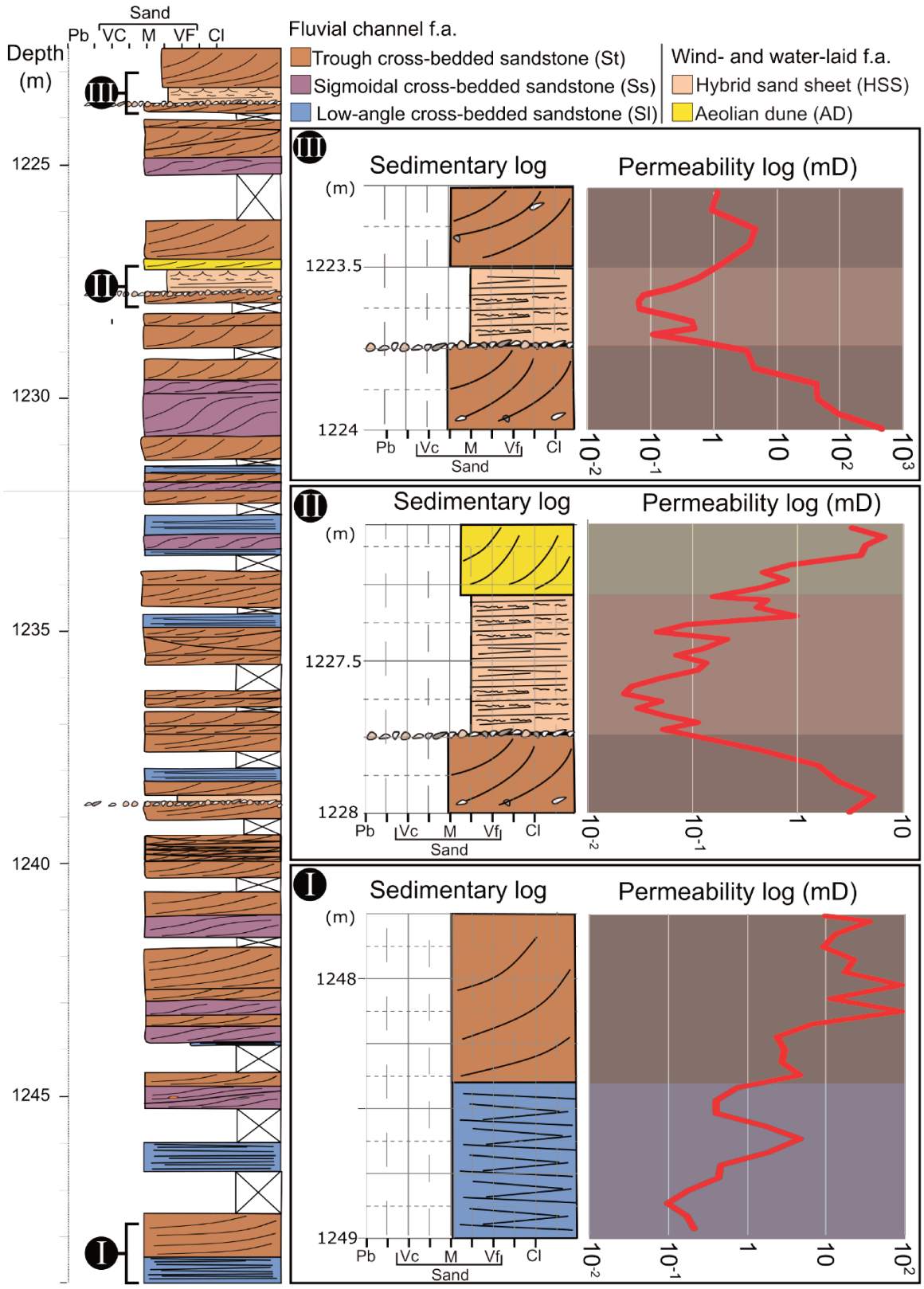


Figure 3-12: Permeability logs tied with sedimentary log from core samples. Similar trends as those observed in outcrop data of permeability response when transecting the distinct facies and facies associations (f.a.) (see Fig. 3-5).

The findings emphasise the importance of understanding quantitatively sedimentary facies architecture before interpreting petrophysical data. Haffen et al. (2013) indicated preferential flow zones by interpreting thermal gradient logs and associating them with porosity and permeability measurements in well EPS1. The authors highlighted fluvio-aeolian deposits as preferential fluid-flow pathways, and braided river deposits as relatively low permeability zones in the LGV. However, the absence of facies-scale control in the study introduces uncertainties, given that (i) it is not mentioned that these fluvio-aeolian deposits are highly compartmentalised due to the presence of laterally extensive and low permeability levels of wind- and water-laid facies associations; (ii) potentially high porosity and permeability measurements may be derived from poorly connected sand bodies, such as AD; and (iii) the nomenclature used is confusing since the fluvial channel facies associations were deposited by braided channels, which present relatively high permeability in these fluvial and aeolian intercalations. Thus, the association of braided river deposits with low permeability, as presented by the authors, is not supported by the measurements presented here. Finally, their findings related to preferential flow zones in the LGV might be more influenced by the local effect of fractures than by depositional environment controls.

Goupil et al. (2022) undertook a study involving permeability and porosity measurements on horizontally stratified facies identified in EPS1 well samples, which correspond to facies Sl and HSS. Their objective was to explore the anisotropy within the Buntsandstein Gr. deposits. While their work provides valuable insights into the anisotropy of horizontally stratified sandstones, it is important to note that facies Sl and HSS constitute only 12% and 3%, respectively, of the overall LGV thickness (Bofill et al., 2024), and display distinct compositional and diagenetic characteristics compared to the predominant facies St. Therefore, caution should be taken when upscaling the characteristics of facies Sl and HSS to the entire formation.

We highlight that the porosity-permeability trends for facies Sl and HSS from outcrops, and the data from Goupil et al. (2022) from borehole samples, are very similar (Fig. 3-13), suggesting consistency in the relationship between porosity and permeability across outcrop and subsurface, despite the differences in absolute values. In addition to the horizontally stratified sandstones, figure 3-13 also shows a larger dataset of permeability and porosity values for sandstone samples taken from well EPS1 across the Buntsandstein Group (data from Griffiths et al., 2016; Heap et

al., 2017; Kushnir et al., 2018, 2023). This dataset is not constrained by facies, nevertheless, the overall permeability and porosity relationship in outcrop agree with the subsurface (Fig. 3-13).

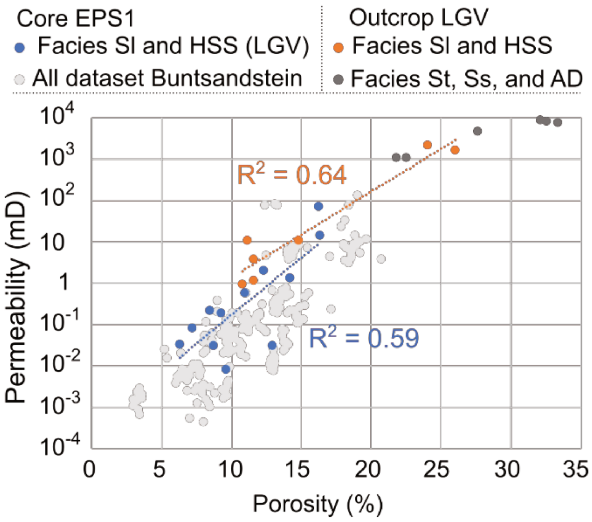


Figure 3-13: Permeability and connected porosity measured from plug samples from outcrops (data from this study; orange and dark grey symbols) and from core samples of the well EPS1 (data from Goupil et al., 2022; blue symbols). Also included are laboratory data for other sandstones from the Buntsandstein from EPS1 (data from Griffiths et al., 2016; Heap et al., 2017; Kushnir et al., 2018, 2023; light grey symbols). All data are gas permeability measurements collected under a confining pressure of 1 MPa. LGV = Lower Grès Vosgien Formation; St = facies trough cross-bedded sandstone; Ss = facies sigmoidal cross-bedded sandstone; Sl = facies low-angle cross-bedded sandstone; AD = aeolian dune; HSS = hybrid sand sheet.

Considering the usefulness of outcrops as reservoir analogues for the LGV, figure 3-14 presents a compilation of predictions based on sedimentology, petrophysics, and petrography data. A facies conceptual model is shown in figure 3-14A based on data from Bofill et al. (2024), where core samples from the well EPS1 provided the temporal (vertical) distribution of facies associations, and their respective facies, and outcrop data revealed their spatial (lateral) extension, geometries, and transitions. Such association between core and outcrop data improve reservoir facies modelling in braided fluvial deposits, where the applicability of spatial statistical methods is limited due to the numerous erosional and depositional processes associated with these systems (Castle et al., 2004). Outcrop and core samples exhibited a similar relationship between permeability heterogeneity and sedimentary depositional controlling factors, despite the distinct range of absolute permeability values between them. In the fluvial channel f.a., the controlling factor responsible for permeability heterogeneity was the variation in Froude-number within the braided channels, with higher Froude numbers generating facies with lower permeability (Fig. 3-14B). In the wind- and water-laid f.a.,

the depositional controlling factor was the distinct climatic conditions that enabled the accumulation of highly permeable AD in more arid conditions, and low-permeability HSS in more humid conditions (Fig. 3-14B). Finally, similar relationships between petrographic characteristics and permeability data observed in outcrops (Fig. 3-14C) are expected in subsurface.

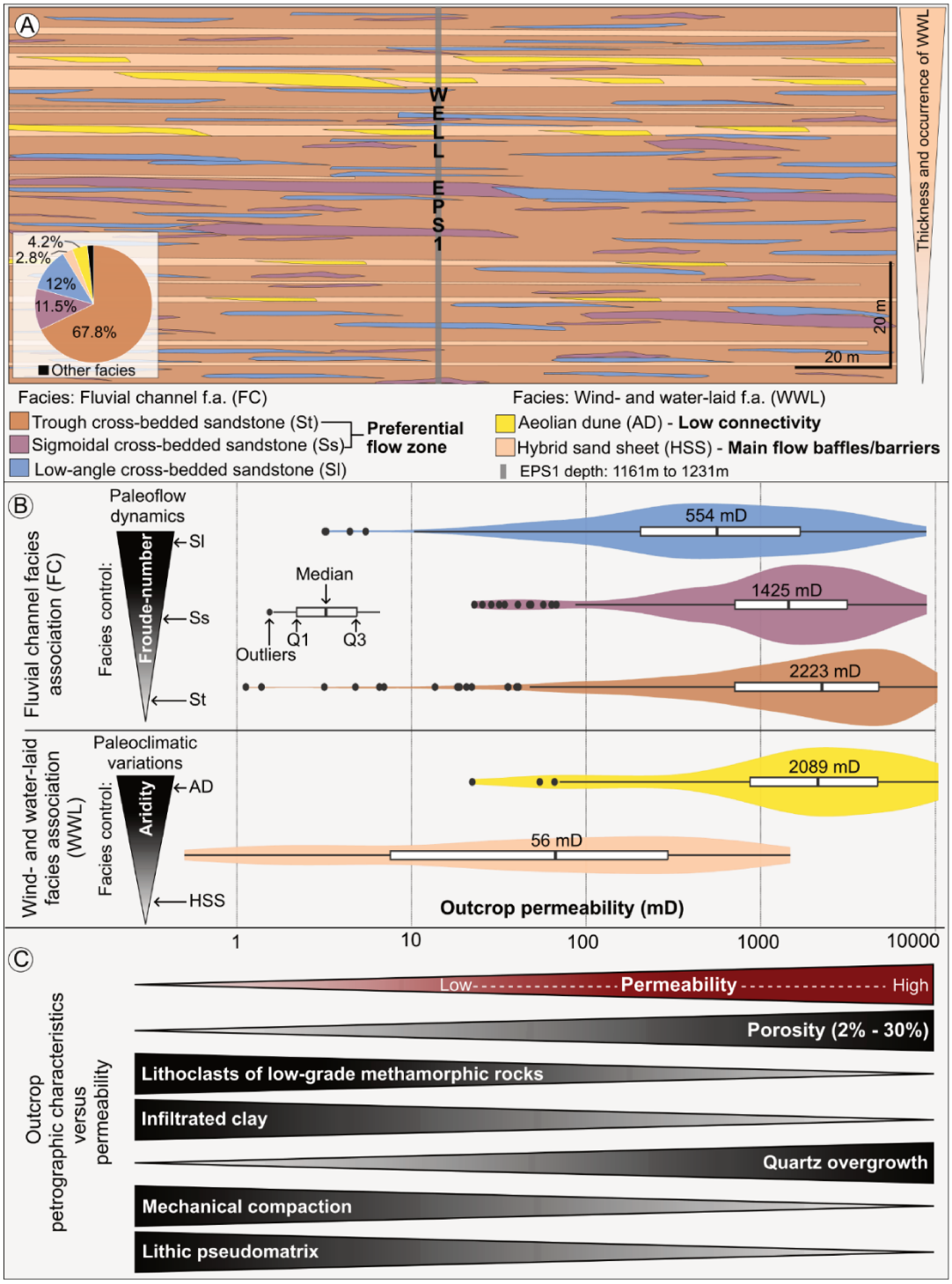


Figure 3-14: (A) Geological conceptual model of facies distribution in the upper part of the Lower Grès Vosgien Formation (LGV), based on the well EPS1, and outcrop data from Bofill et al. (2024); (B) compilation of the two

facies association in the LGV, their controlling factors of facies deposition, and permeability distribution per facies; (C) relationship between the permeability responses and the main petrographic characteristics.

3.6. CONCLUSIONS

This study investigates how primary sedimentary processes control the distribution of permeability heterogeneity in a fluvio-aeolian system, at the scale of facies and facies association, and whether heterogeneity measured from outcrops can be expected in subsurface at the Lower Triassic Buntsandstein Group, in the Upper Rhine Graben.

The distribution of permeability heterogeneity of sandstones of the Lower Grès Vosgien Formation (LGV) is directly influenced by the distinct sedimentary facies. In the fluvial channel f.a., the trough cross-bedded sandstone (St) exhibited the highest median permeability, followed by the sigmoidal cross-bedded sandstone (Ss), and the low-angle cross-bedded sandstone (Sl), respectively. Given that facies St was deposited under lower flow-regime conditions, facies Ss under transitional conditions from lower to upper flow-regime, and facies Sl deposited under upper flow-regime conditions, it suggests an inverse relationship between fluvial flow-regime and sand body permeability in the LGV.

The wind- and water-laid f.a. represents flow barriers or baffles within the LGV. Hybrid sand sheet (HSS) records the lowest permeabilities. Despite the presence of high-permeability aeolian dunes (AD) in this facies association, the dominant presence of low-permeability HSS associated with it indicates that AD has low connectivity potential.

Compaction is the primary diagenetic process affecting the permo-porosity of the LGV. Mechanical clay infiltration, lithic pseudomatrix formation, and quartz overgrowth also influence pore volume, size, shape, and connectivity. All the aforementioned diagenetic processes primarily occurred during eodiagenesis and affected each sedimentary facies differently, suggesting that despite the diagenetic overprint, primary sedimentary processes and architecture govern the distribution of permeability heterogeneity in the LGV.

Permeability data from outcrops show higher absolute values compared to subsurface data. However, similar porosity-permeability trends are observed between the same facies recognised in outcrops and borehole samples taken from the

geothermal well EPS1. Therefore, certain assumptions can be extrapolated from outcrop to subsurface in the LGV: i) HSS are laterally extensive low permeability deposits, and should be considered as potential flow barriers or baffles; ii) architectural analysis of outcrops revealed that highly permeable AD have low connectivity potential due to associated low permeability HSS; iii) fluvial deposits with significant facies variation, particularly when facies Sl is present, should be considered as more heterogeneous deposits.

4. Chapter 4: The significance of sedimentary facies heterogeneity in solute transport models: case study using an outcrop of the Lower Triassic sandstones aquifer, eastern France

ABSTRACT

Accurately representing subsurface sedimentary facies geometries in fluid-flow models is a critical yet challenging task in hydrogeology. Outcrop studies serve as valuable analogues for subsurface conditions, providing insights into the geometry and distribution of sedimentary facies that borehole data alone cannot offer. The aim of this study is to quantify the effect of decimetre- to metre-scale sedimentary features in sandstones into fluid-flow model results, such as on particles' residence time and macrodispersivity. The focus of this research is the Lower Grès Vosgien Formation in eastern France, an important aquifer for public supply water and lithium-rich geothermal brines; composed of sandstones deposited by braided fluvial and aeolian systems during the Lower Triassic.

A digital outcrop model, combined with quantitative sedimentary characterisation and permeability distribution, is used to develop a realistic vertical 2D hydrogeological conceptual model. The same discretises sedimentary facies with their associated hydraulic conductivity characteristics. The objective is to comprehend the effects of observed heterogeneity on fluid-flow modelling results, including the breakthrough curve of particles' residence time, longitudinal macrodispersivity, and upscaled anisotropy. These effects are then quantified across five progressively simplified hydrostratigraphic conceptual models.

Longitudinal macrodispersivity is calculated using temporal moments analysis. Results indicate that discretisation between two facies associations significantly impacts both horizontal and vertical flow concerning particles' residence time. Macrodispersivities are mainly affected when permeability data is distributed not constrained by the geometries of the sedimentary features. For horizontal flow, failing to discretise individual sedimentary facies results in underestimating preferential flow zones, impacting the prediction of the first particle arrivals, and highlighting potential inefficiencies in groundwater contaminant remediation plans. The long tailing observed in particles' residence time distribution suggests that Fickian concepts cannot describe

macrodispersion for the model domain. Moreover, discretisation between distinct facies associations—fluvial channel and wind- and water-laid facies—generates an upscaled anisotropy (Kv/Kh) of 0.3, demonstrating the significant role of sedimentary heterogeneity in hydrogeological modelling.

4.1. INTRODUCTION

The representation of subsurface sedimentary facies in fluid-flow models carries inherent uncertainties due to the complex spatial variability of sedimentary deposits (Miall, 1988; Høimyr et al., 1993), which can significantly influence the fluid movement and solute transport in groundwater systems (Davis et al., 1993; Koltermann & Gorelick, 1996; Dai et al., 2004; Possemiers et al., 2012; Thompson et al., 2019; Ren et al., 2022; Yin et al., 2023). Understanding decimetre- to metre-scale sedimentary features, at a particular site, is essential to characterise the local permeability distribution of the aquifer, the longitudinal dispersivity of dissolved compounds, and consequently the subsurface movement of fluids and spreading of solutes at that location (Gelhar et al., 1992; Zheng & Gorelick, 2005; Ramanathan et al., 2010; Ren et al., 2022).

The application of sedimentary facies analysis has been widely used to increase the efficiency of hydrocarbon exploration (Walker and James, 1992; Høimyr et al., 1993), however, the same practice still lags behind in groundwater studies (Crooijmans et al., 2016; Aberg et al., 2021). Primarily, the clarification of the concept of sedimentary facies is required. It consists of a body of rock characterised by a particular combination of lithology(ies), physical and biological structures, distinct from the surrounding rock bodies (Walker and James, 1992). Facies can be combined into facies associations, which refers to a group of facies genetically related to one another, recording some environmental significance (Collinson, 1969), and in architectural elements, which is a morphological subdivision characterised by a distinct assemblage of facies, geometries, and depositional process (Walker and James, 1992). By identifying the facies, facies associations, and architectural elements, the next step is to define the depositional environment in which they were formed, by comparing them with modern examples (Walker and James, 1992). Depositional systems reveal the three-dimensional assemblage of facies, facies associations, and architectural elements, with a direct link between the sedimentary process and the depositional

environment (Posamentier et al., 1988). In this study, the facies analysis generated by Bofill et al. (2024) – Chapter 2 of this thesis – for the Lower Grès Vosgien Formation (LGV) is used.

Outcrop studies offer valuable analogues for subsurface conditions (e.g., Jussel. 1989; Alexander, 1993; Aigner et al., 1996; Rogiers et al., 2013; Howell et al., 2014; Weissmann et al., 2015; Thompson et al., 2019), providing insights into the geometry and distribution of sedimentary facies that are difficult to obtain from borehole data alone. Although hydraulic properties measured from outcrops may not exhibit similar absolute values compared to subsurface conditions due to distinct diagenetic stages (Koltermann & Gorelick, 1996; Rogiers et al., 2013; Busch et al., 2022), outcrop measurements can be useful in a relative sense (Koltermann & Gorelick, 1996). See Chapter 3 for details.

Integrating quantitative facies analysis with field measurements of permeability from outcrops enhances the realism of hydrogeological models and improves our understanding of subsurface flow dynamics (Alexander, 1993; Theel et al., 2020). This approach is particularly beneficial for regions dominated by sandstone facies deposited in braided fluvial and aeolian systems, where significant permeability variations exist despite the absence of mudstone layers (e.g., Chandler et al., 1989; Fischer et al., 2007; Newell et al., 2019; Thompson et al., 2019), such as in the LGV. In Chapter 3, it is shown that even medium-grained sandstones deposited in braided fluvial channels can present permeability contrasts of more than two orders of magnitude when related to distinct sedimentary facies (i.e., trough cross-bedded sandstones versus low-angle cross-bedded sandstones), underscoring the presence of unknown unknowns (sensu Hunt & Welter, 2010) in hydrogeological conceptual models, given that the main proxy used to recognise distinct sedimentary facies as distinct hydrostratigraphic units is the difference in grain sizes (Koltermann & Gorelick, 1996).

In this chapter, we use a digital outcrop model (Fig. 4-1), associated with the quantitative sedimentary characterisation provided by Bofill et al. (2024) – Chapter 2 of this thesis – and permeability distribution analysis between facies and facies associations presented in Chapter 3, to develop realistic vertical 2D hydrogeological conceptual models where sedimentary facies are discretised with their associated hydraulic conductivity characteristics. The chosen outcrop, located in eastern France at the Northern Vosges region (Fig. 4-1A), records the main features observed by Bofill

et al. (2024) at the LGV, such as the dominance of facies from the fluvial channel facies association (FC), mainly represented by facies trough cross-bedded sandstone (St), followed by facies sigmoidal cross-bedded sandstone (Ss) and low-angle cross-bedded sandstone (Sl), both with similar proportions. Facies St, Ss, and Sl are predominantly composed of medium-grained (⌀ 0.25 – 0.5 mm) sandstones, and their deposition is related to the flow regime within the fluvial channels (Bofill et al., 2024). The outcrop also records two laterally extensive decimetre-scale thick layers of wind- and water-laid facies association (WWL) (Bofill et al., 2024). The WWL is composed of fine-grained (⌀ 0.125 – 0.25 mm) sandstones, and its deposition occurred in a context where fluvial activity was absent, and the processes controlling the deposition of sediments were wind transport, water table level fluctuations, and ephemeral floods (Bofill et al., 2024). The WWL closer to the base of the outcrop extrapolates the dimensions of the outcrop, while the WWL closer to the top of the outcrop is laterally eroded by the overlying FC deposits. The described facies from the FC, and the WWL layers, exhibit thickness of decimetre- to metre-scale, which previous studies have shown to directly influence the dispersivity of solutes in porous aquifers (Zheng & Gorelick, 2005; Ramanathan et al., 2010; Ren et al., 2022).

Solute dispersion occurs due to a non-uniform velocity distribution within a single flow-conduit, variations of velocities from pore to pore, and transverse velocity components due to the matrix tortuosity (Sethi and Di Molfetta, 2019). A macrodispersivity transport component can be used where these velocity variations can no longer be represented, which leads to mixing the distinct convective solute transport of the individual sedimentary elements (Dagan, 1990). In other words, the term macrodispersion stands for dispersive mixing caused by aquifer heterogeneities. Field observations have shown that when considering regional solute transport, dispersive mixing in the direction of flow in a real aquifer is significantly greater than the dispersion measured in laboratory experiments (Gelhar et al., 1979). Thus, the longitudinal dispersivities determined in the field can be several orders of magnitude higher than the grain-size-related dispersivity and vary depending on the degree of heterogeneity of the subsurface and the size of the heterogeneities (Gelhar et al., 1979).

In theory, in a sufficiently large-scale observation over which both the convective and dispersive transport components, via a homogeneous equivalent system, can be

averaged in a meaningful way, the dispersive transport in a heterogeneous aquifer can be described using a constant dispersion coefficient, and by Fick's dispersion approach (Gelhar et al., 1979). Fick's approach refers to the random process of particles' movement in response to uneven distribution of heat, pressure, and concentrations (Kaufmann, 1998). Before reaching this averaging volume, the dispersion coefficient is scale-dependent and increases steadily until an asymptotic macrodispersion coefficient is reached (e.g. Gelhar and Axness, 1983). However, it is not a consensus that an asymptotic regime is ever reached in natural formations (Dagan, 1988).

The objective of this chapter is to assess the influence of the observed heterogeneity described in Chapter 3 on the modelling of horizontal and vertical fluid-flow, such as the breakthrough curve of particles' residence time across the model domain, the longitudinal macrodispersivity, and the upscaled anisotropy. Knowledge of all heterogeneities of the aquifer structure enables a priori-detailed modelling of convective and dispersive mass transport (Schäfer, 1991). By extracting individual sedimentary features — facies and facies associations — from the aquifer structure, fluid-flow is simulated in five progressively simplified aquifer scenarios. The impact of these sedimentary features on the results of solute transport modelling is then analysed. Additionally, the implications of assigning hydraulic conductivity (K) deterministically (using the median value) or stochastically (based on the distribution of K values) across the model domain are also examined.

4.2. METHODS

4.2.1. From outcrop to discretised conceptual model

An orthomosaic image of one outcrop – the Falkenstein Castle ruin, in the Vosges du Nord Region (Fig. 4-1A) – was created by importing drone images acquired with an overlap of approximately 70% into the software Agisoft Metashape ® (Fig. 4-1B). This orthomosaic was then imported into Inkscape 1.2.2., where the distinct facies and facies associations were manually delimited, resulting in a realistic 2D vertical section of an aquifer representing its sedimentary heterogeneities at the scale of sedimentary facies (decimetre-scale) (Fig. 4-2).

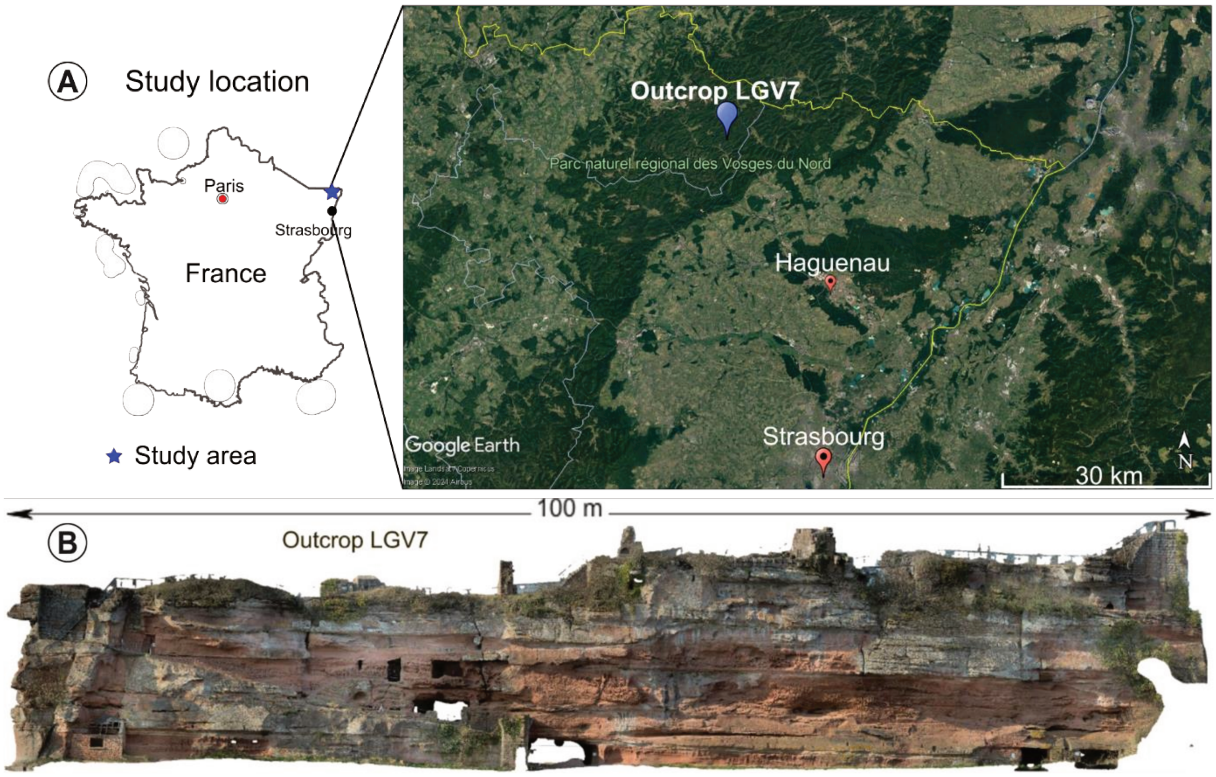


Figure 4-1: (A) Location of the outcrop (LGV7) used for this study; (B) face of the outcrop (Falkenstein Castle ruin – LGV7) used to realistically represent a 2D vertical section of an aquifer.

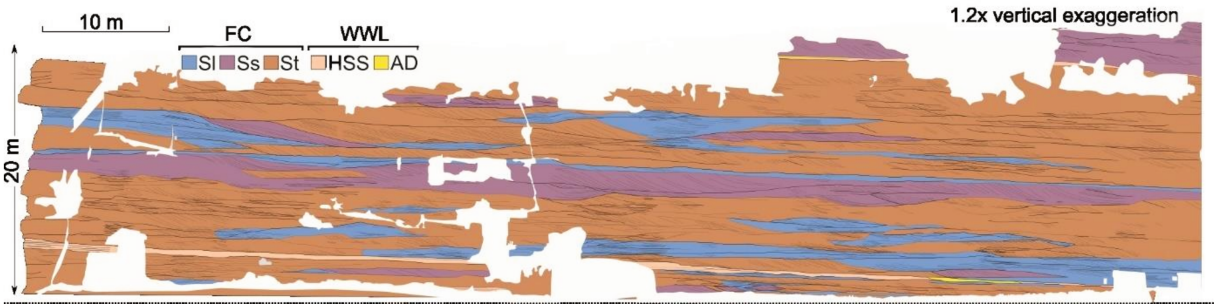


Figure 4-2: Interpretation of outcrop LGV7, showing zones of dominance of specific sedimentary facies, in their respective facies association. FC = Fluvial channel facies association; WWL = wind- and water-laid facies association; St = trough cross-bedded sandstone facies; Ss = sigmoidal cross-bedded sandstone facies; Sl = low-angle cross-bedded sandstone facies; HSS = hybrid sand sheet facies; AD = aeolian dune facies.

A “dfx file” was generated from the interpreted vertical section and imported to the numerical tool FEFLOW 8.0®. Polygons were then manually drawn (Fig. 4-3), representing zones where the facies St, Sl, Ss, from the fluvial channel facies association, and the facies HSS and AD, from the wind-and water-laid facies association, were dominant.

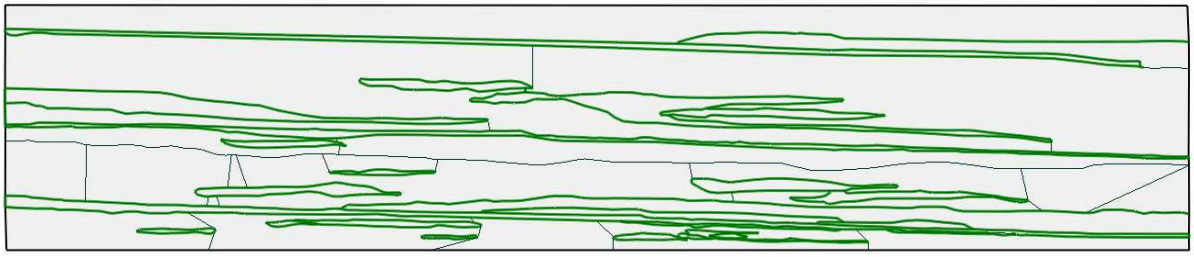


Figure 4-3: Polygons generated in FEFLOW 8.0.®

A triangle mesh type was generated with local refinement at the edges of the polygons, resulting in a total of 230406 mesh elements (Fig. 4-4) (n° of elements per facies: St = 107388; Ss = 31571; Sl = 60193; and HSS = 31354). A built-in mesh smoothing tool was applied to improve the mesh quality (Fig. 4-5). A better mesh quality indicates a smaller distribution of triangles' internal angles, which increases the numerical stability (Diersch, 2014). The closer the maximum internal angles are to 60°, the better the overall mesh quality (Diersch, 2014). Each polygon was classified as corresponding to specific facies, which was then assigned to each mesh element by FEFLOW 8.0®.

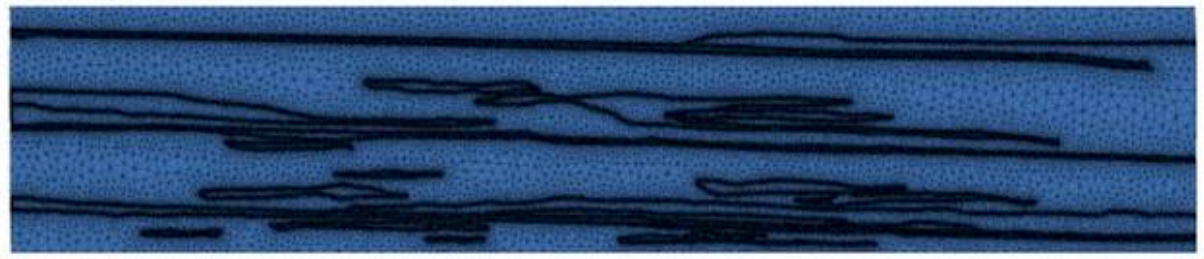


Figure 4-4: Mesh of the numerical flow model, refined at the zones of specific facies polygon edges.

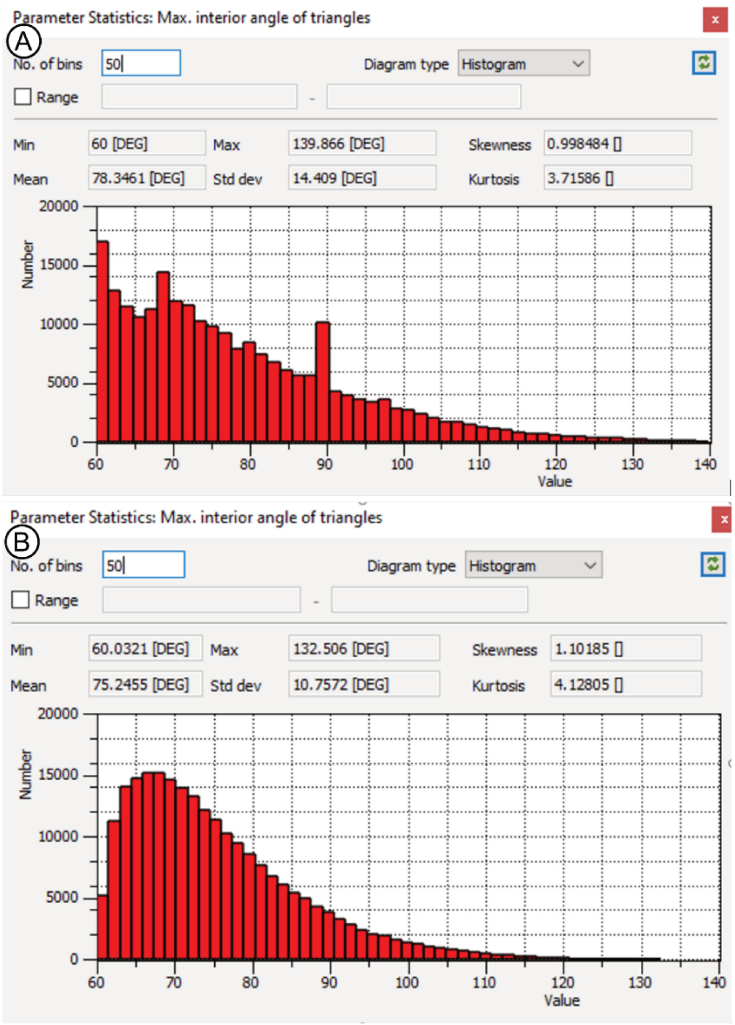


Figure 4-5: Mesh optimised using a built-in tool from FEFLOW, that improves the mesh quality by smoothing the distribution of internal angles of the mesh elements. (A) Before mesh smoothing; (B) after mesh smoothing.

Intrinsic permeability data determined with the air-permeameter (Tiny Perm3) was transformed to hydraulic conductivity (K) [ms^{-1}] values. Permeability (k) [m^2] is ideally fluid-independent and is related to the properties of the porous media (Loll et al., 1999). The relationship between k and K is described by:

$$K = k \frac{\rho_w g}{\eta_w} \quad \text{(Eq. 1)}$$

where ρ_w is the water density [kgm^{-3}], g is the gravitational acceleration [ms^{-2}], and η_w is the dynamic viscosity of water [kgm^{-1}s^{-1}]. At 20 C°, η_w = 1.003 kgm^{-1}s^{-1} (Kestin et al., 1978).

A single porosity value of 15% was applied for the entire model domain, based on thin-sections (Fig.3-10 from Chapter 3) and petrophysical measurements (Fig. 3-13 from Chapter 3). The distinct approaches used to populate the mesh elements to have

various scenarios of K distribution representation are presented in the following sections.

4.2.2. Stochastic distribution of K

In scenarios where the hydraulic conductivity (K) was stochastically distributed, the original K dataset was log-transformed to approximate a normal distribution, allowing the application of the widely used Monte Carlo sampling method. This method randomly samples a specific number of datasets within a prescribed mean and standard deviation values. To prevent the sampling of extreme values not observed in the physical data, a mechanism called truncated normal distribution was applied by including maximum and minimum values associated with the prescribed data distribution (Burkardt, 2023).

However, even after log transformation, the original K data exhibited a negatively skewed distribution (Fig. 3-3 from Chapter 3), whereas the Monte Carlo sampling yielded normally distributed datasets. This consistently resulted in median and mean sampled values that were lower than those of the original data. To address this discrepancy and ensure that the median values of K obtained through Monte Carlo sampling were not significantly lower than those of the original dataset, a trial-and-error approach was adopted. Extreme lower values were systematically removed from the original dataset before conducting Monte Carlo sampling, aiming to achieve a minimum ratio of 0.9 between the median of the Monte Carlo sampled dataset and the median of the original dataset (Tables 4-1 and -3). This process resulted in the removal between 5% (two standard deviations from the mean) and 9% of the original dataset to generate a realistic K dataset – based on median values – from the Monte Carlo sampling.

Given the large variance of K in facies HSS (Table 4-1), and the fact that the distribution of original K data for these facies remained substantially different from a normal distribution even in the log domain (Fig. 3-3 from Chapter 3), a ratio of 0.72 (Table 4-1) between the median of the Monte Carlo sampled and the median of the original dataset was accepted, to avoid the removal of a large percentage of the original dataset to fit the original and Monte Carlo sampled median values.

During this process, the standard deviations used for the Monte Carlo sampling were also smaller than the original data, given that extreme values were removed, reaching between 42% and 70% of the standard deviation from the original dataset.

Monte Carlo sampling from the truncated normal distribution was implemented using the open-source Python library 'Scipy.stats', specifically the 'Truncnorm' module (code in annex).

The number of K datasets to be sampled using the Monte Carlo approach was defined to be equal to the number of mesh elements to be filled with K data. This number was accessed by exporting the mesh elements as a "DAT" file from FEFLOW 8.0®, with each row representing a mesh element, and columns indicating: (i) their centre position in the model domain (x and z); (ii) their prescribed facies (assigned during mesh generation from polygons), and (iii) their K values. Subsequently, the K values in the exported "DAT" file columns were replaced from the K dataset resulting from Monte Carlo sampling, for each facies. This modified .DAT file was then imported back into FEFLOW 8.0®, resulting into stochastically distributed K values for each facies.

4.2.3. Deterministic distribution of K

Among the various scenarios of permeability distribution, deterministic approaches for attributing K values were also employed, constraining K by the geometry of sedimentary features. These deterministic values were derived from the median K. The use of median values is preferable for representing non-normally distributed datasets, as the mean can be more influenced by extreme values.

4.2.4. Fluid-flow and particle tracking modelling

The fluid-flow modelling was conducted in a 2D vertical projection, under saturated and steady-state flow conditions, using the software FEFLOW 8.0®. FEFLOW 8.0® uses a multidimensional finite element method, which handles complex geometric situations to simulate groundwater flow and transport models (Diersch, 2014). The general flow equation is based on the macroscopic law of conservation of mass:

$$S_s \frac{\partial h}{\partial t} = \frac{\partial}{\partial x_i}\left(K_{ij} \frac{\partial h}{\partial x_j}\right) - Q \qquad \text{(Eq. 2)}$$

where, S_s is the specific storage, which in the case of the present study is zero due to the assumed steady state flow condition, h is the hydraulic head, t is the time, K is the hydraulic conductivity, x is the spatial coordinate, i and j are the coordinate directions, and Q is the local sources and sinks per unit volume, which are supposed to be zero.

A fixed hydraulic head boundary condition was applied uniformly over depth at both ends of the model to induce a predominantly horizontal groundwater flow, with a hydraulic gradient of 0.018 estimated from a potentiometric map of the Lower Triassic aquifer from hydrogeological atlas of the Rhine-Meuse basin (BRGM, 2002), at the Bas-Rhin department in France. Additionally, vertical flow was also simulated by applying fixed hydraulic heads at both upper and lower model extremities, to simulate flow perpendicular to the sedimentary bedding (Fig. 4-6). Where no boundary conditions are specified to the model domain limits, FEFLOW 8.0®, by default, attributes as impermeable limits (no-flow boundary condition, Fig. 4-6), i.e. no water can flow into or out of the model.

Forward particle tracking was employed to access residence time across the model domain by adding particles in all mesh elements in the upstream model boundary. This approach resulted in 369 particles for the horizontal flow, and 213 particles for the vertical flow. To confirm if all possibilities of particle paths across the model domain were incorporated into the analysis, several runs were conducted until a stabilisation of the cumulative mean of the particles' residence time was observed (Fig. 4-7). This was particularly applied to the scenarios where K was distributed stochastically, given the complexity of K distribution that creates several possibilities of particles paths across the model domain.

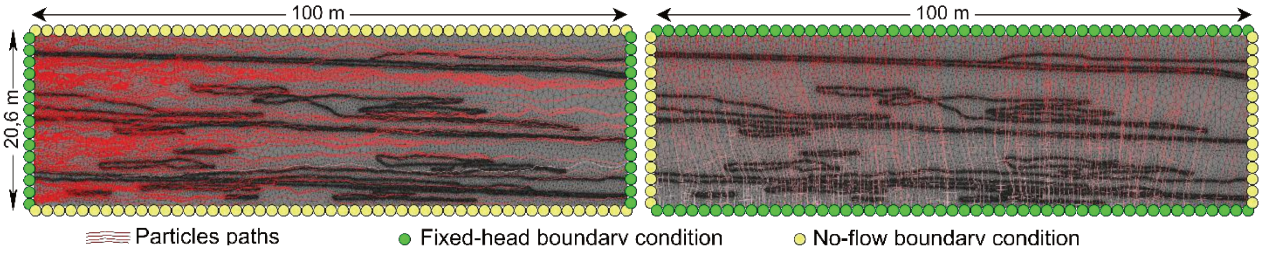


Figure 4-6: Boundary conditions for horizontal flow (left) and vertical flow (right), to run the particle tracking across the model domain.

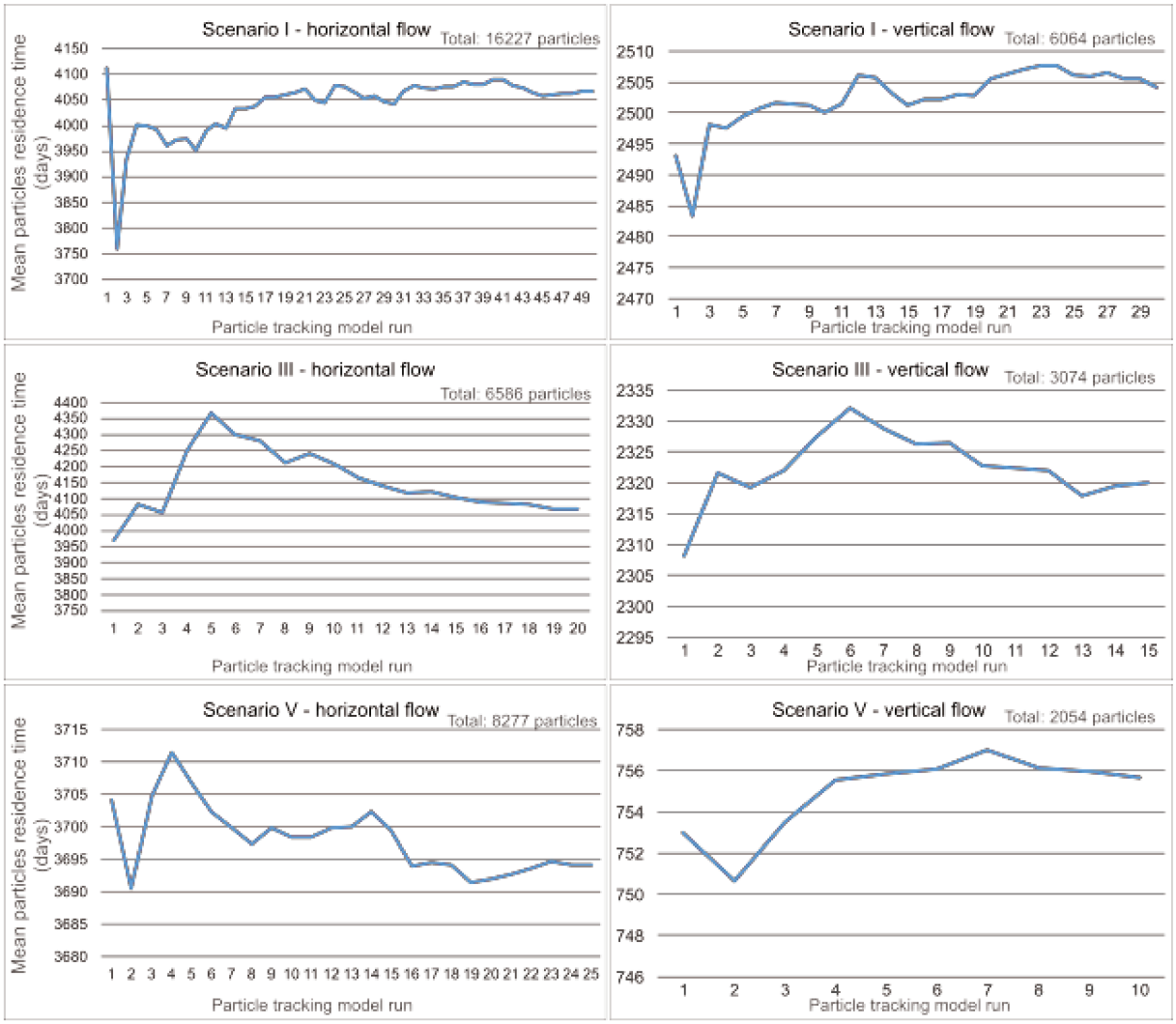


Figure 4-7: Cumulative mean stabilisation behaviour of particles' residence time.

4.2.5. Quantification of upscaled anisotropy

Considering that the dimensions of the model (length of x = 100 m; height of z = 20.6 m) are rather small when considering groundwater flow at a regional scale, which may often represent the size of a single cell, the anisotropy generated by each heterogeneity scenario is calculated when upscaled. After each run, FEFLOW 8.0.® automatically calculates the average flow rate Q (m^3d^{-1}) across the model domain. Thus, it is possible to calculate the upscaled hydraulic conductivity (K_{up}) by applying Darcy's law:

$$K_{up} = \frac{Q\Delta L}{A\Delta h} \quad , \qquad \text{(Eq. 3)}$$

where A is the cross-sectional area (m^2) which is considered as a section of 1 m width

and 20.6 m in the vertical direction (outcrop's height) for horizontal flow, and a section of 1 m width and 100 m in the horizontal direction (outcrop's length) for vertical flow, Δh is the hydraulic head difference between the two extremities of the model, and ΔL is the length of the model. The upscaled anisotropy is calculated as:

$$Upscaled\ anisotropy = \frac{K_{up\ vertical}}{K_{up\ horizontal}} \quad \text{(Eq. 4)}$$

4.2.6. Quantification of macrodispersivity using time moments analysis

The analysis of time moments has been widely used for the interpretation of breakthrough curves obtained from tracer tests in porous aquifers (e.g. Kreft and Zuber, 1978; Valocchi, 1985; Schäfer, 1991). In this study, the residence time of water particles calculated for the different scenarios was analysed with the time moment method. Each particle is assumed to represent a fixed constant mass of tracer per water volume, and all particles are introduced at the model inlet simultaneously. Presenting the calculated arrival times of the different particles at the model outlet in the form of frequency, may then be interpreted as the concentration breakthrough of a tracer [$c(x_0, t)$], where x_0 is the model outlet.

The time moments of a given concentration distribution [$c(x, t)$] are defined as $M_{n,t}$ (Aris, 1958)

$$M_{n,t} = \int_0^\infty t^n\, c(x,t)\, dt, \quad \text{(Eq. 5)}$$

where, $M_{n,t}$ is the nth time moment around the origin ($t = 0$). In analogy to the spatial moment method, it is calculated the normalised time moments $m_{n,t}$, where the first normalised time moment ($m_{1,t}$) corresponds to the mean residence time of the particles.

$$m_{1,t} = \frac{M_{1,t}}{M_{0,t}} \quad \text{(Eq. 6)}$$

where $M_{0,t}$ refers to the total mass of the tracer injected in the constant flow rate at the model's inlet. In this study, this refers to the total of particles used in the analysis. Given the distinct number of particles analysed for each scenario (Fig. 4-7), and aiming to normalise all scenarios for the same initial concentration, it is considered $M_{0,t}$= 1, corresponding to 100% of the particles, and $c(x, t)$ as the percentage of particles observed arriving at the model outlet.

In the case of an instantaneous injection of tracer mass (Dirac-impuls), the mean flow velocity (U) across the total length of the model domain travelled by particles (x_0) is expressed by (Kreft and Zuber, 1978)

$$U = \frac{x_0}{m_{1,t}} \quad \text{(Eq. 7)}$$

Higher order time moments are usually represented as central moments ($\mu_{n,t}$), calculated by:

$$\mu_{n,t} = \frac{\int_0^\infty (t - m_{1,t})^n c(x,t)\, dt}{M_{0,t}} \quad \text{(Eq. 8)}$$

The second central time moment ($\mu_{2,t}$) corresponds to the variance of the concentration distribution. In the case of a Dirac-impuls injection of tracer mass, the longitudinal dispersion coefficient (D_L) is calculated by (Kreft and Zuber, 1978)

$$D_L = \frac{\mu_{2,t} U^3}{2x_0} \quad \text{(Eq. 9)}$$

And, finally, the longitudinal dispersivity ($\propto_L$) is then determined by

$$\propto_L = \frac{D_L}{U} \quad \text{(Eq. 10)}$$

4.3. RESULTS

4.3.1. Scenarios of hydraulic conductivity (K) distribution

This section presents the six distinct scenarios of hydrostratigraphic conceptualisation. To enhance clarity and provide a comprehensive understanding, certain methodological details are integrated with the results, such as detailed description of the criteria used for distributing K in each scenario. This integrated approach ensures that the rationale behind the distribution criteria is immediately clear in the context of the outcomes observed.

- Scenario I – Stochastic K discretised by facies (reference model)

In Scenario I, K was stochastically distributed across the mesh elements within each facies group polygon (Fig. 4-8). This scenario is used hereafter as a reference model because it is discretised by facies, and it comprises the distribution of K values

measured in the field. Therefore, is the most realistic representation among the distinct scenarios.

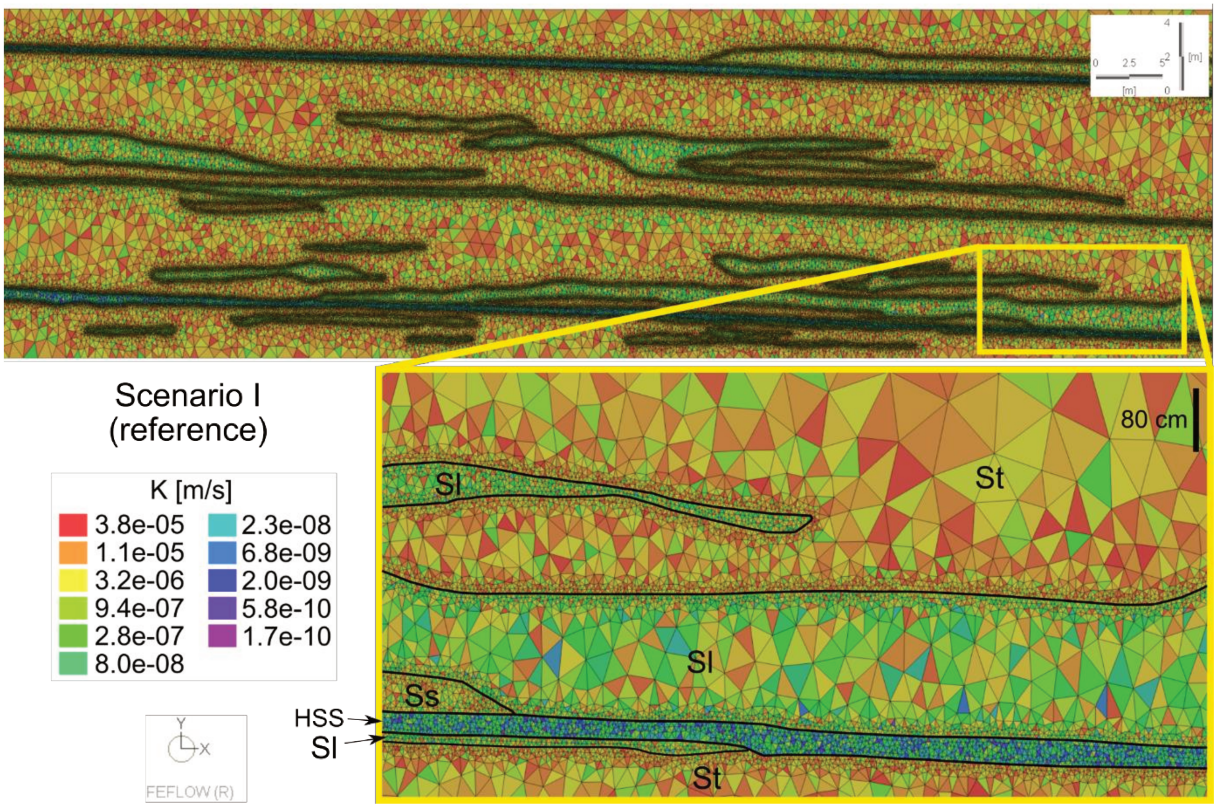


Figure 4-8: Scenario I used as a reference conceptual model, since incorporates the highest complexity. Discretised by facies, with hydraulic conductivity (K) distributed stochastically. Facies codes: St = trough cross-bedded sandstone; Ss = sigmoidal cross-bedded sandstone; Sl = low-angle cross-bedded sandstone; HSS = hybrid sand sheet sandstone. Remark: the dark lines shown in the overview correspond to very fine discretised grid with a high number of triangular cells.

Table 4-1 presents the original median K values (Ko) per facies, and their variance [σ^2(o)], along with the Monte Carlo sampling median K (Kmc) and variance [σ^2(mc)]. Also, it presents the ratio Kmc/Ko to exhibit how much the simulated data approximates the original data.

Table 4-1: Permeability data used in Scenario I. Original median hydraulic conductivity (Ko) measured in the field, and median hydraulic conductivity of the stochastically generated data by Monte Carlo sampling (Kmc). σ2(o) is the variance of the original dataset in the log domain; σ2(mc) is the variance of the stochastically generated data, in the log domain. Kmc/Ko indicates how much the simulated data approximates the real data.

Facies	Ko (ms^{-1})	σ^2(o)	Kmc (ms^{-1})	σ^2(mc)	Kmc/Ko
St	5.9×10^{-6}	0.69	5.8×10^{-6}	0.19	0.98
Ss	3.4×10^{-6}	0.48	3.1×10^{-6}	0.28	0.90
Sl	1.1×10^{-6}	0.66	1.1×10^{-6}	0.47	0.99
HSS	6.6×10^{-8}	1.4	4.8×10^{-8}	0.67	0.72

- Scenario II - Deterministic K discretised by facies

In Scenario II, the original median of each facies K (Ko in Table 4-1) was assigned deterministically to mesh elements within each facies group polygon (Fig. 4-9).

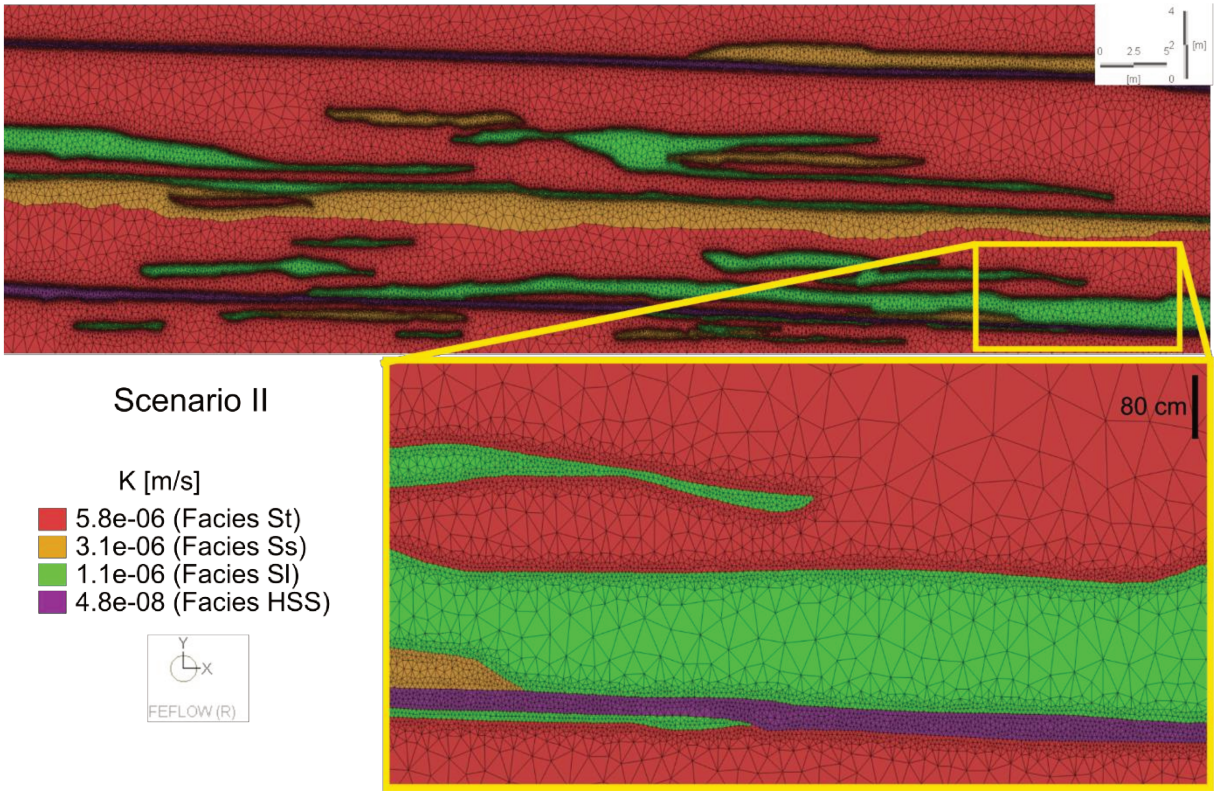


Figure 4-9: Scenario II, discretised by facies, with deterministic hydraulic conductivity (K) based on the median K measured for each facies.

- Scenario III - Stochastic K discretised by facies association

In Scenario III, a weighted K, based on the proportion of each facies within each facies association (Bofill et al., 2024) (Table 4-2), was stochastically distributed across mesh elements within individual facies association group polygon (Fig. 4-10).

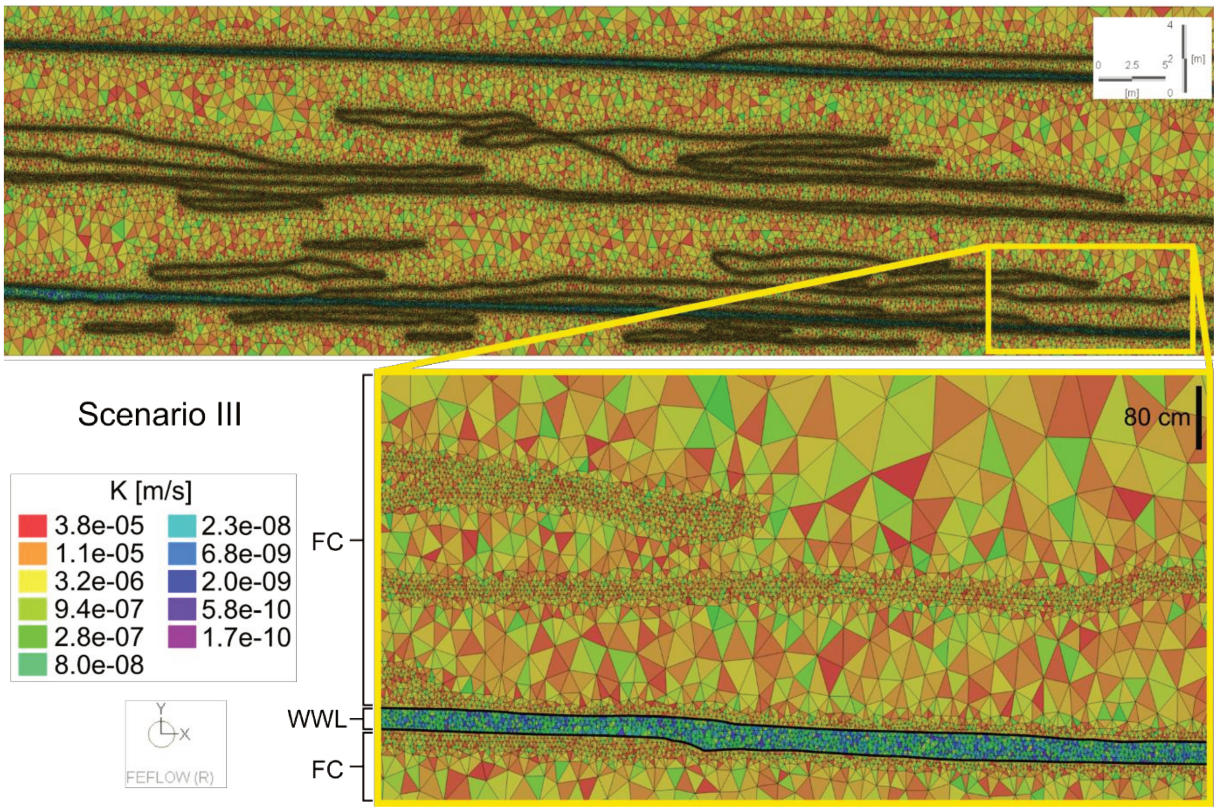


Figure 4-10: Scenario III is discretised by facies associations, with hydraulic conductivity (K) distributed stochastically, based on the weighted K values of the facies comprising each facies association.

Table 4-2: Hydraulic conductivity (K) is based on the weighted median K of the facies association.

Facies association	Facies	Ko (ms^{-1})	% of the facies association thickness (Bofill et al., 2024)	Weighted K (ms^{-1})
Fluvial channel	St	5.9×10^{-6}	74%	4.9×10^{-6}
	Ss	3.4×10^{-6}	12%	
	Sl	1.1×10^{-6}	14%	
Wind- and water-laid	HSS	6.6×10^{-8}	In the studied outcrop it is considered as 100% HSS	6.6×10^{-8}

The original median K and the median K simulated by the Monte Carlo sampling, for both facies associations, are presented in Table 4-3.

Table 4-3: Original weighted median hydraulic conductivity (Ko) measured in the field, and median hydraulic conductivity of the stochastically generated data by Monte Carlo sampling (Kmc), by facies association. Kmc/Ko indicates how much the simulated data approximates the real data.

Facies association	Ko (ms^{-1})	Kmc (ms^{-1})	Kmc/Ko
Fluvial channel	4.9×10^{-6}	4.9×10^{-6}	1.0
Wind- and water-laid	6.6×10^{-8}	4.7×10^{-8}	0.72

- Scenario IV - Deterministic K discretised by facies association

In Scenario IV, a single weighted median K (Table 4-2) was assigned deterministically to mesh elements within each facies association group polygon (Fig. 4-11), based on the proportion of each facies within each facies association (Bofill et al., 2024).

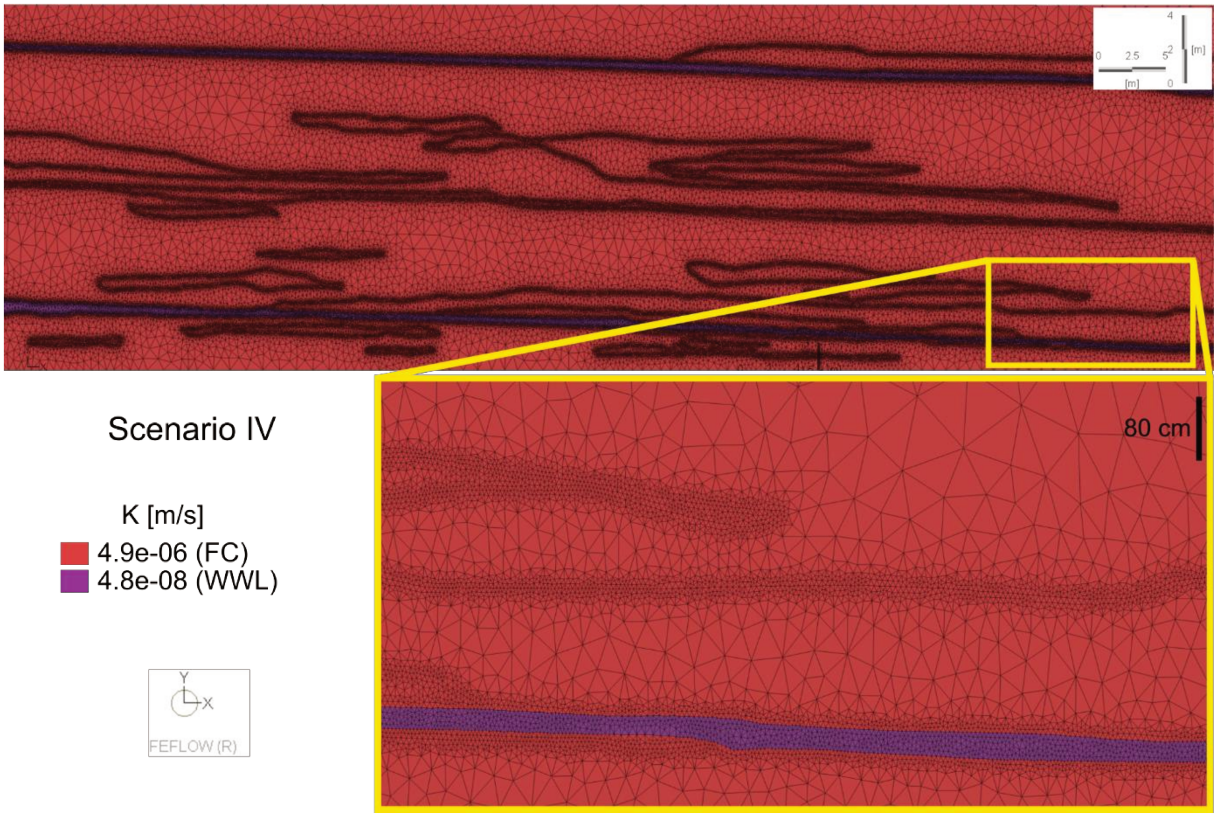


Figure 4-11: Scenario IV is discretised by facies association with deterministic hydraulic conductivity (K) based on the weighted median K values of the facies comprising each facies association.

- Scenario V - Stochastic K not constrained by the geometry of sedimentary features

In Scenario V, the median weighted K was stochastically distributed across mesh elements of the entire model domain (Fig. 4-12).

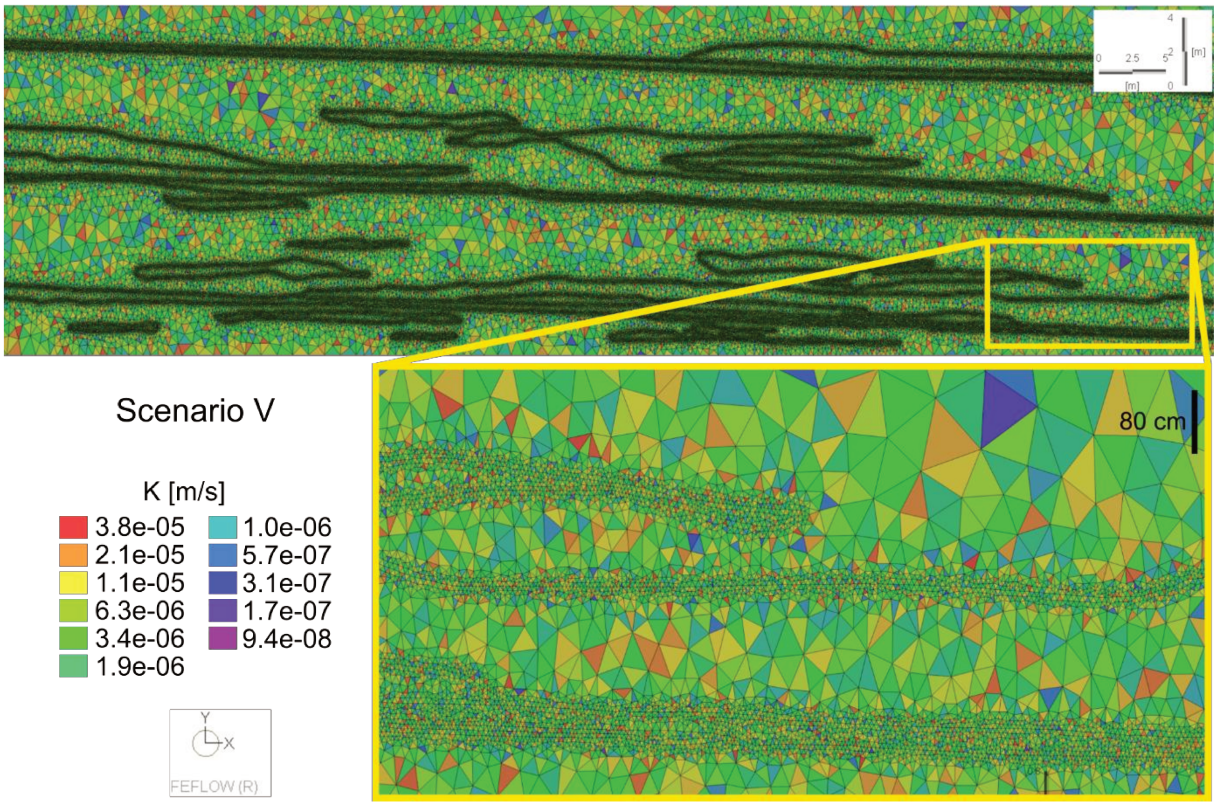


Figure 4-12: Scenario V, weighted hydraulic conductivity (K) distributed stochastically not constrained by sedimentary features geometries, such as facies or facies associations.

The weighted K values were based on the proportion of each facies across the LGV (Bofill et al., 2024) (Table 4-4).

Table 4-4 Hydraulic conductivity (K) is based on the weighted median K of the Lower Grès Vosgien Formation using the proportion of each facies within the Lower Grès Vosgien Formation (Bofill et al., 2024). Ko = original K from field measurements.

Facies	Ko (ms^{-1})	% of the Lower Grès Vosgien Formation thickness (Bofill et al., 2024)	Weighted K (ms^{-1})
St	5.9×10^{-6}	73%	
Ss	3.4×10^{-6}	11%	4.8×10^{-6}
Sl	1.1×10^{-6}	13%	
HSS	6.6×10^{-8}	3%	

- Scenario VI - Deterministic Homogeneous K

In Scenario VI, single weighted median K of $4.8\text{x}10^{-6}$ ms^{-1} (Table 4-4) was assigned to the entire model domain, based on the proportion of each facies across the LGV (Bofill et al., 2024).

4.3.2. Particle tracking - Horizontal flow

Histograms of particles' residence time exhibited distinct behaviour for the different scenarios, highlighted by their distinct skewness, kurtosis, first arrival times of particles, or the residence time of the highest particles' concentration (Fig. 4-13). Detailed descriptions and interpretations are presented in the following sections.

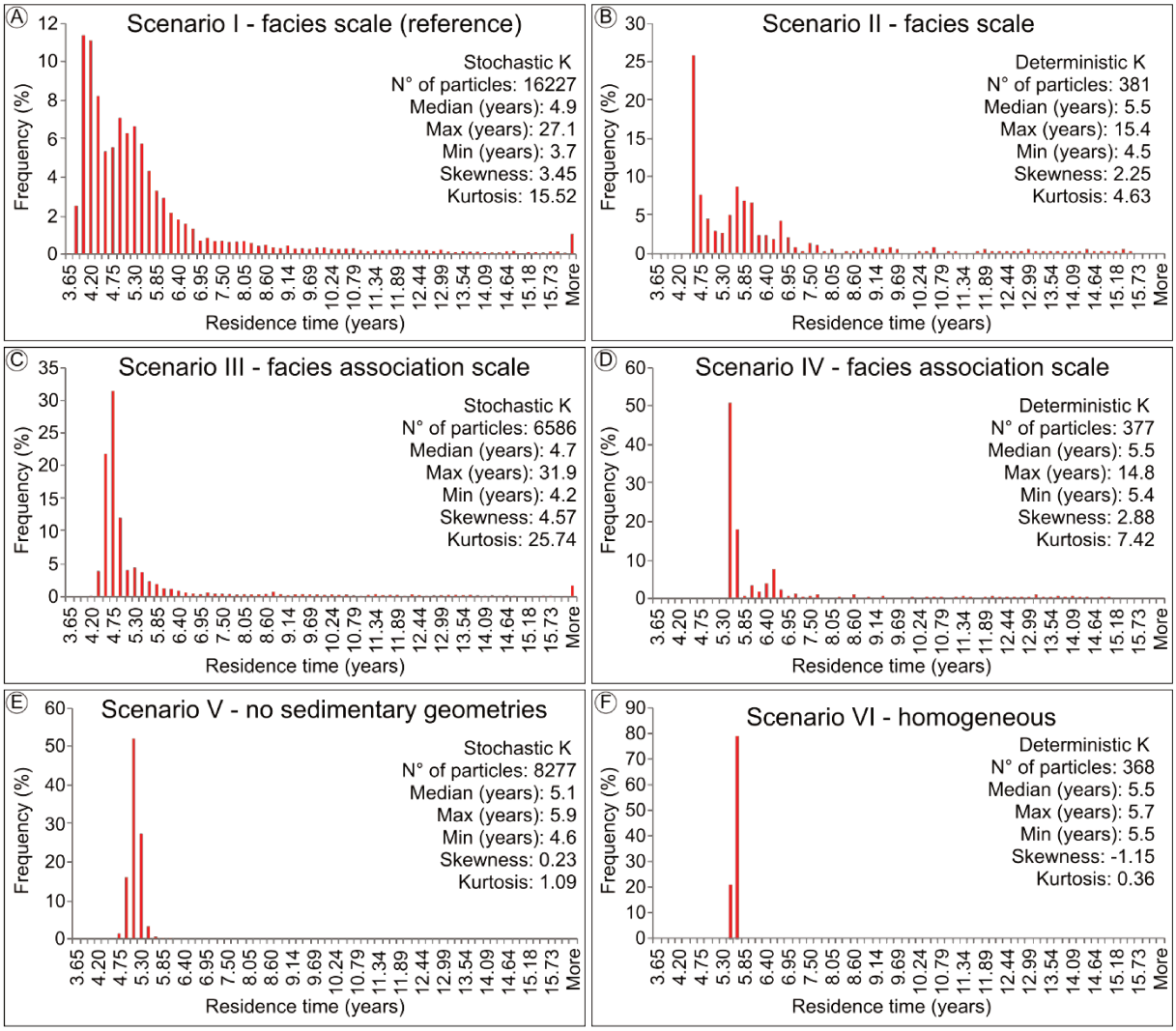


Figure 4-13: Histograms of the horizontal flow particles residence time at the difference scenarios.

4.3.2.1. Description

Scenario I: facies scale – stochastic approach (reference conceptual model)

The histogram illustrating the residence time of particles in Scenario I (Fig. 4-13A) reveals a median concentration occurring at 4.9 years, displaying a highly positive skewness (3.45) with a long tail, whose last particle arrives at 27.1 years of residence time, while the earliest particles are observed at 3.65 years. The kurtosis (15.52)

indicates a sharp peak followed by a gradual tailing. Within the concentration peak, spanning between 3.84 and 6.77 years and representing 86% of total particles, two sub-peaks are notable. The first occurs between 4.02 and 4.39 years, accounting for 30% of the concentration, while the second is observed between 4.75 and 5.48 years, representing 31% of the total particles' concentration. A pronounced long tail extends beyond 6.77 years, with the last 14% of particles arriving after 27.1 years of residence time.

The calculated upscaled horizontal K value for Scenario I is 5.44×10^{-6} ms^{-1}.

Scenario II: facies scale – deterministic approach

The histogram illustrating the residence time of particles in Scenario II (Fig. 4-13B) presents a median concentration occurring at 5.5 years, displaying a highly positive skewness (2.25) with a long tail, which its last particle arrives at 15.4 years of residence time, while the earliest particles are observed at 4.5 years. The kurtosis (4.5) indicates a sharp peak followed by a gradual tailing; however less expressive tailing compared to scenario I. Within the primary concentration peak, spanning between 4.57 and 6.95 years and representing 83% of total particles, three sub-peaks are notable. The first and most expressive occurs at 4.57 years, accounting for 26% of the concentration; the second is observed between 5.48 and 6.03 years, representing 27% of the concentration; while the third and less expressive is observed at 6.77 years, representing 4% of the total particles' concentration. A pronounced long tail extends beyond 6.95 years, with the last 17% of particles arriving after 15.4 years of residence time.

. The horizontal K obtained by upscaling the model domain in scenario II is 4.79×10^{-6} ms^{-1}.

Scenario III: facies association scale – stochastic approach

The histogram illustrating the residence time of particles in Scenario III (Fig. 4-13C) reveals a median concentration occurring at 4.7 years, displaying the highest positive skewness (4.75) and kurtosis (25.74) among the six scenarios. The histogram exhibits a long tail, in which the last particle arrives at 31.9 years of residence time, while the earliest particles are observed at 4.2 years. The high kurtosis indicates a

sharp peak followed by a gradual tailing. Within the concentration peak, spanning between 4.39 and 5.48 years, 81% of total particles arrive. A pronounced long tail extends beyond 5.48 years, with the last 19% of particles arriving after 31.9 years of residence time.

The horizontal K obtained by upscaling the model domain in scenario III is 5.52×10^{-6} ms^{-1}.

Scenario IV - Deterministic K discretised by facies association

The histogram illustrating the residence time of particles in Scenario IV (Fig. 4-13D) reveals a median concentration occurring at 5.5 years, displaying a highly positive skewness (2.88) with a long tail, which its last particle arrives at 14.8 years of residence time, while the earliest particles are observed at 5.4 years. The kurtosis (7.4) indicates a sharp peak followed by a gradual tailing; however less expressive tailing compared to scenario I. Within the primary concentration peak, spanning between 5.48 and 6.58 years and representing 85% of total particles, two sub-peaks are notable. The first and most expressive occurs between 5.48 and 5.67 years, accounting for 68% of the concentration, while the second is observed between 6.4 and 6.77 years, representing 13% of the total particles' concentration. A pronounced long tail extends beyond 6.77 years, with the last 15% of particles arriving after 14.8 years of residence time.

The calculated upscaled horizontal K value for Scenario IV is 4.65×10^{-6} ms^{-1}.

Scenario V: all K data with no sedimentary geometry constrain distributed stochastically

The histogram illustrating the residence time of particles in Scenario V (Fig. 4-13E) reveals a median concentration occurring at 5.1 years, displaying a small positive skewness (0.23) and small kurtosis (1.09), indicating a nearly symmetric close to a normal distribution. The first particle arrives at 4.6 years of residence time, while the latest particles are observed at 5.9 years.

The calculated upscaled horizontal K value for Scenario V is 5.26×10^{-6} ms^{-1}.

Scenario VI: homogeneous conceptual model (single deterministic K)

The histogram illustrating the residence time of particles in Scenario VI (Fig. 4-13F) reveals a median concentration occurring at 5.5 years, displaying the only negative skewness (-1.15) among the six scenarios, and a small kurtosis (0.36). All particles arrive at between 5.48 and 5.67 years.

The upscaled K for Scenario VI is 4.82×10^{-6} ms^{-1}.

4.3.2.2. Interpretation

The peaks and sub-peaks observed in the histograms are directly related to the different hydrostratigraphic units (facies) discretised within the fluvial channel facies association (FC), and the tailing related to the representation of the low permeability wind- and water-laid facies association (WWL).

In Scenario I (Fig 4-13A), given the stochastically distributed K and the significant overlap of K between facies St and Ss, the first peak is interpreted as related to facies St, and the second to facies Sl. Facies Ss represents the transition between the two peaks, influencing both but primarily leaning towards facies St. This interpretation is supported by the confidence interval calculated between the permeability values of the distinct facies, presented in Chapter 3. These calculations confirm that facies St and Ss are not statistically distinct populations in terms of permeability, whereas facies Sl is confirmed as a distinct population.

In Scenario II (Fig. 4-13B) the two sub-peaks attributed to the deterministic distribution of K according to the distinct facies. The first peak is interpreted as related to facies St, with some influence from facies Ss. The transition between the first and second peaks is attributed to facies Ss, and the second peak is attributed to facies Sl, again with some influence from facies Ss. The third and smaller peak is interpreted as related to facies HSS. This interpretation is supported by observations from other scenarios. For example, in scenarios where facies HSS is not individually represented (Fig. 4-13E and -13F), no particles arrive after 6 years of residence time, whereas the third peak of Scenario II occurs at 6.77 years. Additionally, Scenario IV, in which only the two facies associations are deterministically discretised, presents two peaks (Fig. 4-13D), with the second and smaller peak (at 6.77 years) interpreted to be linked to

the WWL facies association (facies HSS), occurring at a similar residence time as the third peak of Scenario II.

In Scenario III (Fig. 4-13C) the single peak is attributed to the grouping of the 3 facies from the FC facies association (St, Ss, and Sl) as a single hydrostratigraphic unit. The WWL facies association is represented by the long tailing. The positively skewed long tailing is interpreted to be linked to the low permeability WWL facies association (represented by facies HSS), which is confirmed by the lack of tailing of scenarios V and VI, where WWL is not individually represented.

The behaviour of the cumulative curves of particles' residence time (Fig. 4-14) directly reflects the behaviour of the histograms. However, the peaks observed in the stochastically distributed K models are smoothed in the cumulative curves, whereas the peaks in the deterministic K models are recognisable S-curved cumulative curves reflecting a typical convective-dispersive concentration breakthrough observed when dispersive mixing can be accurately described with a Fickian modelling approach (Herr et al., 1989).

4.3.2.3. Comparison between scenarios

General comparisons between particles' residence time across the model domain in the different scenarios are presented in Figure 4-15. Scenario I showed the earlier particles arriving among all scenarios (Fig. 4-15B). This is due to the individual discretisation of facies St, which behaved as preferential flow zones due to its highest K. Despite that in Scenario II facies St are also individually discretised, the use of a deterministic median K resulted in the exclusion of mesh elements with K values higher than the median, reducing the preferential flow paths among the mesh elements.

The gradual increase of the minimum particles' residence time (Fig. 4-15B) following the degrees of simplification, is due to the incorporation of lower K values at the preferential flow zones.

All simplified scenarios (II, III, IV, V, and VI) misrepresented the arrival of the first particles compared to Scenario I. Table 4-5 shows the percentage of particles that had arrived in Scenario I when the first particle arrived in each of the simplified scenarios. Additionally, Table 4-5 presents the percentage of particles that had arrived in Scenario

I after the last particle arrived in each simplified scenario. It also shows the overlap in particle residence time between simplified scenarios and Scenario I.

Table 4-5: Percentage of particles from Scenario I that arrived before the first particles of the other scenarios; after the last particles of the other scenarios; and the overlap of particles that arrived in the same range of residence time observed in Scenario I

	% of particles from Scenario I that arrived before the 1st particle arrives	% of particles from Scenario I that arrived after the last particle arrives	Overlap of particles arriving in the range or residence time observed in Scenario I
Scenario II	38%	1%	61%
Scenario III	25%	0%	75%
Scenario IV	63%	2%	35%
Scenario V	38%	23%	39%
Scenario VI	63%	27%	10%

4.3.2.4. Macrodispersivity

It is observed that the macrodispersion coefficient, and consequently the macrodispersivity, has a direct relationship with the coefficient of variance of particles' residence time across the model domain (Table 4-6).

Gelhar et al. (1992) through a compilation of many field experiments proposed the “scale effect” to longitudinal macrodispersivity as a function of the travel distance, in which the former would be approximately 1/10 of the latter. This agrees with our study, in which the calculated macrodispersivity for scenario I was 9.1 metres, in a model with a longitudinal dimension of 100 metres.

The conceptual models with K distributed deterministically presented systematically lower macrodispersivity than their stochastically distributed K counterparts (in a sense of the same scale of heterogeneity representation), such as scenarios I and II, III and IV, and V and VI (Table 4-6).

For the deterministic scenarios (II, IV, and VI), as heterogeneities were simplified, the macrodispersivity was reduced, in agreement with the concept that macrodispersion is caused by the variability of hydraulic conductivity (e.g. Jussel, 1989, Schäfer, 1991).

It should be noted that we have not reached the so-called asymptotic regime of macrodispersion in all scenarios. Breakthrough curves that show a multi-step increase in concentration or are characterised by a long tailing reflect a pre-asymptotic regime

(Talon et al., 2023) in which macrodispersivity increases with time and path length (Gelhar et al., 1992).

Table 4-6: Results obtained from the horizontal flow.

Scenario	Total of particles analysed	Mean residence time (years)	Median residence time (years)	Coefficient of variation	First particle to arrive (years)	Last particle to arrive (years)	Macro-dispersivity (m)	Upscaled K (ms^{-1})
I	16227	5.64	4.92	0.43	3.65	27.1	9.15	5.44×10^{-6}
II	381	6.25	5.51	0.38	4.49	15.4	7.26	4.79×10^{-6}
III	6586	5.64	4.7	0.48	4.16	31.9	11.35	5.52×10^{-6}
IV	337	6.38	5.48	0.31	5.37	14.8	4.78	4.65×10^{-6}
V	8277	5.15	5.06	0.04	4.63	5.9	0.03	5.26×10^{-6}
VI	368	5.57	5.49	0	5.48	5.5	0	4.82×10^{-6}

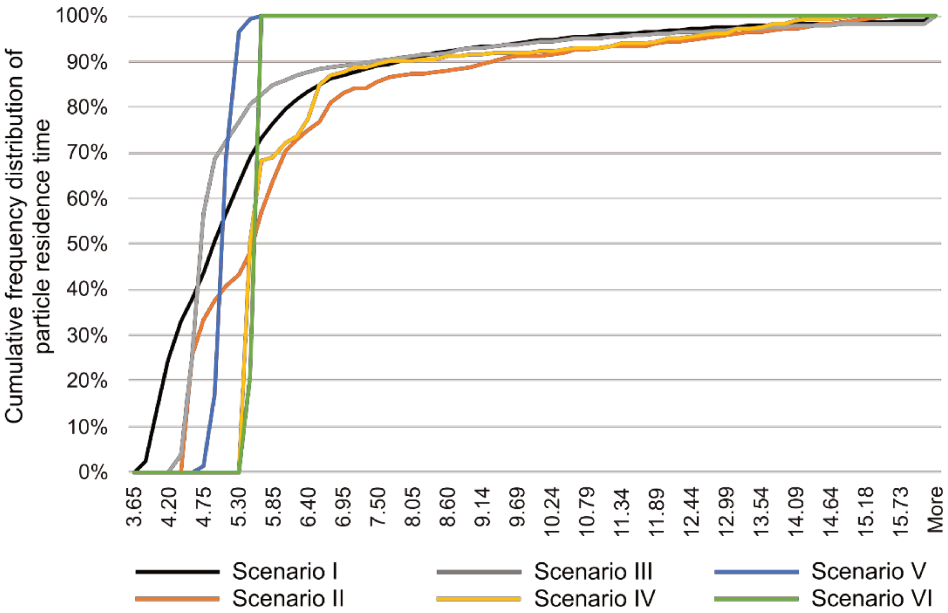


Figure 4-14: Cumulative curves of horizontal flow particles' residence time across the distinct scenarios.

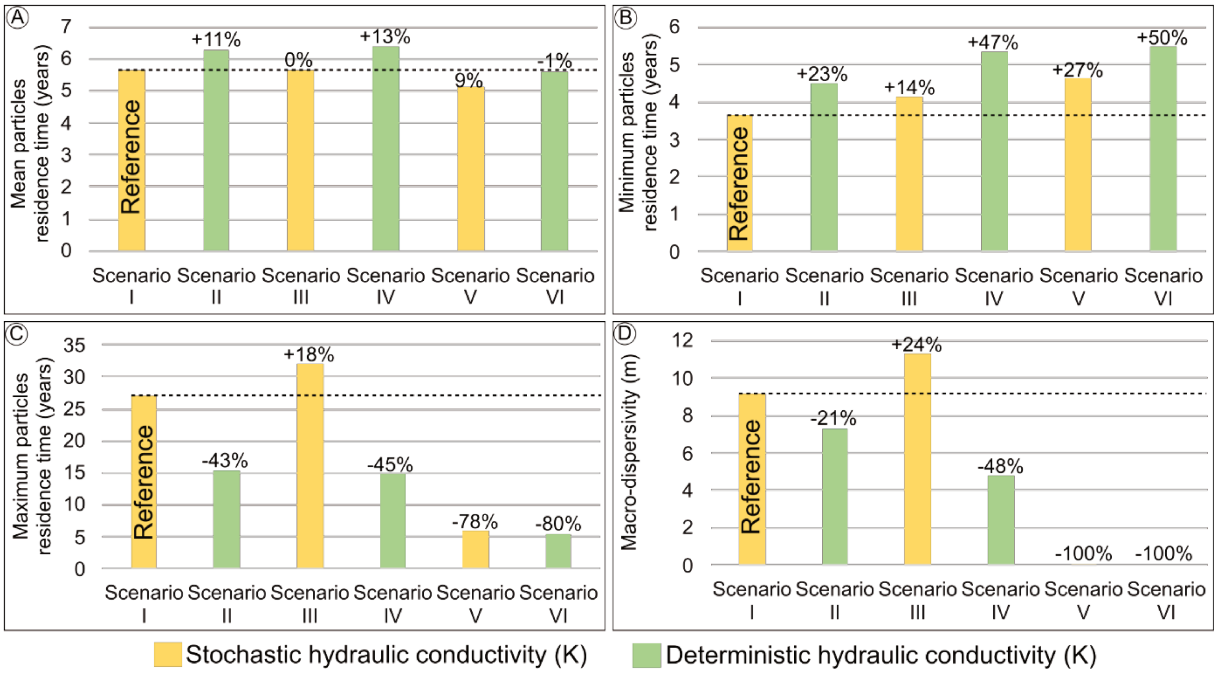


Figure 4-15: Comparison of particle tracking and macrodispersivity results, for the horizontal flow in the different scenarios.

4.3.3. Particle tracking - Vertical flow

The histograms of the residence time of particles in the numerical studies of the vertical flow showed a more symmetrical distribution, confirmed by the skewness close to zero for all scenarios except scenario VI (homogeneous) (Fig. 4-16). Detailed descriptions and interpretations are presented in the following sections.

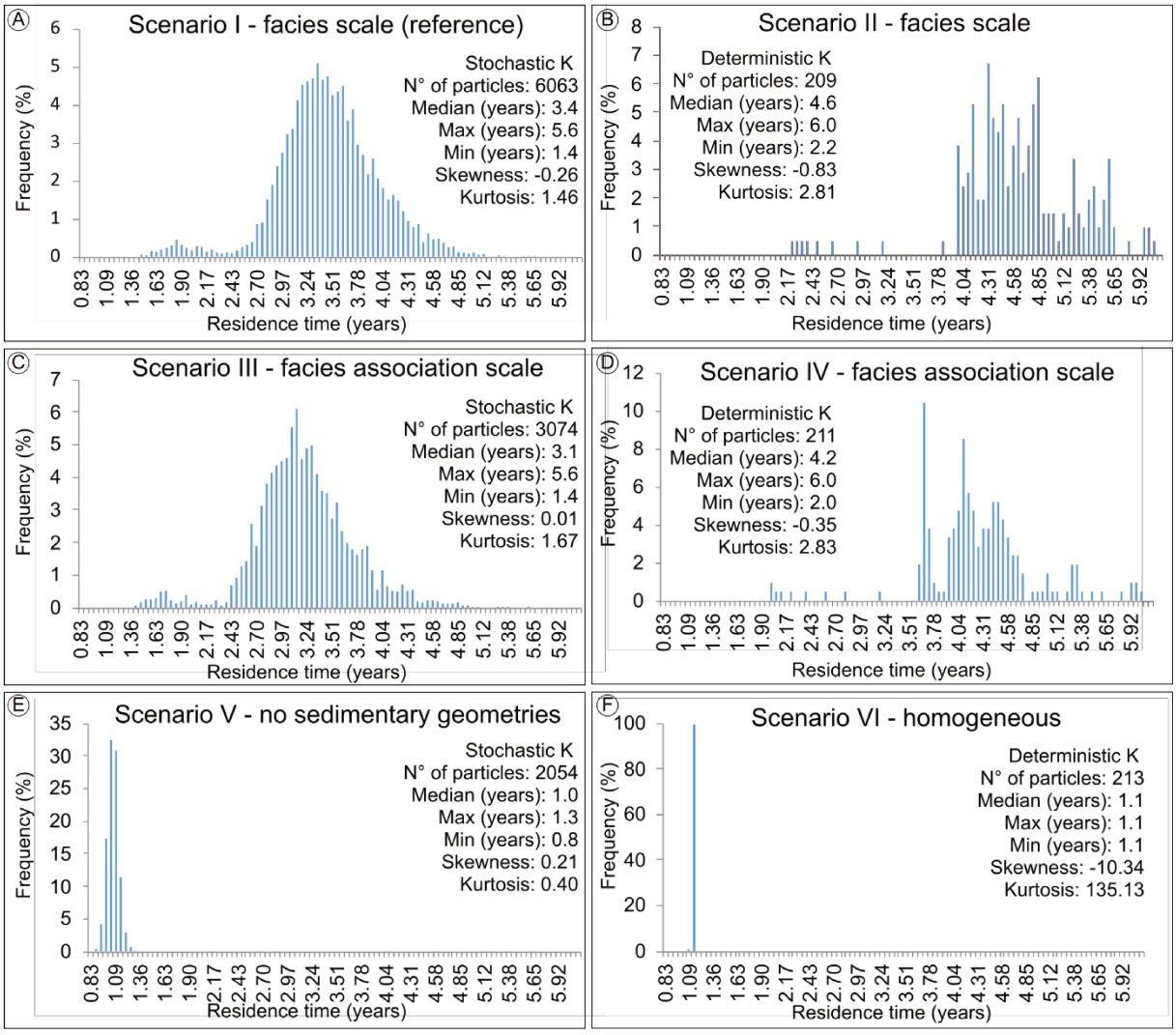


Figure 4-16: Histograms of the vertical flow particles residence time at the difference scenarios.

4.3.3.1. Description

Scenario I: facies scale – stochastic approach (reference conceptual model)

The histogram illustrating the residence time of particles in Scenario I (Fig. 4-16A) reveals a median concentration occurring at 3.4 years, displaying a slightly negative skewness (-0.26), which its earliest particle arrives at 1.4 years of residence time, while the last particles are observed at 5.6 years. The kurtosis (1.46) reflects the relatively high concentration of values around the mean, with a moderate level of peakedness.

The calculated upscaled vertical K value for Scenario I is 1.64×10^{-6} ms^{-1}.

Scenario II: facies scale – deterministic approach

The histogram illustrating the residence time of particles in Scenario II (Fig. 4-16B) reveals a median concentration occurring at 4.6 years, displaying a moderately negative skewness (-0.83), which its earliest particle arrives at 2.2 years of residence time, while the last particles are observed at 6.0 years. The kurtosis (2.81) indicates that the distribution is very close to normal, with a peak and tails that are nearly comparable to those of a normal distribution.

The vertical K obtained by upscaling the model domain in scenario II is 1.26×10^{-6} ms^{-1}.

Scenario III: facies association scale – stochastic approach

The histogram illustrating the residence time of particles in Scenario III (Fig. 4-16C) reveals a median concentration occurring at 3.1 years, displaying a nearly symmetrical distribution (skewness = 0.01), with its earliest particle arrives at 1.4 years of residence time, while the last particles are observed at 5.6 years. The kurtosis (1. 67) reflects the relatively high concentration of values around the mean, with a moderate level of peakedness.

The vertical K obtained by upscaling the model domain in scenario III is 1.84×10^{-6} ms^{-1}.

Scenario IV- Deterministic K discretised by facies association

The histogram illustrating the residence time of particles in Scenario IV (Fig. 4-16D) reveals a median concentration occurring at 4.2 years, with a slightly negative skewness (-0.35), which its earliest particle arrives at 2.0 years of residence time, while the last particles are observed at 6.0 years. The kurtosis (2.83) indicates that the distribution is very close to normal, with a peak and tails that are nearly comparable to those of a normal distribution.

The upscaled vertical K for Scenario IV is 1.39×10^{-6} ms^{-1}.

Scenario V: all K data with no sedimentary geometry constrain distributed stochastically

The histogram illustrating the residence time of particles in Scenario V (Fig. 4-16E) reveals a median concentration occurring at 1 year, displaying a slightly positive skewness (0.21) and small kurtosis (0.4), indicating evenly spread values across the range, with few extreme values (outliers). The first particle arrives at 0.8 years of residence time, while the latest particles are observed at 1.3 years.

The upscaled vertical K for Scenario V is 5.33×10^{-6} ms^{-1} m/s.

Scenario VI: homogeneous conceptual model (single deterministic K)

The histogram illustrating the residence time of particles in Scenario VI (Fig. 4-16F) reveals a median concentration occurring at 1.1 years. There is no necessity to analyse the histogram parameters given that all particles arrive at 1.1 years.

The upscaled K for Scenario VI is 4.82×10^{-6} ms^{-1}.

4.3.3.2. Interpretation

Except for scenario VI, in which all particles arrived practically at the same time, all scenarios presented a relatively symmetrical distribution of particles' residence time, evidenced by their skewness close to zero, and with fewer extreme values when compared to the mean, as indicated by the low kurtosis of particles residence time. This was expected as in the present numerical studies the flow lines cross the dominant high or low permeability layers of the outcrop almost vertically and all particles explore the same flow patterns, which is not the case in the previous horizontal flow study. Therefore, the upscaled hydraulic conductivity does not vary much and the mean residence times are almost the same. In the next section are presented the differences observed between scenarios.

4.3.3.3. Comparison between scenarios

First, the scenarios can be divided into the stochastically and deterministically distributed K, given that the first evident differences observed are related to these two forms of representing the K fields (Figs. 4-17 and -18). The scales of heterogeneities

showed relevant results' differences only when comparing with scenarios V and IV, where no sedimentary geometries are attributed.

In terms of scales of heterogeneities representation, for the facies (I and III) and facies association (II and IV) scale scenarios, the deterministic representation presented delayed particles' residence time results than its stochastic counterparts (Figs. 4-17 and -18A, 4-18B, and -18C). This is attributed to the fact that, when K is represented as a median or mean (deterministic), it excludes the mesh elements (cells) with high K, which would serve as preferential pathways for the particles to flow. That is why the highest differences observed between the stochastic and deterministic are related to the minimum particles' residence time (Fig 4-18B), followed by the mean particles' residence time (Fig. 4-18A), and the lowest differences are related to the maximum particles' residence time.

The cumulative curves of particles' residence time of stochastically distributed K (scenarios I, III and V) showed a smooth shape, with no sharp steps as observed in the deterministic models (scenarios II, IV, and IV). This is due to the lack of alternative pathways within the mesh elements of each facies in deterministic models, resulting in particles taking a similar time to cross the distinct facies, and creating the sharp steps.

By gradually removing the sedimentary geometries, the particles' residence time exhibited behaviour opposite to that observed in the horizontal flow, particularly regarding the minimum particles' residence time. In horizontal flow, there is a delay in the minimum residence time; conversely, in vertical flow, the first particles arrive sooner. This occurs because low permeability layers, especially HSS, are horizontally. Consequently, particles must traverse these layers without the option of using higher permeability preferential pathways. Therefore, although weighting the hydraulic conductivity reduces the overall mean K across the model domain, it eliminates the necessity for particles to cross these low permeability layers.

Although the weighting factor K reduces the overall mean K, it prevents the need for particles to cross low permeability layers, such as facies SI or HSS.

Table 4-7: Results obtained from the vertical flow.

Scenario	Total of particles analysed	Mean residence time (years)	Median residence time (years)	Coefficient of variation	First particle to arrive (years)	Last particle to arrive (years)	Macro-dispersivity (m)	Upscaled K (ms^{-1})
I	6063	3.5	3.4	0.15	1.4	5.6	0.24	1.64×10^{-6}
II	209	4.67	4.6	0.14	2.2	6	0.2	1.26×10^{-6}
III	3074	3.25	3.1	0.16	1.4	5.6	0.27	1.84×10^{-6}
IV	211	4.27	4.2	0.15	2	6	0.24	1.39×10^{-6}
V	2054	1.1	1	0.06	0.8	1.3	0.04	5.33×10^{-6}
VI	213	1.1	1.1	0.01	1.1	1.1	0.001	4.80×10^{-6}

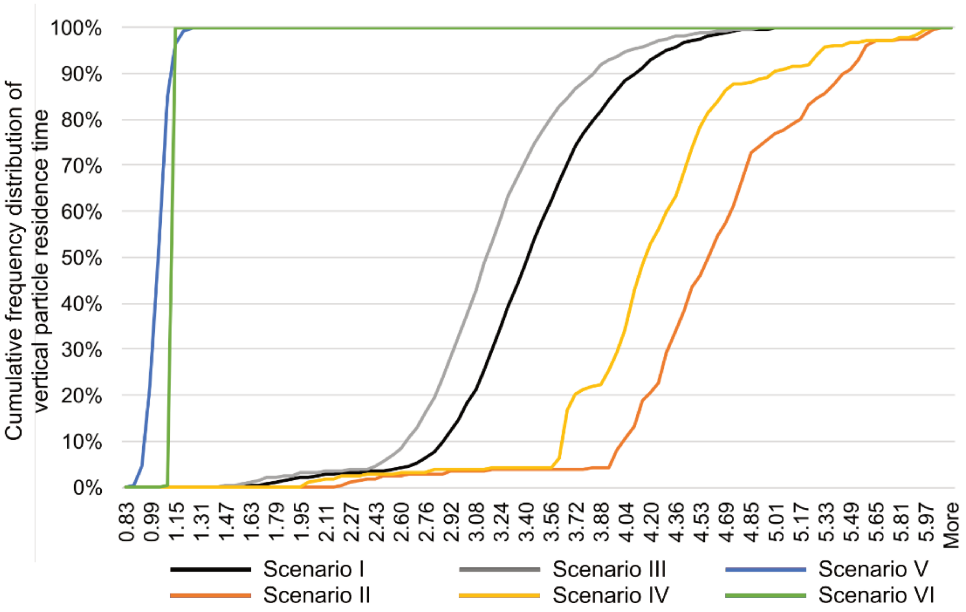


Figure 4-17: Cumulative curves of vertical flow particles' residence time across the distinct scenarios.

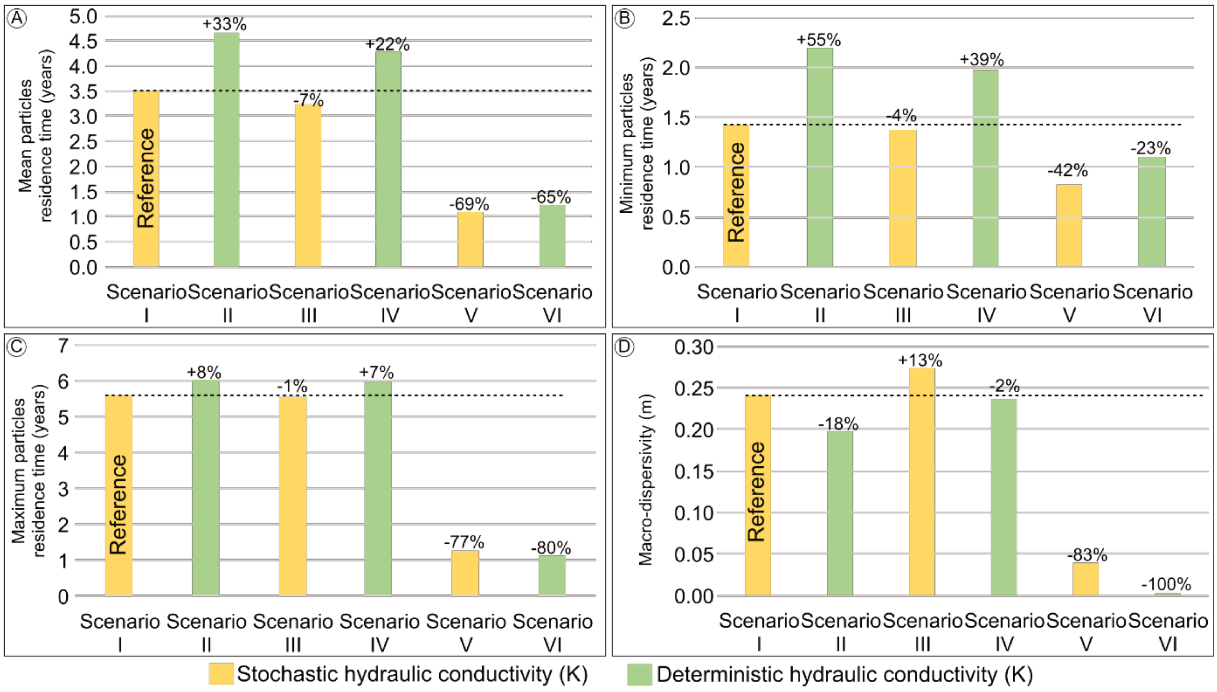


Figure 4-18: Comparison of particle tracking and macrodispersivity results with the reference model (scenario I), for the vertical.

4.3.3. Upscaled anisotropy

When the conceptual model is upscaled, the upscaled K for the horizontal and vertical flow (Tables 4-6 and -7, respectively) generates a particular anisotropy for each scenario. Scenarios I, II, III and IV presented similar upscaled anisotropy (Table 4-8), of c. 0.3. In scenarios V and VI, where no sedimentary features are represented, the upscaled conceptual model is isotropic (Kv/Kh = 1).

Table 4-8: Upscaled anisotropy calculated for each scenario of heterogeneity representation

Scenario	Vertical upscaled K (Kv) (ms^{-1})	Horizontal upscaled K (Kh) (ms^{-1})	Upscaled anisotropy (Kv/Kh)
I	1.64×10^{-6}	5.44×10^{-6}	0.30
II	1.26×10^{-6}	4.79×10^{-6}	0.26
III	1.84×10^{-6}	5.52×10^{-6}	0.33
IV	1.39×10^{-6}	4.65×10^{-6}	0.30
V	5.33×10^{-6}	5.26×10^{-6}	1.01
VI	4.80×10^{-6}	4.82×10^{-6}	1.00

4.4. DISCUSSIONS

Accurately characterising subsurface decimetre-scale heterogeneities is practically impossible (Zheng and Gorelick, 2005). However, outcrops assist in predicting these heterogeneities by providing access to their geometries and relationship with the surrounding structures (e.g., Jussel. 1989; Alexander, 1993;

Aigner et al., 1996; Rogiers et al., 2013; Howell et al., 2014; Weissmann et al., 2015; Thompson et al., 2019). These characteristics have direct implications for controlling particles residence time, and consequently, macrodispersion (Ramanathan et al., 2010).

Results showed that the discretisation between the two facies associations significantly impacts both horizontal and vertical flow, regarding particles' residence time and macrodispersivity. The upper 70 m of the LGV is composed of several intercalations between fluvial channel and wind- and water-laid facies associations (Bofill et al., 2024). There is an upward increase in the frequency of these intercalations, with the fluvial channel facies association preserving an average thickness of 5 m between wind- and water-laid deposits. Given that in the conceptual model used in fluid-flow simulations, the distance between the two wind- and water-laid facies association is c. 13 m, it suggests that the upper section of the LGV should be more affected by the lack of discretisation of the two facies associations in the conceptual model, than the effects shown in this Chapter.

The progressive simplification of the heterogeneous elements discretised in the conceptual model led to a reduction in the overlap between the particles' arrival times in the simplified models and in the reference model. This is particularly significant for remediation strategies, given the importance of predicting the duration and concentration of contaminants reaching specific receptors, such as public water supply wells or ecologically sensitive water bodies.

4.4.3. Effects of different scales of heterogeneity

The fluvial channel facies association represents 93% of the total thickness of the LGV (Bofill et al., 2024), and its facies, St, Ss, and Sl, mainly comprise medium-grained sandstones. The characteristics explaining the different permeability recorded between facies St and Sl are only recognisable through thin-section analysis (see Chapter 3). Thus, considering that the main proxy for distinguishing two hydrostratigraphic units in conceptual models is their differences in grain sizes (Koltermann & Gorelick, 1996; Ramanathan et al., 2010), facies St and Sl are likely to be grouped as a single unit, as presented in Scenarios III, IV, V, and VI.

For horizontal flow, the primary effect observed when these facies were grouped was related to the prediction of the first particles to arrive. Not considering facies St,

Ss, and Sl as distinct facies led to the non-representation of preferential flow zones (facies St). Results showed that, when the first particle arrived in Scenarios III, IV, V, and VI, respectively 25%, 63%, 38%, and 63% of the particles had already arrived in the reference model (Scenario I). This confirms the importance of discretising small-scale heterogeneity when modelling solute transport (e.g. Hakoun et al., 2019; Comolli et al., 2019), highlighting that the failure to account for preferential flow paths in numerical simulations could have direct implications for the effectiveness of groundwater contaminant remediation plans (Zheng and Gorelick, 2005).

4.4.2. Macrodispersivity

Given the distance-related dependency of macrodispersivity (Frind et al., 1987) and the relatively short distance between inflow and outflow in the vertical flow simulations, macrodispersivity analysis is discussed only for the horizontal flow.

The long tailing observed in particles' residence time distribution in Scenarios I, II, III, and IV, resulting from the low permeability sedimentary features (facies Sl and HSS) discretised in these scenarios, indicates that Fick's law cannot describe dispersion for the model domain (Herr et al., 1989). The limitations of Fick's law in real heterogeneity have been widely discussed in the literature (e.g. Matheron and Marsily, 1980; Smith and Schwartz, 1980; Pickens and Grisak, 1981; Dagan, 1988; Herr et al., 1989; Herweijer, 1997; Zheng and Gorelick, 2005).

Fick's law is considered scale-dependent (e.g. Frind et al., 1987), which theoretically means that after a specific distance travelled by the plume of particles, the dispersion tends to achieve the asymptotic condition of a Fickian regime (Gelhar et al., 1979). Therefore, the results showing a non-Fickian dispersion-behaviour may be related to pre-asymptotic conditions, and a larger distance would be needed to dispersion reach an asymptotic value.

This assumption of reaching asymptotic conditions is based on the idea that after a specific distance/time, the heterogeneities can be considered constant, once the particles have explored the complete velocity distribution of the porous media (Kinzelbach, 1988). Therefore, dispersion tends to achieve a constant value after a specific distance/time (Gelhar et al., 1979).

However, the assumption of a statistically homogeneous aquifer structure or constancy of heterogeneity after a certain distance should be approached with caution (Dagan, 1988; Matheron and Marsily, 1980; Herweijer, 1997), especially when considering depositional environment concepts. Porous aquifers result from sediments deposited in specific depositional environments that naturally record progressive or abrupt changes in facies and facies associations in dip and strike directions (Walker and James, 1992). Given that dispersion of solutes is sensitive to the spatial organisation of sedimentary facies type (Ren et al., 2022), it is necessary to understand the characteristics of the depositional environments involved in the formation of the porous aquifer to assess the extent to which an asymptotic condition if achieved, can be considered as valuable. Dagan (1988) suggests that is doubtful that an asymptotic regime is ever attained in natural formations.

4.5. CONCLUSIONS

The generation of a hydrogeological conceptual model, using sedimentological and petrophysical data from outcrops, allowed the simulation of flow and solute transport in a realistic representation of aquifer heterogeneity. Decimetre- to metre-scale sedimentary facies from sandstones deposited by a fluvio-aeolian system, which are often overlooked in fluid-flow models, significantly influence the behaviour of solute transport. Two scales of heterogeneities are presented based on sedimentological criteria: facies scale, where individual facies from two facies associations are discretised; and facies association scale, where heterogeneity discretisation is based solely on the two facies associations. To evaluate the extent to which solute transport modelling outcomes are affected by the discretisation of different facies and facies associations, five different scenarios of heterogeneity representation, with gradual simplification, were generated.

Even when discretising decimetre-scale sedimentary features geometries in conceptual models, it is recommended to distribute K stochastically, given the highly variable hydraulic conductivity observed for individual facies. Results show notable differences in solute transport behaviour between stochastic and deterministic representations of K.

The presence of the laterally extensive wind- and water-laid facies association is responsible for creating an anisotropy (Kv/Kh) of 0.3 if the model domain is upscaled.

The following conclusions are presented separately for horizontal and vertical flow simulations.

Horizontal flow: Most scenarios except for the homogeneous model, presented a highly positively skewed distribution of particles' residence time distribution. The discretisation of heterogeneities in a facies scale, distinguishing the types of medium-grained cross-bedded sandstone facies within the fluvial channel facies association and distributing the hydraulic conductivity (K) stochastically, had a direct effect on the prediction of the arrival time of the first particles that reached the model outlet. Not discretising individual facies by averaging their hydraulic conductivity (K), and/or distributing the K in a deterministic way, resulted in the overestimation of the minimum arrival time of particles reaching the model outlet. In both situations, such overestimation occurred due to misrepresentation of the higher K values recorded in field measurements, which are responsible for preferential flow paths.

In scenarios where the two facies associations were not discretised separately, a significant effect was observed regarding the last particles to arrive at the model outlet, and in the macrodispersivity values.

The gradual simplification of heterogeneities discretised in the conceptual model resulted in a decrease in the overlap between the range of particles' arrival time and that of the reference model. This is particularly important in remediation action plans to predict for how long and in what concentrations contaminants would arrive at a specific receptor, such as water wells for public supply or environmentally sensitive water bodies.

For the reference model, macrodispersion cannot be described by Fick's law for the applied model domain length. The flow conditions are pre-asymptotic, and it is not clear whether they would reach asymptotic conditions by increasing the length of the model domain.

Vertical flow: All scenarios presented a relatively symmetrical distribution of particles' residence time, evidenced by their skewness close to zero. This is explained by flow lines crossing the dominant high or low permeability layers perpendicularly, with all particles exploring similar flow patterns, which is not the case in the horizontal flow. The vertical flow results are significantly affected when geometries of the distinct facies associations (resembling the "layer cake" pattern) are not represented. In terms

of the method of K distribution, the deterministic representation resulted in delayed particles' residence time compared to their stochastic counterparts.

5. Chapter 5: Summary and general conclusions

The aim of this PhD thesis is to advance the understanding of temporal and spatial sedimentary controls on braided fluvial and aeolian systems, how these two systems interacted with each other, the permeability heterogeneity associated with them, and the extent to which such heterogeneity influences the prediction on solute transport in groundwater systems. The study was conducted in the Lower Triassic deposits of the Lower Grès Vosgien Formation (LGV), Buntsandstein Group, eastern France, which is an important aquifer hosting water for public supply and lithium-rich geothermal brines.

The study was conducted using outcrops along the western shoulder of the Upper Rhine Graben, in the Northern Vosges hills, and core samples from a geothermal well in the Graben's axis. This allowed the evaluation of the usefulness of outcrops as aquifer analogues to improve hydrogeological conceptualisation in fluid-flow numerical models.

Chapter 2 is the foundation of this PhD thesis. It presents a quantitative sedimentary facies analysis, in high resolution, to define the facies, architectural elements, and facies associations that are the building blocks of the LGV. It quantifies their granulometry, thickness, geometry, proportion, and palaeocurrent associated with it, allowing to access the paleoenvironmental conditions responsible for their deposition and current architecture.

Two facies associations were identified: fluvial channel facies association (FC), comprising 93% of the total thickness measured for the LGV, and wind- and water-laid facies association (WWL), which accounts for 7%. Seven distinct facies were observed in the FC, however, 98% of its thickness is represented by three: trough cross-bedded sandstone (St), representing 73% of the FC thickness measured; low-angle cross-bedded sandstone (Sl), accounting for 13%, and; sigmoidal cross-bedded sandstone (Ss), comprising 12%. These three facies indicate distinct flow regimes within the fluvial channels, caused either by variations in flow depths or by discharge variabilities of the system. Mudstones were mostly deposited in ephemeral channels, representing 0.1% of the total thickness measured from the FC. The WWL records 60% of its thickness by aeolian dunes (AD), and 40% by hybrid sand sheets (HSS). However, in terms of occurrences, the HSS represents 57 % of the WWL, whilst the AD, 43 %. The WWL records persistent shallow water-table, and ephemeral sheet-floods, which reduced

the availability of dry sands to be transported by the wind, inhibiting the accumulation of AD, resulting in the dominance of occurrences of HSS. In periods of water-table lowering followed by wind saturation with sand, resulted in the deposition of aeolian dunes. Thus, the hybrid sand sheets and the aeolian dunes took place in distinct temporal moments.

The spatial (lateral) and temporal (vertical) distribution of the FC and WWL deposits, the extensive coverage of the fluvial deposits, along with characteristics such as discharge variabilities and the aggradational nature of the system, support a hypothesis that the LGV was part of a large distributive fluvial system (fan/megafan). However, a larger-scale quantitative analysis is necessary for a conclusive characterisation.

In Chapter 3, sedimentary features presented in Chapter 2 are investigated in order to understand whether they record distinct permeability values or if, despite their different conditions of deposition, their permeability is similar. Permeability measurements acquired from outcrops, tied with sedimentary characteristics established in Chapter 2, along with petrographic analysis, allowed the conclusion that the distribution of permeability heterogeneity of sandstones of the LGV is directly influenced by the distinct sedimentary facies. In the FC, facies St recorded the highest permeabilities, followed by facies Ss, and facies Sl, respectively. Analysis showed that facies St and Ss were not statistically different in terms of permeability populations. However, results indicate that variations of flow-regime in the fluvial channel influence permeability variability within its associated deposits. An inverse relationship between flow-regime and sand body permeability is observed. Within the deposits of the WWL, significant permeability contrasts were observed between AD and HSS. Despite the presence of high-permeability aeolian dunes (AD) in this facies association, the dominant presence of low-permeability HSS associated with it indicates that AD has low connectivity potential.

The main diagenetic process affecting the permeability in the LGV is compaction. Samples with a higher proportion of lithoclasts and infiltrated clay recorded a more advanced degree of compaction, whereas samples with a higher percentage of quartz overgrowth exhibited a lower degree of compaction. The majority of quartz overgrowth occurred during eodiagenesis, which helped to protect primary porosity against the effects of compaction. All the aforementioned diagenetic processes affected each

sedimentary facies differently, suggesting that despite the diagenetic overprint, primary sedimentary processes and architecture govern the distribution of permeability heterogeneity in the LGV.

The same facies and facies associations described in outcrops were recognised in core samples. Regarding permeability, data from outcrops show higher absolute values compared to subsurface data. However, similar permeability trends are observed between the same facies. Therefore, certain assumptions can be extrapolated from outcrop to subsurface in the LGV: i) HSS are laterally extensive low permeability deposits, and should be considered as potential flow barriers or baffles; ii) architectural analysis of outcrops revealed that highly permeable AD have low connectivity-potential due to associated low permeability HSS; iii) fluvial deposits with significant facies variation, particularly when facies Sl is present, should be considered as more heterogeneous deposits.

Chapter 4 presents the results of the numerical studies of flow and mass transport in a realistic hydrogeological conceptual model generated using a digital outcrop model associated with sedimentological and petrophysical data. In this conceptual model, individual sedimentary facies were discretised, in a decimetre- to metre-scale. To evaluate the extent to which solute transport modelling outcomes are affected by the discretisation of different facies, five different scenarios of heterogeneity representation, with gradual simplification, are generated. The simplification consists of, first, applying a single deterministic hydraulic conductivity (K) value for each facies, instead of distributing stochastically across the model mesh elements, based on the distribution of K values presented in Chapter 3. Other form of simplification is by grouping the facies into facies associations, removing the geometries of individual facies from the conceptual model, keeping only the geometries of the facies associations described in the previous chapters. And finally, the most simplified models are those where neither facies nor facies associations are discretised, and permeability data do not follow any geometric control.

Results showed that, given the highly variable hydraulic conductivity observed for individual facies, it is recommended to distribute K stochastically. Notable differences in solute transport behaviour between stochastic and deterministic representations of K are observed.

The presence of the laterally extensive wind- and water-laid facies association is responsible for creating an anisotropy (Kv/Kh) of 0.3 if the model domain is upscaled.

The following conclusions are presented separately for horizontal and vertical flow simulations.

Horizontal flow: Most scenarios except for the homogeneous model, presented a highly positively skewed distribution of particles' residence time distribution. The discretisation of heterogeneities on a facies scale, distinguishing the types of medium-grained cross-bedded sandstone facies within the fluvial channel facies association and distributing the hydraulic conductivity (K) stochastically, had a direct effect on the prediction of the arrival time of the first particles that reached the model outlet. Not discretising individual facies by averaging their hydraulic conductivity (K), and/or distributing the K in a deterministic way, resulted in the overestimation of the minimum arrival time of particles reaching the model outlet. In both situations, such overestimation occurred due to misrepresentation of the higher K values recorded in field measurements, which are responsible for preferential flow paths.

In scenarios where the two facies associations were not discretised separately, a significant effect was observed regarding the last particles to arrive at the model outlet, and in the macrodispersivity values.

The gradual simplification of heterogeneities discretised in the conceptual model resulted in a decrease in the overlap between the range of particles' arrival time and that of the reference model. This is particularly important in remediation action plans to predict for how long and in what concentrations contaminants would arrive at a specific receptor, such as water wells for public supply, or environmentally sensitive water bodies.

For the reference model, macrodispersion cannot be described by Fick's law for the applied model domain length. The flow conditions are pre-asymptotic, and it is not clear whether they would reach asymptotic conditions by increasing the length of the model domain.

Vertical flow: all scenarios presented a relatively symmetrical distribution of particles' residence time, evidenced by their skewness close to zero. This is explained by flow lines crossing the dominant high or low permeability layers perpendicularly,

with all particles exploring similar flow patterns, which is not the case in the horizontal flow. The vertical flow results are significantly affected when geometries of the distinct facies associations (resembling the “layer cake” pattern) are not represented. In terms of the method of K distribution, the deterministic representation resulted in delayed particles’ residence time compared to their stochastic counterparts.

5.1. FUTURE RESEARCH MAY FOCUS ON:

Future research may benefit from expanding the scope of high-resolution facies analysis, coupled with permeability data, to other Lower Triassic formations within the Upper Rhine Graben. In particular, studying the Upper Grès Vosgien formation (UGV), which exhibits similar facies and facies associations yet with distinct architecture and facies proportions, could reveal whether the relationships between facies and permeability identified in this work are consistent across the UGV. Such comparisons would not only validate the findings of this study, but also potentially uncover new patterns that contribute to the sedimentary control on permeability heterogeneity distribution.

Future studies could focus on unravelling the source, and the mechanisms of transport and deposition responsible for the distribution of lithoclasts of low-grade metamorphic rocks, given that their presence has shown to be an important factor in the lower permeability facies, such as in the hybrid sand sheet and the fluvial facies Sl.

Additionally, the spatial (lateral) and temporal (vertical) extrapolation of the study area may confirm whether the Buntsandstein Group, in eastern France, was deposited in the context of a large distributive fluvial system (megafan). This can be achieved by quantifying spatial changes in channel dimensions and amalgamation, grain size, and floodplain preservation.

Regarding the numerical flow study, a quantitative characterisation of porosity distribution may be conducted to understand how differences in kinematic porosity among facies impact solute transport results. Furthermore, using an outcrop with greater length could reveal whether asymptotic conditions for macrodispersivity are achieved after a certain distance of solute transport. Finally, applying spatial moments analysis, in addition to the temporal moments approach, may elucidate how macrodispersivity evolves across the model domain, from the inlet to the outlet. Enhancing the understanding of the effects of heterogeneity on solute dispersion in

time and space will refine solute transport models in aquifers previously characterised as homogeneous, such as the Lower Grès Vosgien Formation.

6. REFERENCES

Åberg, S.C., Aberg, A.K., Korkka-Niemi, K, 2021. Three-dimensional hydrostratigraphy and groundwater flow models in complex Quaternary deposits and weathered/fractured bedrock: evaluating increasing model complexity. Hydrogeology Journal. 29, 1043-1074. https://doi.org/10.1007/s10040-020-02299-4

Ahlbrandt, T.S., 1979. Textural parameters of eolian deposits: United States Geological Survey Professional Paper 1052 p. 21-51.

Aichholzer, C., 2019. Le log complet de la stratigraphie de la zone rhénane ainsi que les modalités stratigraphiques, sédimentaires et structurales de la transition « socle-couverture ». Aplication a la géothermie profonde. PhD thesis. Université de Strasbourg. École doctorale des Sciences de la Terre et de l'Environnement (ED413), Intitut de Physique du Globe de Strasbourg (UMR7516). 546 p. (In French).

Alberti , F. A. V. 1834. Beitrag zu einer Monographiedes Bunten Sandsteins, Muschelkalks und Keupers, und die Verbindung dieser Gebilde zu einer Formation.

Aigner, T., Aspiron, U., Hornung, J., Junghans, W.-D., Kostrewa, R., 1996. Integrated outcrop analogue studies for Triassic alluvial reservoirs: Examples from southern Germany. Journal of Petroleum Geology. 19, 393-406.

Akoglu, H., 2018. User's guide to correlation coefficients. Turkish Journal of Emergency Medicine, 18, 91-93.

Alexander, 1993. A discussion on the use of analogues for reservoir geology. In: Ashton, M. (ed.), 1993. Advances in Rervoir Geology, Geological Society Special Publications. 69, 175-194.

Alexander, J., Bridge, J.S., Cheel, R.J., Leclair, S.F., 2001. Bedforms and associated sedimentary structures formed under supercritical water flows over aggrading sand beds. Sedimentology. 48, 133-152.

Alexander, J., Herbert, C.M., Fielding, C.R., Amos, K.J., 2020. Controls on channel deposits of highly variable rivers: comparing hydrology and event deposits in the Burdekin River, Australia. Sedimentology. 67, 2721-2746.

Allen, J.R.L. and Leeder, M.R., 1980. Criteria for the instability of upper-stage plane beds: Sedimentology. 27, p. 209–217. doi:10.1111/j.1365-3091.1980.tb01171.x.

Allen, J.R.L., 1982. Developments in Sedimentology: Sedimentary Structures, their Character and Physical Basis. Volume 1. 613 p.

Allen, J.R.L., 1983a. Studies in fluviatile sedimentation: bars, bars-complexes and sandstone sheets (Low sinuosity braided streams) in the Brownstones (L/ Devonian), Welsh Borders, Sedimentary Geology. 33, 237-239.

Allen, J.R.L., 1983b. Gravel overpassing on humpback bars supplied with mixed sediment: examples from the Lower Old Red Sandstone, southern Britain. Sedimentology. 30, 285-294.

Allmendinger, R. W., Cardozo, N., AND Fisher, D., 2012. Structural geology algorithms: Vectors and tensors in structural geology: Cambridge University Press.

Al-Masrahy, M.A. and Mountney, N.P., 2013. Remote sensing of spatial variability in aeolian dune and interdune morphology n the Rub' Al-Khali, Saudi Arabia. Aeolian Research. 11, 155-170.

Al-Masrahy, M.A. and Mountney, N.P., 2015. A classification scheme for fluvial-aeolian system interaction in desert-margin settings. Aeolian Research. 17, 67-88.

Alshakri, J., Hampson, G., Jacquemyn, C., Jackson, M., Petrovskyy, D., Geiger, S., Silva, J., Judice, S., Rahman, F., Costa Sousa, M., 2022. A Screening Assessment of the Impact of Sedimentological Heterogeneity on CO 2 Migration and Stratigraphic-Baffling Potential: Sherwood and Bunter Sandstones, UK. Geological Society, London, Special Publications. 528. 10.1144/SP528-2022-34.

Anderson, M.P., Woessner, W.W., Hunt, R.J., 2015. Applied Groundwater Modeling: Simulation of Flow and Advective Transport. Academic Press. Second Edition. 602 p.

Aquilina, L., Pauwels, Genter, A., Fouillac, C., 1997. Water-rock interaction processes in the Triassic sandstone and the granitic basement of the Rhine Graben: Geochemical investigation of a geothermal reservoir. Geochimica et Cosmochimica Acta. 61, N° 20, 4281-4295.

Arévalo, O.J., Colombera, L., Mountney, N.P., Basilici, G., Soares, M.V.T., 2022. Variations in water discharge at different temporal scales in a mud-prone alluvial

succession: The Paleocene-Eocene of the Tremp-Graus Basin, Spain. Sedimentary Geology. 433, 24 p. https://doi.org/10.1016/j.sedgeo.2022.106122

Aris, R., 1958. On the dispersion of linear kinematic waves, Proc. R. Soc. A and B, 245(1241), 268, doi:10.1098/rspa.1958.0082.

Banks E.W., Morgan, L.K., Loui, A.J.S., Dempsey, D., Wilson, S.R., 2022. Active distributed temperature sensing to assess surface water-groundwater interaction and river loss in braided river systems. Journal of Hydrology. 615, 12 p. https://doi.org/10.1016/j.jhydrol.2022.128667

Barrieu, P., Bellamy, N., Sinclair-Desgagné, B., 2017. Assessing contaminated land cleanup costs and strategies. Applied Mathematical Modelling. 42, 478-492. http://dx.doi.org/10.1016/j.apm.2016.10.015

Basilici, G, Mesquita, A.F., Soares, M.V.T.S., Janočko, J., Mountney, N.P., Colombera, L., 2021. A Mesoproterozoic hybrid dry-wet aeolian system: Galho do Miguel Formation, SE Brazil. Precambrian Research. 359, 23 p.

Bauer, J.F.; Krumbholz, M.; Luijendijk, E.; Tanner, D.C., 2019. A numerical sensitivity study of how permeability, porosity, geological structure, and hydraulic gradient control the lifetime of a geothermal reservoir. Solid Earth. 10, 2115-2135.

Belle, G.V., Martin, D.C., 1993. Sample size as a function of Coefficient of Variation and Ration of Means. The American Statistician. 43, N°3, 165-167.

Bhattacharyya, A., Morad, S., 1993. Proterozoic braided ephemeral fluvial deposits: an example from the Dhandraul Sandstone Formation of the Kaimur Group, Son Valley, central India. Sedimentary Geology. 84, 101-114

Bjørlykke, 2014. Relationships between depositional environments, burial history, and rock properties. Some principal aspects of diagenetic process in sedimentary basins. Sedimentary Geology. 301, 1-14. http://dx.doi.org/10.1016/j.sedgeo.2013.12.002

Blevins, R.D., 1984. Applied Fluid Dynamics Handbook, Van Nostrand Reinhold Co., Inc., New York.

Bofill, L.M., Bozetti, G., Schäfer, G., Ghienne, J.F., Schuster, M., Scherer, C., Souza, E., 2024. Quantitative facies analysis of a fluvio-aeolian system: Lower Triassic

Buntsandstein Group, eastern France. Sedimentary Geology. 465, 106634. 22 p. https://doi.org/10.1016/j.sedgeo.2024.106634

Bongiolo, D.E., Scherer, C.M.S., 2010. Facies architecture and heterogeneity of the fluvial-aeolian reservoirs of the Sergi formation (Upper Jurassic), Reconcavo Basin, NE Brazil. Marine and Petroleum Geology. 27, 1885 – 1897.

Botsch, R.E., 2011. Chapter 12. Significance and Measures of Association. Political Science Program. Aiken University of South Carolina. Accessed on July 26th, 2023. https://polisci.usca.edu/apls301/Text/Chapter%2012.%20Significance%20and%20Measures%20of%20Association.htm

Bouly, S., Demassieux, L., 1996. Structure, caractéristiques et fonctionnement du réservoir aquifère des Grès Inférieurs du Trias en Lorraine. La houille blanche (76). In French.

Bourbie, T., & Zinszner, B., 1985. Hydraulic and acoustic properties as a function of porosity in Fontainebleau sandstone. Journal of Geophysical Research: Solid Earth, 90(B13), 11524-11532.

Bourquin, S., and Guillocheau, F., 1996. Keuper stratigraphic cycles in the Paris Basin and comparison with cycles in other Peritethyan basins (German Basin and Bresse-Jura Basin). Sedimentary Geology. 105. 159-182. 10.1016/0037-0738(95)00153-0.

Bourquin, S., and Durand, M., 2006. International field workshop on “The Triassic of Eastern France”, October 2-7, 2006. HAL archives-ouvertes.fr. 81p.

Bourquin, S., Peron, S., Durand, M., 2006. Lower Triassic sequence stratigraphy of the western part of the Germanic Basin (west of Black Forest): Fluvial system evolution through time and space. Sedimentary Geology. 186, 187 – 211.

Bourquin, S., Guillocheau, F., Peron, S., 2009. Braided rivers within an arid alluvial plain (example from the Lower Triassic, western German Basin): recognition criteria and expression of stratigraphic cycles. Sedimentology. 56, p. 2235 – 2264. doi: 10.1111/j.1365-3091.2009.01078.x

BRGM, 2002. Grès du Trias inférieur (GTI) – Code 210. Atlas hydrogéologique du bassin Rhin-Meuse (Octobre 2002). https://sigesrm.brgm.fr/La-BD-RHF-R-V1-dans-le-bassin-Rhin-Meuse, accessed on 10th of May, 2023.

BRGM, 2023. Plan d'aménagement et de gestion durable (PAGD) du SAGE Nappe des Grès du Trias Inférieur. Département des Vosges. https://www.gesteau.fr/document/sage-nappe-des-gres-du-trias-inferieur-plan-damenagement-et-de-gestion-durable Accessed on 20th of July, 2024.

Bridge, J.S., 2003, Rivers and Floodplains: Oxford, U.K., Blackwell, 491 p.

Bristow C. and Mountney N.P., 2013. Aeolian Stratigraphy. In: SHRODER, J.F., 2013. Treatise on Geomorphology. 11, p. 246-268. San Diego: Academic Press.

Brookfield, M.E., 2008. Palaeoenvironments and palaeotectonics of the arid to hyperarid intracontinental latest Permian- late Triassic Solway basin (U.K.). Sedimentary Geology. 210, 27-47.

Brookfield, M.E., 1992. Eolian systems. In: Walker, R.G., James, N.P. (Eds.), Facies Models - in Response to Sea Level Change.

Brookfield, M.E., and Silvestro, S., 2010. Eolian systems. In: James, N.P., and Dalrymple, R.W., 2010. Facies Models 4. Geotext6. 574 p.

Bulmer, M., 2024. A Portable Introduction to Data Analysis. The University of Queensland. DOI: https://doi.org/10.14264/12dc235

Burkardt, J., 2023. The Truncated Normal Distribution. Department of Scientific Computing, Florida State University. Accessed through https://people.sc.fsu.edu/~jburkardt/presentations/truncated normal.pdf.

Busch, B.; Spitzner, A.D.; Adelmann, D.; Hilgers, C., 2022. The significance of outcrop analog data for reservoir quality assessment: A comparative case study of Lower Triassic Buntsandstein sandstones in the Upper Rhine Graben. Marine and Petroleum Geology. 141, 105701. https://doi.org/10.1016/j.marpetgeo.2022.105701

Cain, S.A. and Mountney, N.P., 2009. Spatial and temporal evolution of a terminal fluvial fan system: the Permian Organ Rock Formation, South-east Utah, USA. Sedimentology. 56. 1774-1800. Doi: 10.1111/j.1365-3091.2009.01057.x

Caputo, M.V., 2023. Adhesion-ripple structures in Quaternary carbonate eolianites, San Salvador Island, The Bahamas. In: Griffing, D., Hulmann, M., and Dexter, T., 2023. Proceedings of the Third Joint Symposium on the Natural History and Geology of the Bahamas.

Cardozo, N., and Allmendinger, R.W., 2013. Spherical projections with OSXStereonet. Computers and Geosciences, 51, 193 – 205. doi:10.1016/ j.cageo.2012.07.021.

Carling, P.A., 1990. Particle over-passing on depth-limited gravel bars. Sedimentology. 37, p. 345-355.

Carr-Crabaugh, M. and Kocurek, G., 1993. Entrada Sandstone: an example of a wet aeolian system. In: The Dynamics and Environmental Context of Aeolian Sedimentary Systems. Geological Society London Special Publication. 72, 103-126.

Carr-Crabaugh, M. and Kocurek, G., 1998. Continental sequence stratigraphy of a wet eolian system: a key to relative sea-level change. Relative Role of Eustasy, Climate, and Tectonismo in Continental Rocks, SEPM Special Publication. 59, 17 p.

Castle, J.W., Molz, F.J., Lu, S., Dinwiddie, C.L., 2004. Sedimentology and fractal-based analysis of permeability data, John Henry Member, Straight Cliffs Formation (Upper Cretaceous), Utah, U.S.A. Journal of Sedimentary Research. 75, 270-284.

Castro, A.P., Guedes, C.C.F., Vesely, F.F., Silveira, D.M., Neves., L.F., 2023. Provenance, diagenesis and reservoir quality of sandstones facies of the Maracangalha Formation, Reconcavo Basin – Northeastern Brazil. Marine and Petroleum Geology. 158, 26 p. https://doi.org/10.1016/j.marpetgeo.2023.106548

Chandler, M. A., Kocurek, G., Goggin, D.J., Lake, L.W., 1989. Effects of Stratigraphic Heterogeneity on Permeability in Eolian Sandstone Sequence, Page Sandstone, Northern Arizona. The American Association of Petroleum Geologist Bulletin.73, 5, 658-668.

Clemmensen, L.B., Abrahamsen, K., 1983. Aeolian stratification and facies association in desert sediments, Arran basin (Permian), Scotland. Sedimentology. 30, 311-339.

Clemmensen, L.B., Tirsgaard, H., 1990. Sand-drift surfaces: a neglected type of bounding surface. Geology 18, 1142–1145.

Clemmensen, L.B. , 1991. Controls on aeolian sand sheet formation exemplified by the Lower Triassic of Helgoland. Acta Mechanica, 2: 161-170.

Collinson, J., Mountney, N., Thompson, D., 2006. Sedimentary structures. Third edition. Terra Publishing. 359 p.

Collinson, J.D., 1969. The sedimentology of the Grindslow shales and the Kinderscout Grit: a deltaic complex in the Namurian of northern England. Journal of Sedimentary Research. 39, 194-221.

Collinson, J.D., 1996. Alluvial sediments. In: Reading, H.G., 1996. Sedimentary Environments: Processes, Facies and Stratigraphy. University of Oxford. 3rd Edition.

Collinson, J.D., Mountney, N., Thompson, D., 2006. Sedimentary structures. 3rd Edition. Terra Publishing, England, 292 p.

Colombera, L., Mountney, N.P., McCaffrey, W.D., 2013. A quantitative approach to fluvial facies models: Methods and example results. Sedimentology. 60(6). 1526-1558. https://doi.org/10.1111/sed.12050

Colombera, L., Mountney, N.P., 2019. The lithofacies organization of fluvial channel deposits: A meta-analysis of modern rivers. Sedimentary Geology. 383, 16-40. https://doi.org/10.1016/j.sedgeo.2019.01.011

Colombera, L., Reesink, A.J.H., Duller, R.A., Jeavons, V.A., Mountney, N.P., 2024. The thickness variability of fluvial cross-strata as a record of dune disequilibrium and palaeohydrology proxy: A test against channel deposits. Sedimentology. 71, 590-618.. doi: 10.1111/sed.13147

Comolli, A., Hakoun, V., Dentz, M., 2019. Mechanisms, Upscaling, and Prediction of Anomalous Dispersion in Heterogeneous Porous Media. Water Resources Research. 55, 8197-8222. https://doi.org/10.1029/2019WR024919

Cosgrove, G.I.E., Colombera, L., Mountney, N.P., 2022. The role of subsidence and accommodation generation in controlling the nature of the aeolian stratigraphic record. Journal of the Geological Society. 179, 23 p. https://doi.org/10.6084/m9.figshare.c.5515695.v1

Cowan, G., 1993. Identification and significance of aeolian deposits within the dominantly fluvial Sherwood Sandstone Group of the East Irish Sea Basin UK. In: NORTH, C.P. and PROSSER, D.J., 1993. Characterization of Fluvial and Aeolian Reservoirs. Geological Society Special Publication. No 73, 231-245.

Coyler, A., Butler, A., Peach, D., Hughes, A., 2021. How groundwater time series and aquifer property data explain heterogeneity in the Permo-Triassic sandstone aquifers of the Eden Valley, Cumbria, UK. Hydrogeology Journal. https://doi.org/10.1007/s10040-021-02437-6

Crooijmans, R.A., Willems, C.J.L., Nick, H.M., Bruhn, D.F., 2016. The influence of facies heterogeneity on the doublet performance in low-enthalpy geothermal sedimentary reservoirs. Geothermics. 64, 209-219. http://dx.doi.org/10.1016/j.geothermics.2016.06.004

Crowell, C.J., 1955. Directional-Current Structures from the Prealpine Flysch, Switzerland. Bulletin of the Geological Society of America. 68, 1361 – 1384.

Dachroth, W., 1985. Fluvial sedimentary styles and Associated Depositional Environments in the Buntsandstein Wes of River Rhine in Saar Area and Pfalz (F.R. Germany) and Vosges (France). In: Mader, D., Aspects of fluvial sedimentation in the Lower Triassic Buntsandstein of Europe. Lecture notes in Earth Sciences. 4: 197-248, Berlin/Heidelberg / New York / Tokio (Springer).

Dagan, G., 1988. Review of stochastic theory of transport in groundwater flow. In: Custodio, E., Gurgui, A., Ferreira, J.P.L., 1988. Groundwater Flow and Quality Modelling. Reidel Publishing Company. 224, 834 p.

Dagan, G., 1990. Transport in heterogeneous porous formations: Spatial moments, ergodicity, and effective dispersion. Water Resources Research. 26, 1281-1290. https://doi.org/10.1029/WR026i006p01281

Dai, Z.; Ritzi Jr., R.W.; Huang, C.; Rubin, Y.N.; Dominic, D.F., 2004. Transport in heterogeneous sediments with multimodal conductivity and hierarchical organization across scales. Journal of Hydrology. 294, p. 68-86. https://doi.org/10.1016/j.jhydrol.2003.10.024

Dalrymple, R.W., 2010. Interpreting sedimentary successions: Facies, Facies Analysis and Facies Models. In: James, N.P., and Dalrymple, R.W., 2010. Facies Models 4. Geotext6. 574 p.

Davidson, S.K., Hartley, A.J., Weissmann, G.S., Nichols, G.J., Scuderi, L.A., 2013. Geomorphic elements on modern distributive fluvial systems. Geomorphology. 180-181, 82-95. http://dx.doi.org/10.1016/j.geomorph.2012.09.008

Davis, J.C., 2002. Statistics and Data Analysis in Geology, Third Edition: John Wiley and Sons, 638 p.

Davis, J.M., Lohmann, R.C., Phillips, F.M., Wilson, J.L., Love, D.W., 1993. Architecture of the Sierra Ladrones Formation, central New Mexico: Depositional controls on the permeability correlation structure. Geological Society of America Bulletin. 105, 998-1007.

De Raaf J.F.M., Reading, H.G., and Walker, R.G., 1965. Cyclic sedimentation in the Lower Westphalian of North Devon, England. Sedimentology. 4, 1 - 52.

De Ros, L.F., Goldberg, K., Abel, M., Victorinetti, F., Mastella, L. and Castro, E., 2007. Advanced acquisition and management of petrographic information from reservoir rocks using the PETROLEDGE® System. In: AAPG Annual Conference and Exhibition, 1-4 April, Long Beach, USA, Extended Abstracts, 6.

DeLuca, J.L. and Eriksson, K.A., 1989. Controls on synchronous ephemeral- and perennial-river sedimentation in the middle sandstone member of the Triassic Chinle Formation, northeastern New Mexico, U.S.A. Sedimentary Geology. 61, 155-175.

Deynoux, M., Duringer, P., Gall, J.C., Grauvogel-Stamm, L., Simon, G., 1997. Permian and Triassic of the northern Vosges mountains. Field trip guide book -18th European Regional Meeting of Sedimentology, Heidelberg, September 2-4. 11 p.

Diersch, H.J.G., 2014. FEFLOW: Finite Element Modeling of Flow, Mass and Heat Transport in Porous and Fractured Media. Springer, Heidelberg, Germany. https://doi.org/10.1007/978-3-642-38739-5_1

Dixon, J.C., 2014. Lag Deposit. In: Encyclopedia of Planetary Landforms. Springer, New York, NY. https://doi.org/10.1007/978-1-4614-9213-9_214-1

Dixon, S.A., Summers, D.M., Surdam, R.C., 1989. Diagenesis and preservation of porosity in Norphlet formation (Upper Jurassic), southern Alabama. AAPG Bull. 73 (6), 707 - 728.

Dreyer, T., 1993. Geometry and facies of large-scale flow units in fluvial-dominated fan-delta-front sequences. In: Ashton, M. (ed.), 1993. Advances in Reservoir Geology. Geological Society Special Publication. 69, 135-174.

Dugamin, E.J.M., Richard, A., Cathelineau, M., Boiron, M.C., Despinois, F., Brisset, A., 2021. Groundwater in sedimentary basin as potential lithium resource: a global prospective study. Scientific Reports, Nature Portfolio. https://doi.org/10.1038/s41598-021-99912-7

Duller, R.A., Mountney, N.P., Russell, A.J., Cassidy, N.C., 2008. Architectural analysis of a volcaniclastic jökulhlaup deposit, southern Iceland: sedimentary evidence for supercritical flow. Sedimentology. 55, 939–964.

Durand, M., 1978. Paléocourants et reconstituition paléogeographique: l'exemple du Buntsandstein dans les Vosges Méridionales, Thesis, Université de Nancy-I. (In French).

Durand, M., and Bourquin, S., 2013. Criteria for the identification of ventifacts in the geological record: A review and new insights. Comptes Rendus Geoscience. 345. 111-125. 10.1016/j.crte.2013.02.004.

Duringer, P., Aichholzer, C., Orciani, S., Genter, A., 2019. The complete lithostratigraphic section of the geothermal wells in Rittershoffen (Upper Rhine Graben, eastern France): a key for future geothermal wells. BSGF Earth Sciences Bulletin 2019, 190008 Available at www.bsgf.fr.

Dutton, S.P., Loucks, R.G., Day-Stirrat, R.J., 2012. Impact of regional variation in detrital mineral composition on reservoir quality in deep to ultradeep lower Miocene sandstones, western Gulf of Mexico. Marine and Petroleum Geology. 35, 139-153. doi:10.1016/j.marpetgeo.2012.01.006

Ellis, D., 1993. The Rough Gas Field: distribution of Permian aeolian and non-aeolian reservoir facies and their impact on field development. In: North, C.P. & Prosser, D.J. (eds), 1993. Characterization of Fluvial and Aeolian Reservoirs. Geological Society Special Publications. 73, 265-277.

Ethridge, E.G., Skelly, R.L., Bristow, C.S., 1999. Avulsion and crevassing in the sandy, braided Niobrara River: complex response to base-level rise and aggradation. Fluvial sedimentology - Special Publication International Association of Sedimentologists. 28, 179-191. IBSN: 978-0-632-05354-4.

Farquharson, J. I., Heap, M. J., Lavallée, Y., Varley, N. R., & Baud, P., 2016. Evidence for the development of permeability anisotropy in lava domes and volcanic conduits. Journal of Volcanology and Geothermal Research, 323, 163-185.

Farraj, A.A., Harvey, A.M., 2004. Late Quaternary interactions between aeolian and fluvial processes: a case study in the northern UAE. Journal of Arid Environments. 56, 235-248.

Fetting, C., 2020. The European Green Deal. ESDN Report, December 2020, ESDN Office, Vienna.

Fielding, C.R., 2006. Upper e sheets, lenses and scour fills: Extending the range of architectural elements for fluvial sediment bodies. Sedimentary Geology. 170:1-4, p. 227-240. doi: 10.1016/j.sedgeo.2006.05.009

Fielding, C.R., Allen, J.P., Alexander, J., Gibling, M.R., 2009. Facies model for fluvial systems in the seasonal tropics and subtropics. Geology. 37, n°7, 623-626. doi: 10.1130/G25727A.1

Fielding, C.R., Ashworth, P.J., Best, J.L., Prokocki, E.W., Smith, G.H.S., 2012. Tributary, distributary and other fluvial patterns: What really represents the norm in the continental rock record? Sedimentary Geology. 261-262, 15-32. doi:10.1016/j.sedgeo.2012.03.004

Fielding, C.R., Alexander, J., Allen, J.P., 2018. The role of discharge variability in the formation and preservation of alluvial sediment bodies. Sedimentary Geology. v.365, 1-20.

Fischer, C., Gaupp, R., Dimke, M., Sill, O., 2007. A 3D high resolution model of bounding surfaces in aeolian-fluvial deposits: an outcrop analogue study from the Permian Rotliefend, Northern Germany. Journal of Petroleum Geology. 30, 257-274.

Fisher, R.S., Barton, M.D., Tyler, N., 1992. Quantifying reservoir heterogeneity through outcrop characterization: 2. Architecture, lithology, and permeability

distribution of a seaward-stepping fluvial-deltaic sequence, Ferron Sandstone (Cretaceous), Central Utah. Topical report 11/01/89 – 11/30/92. Bureau of Economic Geology. 90 p.

Flexer, V., Baspineiro, C.F., Galli, C. I., 2018. Lithium recovery from brines: A vital raw material for green energies with a potential environmental impact in its mining and processing. Science of The Total Environment. 639, 188-1204. https://doi.org/10.1016/j.scitotenv.2018.05.223

Folk, R.L., Ward, W., 1957. Brazos River bar: a study in the significance of grain size parameters. Journal of Sedimentary Petrology. 27, 3-26.

Folk, R.L., Andrews, P.B., Lewis, D.W., 1970. Detrital sedimentary rock classification and nomenclature for use in New Zeland. New Zealand Journal of Geology and Geophysics. 13, 937-968. http://dx.doi.org/10.1080/00288306.1970.10418211

Folk, R.L., 1980. Petrology of sedimentary rocks. Hemphill, Austin.

Fries, D., Lebouil, S., Maurer, V., Martin, C., Baujard, C., Ravier, G., Bobuais, R., Amari, S., 2022. Lithium extraction through pilot scale test under real geothermal conditions of the Upper Rhine Graben. European Geothermal Congress, 2022. Berlin, Germany, 17 – 21 October, 2022. 8 p.

Frind, E.O., Sudicky, E.A., Schellenberg, S.L., 1987. Micro-scale modelling in the study of plume evolution in heterogeneous media. In: Custodio, E., Gurgui, A., Ferreira, J.P.L., 1988. Groundwater Flow and Quality Modelling. Reidel Publishing Company. 224, 834 p.

Fryberger, S.G., and Schenk, C., 1981. Wind sedimentation tunnel experiments on the origins of aeolian strata. Sedimentology. 28, 805 – 821.

Fryberger, S.G., Schenk, C.J., 1988. Pin stripe lamination: a distinctive feature of modern and ancient eolian sediments. Sedimentary Geology. 55. 1-15.

Fryberger, S.G., Schenk, C.J., Krystink, 1988. Stokes surfaces and the effects of near surface groundwater-table on aeolian deposition. Sedimentology. 35, 21-41.

Fryberger, S.G., 1991. A review of aeolian bounding surfaces, with examples from the Permian Minnelusa Formation, USA. In: North, C.P. & Prosser, D.J., 1993,

Characterization of Fluvial and Aeolian Reservoirs, Geological Society Special Publication, No 73, 167-197.

FRYBERGER, S. G., HESP, P., HASTINGS, K., 1992. Aeolian granule ripple deposits, Namibia. Sedimentology. 39, 319–331. doi:10.1111/j.1365-3091.1992.tb01041.x

Galeazzi, C.P., Almeida, R.P., Prado, A.H., 2021. Linking rivers to the rock record: Channel patterns and paleocurrent circular variance. Geology. p. 1402-1407. https://doi.org/10.1130/G49121.1

Gall J., 1972. Permanence du régime de chenaux et de flaques dans les Vosges du Nord pendant toute la durée du Buntsandstein. In: Sciences Géologiques. Bulletin, tome 25, n°4, 1972. Sédimentologie et géochimie de la surface. 307- 322. (In French).

Gall, J., Durand, M., Muller, E., 1977. Le Trias de part et d'autre du Rhin. Corrélations entre les marges et le centre du bassin germanique. Bulletin du B.R.G.M. (deuxième série). Section IV, n°3 – 1977, 193-204. (In French).

Gelhar, L.W., Gutjahr, A.L., Naff, R.L., 1979. Stochastic analysis of macrodispersion in stratified aquifer. Water Resources Research. 15, 11 p.

Gelhar, L.W., Welty, C., Rehfeldt, K.R., 1992. A Critical Review of Data on Field-Scale Dispersion in Aquifers. Water Resources Research. 28, 1955-1974.

Geluk, M., McKie, T., Kilhams, B., 2018. An introduction to the Triassic: current insights into the regional setting and energy resource potential of NW Europe. In Kilhams, B., Kukla, P.A., Mazur, S., McKie, T., Mijnlieff, H.F., Van Ojik, K., 2018. Mesozoic Resource Potential in the Southern Permian Basin. Geological Society, London, Special Publications, 469. https://doi.org/10.1144/SP469.1

Gérard, A., Genter, A., Kohl, T., Lutz, P., Rose, P., Rummel, F., 2006. The deep EGS (Enhanced Geothermal System) project at Soultz-sous-Forêts (Alsace, France). Geothermics. 35, 473-483.

Gerdes, G., 2007. Structures left by modern microbial mats in their host sediments. Chapter 2 In: Atlas of microbial mat features preserved within the clastic rock record,

Shieber, J., Bose, P.K., Eriksson, P.G., Banerjee, S., Sarkar, S., Altermann, W., and Catuneanu, O., Elsevier, 5-38.

Ghienne, J.F, Deynoux, M, Jeannetter, D., 1994. Structures sédimentaires, discontinuités et caractères pétrophysiques des grès du Buntsandstein des Vosges du Nord, Trias de l'Est de la France. C.R. Acad. Sci. Paris, t. 319, série II, 1351 - 1358. (In French, abstract in English).

Ghienne, J.F, Girard, F., Moreau, J., Rubino, J.L., 2010. Late Ordovician climbing-dune cross-stratification: a signature of outburst floods in proglacial outwash environments? Sedimentology. 57, 1175-1198. doi: 10.1111/j.1365-3091.2009.01142.x

Ghinassi, M., Magi, M., Sagri, M., Singer, B.S., 2004. Arid climate 2.5 Ma in the Plio-Pleistocene Valdrano Basin (Northern Apennines, Italy). Paleogeography, Paleoclimatology, Paleoecology. 207, 37-57. doi:10.1016/j.palaeo.2004.01.020

Glaas, C., Vidal., J., Genter, A., 2021. Structural characterization of naturally fractured geothermal reserovoirs in the central Upper Rhine Graben. Journal of Structural Geology. 148, 104370. https://doi.org/10.1016/j.jsg.2021.104370

Goggin, D.J., Chandler, M.A., Kocurek, G., Lake, L.W., 1992. Permeability transects of eolian sands and their use in generating random permeability fields. Society of Petroleum Engineers Evaluation. 10 p.

Goupil, M., Heap, M., Baud, P., 2022. Permeability anisotropy in sandstones from the Soults-sous-Forêts geothermal reservoir (France): implications for large-scale fluid flow modelling. Geothermal Energy. 10:32, 23 p. https://doi.org/10.1186/s40517-022-00243-1

Griffiths, L., Heap, M. J., Wang, F., Daval, D., Gilg, H. A., Baud, P., Schmittbuhl, J., Genter, A.., 2016. Geothermal implications for fracture-filling hydrothermal precipitation. Geothermics, 64, 235-245.

Grimmer, J.C., Ritter, J.R.R., Eisbacher, G.H., Fielitz, W., 2017. The Late Variscan control on the location and asymmetry of the Upper Rhine Graben. International Journal of Earth Sciences. 106, 827-853.

Gross, E.C., Carr, M., Jobe, Z.R., 2022. Three-dimensional bounding surface architecture and lateral facies heterogeneiry of a wet aeolian system: Entrada Sandstone, Utah. Sedimentology. 70, 145-178.

Guillocheau F., Peron S, Bourquin S., Dagallier G. et Robin C., 2002. Les sédiments fluviatiles (faciès Buntsandstein) du Trias inférieur et moyen de l'Est du Bassin de Paris. Bull. Information Géol. Bassin de Paris, 39, 5-12.

Guillocheau, F., Robin, C., Allemand, P., Bourquin, S., Brault, N., Dromart, G., Friedenberg, R., Garcia, J.P., Gaulier, J.M., Gaumet, F., Grosdoy, B., Hanot, F., Le Strat, P., Mettraux, M., Nalpas, T., Prijac, C., Rigollet, C., Serrano, O., Grandjean, G., 2000. Meso-Cenozoic geodynamic evolution of the Paris Basin: 3D stratigraphic constraints. Geodin. Acta. 13, 189–246

Haffen, S. ; Geraud, Y. ; Diraison, M. ; Dezayes, C., 2013. Determination of fluid-flow zones in a geothermal sandstone reservoir using thermal conductivity and temperature logs. Geothermics. 46, 32-41. https://doi.org/10.1016/j.geothermics.2012.11.001

Hajek, E.A., Heller, P.L., Sheets, B.A., 2010. Significance of channel-belt clustering in alluvial basins. Geology. 38, n°6, 535-538. doi: 10.1130/G30783.1

Hakoun, V., Comolli, A., Dents, M., 2019. Upscaling and Prediction of Lagrangian velocity dynamics in heterogeneous porous media. Water Resources Research. 55, 3976-3996. https://doi.org/10.1029/2018WR023810

Hansford, M.R., Plink-Björklund, P., 2020. River discharge variability as the link between climate and fluvial fan formation. Geology. 5 p. https://doi.org/10.1130/G47471.1

Hans-Jörg, G.D., 2014. Finite Element Modeling of Flow, Mass, and Heat Transport in Porous and Fractured Media. Springer Berlin, Heidelberg. 996 p. https://doi.org/10.1007/978-3-642-38739-5

Hartley, A.J., Weissmann, G.S., Nichols, G.J., Warwick, G.L., 2010. Large distributary fluvial systems: characteristics, distribution, and controls on development. Journal of Sedimentary Research. 80, 167-183. DOI: 10.2110/jsr.2010.016

Hartley, A.J., Owen, A., 2022. Paleohydraulic analysis of an ancient distributive fluvial system. Journal of Sedimentary Research. v.92, 445-459. DOI: 10.2110/jsr.2021.062

Havholm, K.G. and Kocurek, G., 1994. Factors controlling aeolian sequence stratigrapgy: clues from super bounding surface features in the Middle Jurassic Page Sandstone. Sedimentology. 41, 913-934.

Heap, M. J., & Kennedy, B. M., 2016. Exploring the scale-dependent permeability of fractured andesite. Earth and Planetary Science Letters, 447, 139-150.

Heap, M. J., 2019. The influence of sample geometry on the permeability of a porous sandstone. Geoscientific Instrumentation, Methods and Data Systems, 8(1), 55-61.

Heap, M. J., Kushnir, A. R., Gilg, H. A., Wadsworth, F. B., Reuschlé, T., & Baud, P., 2017. Microstructural and petrophysical properties of the Permo-Triassic sandstones (Buntsandstein) from the Soultz-sous-Forêts geothermal site (France). Geothermal Energy, 5, 1-37.

Heidsiek, M., Butscher, C., Blum, P., Fischer, C., 2020. Small-scale diagenetic facies heterogeneity controls porosity and permeability pattern in reservoir sandstones. Environmental and Earth Sciences. 79:425. 14 p. https://doi.org/10.1007/s12665-020-09168-z

Herivaux, C., Marechal, J., 2019. Prise en compte des services dépendants des aquifères dans les démarches d'évaluation des services écosystémiques. Rapport final, BRGM/RP-68929-FR. 107 p. (In French).

Herr, M., Schäfer, G., Spitz, K., 1989. Experimental studies of mass transport in porous media with local heterogeneities. Journal of Contaminant Hydrology. 4, 127-137.

Herweijer, J.C., 1997. Sedimentary heterogeneity and flow towards a well: Assessment of flow through heterogeneous formations. PhD Thesis. Vrije Universiteit. 273 p.

Hesp, P.A., Walker, I.J., 2013. Coastal dunes. In: Shroder, J., Lancaster, N., Sherman, D.J.; Baas, A.C.W., 2013. Treatise on Geomorphology. Academic Press, San Diego, CA, 11. Aeolian Geomorphology, 328-355.

Hjellbakk, A., 1997. Facies and fluvial architecture of a high-energy braided river: the Upper Proterozoic Segglodden Member, Varanger Peninsula, northern Norway. Sedimentary Geology. 131-161.

Høimyr, O., Kleppe, A., Nystuen, J.P., Effects of heterogeneities in a braided stream channel sandbody on the simulation of oil recovery: a case study from the Lower Jurassic Statfjord Formation, Snorre Field, North Sea. From: Ashton, M. (ed.), 1993. Advances in Reservoir Geology. Geological Society Special Publication. 69, 105-134.

Hornung, J.; Aigner, T., 1999. Reservoir and aquifer characterization of fluvial architectural elements: Stubensandstein, Upper Triassic, southwest Germany. Sedimentary Geology. 129, 215-280. https://doi.org/10.1016/S0037-0738(99)00103-7

Hossain, S., Hampson, G.J., Jacquemyn,C., Jackson, M.D., Chiarella, D., 2024. Permeability characterisation of sedimentological facies in the Bunter Sandstone Formation, Endurance CO2 Storage Site, Offshore UK. International Journal of Greenhouse Gas Control. 135, 104140. https://doi.org/10.1016/j.ijggc.2024.104140

Hosseini, E., Gholami, R., Hajivand, F., 2019. Geostatistical modeling and spatial distribution anaysis of porosity and permeability in the Shurijeh-B reservoir of Khangiran gas field in Iran. Journal of Petroleum Exploration and Production Technology. 9, 1051-1073. https://doi.org/10.1007/s13202-018-0587-4

Hounslow, M., and Ruffell, A., 2006. Triassic: seasonal rivers, dusty deserts and saline lakes. In P. F. Rawson, & P. Brenchley (Eds.), The Geology of England & Wales. (pp. 295-325). Geological Society of London.

Howell, J., Mountney, N., 1997. Climatic cyclity and accommodation space in arid to semi-arid systems: an example from the Rotliegend group of the UK Southern North Sea. In: Ziegler, K., Turner, P., Daines, S.R. (Eds.), Petroleum Geology of the Southern North Sea: Future Potential. Geological Society, London, Special Publication, vol. 123, pp. 63e86.

Howell, J.A., Martinius, A.W., Good, T.R., 2014. The application of outcrop analogues in geological modelling: a review, present status and future outlook. Geological Society of London. Special Publications. 387 (1), 1–25. https://doi.org/10.1144/sp387.12.

Höyng, D., D'Affonseca, F.M., Bayer, P., Oliveira, E.G., Perinotto, J.A.J., Reis, F., Weiß, H., Grathwohl, P., 2014. High-resolution aquifer analog of fluvial-aeolian sediments of the Guarani aquifer system. Environmental Erath Sciences. 71, 3081 – 3094.

Hudon-Gagnon, E., Chesnaux, R., Cousineau, P.A., Rouleau, A., 2015. A hydrostratigraphic simplification approach to build 3D groundwater flow numerical models: example of a Quaternary deltaic deposit aquifer. Environ Earth Sci 74, 4671–4683. https://doi.org/10.1007/s12665-015-4439-y

Hunter, R.E., 1977a. Basic types of stratification in small eolian dunes. Sedimentology. 24, 361 – 387.

Hunter, R.E., 1977b. Terminology of cross-stratified sedimentary layers and climbing-ripple structures. Journal of Sedimentary Petrology. 47, 697 – 706.

Istok, J.D., 1989. Groundwater modelling by the finite element method. American Geophysical Union Water Resources monograph. ISBN 0-87590-317-7

James, N.P., and Dalrymple, R.W., 2010. Facies Models 4. GEOtext 6. Geological Association of Canada.

Jerram, D.A., 2001. Visual comparators for degree of grain-size sorting in two and three-dimensions. Computers & Geosciences. 27, 485-492. https://doi.org/10.1016/S0098-3004(00)00077-7

Jones, L.S. and Blakey, R.C., 1997. Eolian-fluvial interaction in the Page Sandstone (Middle Jurassic) in south-central Utah, USA – a case study of erg-margin processes. Sedimentary Geology. 109, 181-198.

Jussel, P., 1989. Stochastic description of typical inhomogeneities of hydraulic conductivity in fluvial gravel deposits. In: Kobus, H.E., Kinzelbach, W., 1989. Proceedings of the International Symposium on Contaminant Transport in Groundwater, Stuttgart, 4-6 April 1989.

Kahn, J.S., 1956. Analysis and distribution of packing properties in sand-sized sediments: 2. The distribution of the packing measurements and an example of packing analysis. The Journal of Geology. 64, 6.

Kaufmann, R.S. (1998). Fick's law. In: Geochemistry. Encyclopedia of Earth Science. Springer, Dordrecht. https://doi.org/10.1007/1-4020-4496-8_123

Kendall, M. G., 1938. A New Measure of Rank Correlation, Biometrika, 30, 81-93.

Kestin, J., Sokolov, M., Wakeham, W.A., 1978. Viscosity of Liquid Water in the Range -8°C to 150°C. J. Phys. Chem. Ref. Data. 7, 3.

Kifumbi, C., Scherer, C.M.S., Michel, R.D.L., Reis, A.D., Guadagnin, F., Souza, E.G., Ferronato, J.P.F., JONES, F.H., 2023. Spatial and temporal variation in the evolution of ancient aeolian dune-field. The Pennsylvanian Piaui Formation (Parnaiba Basin), Brazil. Sedimentary Geology. 451. https://doi.org/10.1016/j.sedgeo.2023.106398

Kinzelbach, W., 1988. A random walk method in pollutant transport simulation. In: Custodio, E., Gurgui, A., Ferreira, J.P.L., 1988. Groundwater Flow and Quality Modelling. Reidel Publishing Company. 224, 834 p.

Kocurec, G., Nielson, J., 1986. Conditions favourable for the formation of warm-climate aeolian sand sheets. Sedimentology. 33, 795 – 816. https://doi.org/10.1111/j.1365-3091.1986.tb00983.x.

Kocurek, G. and Fielder, G., 1982. Adhesion structures. Journal of Sedimentary Petrology. 2. No. 4, 1229-1241.

Kocurek, G. and Nielson, J., 1986. Conditions favourable for the formation of warm climate sand seas. Sedimentology. 33, 795-816.

Kocurek, G., 1988. First-order and super bounding surfaces in eolian sequences – Bounding surfaces revisited. Sedimentary Geology. 56, 193-206.

Kocurek, G., 1991. Interpretation of ancient eolian sand dunes. Annu. Rev. Earth Planet. Sci. 19, 43-75.

Kocurek, G., Fielder, G., 1982. Adhesion structures. Journal of Sedimentary Petrology 2 (4), 1229–1241.

Kölbel, L., Kölbel, T., Sauter, M., Schäfer, T., Siefert, D., 2020. Identification of fracture zones in geothermal reservoirs in sedimentary basins: A radionuclide-based approach. Geothermics. 85, 10 p.

Kölbel, T, Genter, A., 2017. Enhanced geothermal systems: the Soultz-sous-Forêts project, 243–248. In: UYAR, T.S., 2017. Towards 100% Renewable Energy: Techniques, Costs and Regional Case-Studies. https://doi.org/ 10.1007/978-3-319-45659-1_25

Koltermann, C.E. & Gorelick, S.M., 1996. Heterogeneity in sedimentary deposits: A review of structure-imitating, process-imitating, and descriptive approaches. Water Resources Research. 32, 2617-2658.

Konikow, L.F., 2011. The Secret to Successful Solute-Transport Modeling. Ground water. 49, 144 – 159.

Kontny, A., Bush, B., Schenk, J., Khasanov, I., 2023. Characterization of pore space in Permo-Triassic sandstone from SW-Germany using the anisotropy of magnetic susceptibility. International Journal of Earth Sciences. 112, 2223 – 2246. https://doi.org/10.1007/s00531-023-02352-z

Kreft A., Zuber A., 1978. On the physical meaning of the dispersion equation and its solutions for different initial and boundary conditions. Chem. Eng. Sci 33, 1471-1480.

Kukulski, R.B., Hubbard, S.M., Moslow, T.F., Raines, M.K., 2013. Basin-scale stratigraphic architecture of upstream fluvial deposits: Jurassic-Cretaceous foredeep, Alberta basin, Canada. Journal of Sedimentary Research. 83, 704-722. DOI: 10.2110/jsr.2013.53

Kushnir, A. R., Heap, M. J., & Baud, P., 2018. Assessing the role of fractures on the permeability of the Permo-Triassic sandstones at the Soultz-sous-Forêts (France) geothermal site. Geothermics, 74, 181-189.

Kushnir, A. R., Heap, M. J., Baud, P., Reuschlé, T., & Schmittbuhl, J., 2023. Reactivation of variably sealed joints and permeability enhancement in geothermal reservoir rocks. Geothermal Energy, 11(1), 32.

Lane, T.I., Nanson, R.A., Ainsworth, R.B., Vakarelov, B.K., 2023. The Holocene Mitchell Megafan, Gulf of Carpentaria, Australia. Chapter 12 in: Wilkinson, M.J. and Gunnell, Y., 2023. Fluvial Megafans on Earth and Mars. https://doi.org/10.1017/9781108525923

Lang, J., Le Heron, D.P, Berg, J.V.D., Winsemann, 2021. Bedforms and sedimentary structures related to supercritical flows in glaciogenic settings. Sedimentology. 68, 1539 – 1579. doi: 10.1111/sed.12776

Lang, J., Winsemann, J., 2013. Lateral and vertical facies relationships of bedforms deposited by aggrading supercritical flows: From cyclic steps to humpback dunes. Sedimentary Geology. 269, 36-54. https://doi.org/10.1016/j.sedgeo.2013.08.005

Langford, R.P., 1989. Fluvial-aeolian interactions: Part I, modern systems. Sedimentology. 36, 1023-1035.

Leary, K.C.P., Ganti, V., 2019. Preserved Fluvial Cross Strata Record Bedform Disequilibrium Dynamics. Geophysical Research Letters. 47, 11 p. https://doi.org/ 10.1029/2019GL085910

Leclair, S.F., Brigde, J.S., 2001. Quantitative interpretation of sedimentary structures formed by river dunes. Journal of Sedimentary Research. 71, N 5, 713-716.

Leier, A.L., Decelles, P.G., Pelletier, J.D, 2005. Mountains, monsoons and megafans. Geology. 33, 289-292. https://doi.org/10.1130/G21228.1

Leleu, S., Hartley, A.J., Williams, B.P.J., 2009. Large-scale alluvial architecture and correlation in a Triassic pebbly braided river system, Lower Wolfville Formation (Fundy basin, Nova Scotia, Canada). Journal of Sedimentary Research. 79, 265-286. DOI: 10.2110/jsr.2009.034

Lervik, K., S., Spencer, A., M., Warrington, G., 1989. Outline of Triassic stratigraphy and structure in the central and northern North Sea. In: Collinson, J.D. (eds) Correlation in Hydrocarbon Exploration. Springer, Dordrecht. https://doi.org/10.1007/978-94-009-1149-9_14

Li, S., Yu, X, Chen, B., Li, S., 2015. Quantitative characterization of architecture elements and their response to base-level change in a sandy braided fluvial system at a mountain front. Journal of Sedimentary Research. 85, 1285-1274. DOI: http://dx.doi.org/10.2110/jsr.2015.82.

Li, W., ColomberA, L., Yue, D., Mountney, N., 2022. Controls on the morphology of braided rivers and braided bars: An empirical characterization of numerical models. Sedimentology. 21 p. doi: 10.1111/sed.13040

Liu, K., Boult, P., Painter, S., Paterson, L., 1996. Outcrop analog for sandy braided stream reservoirs: Permeability patterns in the Triassic Hawkesbury Sandstone, Sydney Basin, Australia. AAPG Bulletin. 80, 1850-1866.

Lowden, B.D., 1993. A methodology for the quantification of outcrop permeability heterogeneities through probe permeametry. PhD thesis, Department of Mineral Resources Engineering, Imperial College, the University of London. January, 1993. 332 p.

Lyster, S.J., Whittaker, A.C., Hajek, E.A., Ganti, V., 2022. Field evidence for disequilibrium dynamics in preserved fluvial cross-strata: A record of discharge variability of morphodynamic hierarchy? Earth and Planetary Sciences Letters. 579. 12p. https://doi.org/10.1016/j.epsl.2021.117355

Mader, D., 1985. Aspects of fluvial sedimentation in the Lower Triassic Buntsandstein of Europe. Lecture notes in earth sciences. 634 p.

Makeen, Y.M., Shan, X., Lawal, M., Ayinla, H.A., Su, S., Yelwa, N.A., Liang, Y., Ayuk, N.E., Du, X., 2021. Reservoir quality and its controlling diagenetic factors in the Bentiu Formation, Northeastern Muglad Basin, Sudan. Scientific Reports 11, 18442. https://doi.org/10.1038/s41598-021-97994-x

Manna, M.O., Scherer, C.M.S., Bállico, M.B., Reis, A.D., Moraes, L.V., Ferrari, L.A.B., Roisenberg, H.B., Oliveira, V.G., 2021. Changes in fluvial architecture induced by discharge variability, Jaicós Formation (Silurian-Devonian), Parnaíba Basin, Brazil. Sedimentary Geology, 420, 23 p. https://doi.org/10.1016/j.sedgeo.2021.105924.

Matheron, G., and Marsily G. D., 1980. Is transport in porous media always diffusive? A counterexample. Water Resources Research. 16, 901-917.

Matinkia, M., Hashami, R., Mehrad, M., Hajsaeedi, M.R., Velayati, A., 2023. Prediction of permeability from well logs using a new hybrid machine learning algorithm. Petroleum, 9, 108-123.

McCann, T., Pascal, C., Timmerman, M.J., Krzywiec, P., López-Gómez, J., Wetzel, A., Krawczyk, C.M., Rieke, H., Lamarche, J., 2006. Post-Variscan (and Carboniferous – Early Permian) basin evolution in Western and Central Europe. In:

Gee, D.G., and Stephenson, R.A., 2006. European Lithosphere Dynamics. The Geological Society of London, Memoirs. 32, 355-388.

McKie, T., 2011. Architecture and behavior of dryland fluvial reservoirs, Triassic Skagerrak Formation, Central North Sea. In: Davidson, S.K., Leleu, S., North, C.P. (Eds.), From River to Rock Record: The Preservation of Fluvial Sediments and their Subsequent Interpretation. 97. SEPM Special Publication, 189–214.

McLeod, J.S., Wood, J., Lyster, S.J, Valenza, J.M., Spencer, A.R.T, Whittaker, A.C., 2023. Quantitative constraints on flood variability in the rock record. Nature Communications. 14:3362. 12 p. https://doi.org/10.1038/s41467-023-38967-8.

Medici, G., Boulesteix, K., Mountney, N.P., West, L.J., Odling, N.E., 2015. Palaeoenvironmental of braided fluvial systems in different tectonic realms of the Triassic Sherwood Sandstone Group, UK. Sedimentary Geology. 329, 188-210. http://dx.doi.org/10.1016/j.sedgeo.2015.09.012

Ménillet, F., Coulombeau, C., Geissert, F., Konrad, H.J., Schwoerer, P., 1989. Notice explicative de la feuille Lembach. 1 :50.000 Geological map of France. BRGM. Orleans, 91 p. (in French).

Ménillet, F., Geissert, F., Party, J.P., Haug, E., Hoff, H., Schnaebele, R., Schumacher, E. et Van Werveke, L., (à paraître en 2015) – Carte géologique de la France à 1/50 000, feuille n° 198, HAGUENAU, 2e édition. Notice explicative par Ménillet F., Party J.P., Durand M., Genter, A.

Miall, A.D., 1977. A Review of the Braided-River Depositional Environment. Earth-Sciences Reviews. 13, 1-62.

Miall, A.D., 1985. Architectural-Element Analysis: A New Method of Facies Analysis Applied to Fluvial Deposits. Earth Science Reviews. 22, 261 – 380.

Miall, A.D., 1988. Architectural elements and bounding surfaces in fluvial deposits: anatomy of the Kayenta formation (Lower Jurassic), Southwest Colorado. Sedimentary Geology. 55, 233-262.

Miall, A.D., 2006. The Geology of Fluvial Deposits: Sedimentary Facies, Basin Analysis, and Petroleum Geology. 4th corrected printing. Springer. 599 p.

Miall, A.D., 2010. Alluvial deposits. In: James, N.P., and Dalrymple, R.W., 2010. Facies Models 4. Geotext6. 574 p.

Middleton, G.V., 1973. Johannes Walther's Law of the Correlation of Facies. Geological Society of America, Bulletin. 84, 979 – 988.

Loll, P., Moldrup, P., Schjonning, P., Riley, H., 1999. Predicting saturated hydraulic conductivity from air permeability: Application in stochastic water infiltration modeling. Water Resources Research. 35, 2387-2400.

Morad, S.; Al-Ramadan, K.; Ketzer, J.M.; De Ros, L.F., 2010. The impact of diagenesis on the heterogeneity of sandstone reservoirs: A review of the role of depositional facies and sequence stratigraphy. AAPG Bulletin. 94, 1267 – 1309.

Moraes, M.A.S., De Ros, L.F., 1990. Infiltrated clays in fluvial Jurassic Sandstones of Reconcavo Basin, northeastern Brazil. Journal of Sedimentary Petrology. 60, 809-819.

Mountney, N., Howell, J., Flint, S., Jerram, D., 1999. Climate, sediment supply and tectonics as controls on the deposition and preservation of the aeolian-fluvial Etjo Sandstone Formation, Namibia. Journal of the Geological Society. 156, 771-777.

Mountney, N., Thompson, D.B., 2002. Stratigraphic evolution and preservation of aeolian dune and damp/wet interdune strata: an example from the Triassic Helsby Sandstone Formation, Cheshire Basin, UK. Sedimentology, 49, 805-833. https://doi.org/10.1046/j.1365-3091.2002.00472.x

Myrow, P.M., Jerolmack, D.J., Perron, J.T., 2018. Bedform disequilibrium. Journal of Sedimentary research. 88, 1096–1113.

Nelson, P. H., 1994. Permeability-porosity relationships in sedimentary rocks. The Log Analyst, 35(03).

Newell, A.J., 2001. Bounding surfaces in a mixed aeolian-fluvial system (Rotliegend, Wesses Basin, SW UK). Marine and Petroleum Geology. 18, 339-347.

Newell, A.J., Pourmalek, A., Butcher, A.S., Shariatipour, S.M., 2019. The importance of lithofacies control on fluid migration in heterogeneous aeolian formations for geological CO2 storage: Lessons from observational evidence and modelling of

bleached palaeoreservoirs at Salt Wash Graben. 91, 17 p. https://doi.org/10.1016/j.ijggc.2019.102841

Noffke, N., Gerdes, G., Klenke, T., and Krumbein, W.E., 1996. Microbially induced sedimentary structures – Examples from modern sediments of siliciclastic tidal flats: Zentralblatt für Geologie und Paläontologie, v. I, 307–316.

Núñez-González, F., and Martín-Vide, 2010. Downstream-migrating antidunes in sand, gravel and sand-gravel mixtures. River Flow, Dittrich, Koll, Aberle & Geisenhainer (eds). 8 p.

O'Sullivan, J., Araya, N., Popineau, J., Renaud, T., Riffault, J., 2023. A Natural State and Production Forecast Model of the Santon Sea Geothermal Field for Lithium Extraction. GRC Transactions. 47, 20 p.

Ohata, K., Naruse, H., Izumi, N., 2022. Upper and lower plane bed definitions revised. Progress in Earth and Planetary Science. 9:23. 13 p. https://doi.org/10.1186/s40645-022-00481-8

Paim, P.S.G. and Scherer, C.M.S., 2007. High-resolution stratigraphy and depositional model of wind- and water-laid deposits in the ordovician Guaritas rift (Southernmost Brazil). Sedimentary Geology. 202, 776-795. doi:10.1016/j.sedgeo.2007.09.003

Paola, C., Borgman, L., 1991. Reconstructing random topography from preserved stratification. Sedimentology. 38, 553-565.

Paxton, S.T.; Szabo, J.O.; Ajdukiewicz, J.M.; Klimentidis, R.E., 2002. Construction of an intergranular volume compaction curve for evaluating and predicting compaction and porosity loss in rigid-grain sandstone reservoirs. AAPG Bulletin. 86, 2047-2067.

Perriaux, J., 1961. Contribuition à la géologie des Vosges gréseuses. Strasbourg: Service de la carte géologique d'Alsace et de Lorraine. 1-236. (In French).

Pickens, J.F., and Grisak, G.E., 1981. Scale-dependent dispersion in a stratified granular aquifer. Water Resources Research. 17, 1191-1211.

Plink-Björklund, P., 2015. Morphodynamics of rivers strongly affected by monsoon precipitation: Review of depositional style and forcing factors. Sedimentary Geology. 323, 110-147. http://dx.doi.org/10.1016/j.sedgeo.2015.04.004

Porter, M.L.,1987. Sedimentology of an ancient erg margin: the Lower Jurassic Aztec Sandstone, southern Nevada and southern California. Sedimentology, 34, 661- 680.

Posamentier, H.W., Jervey, M.T., and Vail, P.R., 1988. Eustatic controls on clastic deposition I – conceptual framework. In: Wilgus, C.K., et. Al., eds., Sea-level changes: an integrated approach: Society of Economic Paleontologists and Mineralogists, Special Publications 42, p. 109-124.

Possemiers, M.; Huysmans, M.; Peeters, L. ; Batelaan, O.; Dassargues, A., 2012. Relationship between sedimentary features and permeability at different scales in the Brussels Sands. Geologica Belgica. 15/3, 156-164.

Priddy, C.L., Clark, S.M., 2021. Spatial variation in the sedimentary architecture of a dryland fluvial system. Sedimentology. 68. 2887-2917.

Puig, J.M., Cabello, P., Howell, J., Arbués, P., 2019. Three-dimensional characterisation of sedimentary heterogeneity and its impact on subsurface flow behaviour through the braided-to-meandering fluvial deposits of the Castissent Formation (late Ypresian, Tremp-Graus Basin, Spain). Marine and Petroleum Geology. 103, 661-680. https://doi.org/10.1016/j.marpetgeo.2019.02.014

Quandt, D., Busch, B., Schimidt, C., Hilgers, C., 2022. Diagenesis and controls on reservoir quality of Lower Triassic red bed sandstones (Buntsandstein) from a marginal basin facies, southwest Germany. Marine and Petroleum Geology. 142, 17 p. https://doi.org/10.1016/j.marpetgeo.2022.105744

Ramanathan R.; Ritzi Jr., R.W.; Allen-King, R.M., 2010. Linking hierarchical stratal architecture to plume spreading in a Lagrangian-based transport model: 2. Evaluation using new data from the Borden Site. Water Resources Research. 46, 1. DOI:10.1029/2007WR006282.

Reesink, A.J.H, Van Den Berg, J.H., Parsons, D.R ., Amsler, M.L., Best, J.L., Hardy, R.J., Orfeo, O., Szupiany, R.N., 2015. Extremes in dune preservation: Controls on the completeness of fluvial deposits. Earth-Science Reviews. 150, 652-665. http://dx.doi.org/10.1016/j.earscirev.2015.09.008

Reis, A.D., Scherer, C.M.S., Owen, A., Amarante, F.B., Ferronato, J.P.F., Pantopoulos, G., Souza, E.G., Ballico, M.B., Aguilar, C.A.G., 2022. A quantitative depositional model of a large distributive fluvial system (megafan) with terminal

aeolian interactions: the Upper Jurassic Guará DFS in southwestern Gondwana. Journal of Sedimentary Research. 92, 460-485. DOI: 10.2110/jsr.2021.040

Ren, W.; Ershadnia, R.; Wallace, D.W.; LaBolle, E.M.; Dai, Z.; Barros, F.P.L.; Soltanian, M.R., 2022. Evaluating the Effects of Multiscale Heterogeneous Sediments on Solute Transport Mixing and Effective Dispersion. Water Resources Research. 58, 9. https://doi.org/10.1029/2021WR031886

Rittner, M., Vermeesch, P., Carter, A., Bird, A., Stevens, T., Garzanti, E., Vezzoli, G., Dutt, R., Xu, Z., Lu, H., 2016. The provenance of Taklamakan desert sand. Earth and Planetary Science Letters. 437, 127–137.

Rodríguez-López, J.P., Clemmensen, L.B., Lancaster, N., Mountey, N.P., Veiga, G.D., 2014. Archean to Recent aeolian sand systems and their sedimentary record: Current understanding and future prospects. Sedimentology. 61, 1487-1534.

Røe, S., 1987. Cross-strata and bedforms of probable transitional dune to upper-stage plane-bed origin from a Late Precambrian fluvial sandstone, northern Norway. Sedimentology. 34, 89-101.

Rogiers, B., Beerten, K., Smeekens, T., Mallants, D., Gedeon, M., Huymans, M., Batelaan, O., Dassargues, A., 2013. The usefulness of outcrop-analogue air-permeameter measurements for analysing aquifer heterogeneity: testing outcrop hydrogeological parameters with independent borehole data. Hydrology and Earth System Sciences. 17, 5155-5166. doi:10.5194/hess-17-5155-2013

Rossi, C., Kälin, O., Arribas, J., Tortosa, A., 2002. Diagenesis, provenance and reservoir quality of Triassic TAGI sandstones from Ourhoud field, Berkine (Ghadames) Basin, Algeria. Marine and Petroleum Geology. 19, 117–142.

Rubin, D.M., and Hunter, R.E., 1982. Bedform climbing in theory and nature. Sedimentology. 29, 121 – 138.

Sambrook Smith, G.H., Best, J.L., Ashworth, P.J., Fielding, C.R., Goodbred, S.L., Prokocki, E.W., 2010. Fluvial form in modern continental sedimentary basins: distributive fluvial systems: Comment. Geol. Forum. 38, e230. http://dx.doi.org/10.1130/G31507C.1

Sanjuan, B., Gourcerol, B., Millot, R., Rettenmaier, D., Jeandel, E., Rombaut, A., 2022. Lithium-rich brines in Europe: An up-date about geochemical characteristics and implications for potential Li resources. Geothermics. 101, 18 p.

Sauderson, H.C., Lockett, F.P.J., 1983. Flume Experiments on bedforms and structures at the dune-plane bed transition. Special Publications International Association of Sedimetologists. 6, 49-58.

Schäfer G., 1991. Einfluß von Schichtenstrukturen und lokalen Einlagerungen auf die Längsdispersion in Porengrundwasserleitern. Mitteilungen des Instituts für Wasserbau, Heft 75, Universität Stuttgart, 154p., ISBN 3-921694-75-2.

Schäfer, G. & Kobus, H.E., 1989. Mass transport in an artificial heterogeneous aquifer: Experiments and numerical modelling. In: Kobus & Kinzelbach, 1989. Contaminant Transport in Groundwater. Balkema, Rotterdam. ISBN 90 6191 879 0

Sharp, R.P., 1963. Wind ripples: Journal of Geology. 71, 617 – 636.

Scherer, C.M.S., 2000. Eolian dunes of the Botucatu Formation (Cretaceous) in southernmost Brazil: morphology and origin. Sedimentary Geology. 137, 63-84. https://doi.org/10.1016/S0037-0738(00)00135-4.

Scherer, C.M.S. and Lavina, E.L.C., 2005. Sedimentary cycles and facies architecture of aeolian-fluvial strata of the Upper Jurassic Guará Formation, southern Brazil. Sedimentology. 52, 1323-1341. doi: 10.1111/j.1365-3091.2005.00746.x

Scherer, C.M.S., Goldberg, K., Bardola, T., 2015. Facies architecture and sequence stratigraphy of an early post-rift fluvial succession, Aptian Barbalha Formation, Araripe Basin, northeastern Brazil. Sedimentary Geology. 322, 43-62. http://dx.doi.org/10.1016/j.sedgeo.2015.03.010.

Schmidt, C., 2020. Compaction and cementation controls on reservoir quality in Buntsandstein red beds. PhD dissertation from the KIT Faculty of Civil Engineering, Earth and Environmental Sciences of the Karlsruhe Institute of Technology (KIT)

Scorgie, J.C., Worden, R.H., Utley, J.E.P., Roche, I.P., 2021. Reservoir quality and diagenesis of Triassic sandstones and siltstones from arid fluvial and playa margin environments: A study of one of the UK’s earliest producing oilfields. Marine and Petroleum Geology. 131, 28 p. https://doi.org/10.1016/j.marpetgeo.2021.105154

Sethi, R., Di Molfetta, A., 2019. Groundwater Engineering. Springer Tracts in Civil Engineering. https://doi.org/10.1007/978-3-030-20516-4_10

Sharma, N., Whittaker, A.C., Watkins, S.E., Valero, L., Verite, J., Puigdefabregas, C., Adatte, T., Garces, M., Guillocheau, F., Castelltort, S., 2023. Water discharge variations control fluvial stratigraphic architecture in the Middle Eocene Escanilla formation, Spain. Nature Scientific Reports. 15 p. https://doi.org/10.1038/s41598-023-33600-6

Sheykhinasab, A., Mohseni, A.A., Bahari, A.B., Naruei, E., Davoodi, S., Aghaz, A., Mehrad, M., 2023. Prediction of permeability of highly heterogeneous hydrocarbon reservoir from conventional petrophysical logs using optimized data-driven algorithms. Journal of Petroleum Exploration and Production Technology. 13, 661-689. https://doi.org/10.1007/s13202-022-01593-z

Skelly, R.L., Bristow, C.S., Ethridge, F.G., 2003. Architecture of channel-belt deposits in an aggrading shallow sandbed braided river: the lower Niobrara River, northeast Nebraska. Sedimentary Geology. 158. 249-270. doi:10.1016/S0037-0738(02)00313-5

Smith, J.M., and Schwartz, F.W., 1980. Mass transport 1, A stochastic analysis of macroscopic dispersion. Water Resources Research. 16, 303-313.

Smith, N.D., 1970. The Braided Stream Depositional Environment: Comparison of the Platte River with Some Silurian Clastic Rocks, North-Central Appalachians. Geological Society of Ameruica Bulletin. 81, 2993 – 3014.

Snowdon, A. P., Normani, S. D., Sykes, J. F., 2021. Analysis of crystalline rock permeability versus depth in a Canadian Precambrian rock setting. Journal of Geophysical Research: Solid Earth, 126, 21 p. https://doi.org/10.1029/2020JB020998

Southard, J. B., Boguchwal, L. A. 1 990. Bed configurations in steady unidirectional water flows. Part 2. Synthesis of flume data. J. Sediment. Petrol. 60, 658-79.

Southard, J.B., 1991. Experimental determination of bed-form stability. Annual Review of Earth and Planetary Sciences. 19(1), 423-455. DOI: 10.1146/annurev.ea.19.050191.002231

Steel, R.J., Thompson, D.B., 1983. Structures and textures in Triassic braided stream conglomerates ('Bunter' Pebble Beds) in the Sherwood Sandstone Group, North Staffordshire, England. Sedimentology. 30, 341-367.

Talon, L., Ollivier-Triquet, E., Dentz, M., Bauer, D., 2023. Transient dispersion regimes in heterogeneous porous media: On the impact of spatial heterogeneity in permeability and exchange kinetics in mobile-immobile transport. Advances in Water Resources. 174, 104425. https://doi.org/10.1016/j.advwatres.2023.104425

Teichert, C., 1958. Concepts of facies. Bulletin of the American Association of Petroleum Geologists. 42, 2718-2744.

Theel, M., Huggenberger, P. & Zosseder, K. Assessment of the heterogeneity of hydraulic properties in gravelly outwash plains: a regionally scaled sedimentological analysis in the Munich gravel plain, Germany. Hydrogeol J 28, 2657–2674 (2020). https://doi.org/10.1007/s10040-020-02205-y

Théobald, N., Perriaux, J., Langenfeld, F., Both, J., 1967. Carte géologique 1/50000 Bitche- Walschbronn XXXVIII3. (In French).

Thompson, J., Parkes, D., Hough, E., Wakefield, O., 2019. Using core and outcrop analogues to predict flow pathways in the subsurface: examples from the Triassic sandstones of north Cheshire, UK. Advances in Geosciences. 49, 121-127.

Trewin, N., 1993. Mixed aeolian sandsheet and fluvial deposits in the Tumblagooda Sandstone, Western Australia. In: NORTH, C.P. and PROSSER, D.J. (eds), 1993, Characterization of Fluvial and Aeolian Reservoirs. Geological Society Special Publications. No 73, 219-230.

Valocchi A.J., 1985. Validity of the local equilibrium assumption for modeling sorbing solute transport through homogeneous soils. Water Resour. Res. 21 (6), 808-820.

Vaute, L., Gigleux, S., Ngyen-The, 2007. Eaux souterraines du départment des Vosges: Caractérisation des principals ressources exploitables et revision du modèle de gestion de la nappe des grés du Trias inférieur. Rapport final, BRGM/RP-55653-FR. 396 p. (In French).

Vaute, L., Innocent, C., Fourniguet, 2013. Actualisation du modèle hydrogeologique de la nappes des grès du Trias en Lorraine. Rapport final. BRGM/RP-62405-FR. 60p. (In French).

Veiga, G.D., Spalletti, L.A., Flint, S., 2002. Aeolian/Fluvial interaction and high-resolution sequence stratigraphy of a non-marine lowstand wedge: the Avilé Member of the Agrio Formation (Lower Cretaceous), central Neuquén Basin, Argentina. Sedimentology. 49, 1001-1019. DOI: 10.1046/j.1365-3091.2002.00487.x

Ventra, D. and Moscariello, A., 2023. Geology of Fluvial-Fan Deposits: Facies Patterns, Architectural Organisation and Implications for Economic Geology. Chapter 14 in: Wilkinson, M.J. and Gunnell, Y., 2023. Fluvial Megafans on Earth and Mars. https://doi.org/10.1017/9781108525923

Vernoux, J.F., Genter, A., Razin, P., Vinchon, C., 1995. Geological and petrophysiscal parameters of a deep fractured sandstone formation as applied to geothermal exploitation, EPS-1 borehole, Soultz-sous-Forets, France. Rapport BRGM R 35622, 70 p.

Vidal, J., Genter, A., 2018. Overview of naturally permeable fractured reservoirs in the central and southern Upper Rhine Graben: Insights from geothermal wells. Geothermics. 74, 53-73. https://doi.org/10.1016/j.geothermics.2018.02.003

Wadsworth, F. B., Vasseur, J., Heap, M. J., Carbillet, L., Dingwell, D. B., Reuschlé, T., & Baud, P., 2023. A universal model for the permeability of sintered materials. Acta Materialia, 250, 118859.

Walker, R.G., 1992. Facies, facies models and modern stratigraphic concepts. In: Walker, R.G., James, N.P. (Eds.), Facies Models - in Response to Sea Level Change, 1–14. ISBN 0-0919216-49-8

Walker, S., Holbrook, J., 2023. Structures, architecture, vertical profiles, paleohydrology and taphonomy of an upper-flow-regime-dominated fluvial system, the Triassic Dockum Group of the Palo Duro Canyon, Texas. Sedimentology. 70, 645-684. doi: 10.1111/sed.13041.

Wang, H.F., and Anderson, M.P., 1995. Introduction to groundwater modelling: Finite Difference and Finite Element Methods. Academic Press. 249 p.

Wang, J., Plink-Björklund, P., 2019. Stratigraphic complexity in fluvial fans: Lower Eocene Green River Formation, Uinta Basin, USA. Basin Research. 31, 892-919. https://doi.org/10.1111/bre.12350

Weissmann, G.S., Hartley, A.J., Nichols, G.J., Scuderi, L.A., Olson, M., Buehler, H., Banteah, R., 2010. Fluvial form in modern continental sedimentary basins: distributive fluvial systems. Geology. 38, 39–42.

Weissmann, G.S., Hartley, A.J, Scuderi, L.A., NIchols, G.J., Owen, A., Wright, S., Felicia, A.L., Holland, F., Anaya, F.M.L., 2015. Fluvial geomorphic elements in modern sedimentary basins and their potential preservation in the rock record: A review. Geomorphology. 205, 187-219. https://doi.org/10.1016/j.geomorph.2015.09.005

Weissmann, G.S., Pickel, A., McNamara, K.C., Frechette, J.D., Kalinovich, I., Allen-King, R.M., Jankovic, I., 2015. Characterization and quantification of aquifer heterogeneity using outcrop analogs at the Canadian Forces Base Borden, Ontario, Canada. Geological Society of America Bulletin. 127, 1021-1035. doi: 10.1130/B31193.1

Wilkinson, J.M., Gunnel, Y., 2023. Megafans as Major Continental Landforms. Chapter 1 in: Wilkinson, M.J. and Gunnell, Y., 2023. Fluvial Megafans on Earth and Mars. https://doi.org/10.1017/9781108525923.

Witherspoon, P.A., Neuman, S.P., 1972. Finite Element Methods in Hydrogeology. BRGM. 72 SGN 374 AME.

Wizevich, M.C., 1992. Sedimentology of Pennsylvanian quartzose sandstones of the Lee Formation, central Appalachian Basin: fluvial interpretation based on lateral profile analysis. Sedimentary Geology. 78, 1–47.

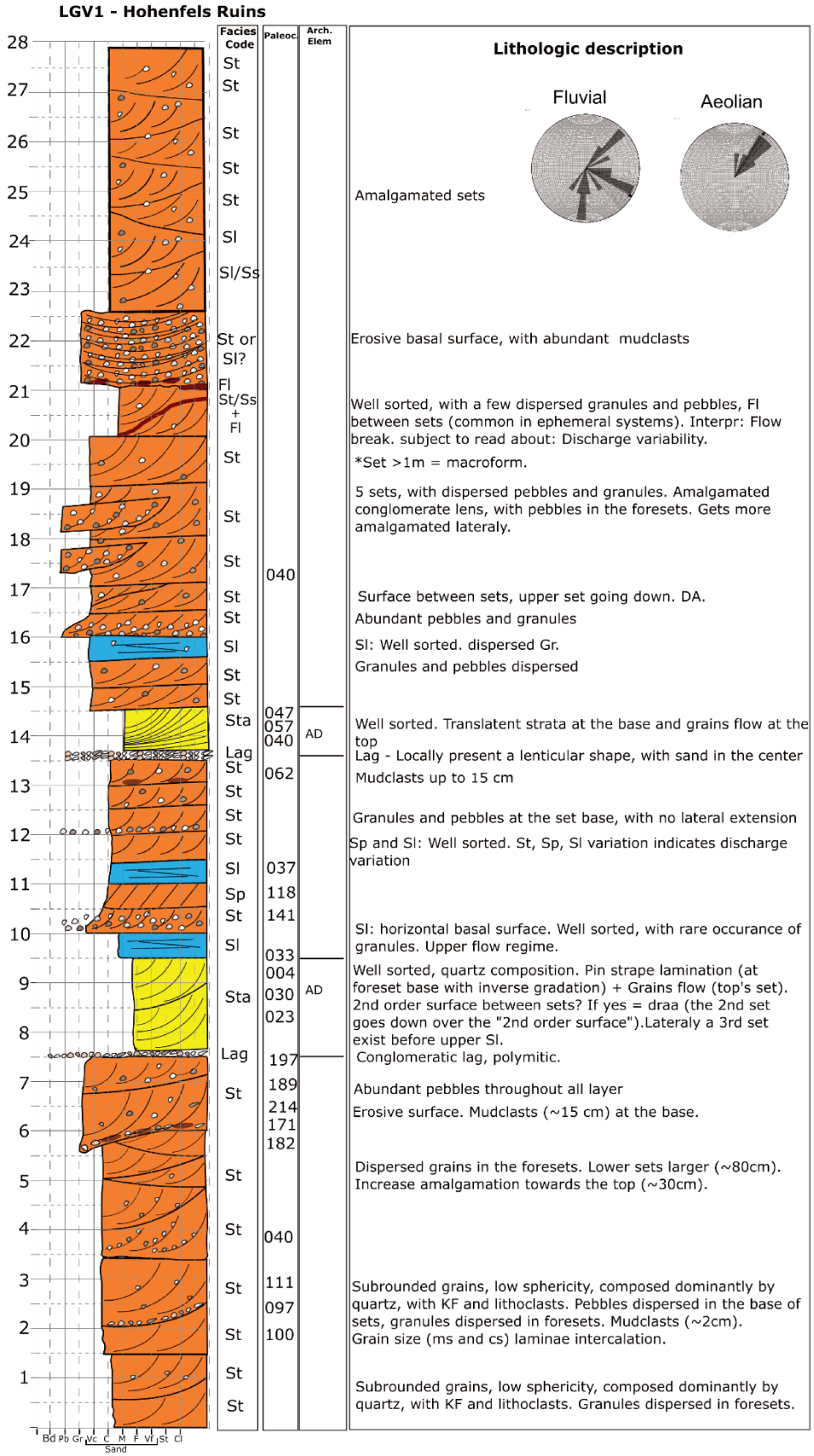
Yin, M.; Ma, R.; Zhang, Y. ; Lin, J. ; Guo, Z. ; Zheng, C., 2023. Competitive control of multiscale aquifer heterogeneity on solute transport in an alluvial aquifer. Journal of Hydrology. 616, 128819. https://doi.org/10.1016/j.jhydrol.2022.128819

Zellman, K.L., Plink-Björklund, P., Fricke, H.C., 2021. Testing hypotheses on signatures of precipitation variability in the river and floodplain deposits of the Paleogene San Juan Basin, New Mexico, U.S.A. Journal of Sedimentary Research. 90, 1770-1801. DOI: 10.2110/jsr.2020.75

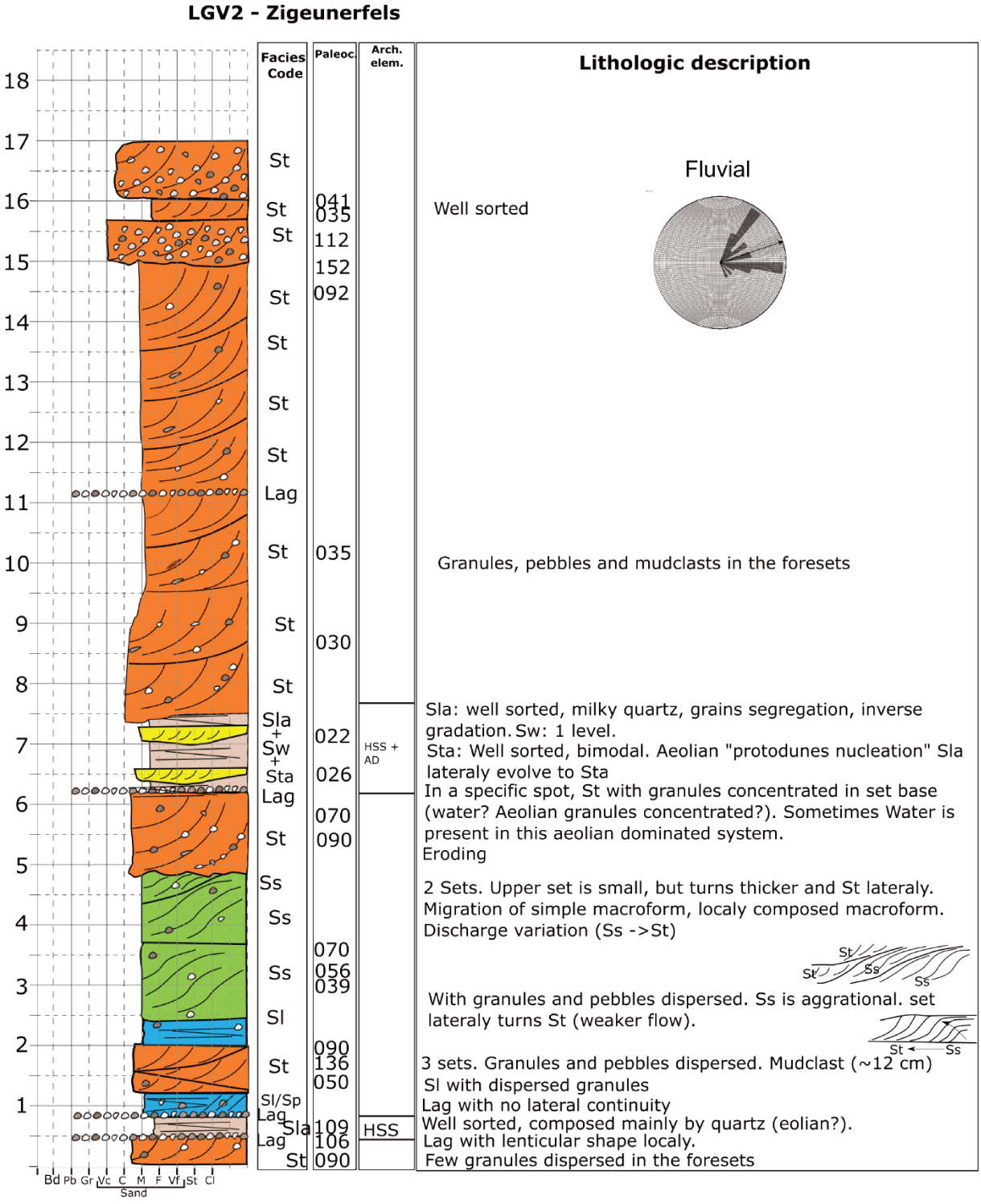
Zheng, C. & Gorelick, S.M., 2005. Analysis of Solute Transport in Flow Fields Influenced by Preferential Flowpaths at the Decimeter Scale. Groundwater. 41, 142-155. https://doi.org/10.1111/j.1745-6584.2003.tb02578.x

ANNEX

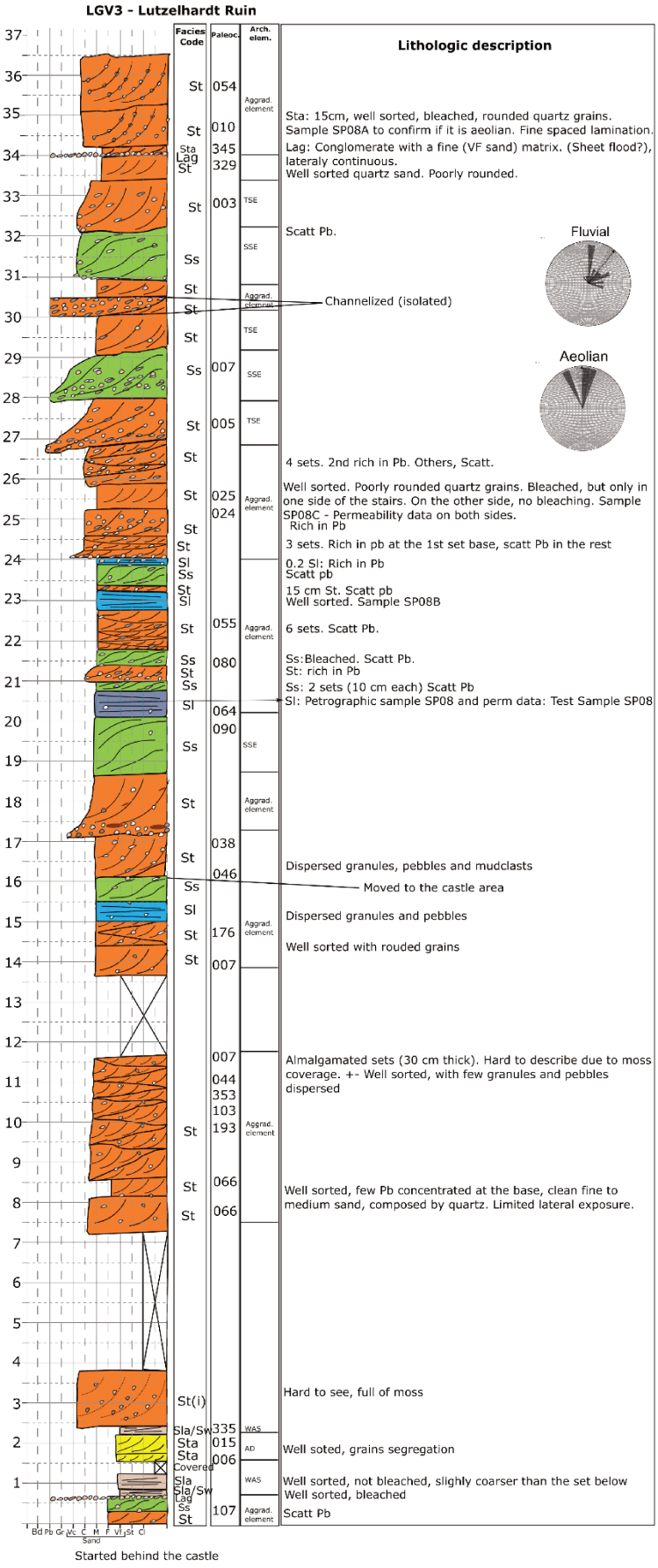
Sedimentary log outcrop LGV1



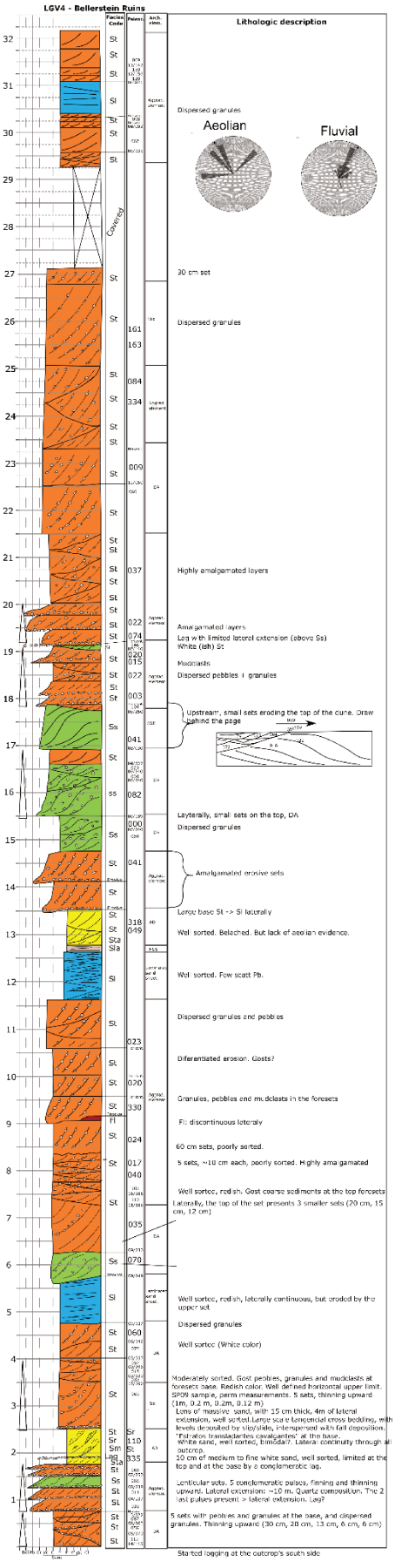
Sedimentary log outcrop LGV2



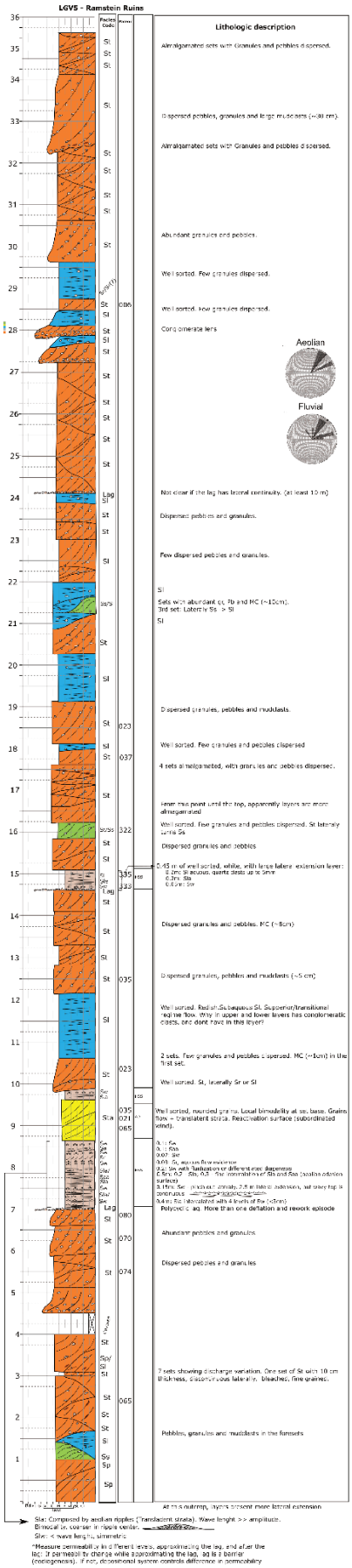
Sedimentary log outcrop LGV3



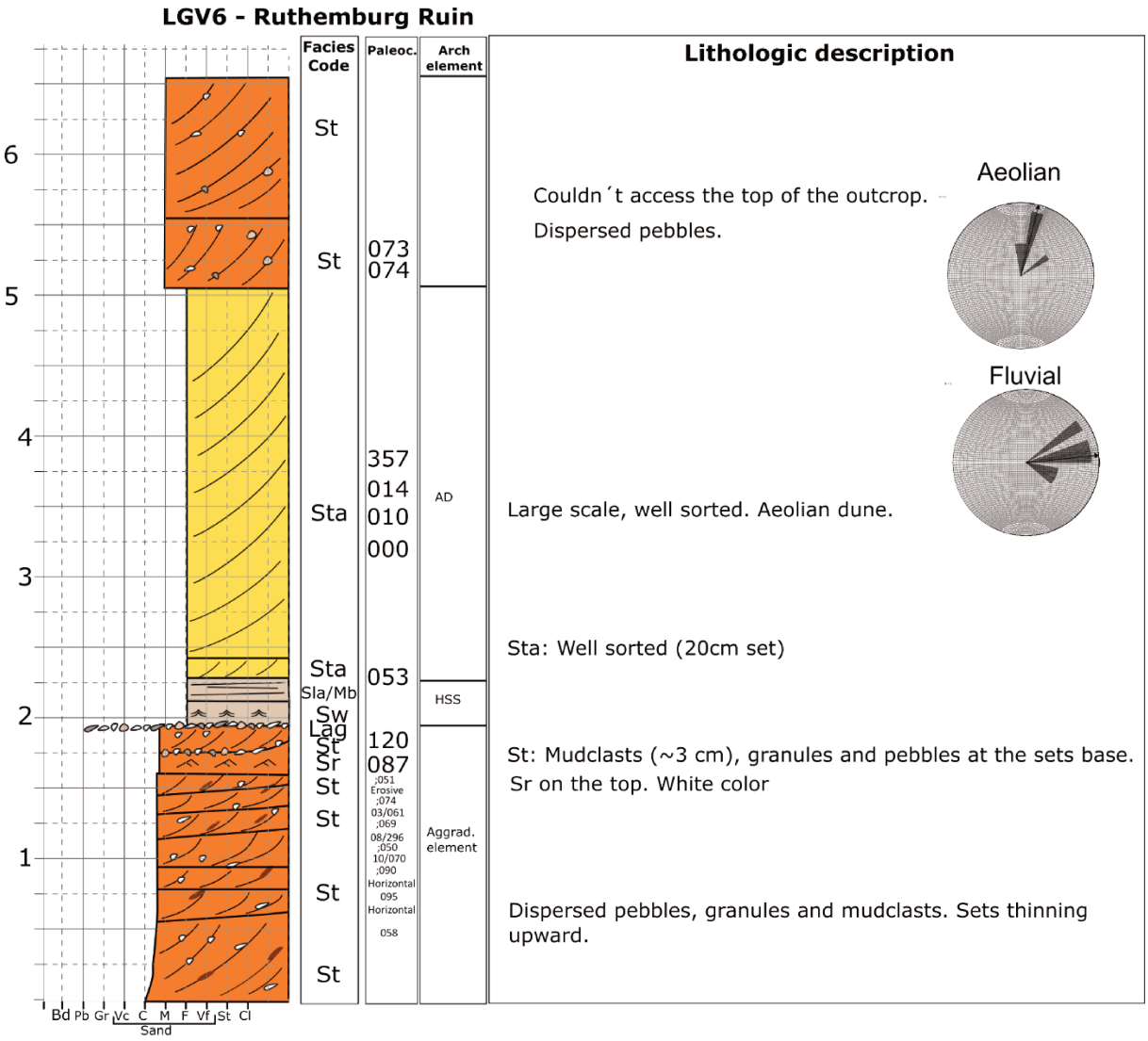
Sedimentary log outcrop LGV4



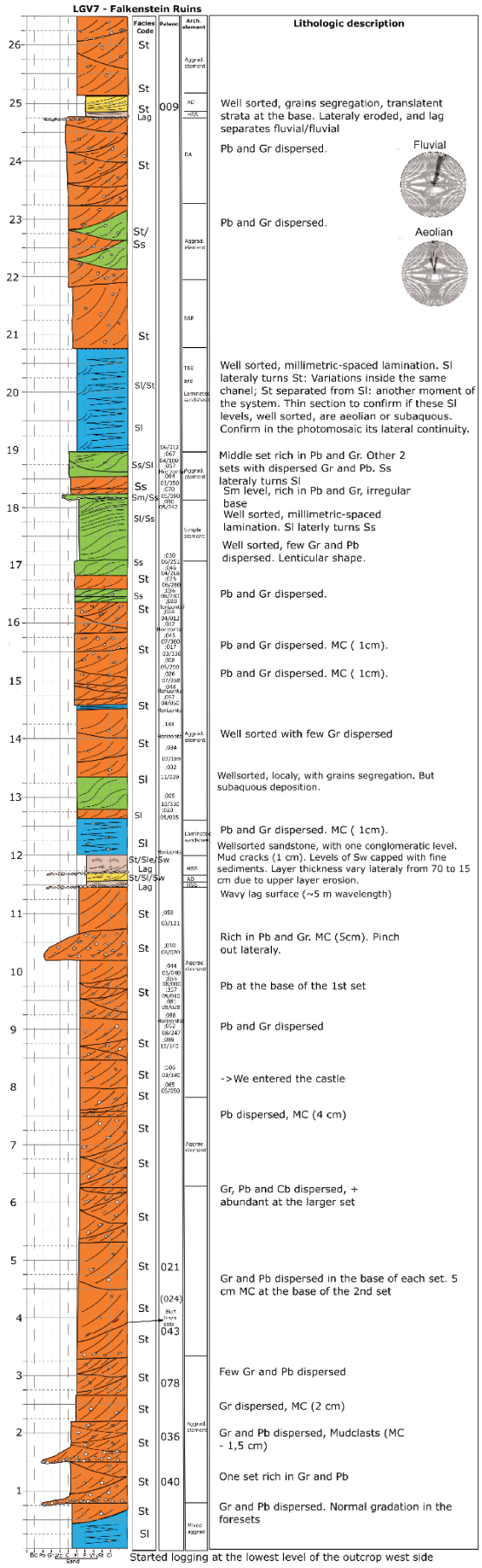
Sedimentary log outcrop LGV5



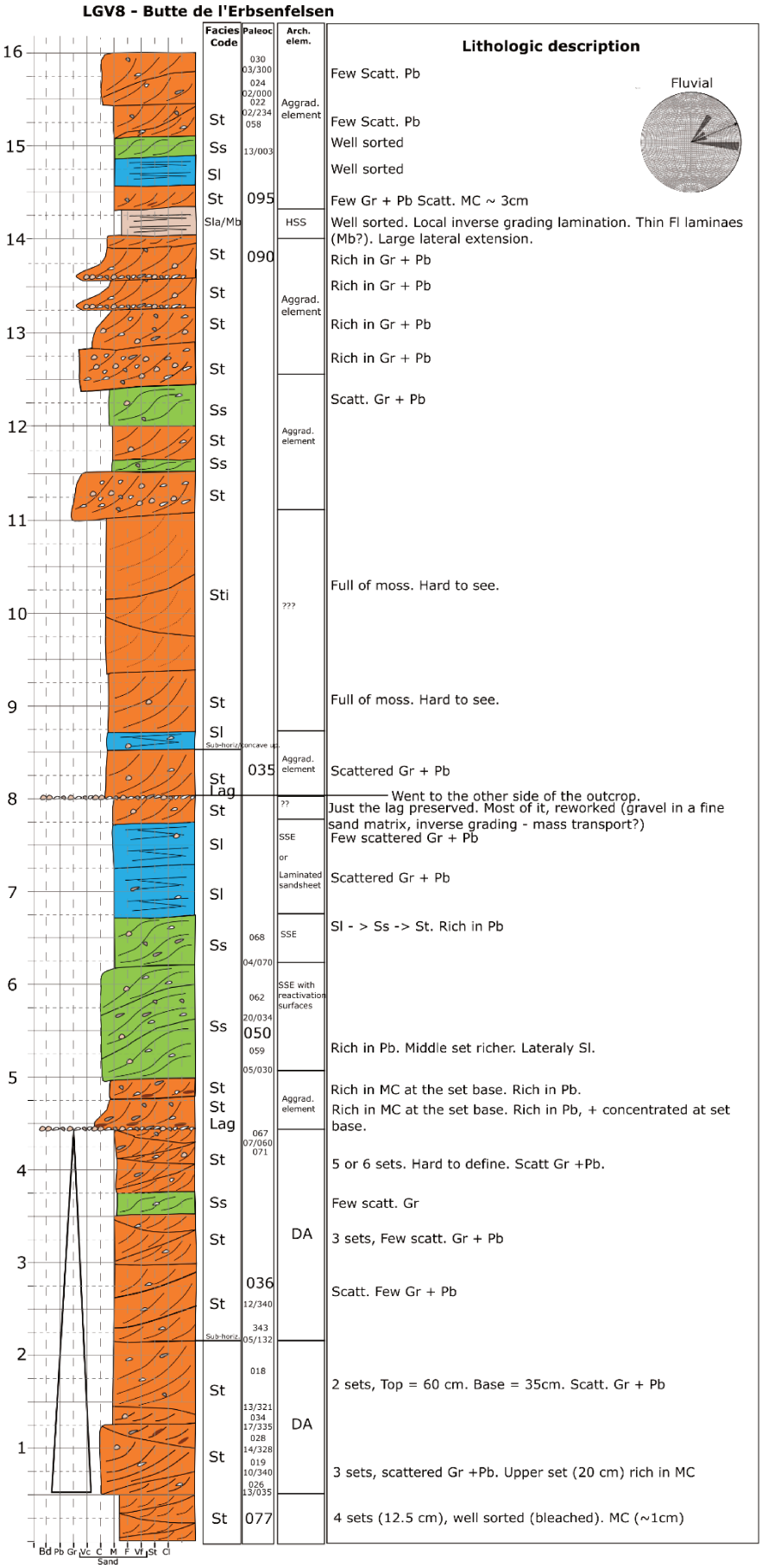
Sedimentary log outcrop LGV6



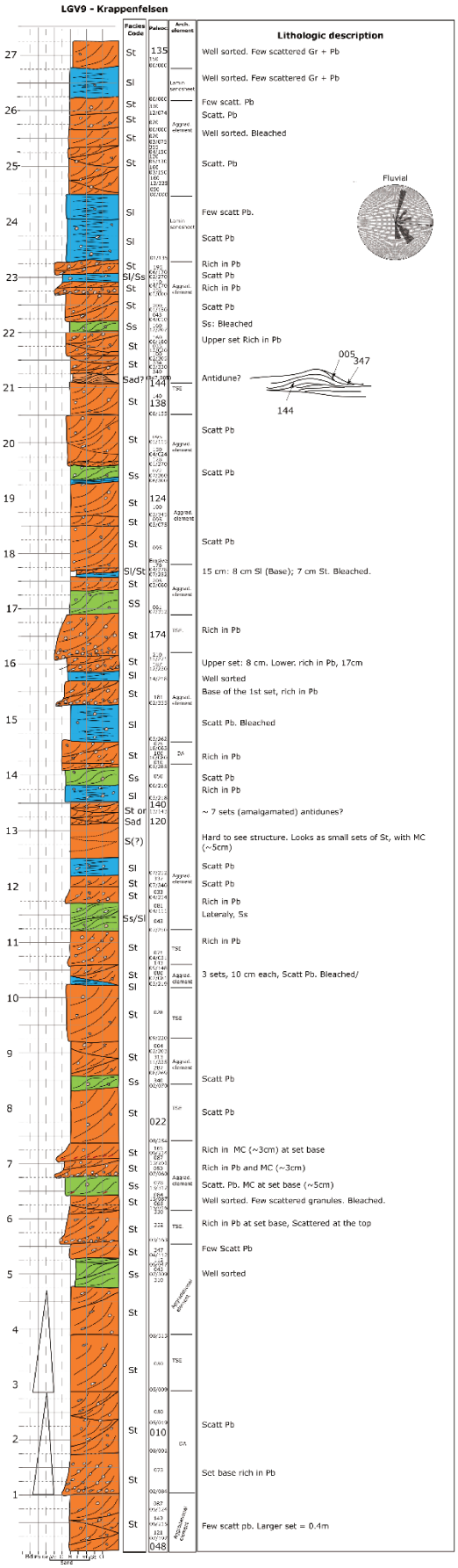
Sedimentary log outcrop LGV7



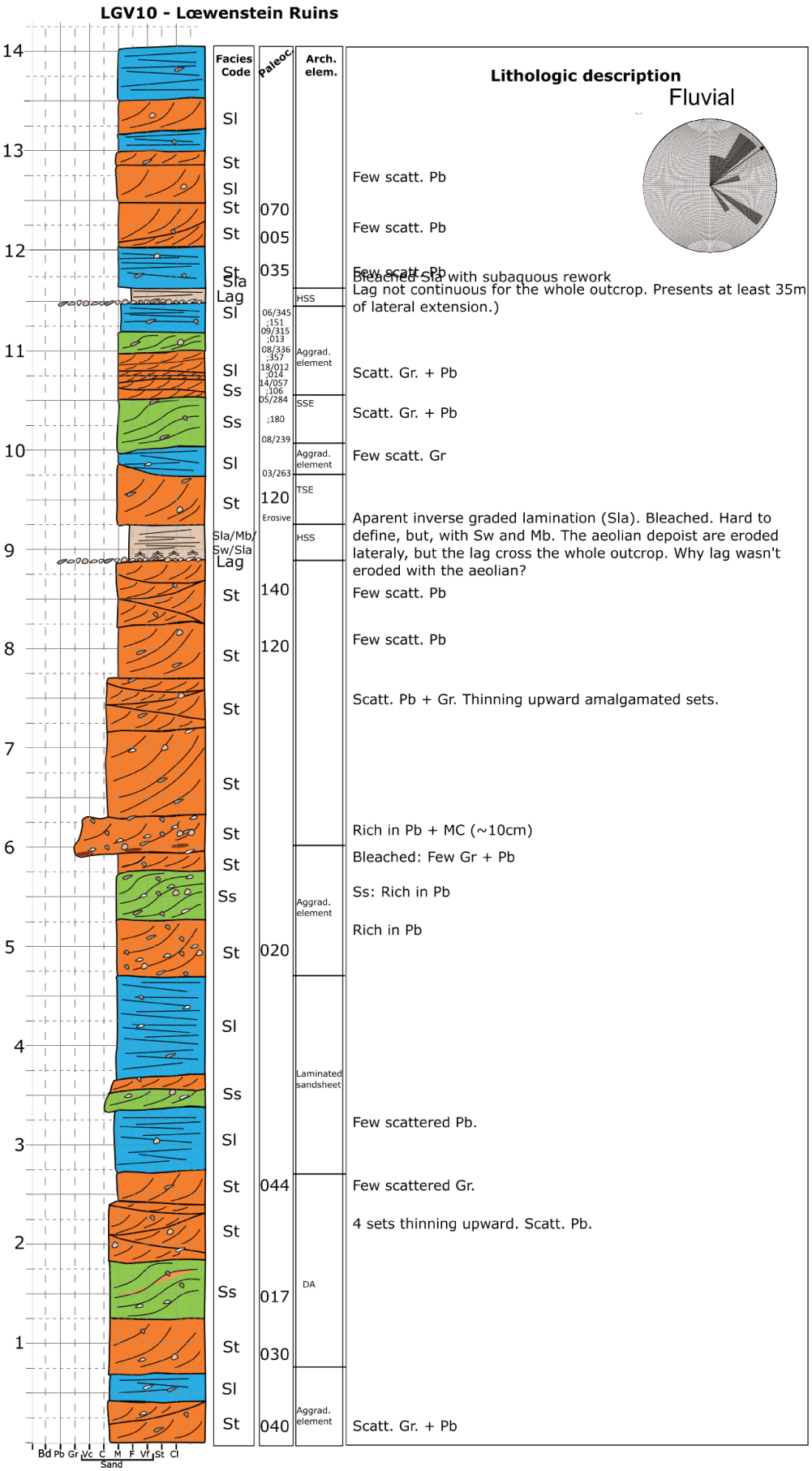
Sedimentary log outcrop LGV8



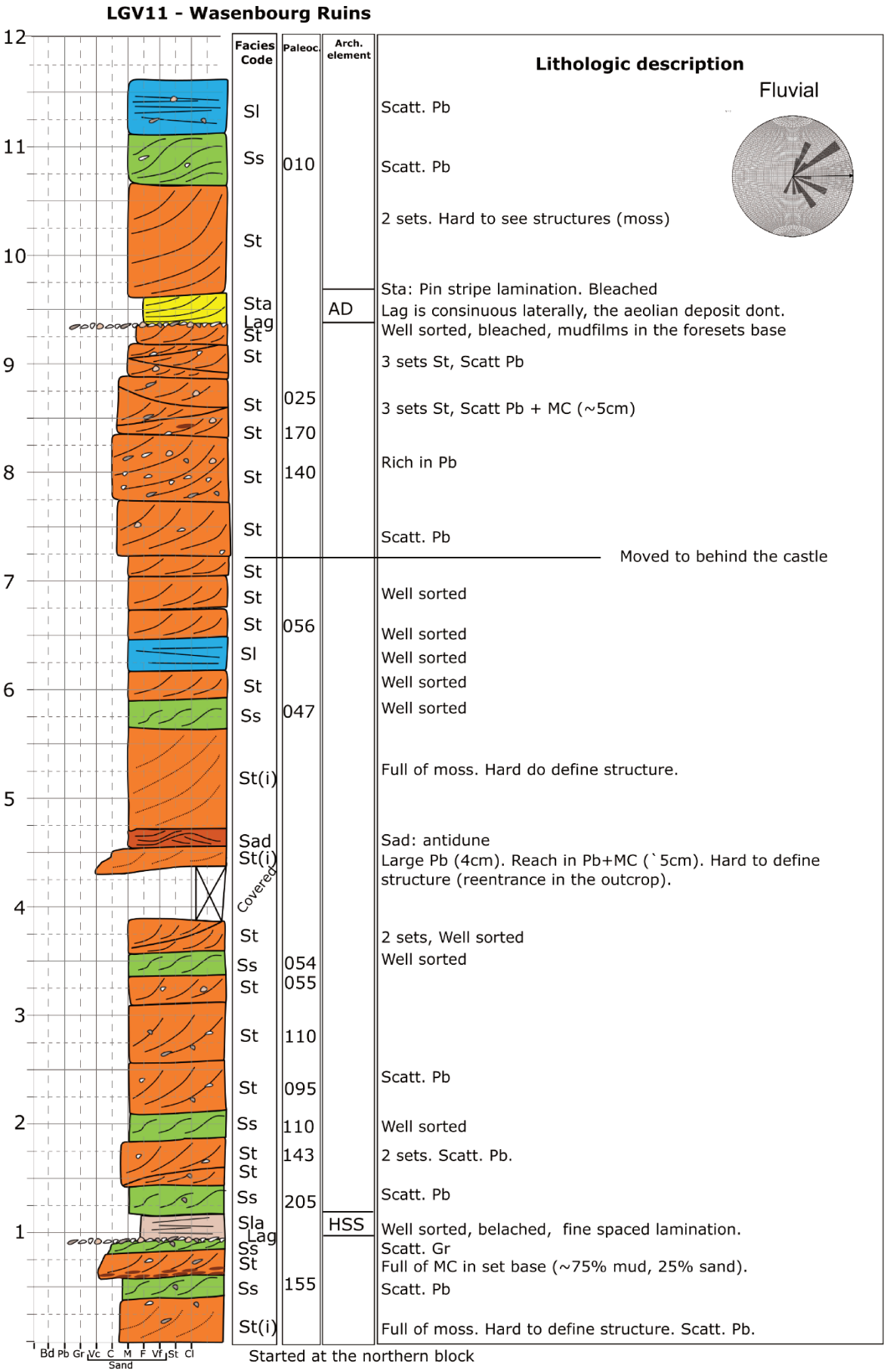
Sedimentary log outcrop LGV9



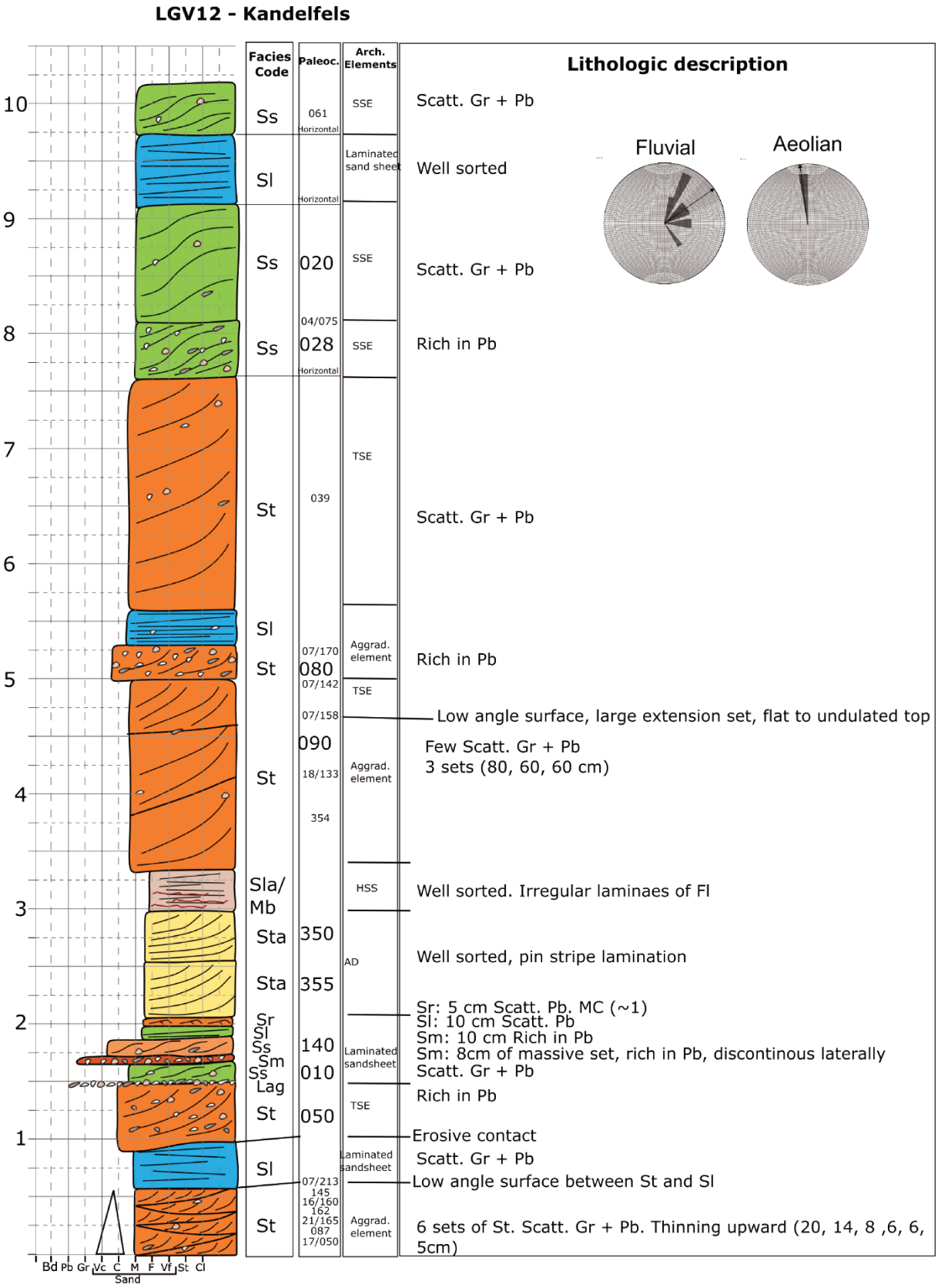
Sedimentary log outcrop LGV10



Sedimentary log outcrop LGV11



Sedimentary log outcrop LGV12



Sedimentary log from outcrop LGV13 and from the core EPS1 are available upon request, such as excel table with quantitative and qualitative sedimentological data from the logs, and the permeability data.

Python code to generate the stochastic K distribution, constrained by maximum and minimum values:

```
import numpy as np
from scipy.stats import truncnorm
#WWL
# Define the constraints
min_limit = -9.77347633746203
max_limit = -5.66628967642472
# Replace these with the desired mean and standard deviation
mean_original = -7.38645118466121  # Replace with your dataset's mean
std_dev_original = 1.18972593368279  # Replace with your dataset's standard deviation
num_samples = 31354  # Change to the desired number of samples
# Calculate the lower and upper bounds for the truncated distribution
a = (min_limit - mean_original) / std_dev_original
b = (max_limit - mean_original) / std_dev_original
# Generate synthetic data following a truncated normal distribution
WWL_data_trunc2 = truncnorm.rvs(a, b, loc=mean_original, scale=std_dev_original, size=num_samples)
# Save synthetic data to a CSV file
np.savetxt("WWL_data_trunc2.csv", WWL_data_trunc2, delimiter=",")
```

Université de Strasbourg

Lucas MEDEIROS BOFILL

École et observatoire des sciences de la Terre
Université de Strasbourg

From Outcrop to Fluid-Flow: Sedimentary Architecture, Permeability Heterogeneity, and Effect of Sedimentary Facies in Fluid-Flow Modelling: A Case Study of the Middle Buntsandstein Continental Sandstones (Lower Triassic, Eastern France)

Résumé

Au fossé rhénan supérieur, dans l'est de la France, le Buntsandstein du Trias inférieur constitue un important réservoir d'eau souterraine et de saumures géothermiques riches en lithium. L'objectif scientifique de cette étude est de comprendre l'architecture de la Formation du Grès Vosgien inférieur (LGV), Buntsandstein moyen ; comment les processus sédimentologiques, à différentes échelles, génèrent des hétérogénéités significatives de perméabilité ; et l'effet de telles hétérogénéités sur les résultats de la modélisation des flux de fluides. L'étude utilise une caractérisation sédimentologique à haute résolution, par le biais de descriptions de profils verticaux, de modèles numériques d'affleurements et d'analyses pétrographiques. Ensuite, les mesures de perméabilité sont couplées aux données sédimentologiques, afin d'identifier différentes échelles de contrôles sédimentaires sur la distribution de la perméabilité. Enfin, un modèle conceptuel hydrostratigraphique réaliste en 2D est généré comme référence, pour évaluer comment différents scénarios de simplification des hétérogénéités impactent la modélisation des flux de fluides, en ce qui concerne le temps de résidence des particules, la macro-dispersivité et l'anisotropie mise à l'échelle.

Les résultats indiquent que 93% du LGV est composé de grès déposés par un système fluvial en tresses, avec des indices suggérant que la variabilité du débit était un facteur de contrôle principal de la distribution des faciès sédimentaires et des hétérogénéités.

Le modèle de superposition du LGV révèle des périodes où les processus fluviaux étaient absents, et les processus éoliens dominaient le transport et le dépôt des sédiments, constituant 7% de l'épaisseur totale du LGV. Les dépôts éoliens montrent des indications de la présence persistante d'eau dans le système, soit en raison de la montée de la nappe phréatique, soit de crues éphémères.

Dans l'association de faciès des chenaux fluviaux, une relation inverse entre les conditions du régime fluvial et la perméabilité de ses faciès est observée. Dans l'association de faciès déposés par le vent et l'eau (WWL), la distribution de la perméabilité est directement influencée par les conditions climatiques, où des feuilles de sable hybrides à faible perméabilité ont été déposées dans des conditions plus humides, et des dunes éoliennes à haute perméabilité dans des conditions plus arides. Cependant, malgré la haute perméabilité des dunes éoliennes, l'architecture des WWL implique un faible potentiel de connectivité. La compaction est le principal processus influençant la perméabilité et la porosité du LGV. Les échantillons avec une proportion plus élevée de lithoclastes et d'argile infiltrée ont enregistré un degré de compaction plus avancé, tandis que les échantillons avec un pourcentage plus élevé de surcroissance de quartz ont montré un degré de compaction moindre. La surimpression diagénétique a affecté les différents faciès de manière distincte, indiquant que les processus et l'architecture sédimentaires primaires régissent la distribution des hétérogénéités de perméabilité dans le LGV. Les données de perméabilité provenant des affleurements ont montré des valeurs médianes jusqu'à trois ordres de grandeur plus élevées que celles des données de subsurface. Cependant, les mêmes faciès, et des tendances similaires des réponses porosité-perméabilité relatives aux différents faciès, sont observées entre les affleurements et les échantillons de forage, mettant en évidence la sédimentologie comme un proxy indispensable pour les études d'hétérogénéité des réservoirs.

Les simulations de flux de fluides démontrent que les simplifications du modèle, que ce soit par l'imputation de valeurs de perméabilité déterministes (moyenne) ou par la distribution stochastique de la perméabilité sans contrainte des architectures sédimentaires réalistes, impactent directement les flux horizontaux et verticaux concernant le temps de résidence des particules. Les macrodispersivités sont principalement affectées lorsque les données de perméabilité ne sont pas distribuées en tenant compte des géométries des caractéristiques sédimentaires. Pour le flux horizontal, le fait de ne pas discrétiser les faciès sédimentaires individuels conduit à

sous-estimer les zones de flux préférentiel, impactant la prédiction des premières arrivées de particules, et soulignant les inefficacités potentielles dans les plans de remédiation des contaminants des eaux souterraines. La queue longue observée dans la distribution du temps de résidence des particules suggère que les concepts fickiens ne peuvent pas décrire la macrodispersion pour le domaine du modèle. De plus, la discrétisation entre les associations de faciès distinctes - chenal fluvial et faciès déposés par le vent et l'eau - génère une anisotropie mise à l'échelle (Kv/Kh) de 0,3, démontrant le rôle significatif de l'hétérogénéité sédimentaire dans la modélisation hydrogéologique.

Abstract

At the Upper Rhine Graben, in Eastern France, the Lower Triassic Buntsandstein serves as an important reservoir of groundwater and lithium-rich geothermal brines. The scientific objective of this study is to comprehend the architecture of the Lower Grès Vosgien Formation (LGV), Middle Buntsandstein; how sedimentological processes, at different scales, generate significant permeability heterogeneities; and the effect of such heterogeneity in fluid-flow modelling results. The study employs high-resolution sedimentological characterisation, through vertical profile descriptions, digital outcrop model, and petrographic analysis. Subsequently, permeability measurements are coupled with sedimentological data, to identify different scales of sedimentary controls on permeability distribution. Finally, a realistic 2D hydrostratigraphyc conceptual model is generated as a reference, to evaluate how

different scenarios of heterogeneity simplification impact fluid-flow modelling, concerning particle residence time, macro-dispersivity and upscaled anisotropy.

Results indicate that 93% of the LGV is composed of sandstones deposited by a braided fluvial system, with evidence suggesting that discharge variability was a main depositional controlling factor of sedimentary facies and heterogeneity distribution. The LGV stacking pattern reveals periods when fluvial processes were absent, and aeolian processes dominated sediment transport and deposition, constituting 7% of the total LGV thickness. The aeolian deposits record indications of persistent water in the system, either due to water table rise or ephemeral floods

In the fluvial channel facies association, an inverse relationship between fluvial flow regime conditions and the permeability of its facies is observed. In the wind- and water-laid facies association (WWL), permeability distribution is directly influenced by climatic conditions, where low permeability hybrid sand sheets were deposited in more humid conditions, and high permeability aeolian dunes in more arid conditions. However, despite the high permeability of the AD, the architecture of the WWL implies low connectivity potential. Compaction is the main process influencing the permeability and porosity of the LGV. Samples with a higher proportion of lithoclasts and infiltrated clay recorded a more advanced degree of compaction, whereas samples with a higher percentage of quartz overgrowth exhibited a lower degree of compaction. The diagenetic overprint affected the distinct facies differently, indicating that primary sedimentary processes and architecture govern the distribution of permeability heterogeneity in the LGV. Permeability data from outcrops exhibited median values up to three orders of magnitude higher than those from subsurface data. However, the same facies, and similar trends of relative porosity-permeability responses to the distinct facies, are observed between outcrops and borehole samples, highlighting sedimentology as an indispensable proxy for reservoir heterogeneity studies.

Fluid-flow simulations demonstrate that model simplifications, whether through imputing deterministic permeability values (mean), or by stochastically distributing permeability unconstrained by realistic sedimentary architectures, directly impact both horizontal and vertical flow concerning particles' residence time. Macrodispersivities are mainly affected when permeability data is distributed not constrained by the geometries of the sedimentary features. For horizontal flow, failing to discretise individual sedimentary facies results in underestimating preferential flow zones, impacting the prediction of the first particle arrivals, and highlighting potential

inefficiencies in groundwater contaminant remediation plans. The long tailing observed in particles' residence time distribution suggests that Fickian concepts cannot describe macrodispersion for the model domain. Moreover, discretisation between distinct facies associations—fluvial channel and wind- and water-laid facies—generates an upscaled anisotropy (Kv/Kh) of 0.3, demonstrating the significant role of sedimentary heterogeneity in hydrogeological modelling.

Keywords:

Braided fluvial, aeolian, Lower Triassic, Buntsandstein, quantitative facies analysis, sedimentology, permeability, heterogeneity, petrography, fluid-flow, solute transport modelling